ABSTRACT

MODELING AND EXPERIMENTAL VALIDATION OF A SINGLE-FEED SEMI-BATCH PRECIPITATION PROCESS

by
Ernesto Uehara-Nagamine

Crystallization is a widely practiced unit operation throughout the chemical and pharmaceutical process industries. Despite its widespread application, crystallization still suffers a disproportionate number of process difficulties due to the complexity of the steps involved in the process. In particular, the final characteristics of the product are strongly affected by the mixing conditions during the process. The development of a validated modeling approach would be highly valuable for the successful prediction of the crystal characteristics under differing mixing conditions.

In the present work, the single-feed semi-batch precipitation process of barium sulfate in a stirred tank was experimentally studied and numerically predicted using a micromixing model based on CFD. A commercial CFD package (FLUENT) was used to simulate the flow field and predict the energy dissipation rate distributions within the reactor. The precipitation zone originated from the feed point was tracked using a random walk model. Available correlations were used for the calculation of the nucleation and crystal growth rates. The mass transfer coefficient for the crystal growth was assumed to be dependent on both the average crystal size and the local energy dissipation rate. Finally, a micromixing model (E-Model) was incorporated to predict the effects on the final crystal size distribution of a number of operating and geometric variables as well as the effect of vessel scale.

An extensive number of barium sulfate precipitation experiments were conducted to determine the crystal size distribution and validate the proposed model. The effect of the process variables (such as volume ratio, mean initial concentration and stoichiometry ratio), operating conditions (including impeller speed, diameter and off-bottom clearance), and vessel scale on the crystal size distribution were experimentally determined and numerically predicted. In general, very good agreement between experimental data and model predictions was obtained. The model was typically able to capture all of the most important features of the precipitation process. The proposed approach has a significant potential for the prediction of the performance of crystallization processes in industrial applications.

MODELING AND EXPERIMENTAL VALIDATION OF A SINGLE-FEED SEMI-BATCH PRECIPITATION PROCESS

by
Ernesto Uehara-Nagamine

A Dissertation
Submitted to the Faculty of
New Jersey Institute of Technology
In Partial Fulfillment of the Requirements for the Degree of
Doctor of Philosophy in Chemical Engineering

Department of Chemical Engineering

August 2001

APPROVAL PAGE

MODELING AND EXPERIMENTAL VALIDATION OF A SINGLE-FEED SEMI-BATCH PRECIPITATION PROCESS

Ernesto Uehara-Nagamine

Dr. Piero M. Armenante, Dissertation Advisor — Date
Distinguished Professor of Chemical Engineering, NJIT

Dr. Basil C. Baltzis, Committee Member — Date
Professor of Chemical Engineering and Department Chair, NJIT

Dr. Dana E. Knox, Committee Member — Date
Associate Professor of Chemical Engineering, NJIT

Dr. Robert Pfeffer, Committee Member — Date
Distinguished Professor of Chemical Engineering, NJIT

Dr. San Kiang, Committee Member — Date
Director of Chemical Process Engineering, Bristol-Myers Squibb Company

BIOGRAPHICAL SKETCH

Author: Ernesto Uehara-Nagamine

Degree: Doctor of Philosophy

Date: August 2001

Undergraduate and Graduate Education:

- Doctor of Philosophy in Chemical Engineering
  New Jersey Institute of Technology, Newark, NJ, 2001
- Master of Science in Chemical Engineering
  New Jersey Institute of Technology, Newark, NJ, 1996
- Bachelor of Science in Chemical Engineering
  Engineering National University, Lima, Perú, 1984

Major: Chemical Engineering

Presentations and Publications:

Ernesto Uehara-Nagamine and Piero M. Armenante
"Effect of Process Variables on the Single-Feed Semibatch Precipitation of Barium Sulfate," Submitted for publication to *Chemical Engineering Research and Design*, 2001.

Ernesto Uehara-Nagamine and Piero M. Armenante
"Simulation of a Single-Feed Semi-Batch Precipitation Process Using a CFD-Based Micromixing Model," *Biennial Conference of the North American Mixing Forum-MIXING XVIII*, Pocono, Pennsylvania, June 24-29, 2001.

Ernesto Uehara-Nagamine and Piero M. Armenante
"Effect of Process Variables on the Single-Feed Semibatch Precipitation of Barium Sulfate," *Proceedings of the International Symposium on Mixing in Industrial Processes-ISMIP4*, Toulouse, France, May 14-16, 2001.

Piero M. Armenante and Ernesto Uehara-Nagamine

"Simulation of a Single-Feed Semi-batch Precipitation Process Using a Micromixing-Base CFD Model," *Annual Meeting of the American Institute of Chemical Engineers*, Los Angeles, California, November 12-17, 2000.

Piero M. Armenante, Ernesto Uehara-Nagamine, W. Roy Penney, and Victor Atiemo-Obeng

"A Comprehensive Correlation for the Determination of the Minimum Agitation Speed for Solids Suspension in Stirred Tanks," *Annual Meeting of the American Institute of Chemical Engineers*, Los Angeles, California, November 12-17, 2000.

Piero M. Armenante, Ernesto Uehara-Nagamine, and Jessyca Susanto

"Determination of Correlations to Predict the Minimum Agitation Speed for Complete Solid Suspension in Agitated Vessels," *Canadian Journal of Chemical Engineering*, **76**, 413-419, 1998.

Piero M. Armenante and Ernesto Uehara-Nagamine

"Effect of Low Off-Bottom Impeller Clearance on the Minimum Agitation Speed for Complete Suspension of Solids in Stirred Tanks," *Chemical Engineering Science*, **53**(9), 1757-1775, 1998.

Piero M. Armenante and Ernesto Uehara-Nagamine

"Solid Suspension and Power Dissipation in Stirred Tanks Agitated by One or Two Impellers at Low Off-Bottom Impeller Clearances," *Proceedings of the 9th European Conference on Mixing*, Paris, France, March 19-21, 1997.

Piero M. Armenante and Ernesto Uehara-Nagamine

"Solid Suspension in Agitated Vessels Provided with Impellers Having Small Off-Bottom Clearances," *Annual Meeting of the American Institute of Chemical Engineers*, Chicago, Illinois, November 10-15, 1996.

This thesis is dedicated to my mother and my wife

ACKNOWLEDGEMENT

I would like to express my sincere gratitude to my dissertation advisor, Dr. Piero M. Armenante, for his guidance, encouragement and support throughout this research. His advice has been very valuable for the successful completion of this research work.

I would like to acknowledge Dr. Basil C. Baltzis, Dr. Dana Knox, Dr. Robert Pfeffer, and Dr. San Kiang for serving as members of the thesis committee and for their constructive criticism.

I would also like to thank the Department of Chemical Engineering for awarding me a graduate assistantship while pursuing my Ph. D. studies.

This work was partially supported by a grant from the Emission Reduction Research Center sponsored by the Bristol-Myers Squibb Pharmaceutical Research Institute (thanks to Dr. San Kiang) and Schering-Plough Corporation (thanks to Perry Lagonikos). Their contribution is gratefully acknowledged.

I received plenty of expert assistance during this study. Special thanks to Mr. Arthur Pereira from Electrical Engineering, Mr. Dean M. Knape from Information Technology Center, M. Sc. Chandrakant M. Patel and Dr. Dong-Guang Wei from Geo-Environmental Engineering Lab. I am also grateful to the members of the Mixing Lab, for their suggestions and assistance.

I appreciate all my friends from the graduate program in Chemical Engineering who have kindly provided me with help and advice about this research and made my life more enjoyable during my studies.

TABLE OF CONTENTS

TABLE OF CONTENTS
(Continued)

Chapter **Page**

TABLE OF CONTENTS
(Continued)

Chapter **Page**

TABLE OF CONTENTS
(Continued)

Chapter **Page**

TABLE OF CONTENTS
(Continued)

Chapter **Page**

LIST OF TABLES

LIST OF FIGURES

LIST OF FIGURES
(Continued)

LIST OF FIGURES
(Continued)

Figure **Page**

LIST OF FIGURES
(Continued)

Figure **Page**

NOMENCLATURE

a	mean specific surface area of the crystals per unit volume of the suspension, $m^2\ m^{-3}$
$A_{crystal}$	area of crystal, m^2 or μm^2 where otherwise indicated
A_n	model constant in nucleation rate equation, Equation (2.45), dimensionless
b	baffle thickness, mm
B	baffle width, mm
C	impeller off-bottom clearance, as measured from the middle of the impeller to the tank bottom; m
c_1	bulk entrainment coefficient, $c_1 = 2$ for PBT
c_2	impeller discharge coefficient, $c_2 = 0.75$ for PBT
C_i	concentration of species i in the mixing-precipitation zone, kmol m^{-3} or M
$\overline{C_i}$	average component of concentration of species i, kmol m^{-3} or M
C_i'	fluctuating component of concentration of species i, kmol m^{-3} or M
$<C_i>$	concentration of species i in the liquid bulk, kmol m^{-3} or M
C_{ij}	convective term in Reynolds stress tensor transport equation, Equation (2.8), $m^2\ s^{-3}$
C_{iO}	actual initial concentration of species i, kmol m^{-3} or M
C_{iOM}	mean initial concentration of species i, kmol m^{-3} or M
C_μ	constant in turbulent diffusivity equation, Equation (2.19), dimensionless
$C.V.$	coefficient of variation, dimensionless
D	impeller diameter, m
d_{43}	Coulter-Counter mean crystal size, μm
$D_{crystal}$	barium sulfate diffusivity, $m^2\ s^{-1}$

NOMENCLATURE
(Continued)

D_i	molecular diffusivity of species *i*, $m^2 s^{-1}$
D_{ij}	curvature related term in Reynolds stress tensor transport equation, Equation (2.8), $m^2 s^{-3}$
d_{ijk}	diffusive transport in Reynolds stress tensor transport equation, Equation (2.8), $m^3 s^{-3}$
D_m	molecular diffusivity, $m^2 s^{-1}$
D_t	turbulent diffusivity, $m^2 s^{-1}$
E	engulfment intensity parameter, s^{-1}
F_i	external body forces in the *ith* direction, N
G	crystal growth rate, $m s^{-1}$
g_i	gravitational acceleration, $m s^{-2}$
H	height of liquid in the mixing vessel, m
H'	height of mixing vessel, m
k	turbulent kinetic energy, $m^2 s^{-2}$
k_a	area shape factor, dimensionless
k_b	impeller blade thickness, mm
k_D	mass transfer coefficient, $m s^{-1}$
k_d	particle mass transfer coefficient, $m s^{-1}$
k_{Di}	mass transfer coefficient for species *i*, $m s^{-1}$
k_n	model constant in nucleation rate equation, Equation (2.45), dimensionless
k_R	rate constant, Equation (2.16), $kmol^{-1} m^3 s^{-1}$
K_S	solubility product, $kmol^2 m^{-6}$
k_v	volume shape factor, dimensionless

NOMENCLATURE
(Continued)

k_σ	rate constant for surface reaction, $(m\ s^{-1})/(kmol^2\ m^{-6})$
L	characteristic length, m or μm where otherwise indicated
l	scale of inhomogeneity, m
$<L_{avg}>$	mass weighted mean crystal size in the liquid bulk, m or μm where otherwise indicated
L_{avg}	mass weighted mean crystal size in the mixing-precipitation zone, m or μm where otherwise indicated
L_{43}	mass weighted mean crystal size, m or μm where otherwise indicated
L_C	integral length scale for concentration fluctuations, m
Ls	segregation macroscale, m
L_{spec}	specific length per unit volume of suspension, $m\ m^{-3}$
M	molecular weight, $kg\ kmol^{-1}$
$M_{crystal}$	molecular weight of barium sulfate, $kg\ kmol^{-1}$
m_i	*ith* moment of a particle size distribution in the mixing precipitation zone, $m^j\ m^{-3}$
$<m_i>$	*ith* moment of a particle size distribution in the liquid bulk, $m^j\ m^{-3}$
N	agitation speed; rpm (revolutions per minute)
N_{sub}	number of sub-droplets (blob sub-discretization), dimensionless
N_T	total number concentration, $n_o\ m^{-3}$
P	impeller power consumption, $N\ m\ s^{-1}$
p	static pressure, $N\ m^{-2}$
$\bar{p}$	average component of static pressure, $N\ m^{-2}$
p_i'	fluctuating component of static pressure, $N\ m^{-2}$

NOMENCLATURE
(Continued)

P_{ij}	shear generation rate in Reynolds stress tensor transport equation, Equation (2.8), $m^2\ s^{-3}$
q_c	circulation capacity, $m^3\ s^{-1}$
q_f	feed rate of sodium sulfate, $m^3\ s^{-1}$
r	radial distance in cylindrical coordinates, m
R_{ij}	rotational term in Reynolds stress tensor transport equation, Equation (2.8), $m^2\ s^{-3}$
R_N	nucleation rate, $\#\ m^{-3}\ s^{-1}$
r_s	radius of shaft, m
S_a	supersaturation ratio, dimensionless
S_{at}	thermodynamic supersaturation ratio, dimensionless
S_{ij}	curvature related term in Reynolds stress tensor transport equation, Equation (2.8), $m^2\ s^{-3}$
t	Lagrangian time, drop residence time, s
T	vessel diameter; m
t_C	mean circulation time, s
t_D	characteristic time for turbulent dispersion, s
t_{DS}	characteristic time for viscous-convective subrange, s
t_E	characteristic time for engulfment, s
t_{eddy}	eddy lifetime, s
t_{end}	total time a blob remains in the system before next blob addition, s
t_f	time of feed addition, s or min where otherwise indicated
t_G	characteristic time for the crystal growth rate, s

t_{ms}	characteristic time for inertial-convective subrange, s
t_S	characteristic time for inertial-convective disintegration, s
t_s	time of semi-batch operation, s
u	fluid velocity, m s^{-1}
$\bar{u}$	average component of fluid velocity, m s^{-1}
$u_i^{'}$	fluctuating component of fluid velocity, m s^{-1}
$u_{blob,i}$	blob velocity, m s^{-1}
V	volume of mixing-precipitation zone, m^3
$V_{crystal}$	volume of crystal, m^3 or μm^3 where otherwise indicated
V_{iO}	initial volume of the *ith* reactant solution, m^3
$V_{reactor}$	volume of reactor (actual work liquid), m^3
W_b	impeller blade height, m or mm where otherwise indicated
w_s	tangential velocity at the shaft surface, m s^{-1}
$x_{blob,i}$	blob position in the *ith* direction, m
$X_{crystal}$	mass fraction of particles, dimensionless
Y	volume fraction of the mixing-precipitation zone, dimensionless

Greek letters

α_v	ratio of initial reactant solution volumes, V_{AO}/V_{BO}
ε, ε_{ij}	energy dissipation rate, m^2 s^{-3}
ε_{avg}	average (vessel) energy dissipation rate, m^2 s^{-3}
ε_{blob}	blob energy dissipation rate, m^2 s^{-3}

NOMENCLATURE
(Continued)

ε_{ikm}	alternating unit tensor, dimensionless
ε_{zone}	zone energy dissipation rate (as defined in Section 5.1.5), $m^2\ s^{-3}$
ϕ_v	sphericity of the particle, dimensionless
$\gamma_{\pm A^+B^-}$	stoichiometric mean activity coefficient, dimensionless
φ_{ij}	non-dispersive contributions of fluctuating pressure, $m^2\ s^{-3}$
η	stoichiometry ratio of reactants, dimensionless
λ_B	Batchelor microscale, m
λ_k	Kolmogorov microscale, m
ν	kinematic viscosity of solution, $m^2\ s^{-1}$
σ	surface chemical reaction order, dimensionless
ρ	density of solution, kg m^{-3}
$\rho_{crystal}$	density of crystals, kg m^{-3}
$\overline{\rho u_i' u_j'}$	Reynolds stresses, N m^{-2} s^{-1}
τ	torque produced by impeller, N m
τ_{ind}	induction time, s
ζ	normal distributed random variable, dimensionless
ΔC	supersaturation, kmol m^{-3} or M
Ω_k	rotation speed of reference frame, s^{-1}
$<\Psi>$	population density of the particle size distribution in the liquid bulk, m^{-4}
Ψ	population density of the particle size distribution in the mixing-precipitation zone, m^{-4}

Dimensionless numbers

Fr	Froud number, N^2D/g
Po	Power number, $P/(\rho N^3 D^5)$
Re	impeller Reynolds number, $N D^2/\nu$
Re_p	particle Reynolds number, $\varepsilon^{1/3} d_{43}^{4/3}/\nu$
Sc	Schmidt number, $\nu/D_{crystal}$
Sc_t	turbulent Schmidt number, ν/D_t
Sh	Sherwood number, $k_D d_{43}/D_L$

CHAPTER 1

INTRODUCTION

1.1 Fundamentals of Crystallization

Crystallization is an important unit operation for the production of a wide range of chemical and pharmaceutical products. This precipitation process combines particle formation and purification within a single operation which makes it an attractive isolation step in many processes (Price, 1997). There are several possible process objectives that can be achieved by crystallization. These include separation, concentration, solidification, and analysis. In all of the instances in which crystallization is used to carry out a specific process objective, the characteristics of the final product are critical to determine the ultimate success of the product. The key determinants of product quality are the *crystal size distribution* (including *mean crystal size* and *coefficient of variation*), morphology (including habit, or shape, and form), and purity.

Figure 1.1 shows the mechanism of precipitation. In each crystallization system, there is a need to form crystals (*nucleation*), to cause the crystals to grow (*crystal growth*), and to separate the crystals from residual liquid. There are various ways to accomplish these objectives leading to a multitude of processes designed to meet the requirements of product quality. In *reaction crystallization*, a solution of one reactant is often mixed with a solution of the other, and the crystallizing substance (*precipitate*) is formed by a chemical reaction in concentrations exceeding the solubility (*supersaturation*). In these crystallization systems, the slurry undergoes mixing due to mixers and the system hydrodynamics. Frequently, the reaction is fast or very fast, and the mixing conditions influence the crystal size distribution (CSD) significantly.

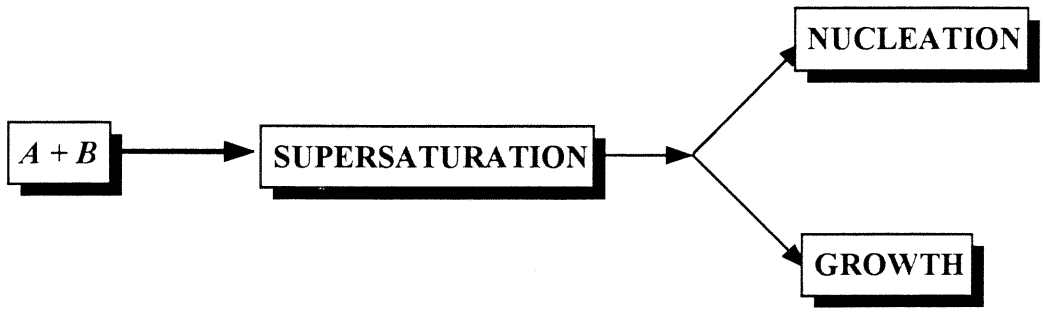

Figure 1.1 Mechanism of precipitation

1.2 Effect of Mixing on Crystallization

Most precipitation processes are conducted in stirred tanks. Different mixing scales can affect the precipitation process. *Macromixing* affects the overall circulation process and determines the residence time distribution. *Mesomixing* affects the interaction between the added plume of fresh feed and the liquid bulk. *Micromixing* affects the mixing at the molecular scale, therefore influencing molecular level processes such as nucleation and crystal growth. For a given vessel geometry, agitator design and operating conditions, a key measure of the degree of macromixing is the average value of the agitation power per unit mass of slurry. Since, this value depends on the position inside the vessel the characterization of the micromixing requires local values of the rate of energy dissipation. Chemical reaction, nucleation, and crystal growth are molecular level processes; therefore, only mixing at the molecular scale can directly influence their course. Micromixing controls the generation of supersaturation and its redistribution, mesomixing and macromixing may determine the environment for micromixing and indirectly affect the supersaturation distribution (Tavare, 1986; Baldyga *et al.*, 1995).

Few engineers are aware of the impact that mixing can have on the effective operation of a crystallizer. Failure to take this phenomenon into account can harm the crystal size distribution, purity, shape and surface area (Garside, 1991, Genk, 1997). The majority of chemical engineering design and modeling approaches to crystallizers assume that the system is perfectly mixed. However, depending on the mode of operation and operating conditions, mixing may become the rate-controlling step for fast precipitation systems. Furthermore, the effect of some important parameters that affect the mixing conditions have not been fully considered in previous research work on precipitation (i.e., impeller diameter and impeller clearance), and there are major contradictions in the literature as to the effect of a key variable such as the impeller speed.

In recent years, theoretical computational fluid dynamics (CFD), and micromixing models have been proposed to model crystallization. CFD techniques are based on the use of statistically averaged balance equations governing mean quantities, using Eulerian or fixed frames of references. The averaging procedure produces an unclosed set of differential equations which requires additional information. However, significant advances in CFD have recently resulted in the possibility of modeling complex flows in stirred tanks, by computing local values of velocity and energy dissipation rate, with a reasonable amount of detail and accuracy (Brucato *et al.*, 1998). Micromixing models are usually constructed in a Lagrangian frame of reference. This formulation is very convenient. By following the history of a fluid element, one can identify and describe the elementary steps forming the overall precipitation process: micromixing, chemical reaction, nucleation and crystal growth. However, the models require detailed estimates of local levels of kinetic energy dissipation rate.

1.3 Objective of This Work and Approach

So far no crystallization simulation that combines all the advantages offered by these two different approaches discussed in the preceding section has been developed. Therefore, the primary objective of this study was to *develop a method based on computational fluid dynamics and a micromixing model, capable of predicting the effect of mixing on the precipitation process and the crystal size distribution*. In this work, the macroscopic flow field was simulated by using a CFD commercial code (FLUENT). The velocity profiles for the feed dispersion and the local turbulent parameters for the application of the micromixing model were obtained from this simulation. The mixing-precipitation zone originating from the feed point was tracked using a random walk model. Available correlations based on extensive experimental data were used for the calculation of the nucleation and crystal growth rates. The mass transfer coefficient for the crystal growth was assumed to be dependent on both the average crystal size and the local energy dissipation rate. The micromixing effect on the precipitation process was modeled by using the engulfment model or E-Model (Baldyga and Rohani, 1987) with self-engulfment (Baldyga and Bourne, 1989). Barium sulfate precipitation experiments were conducted to validate the simulation model and determine the crystal morphology. The effect of process variables (such as volume ratio, mean initial concentration and stoichiometry ratio), operating conditions (including impeller speed, diameter and off-bottom clearance), and vessel scale on the crystal size distribution were experimentally determined as well as numerically predicted. Comparison between the experimental results and the model predictions are quite satisfactory indicating that the model captures the most important features of the precipitation process.

1.4 Literature Review

1.4.1 Initial Studies: Continuous Stirred Tank Reactors (CSTR)

Initial studies of the influence of mixing on crystallization were conducted in continuous stirred tank reactors (CSTR), *i.e.*, the mixed-suspension, mixed-product-removal (MSMPR) crystallizer (Randolph and Larson, 1988). The MSMPR configuration with a single feed entry (Becker and Larson, 1969) and with two feeds entry (Garside and Tavare, 1985) were modeled by assuming the two extreme mixing conditions: complete segregation and maximum mixedness. In these two extreme micromixing limits the conversion is not significantly different, making it difficult to characterize the partial segregation case.

For barium sulfate precipitation in CSTR's, the mean crystal size was observed to increase with the impeller speed. This was attributed either to a turbulent micromixing limitation (Pohorecki and Baldyga, 1983) or turbulent diffusion-limited particle growth (Fitchett and Tarbell, 1990). For double-feed continuous precipitation (Pohorecki and Baldyga, 1988), the effects of intensity of mixing, mean residence time, and initial concentration of the reactants were found to be very different depending on the reactor feeding (unpremixed or premixed).

Several attempts have been made to model CSTRs (Fitchett and Tarbell, 1990; Tavare, 1992; Kim and Tarbell, 1996). CSTR's operating at steady state have been widely used, since they are easy to characterize and analyze. However, the micromixing effects on homogeneous chemical reaction are generally not as pronounced in CSTR as they are in plug flow, batch (Chang *et al.*, 1986; Fitchett and Tarbell, 1990) or semi-batch (Houcine *et al.*, 1997) reactors.

1.4.2 Batch and Semi-Batch Precipitation

Experimental studies on batch and semi-batch precipitation show significant mixing effects. A decrease in the mean particle size when increasing impeller speed was observed during the batch precipitation of barium sulfate (Pohorecki and Baldyga, 1983). In a detailed study (Tosun, 1988) very pronounced mixing effects in barium sulfate precipitation were observed on single-feed and double-feed semi-batch precipitation. A minimum on the curve of particle size versus impeller speed was obtained.

A model including interactions between macromixing and micromixing (Chen *et al.*, 1996) could explain the appearance of a minimum in a plot of the mean particle size versus impeller speed, as observed experimentally by Tosun (1988). The model considered the whole reactor as a combination of two sub-reactors: a plug flow reactor and a well-mixed reactor. The macro-flow pattern of the segregated zone around the feed formed was assumed to be plug flow and the reminder of the vessel was assumed to be macro well mixed. The relative volume level of the two reactors was adjusted to match the experimental mean crystal size.

It is impossible to predict these trends intuitively; however, it is clear that mixing affects generation of supersaturation and its redistribution in a system. In addition, mixing effects in unsteady-state processes are far more difficult to model than in their continuous counterparts (Genk, 2000). It is therefore necessary to incorporate a suitable mixing model in reactive precipitation processes to predict the final product characteristics. Since chemical reaction, nucleation, and crystal growth are molecular level processes, any linking of precipitation kinetics with mixing models should be done at this level. One should be very careful when choosing the model.

1.4.3 Closure Methods

The process of turbulent reactive mixing can be described from the Eulerian perspective. Basically, it consists in trying to solve numerically the Navier–Stokes equation involving nonlinear chemical kinetics. The classical approach involves the time averaging procedure (Bird *et al.*, 1960; Rodi, 1984) which introduces new unknown micromixing terms; the number of unknowns is thus larger than the number of equations and the system of mass balance equations is not closed. This is called the closure problem.

Depending on the process conditions, the results of closure schemes combined with CFD models also show contradictory trends in the precipitation process, which agree in many cases with experimental data. Closure procedures based on the probability density function (PDF) of the concentrations of chemically inert species have been applied to simulate the precipitation process in tubular reactors (Baldyga and Orciuch, 1997; Baldyga *et al.*, 1997a; Marchisio *et al.*, 2000). Applications to stirred tanks in unsteady state are still in development.

Recently, the influence of mixing on the product quality in precipitation has been studied using CFD by neglecting the turbulence fluctuations (perfect micromixing). This is, however, only possible for very slow reaction or steady state CSTR's. Steady state precipitation of barium sulfate has been studied in rectangular flat reactor with jet mixing (Van Leeuwen *et al.*, 1996), tubular reactor with coaxial and tee-junction inlets (Wei and Garside, 1997), and continuous stirred tanks (Garside and Wei, 1998). This approach has also been applied to simulate the influence of hydrodynamics on a double-jet continuous reactor for the precipitation of calcium phosphate (Seckler *et al.*, 1995). Only in the first case, experimental studies were presented.

1.4.4 Micromixing Models

The influence of mixing on the final product characteristics has been studied with the use of micromixing models (Pohorecki and Baldyga, 1983, 1988; Marcant and David, 1991; Åslund and Rasmuson, 1992; David and Marcant, 1994; Baldyga *et al.*, 1995; Phillips *et al.*, 1999; Zauner and Jones, 2000a, 2000b). Micromixing can be adequately represented by the engulfment-deformation-diffusion (EDD) model (Baldyga and Bourne, 1984). The EDD model captures the key physical processes contributing to turbulent mixing. For Schmidt numbers which are not too high ($Sc << 4{,}000$), deformation and diffusion can be neglected (Baldyga and Rohani, 1987; Baldyga and Bourne, 1989), and the intensity of micromixing can be represented only by the engulfment intensity parameter (E-Model). Many experiments have been conducted to check the applicability of the E-Model for complex reactions. E-Model has also been proved to be superior to other models (Baldyga and Bourne, 1990).

The influence of micromixing on precipitation was predicted qualitatively for batch and single-feed semi-batch precipitation of calcium oxalate by means of a simplified E-Model (Marcant and David, 1991). The double feed semi-batch precipitation of calcium oxalate was then studied using this semi-quantitative approach (David and Marcant, 1994). This model was able to qualitatively explain the effects of process parameters such as volume ratio, impeller speed, and feed pipe location on the average size of crystals. Some other models appeared as general cases of the E-Model (Villermaux and Falk, 1994). However, the model cannot be too complex, because it should be linked to the very complex population balance of precipitates. Other models still need research to put them into operating form (Ottino, 1994).

The multiple-time-scale model (Baldyga and Bourne, 1992), which is an extension of the E-Model, describes the interactions between macromixing, mesomixing, and micromixing. It was applied to the process of a double-feed semi-batch precipitation of barium sulfate (Baldyga *et al.*, 1995). The E-Model was applied to a single-feed semi-batch precipitation process to describe the mixing effects on the final CSD and particle morphology (Phillips *et al.*, 1999). The model described mixing on two scales: the microscale and the macroscale. Application of the model was limited to $Sc << 4{,}000$ and slow precipitation addition rates. The flow field and the energy dissipation rate distribution were described employing an experimental flow model (Bourne and Yu, 1994), which divides the reactor content into two regions that have considerably different local energy dissipation rates (Okamoto *et al.*, 1981). With the experimental flow model (EFM) the trajectory of the reaction zone was evaluated from the flow field, and the instantaneous reaction from the energy dissipation rate. The EFM certainly oversimplified the complexity of the actual flow; however, it was based on experimental measurements. When the multiple scale model or the E-Model were applied to experimental results of barium sulfate precipitation, satisfactory agreement between predicted and observed results were obtained.

Zauner and Jones (2000a, 2000b) have recently reported the effect of mixing on the semi-batch precipitation of both calcium oxalate and calcium carbonate. A combined model called Segregated Feed Model incorporating micromixing (E-Model) and CFD was used to predict the influence of process conditions on product particle size. However, the model assumed that nucleation was the only kinetics process occurring in the engulfment zone and used only the value of the energy dissipation rate in the feed point.

1.4.5 Scale-Up of Precipitation Processes

Due to the need to introduce the product into the market, precipitation processes are often scaled up from the laboratory scale to the production scale. Since a fundamental understanding on the effect of increasing the vessel capacity on crystallization processes is lacking, scale-up of commercial precipitation processes is often conducted by trial and error or empirically. In the simplest case, the production-scale precipitator is geometrically similar to the lab-scale precipitator and the same mode of operation is followed. However, dynamic, kinematic, thermal, and/or chemical similarities cannot be established, and it is difficult, if not impossible, to keep constant all the dimensionless groups that characterize the process.

Several scale-up rules have been proposed and experimentally studied in the literature. Scale-up with constant agitation speed (Paul, 1988, 1990) is based on achieving a constant pumping rate per unit volume with scale-up and therefore leads to similar macromixing on different scales, as the circulation time in the reactor remains constant. Scale-up with constant tip speed (Fasano and Penney, 1991a) implies constant shear in the impeller region and can be considered an approximation to scale-up with constant mesomixing, as the blending of the incoming reactant with the bulk or second reactant is closely linked to the shear field in the mixing zone. Scale-up with constant power input per unit volume (Mersmann and Laufhütter, 1985; Bourne and Dell'Alva, 1987; Rice and Baud, 1990; Bourne and Yu, 1994) is probably the most widely used for mixing-limited operations and can be considered scale-up with constant micromixing. The importance of the power input per unit volume for micromixing has been established by relating the micromixing time to the Kolmogoroff length scale of mixing.

The conventional scale-up criteria such as "constant stirrer speed", "constant tip speed", and "constant specific energy input" are all based on the assumption that only one mixing process is limiting (Zauner and Jones, 2000b). If, for example, the power input per unit volume is kept constant with scale-up, the same micromixing behavior could be expected on different scales. The mesomixing time will change with scale-up; as a result, the kinetic rates and particle properties will be different and scale-up will fail. Therefore, the failure of "conventional" criteria may be due to the fact that it is not only one mixing process that can be limiting; rather, for example, an interplay of micromixing and mesomixing can influence the kinetic rates. Thus, by scaling up with constant micromixing times on different scales, the mesomixing times cannot be kept constant but will differ, and consequently the precipitation rates (i.e., nucleation rates) will tend to deviate with scale-up.

CHAPTER 2

THEORETICAL BACKGROUND

2.1 Computational Fluid Dynamics (CFD)

Fluid dynamics in stirred tanks is dominated by the fact that, in most situations of interest, the fluid motion exhibits a chaotic, non-repeating unsteadiness known as turbulent motion. This turbulence is very complex and cannot be resolved at an engineering level. Instead, the equations of motion for laminar flow are averaged over a period of time, long compared with that of the turbulence, producing what are known as the Reynolds averaged Navier-Stokes (RANS) equations. This average procedure lead to the appearance of time-averaged products of fluctuating velocities (Reynolds stresses) that are unknown in the RANS equations and require to be closed. The relevant equations that are used in the simulation of the flow field in stirred tanks are presented below.

2.1.1 Reynolds Averaged Navier-Stokes (RANS) Equations

For a continuous fluid the equation of continuity in laminar flow is (Bird *et al.*, 1960):

$$\frac{\partial}{\partial t}(\rho) + \frac{\partial}{\partial x_j}(\rho u_j) = 0 \tag{2.1}$$

Equation (2.1) is the general form of the mass conservation equation for a closed system and is valid for incompressible as well as compressible flow. Conservation of momentum in the *ith* direction in an inertial reference frame, is described by (Bird *et al.*, 1960):

$$\frac{\partial}{\partial t}(\rho u_i) + \frac{\partial}{\partial x_j}(\rho u_i u_j) = \frac{\partial}{\partial x_j}\left[\mu\left(\frac{\partial u_i}{\partial x_j} + \frac{\partial u_j}{\partial x_i}\right) - \left(\frac{2}{3}\mu\frac{\partial u_l}{\partial x_l}\right)\right] - \frac{\partial p}{\partial x_i} + \rho g_i + F_i \tag{2.2}$$

where p is the static pressure, and g_i and F_i are gravitational acceleration and external body forces in the *ith* direction, respectively. In these equations, the velocity u, and pressure p, represent instantaneous values, and cannot be applied directly to turbulent flow. Furthermore, the density component can also present the fluctuations, in what follows the fluid will be assumed incompressible (i.e., constant ρ).

For the turbulent flow of an incompressible fluid, the instantaneous velocity may be written as the sum of an average and a fluctuating velocity component:

$$u_i = \overline{u_i} + u_i' \tag{2.3}$$

Similarly for the instantaneous pressure:

$$p = \overline{p} + p' \tag{2.4}$$

In Equation (2.3) and Equation (2.4), the average values are defined as the time-averaged values that can be calculated by averaging over a time interval large with respect to the time of turbulent oscillation. When the equations of continuity and motion, which describe the laminar flow, are averaged over this time period, long compared with that of turbulence, the RANS equations are obtained (Bird *et al.*, 1960; Rodi, 1984):

$$\frac{\partial}{\partial x_j}\left(\overline{u_j}\right) = 0 \tag{2.5}$$

and:

$$\begin{aligned} \frac{\partial}{\partial t}\left(\rho\overline{u_i}\right) + \frac{\partial}{\partial x_j}\left(\rho\overline{u_i u_j}\right) = \\ \frac{\partial}{\partial x_j}\left(\mu\left[\frac{\partial\overline{u_i}}{\partial x_j} + \frac{\partial\overline{u_j}}{\partial x_i}\right] - \left(\frac{2}{3}\rho\frac{\partial\overline{u_l}}{\partial x_l}\right)\right) \\ -\frac{\partial(\overline{p})}{\partial x_i} + \rho g_i + F_i + \frac{\partial}{\partial x_j}\left(\rho\overline{u_i' u_j'}\right) \end{aligned} \tag{2.6}$$

Equation (2.6) has the same form as the fundamental momentum balance, Equation (2.2), with velocities now representing time-averaged (or mean-flow, $\overline{u_i}$) values and the effect of turbulence incorporated through the "Reynolds stresses", $\overline{\rho u_i' u_j'}$. Note that $\overline{u_i' u_j'}$ is a symmetric second order tensor since:

$$\overline{u_i' u_j'} = \overline{u_j' u_i'} \tag{2.7}$$

and hence, has six unique terms. The approximate representation of the Reynolds stresses in terms of known or calculable quantities is required to "close" the RANS equations. This process is known as turbulence modeling.

2.1.2 Reynolds Stress Model (RSM)

The main task of turbulence models is to provide expressions or closure models that allow the evaluation of these correlations in terms of mean flow quantities. The turbulence closure models most often used are the k-ε model, the Re-Normalization Group (RNG) k-ε model, and the Reynolds Stress Model (RSM).

The k-ε turbulence model involves equations for the turbulent kinetic energy, k, and for the turbulent energy dissipation rate, ε. However, previous investigators have presented many shortcomings (Abujelala and Lilley, 1984). For the complex highly swirling flows found in stirred tanks, the k-ε model is inadequate and can produce physically incorrect results. Several attempts have been made to improve this model (Sahu and Joshi, 1995; Sahu *et al.*, 1998). A critical overview of CFD simulations using k-ε models has shown that any of these models perform satisfactory simulation without modification (Jenne and Reuss, 1999).

The RNG model looks quite similar to the standard k-ε model, except for the values of the model constants, which are evaluated by theory and not empiricism. This model provides a more fundamental approach to the problem and improves the predictions of the k-ε model. RNG model can be applied when both a turbulent region and a laminar region exist in a domain. Although the RNG model has been recently extended to highly swirling flows, these extensions should be evaluated against experimental data and RSM predictions.

One major limitation of the two-parameter k-ε models is the assumption of isotropy. This implies that the velocity and length scales are the same in all directions. In complex flows, such as highly swirling flows, the velocity and length scales can vary significantly with direction. For such flows, the k-ε models are inadequate and can produce physically incorrect results. The RSM, which computes the individual Reynolds stresses, provided a better alternative in such cases (Launder, 1989).

The transport equations for the individual stresses $\overline{u_i' u_j'}$ appearing in Equation (2.6) can be derived from the momentum equations and contain triple order velocity correlations and pressure velocity correlations that must be modeled to obtain closure. For an incompressible turbulent flow whose large scales are unaffected by viscosity, the transport of the Reynolds stress tensor is conveniently expressed in the symbolic form:

$$\frac{\partial\left(\overline{u_i' u_j'}\right)}{\partial t} + C_{ij} = P_{ij} + \frac{\partial d_{ijk}}{\partial x_k} + \varphi_{ij} - \varepsilon_{ij} + R_{ij} + S_{ij} + D_{ij} \qquad (2.8)$$

where, C_{ij} is the convective transport term:

$$C_{ij} = u_k \frac{\partial \overline{u_i' u_j'}}{\partial x_k} \qquad (2.9)$$

P_{ij} is the shear generation term:

$$P_{ij} = -\left[\overline{u_i' u_k'} \frac{\partial u_j'}{\partial x_k} + \overline{u_j' u_k'} \frac{\partial u_i'}{\partial x_k}\right] \tag{2.10}$$

d_{ijk} is the diffusive transport term:

$$d_{ijk} = \left(\overline{u_i' u_j' u_k'}\right) + \overline{\frac{p}{\rho}\left(\delta_{jk}' u_i' + \delta_{ik}' u_j'\right)} - \nu \frac{\partial\left(\overline{u_i' u_j'}\right)}{\partial x_i} \tag{2.11}$$

φ_{ij} is the pressure strain term:

$$\varphi_{ij} = +\overline{\frac{p}{\rho}\left[\frac{\partial u_i'}{\partial x_j} + \frac{\partial u_j'}{\partial x_i}\right]} \tag{2.12}$$

ε_{ij} is the dissipation term:

$$\varepsilon_{ij} = -2\nu\left[\overline{\frac{\partial u_i'}{\partial x_k} \frac{\partial u_j'}{\partial x_k}}\right] \tag{2.13}$$

and, R_{ij} is the rotational term:

$$R_{ij} = -2\Omega_k\left[\overline{u_j' u_m'} \varepsilon_{ikm} + \overline{u_i' u_m'} \varepsilon_{jkm}\right] \tag{2.14}$$

S_{ij} and D_{ij} are curvature-related source terms that are included when the cylindrical velocity formulation is used (Fluent, 1995). The individual Reynolds stresses are then substituted into the turbulent flow momentum equation.

To close these equations, approximations must be provided for the processes d_{ijk}, φ_{ij} and ε_{ij} in Equation (2.8). Fluent, Inc. (1995) gives a brief description of the approximations used in the RSM model to close the equation set. A more detailed description of several approximations used in the RSM model can be found elsewhere (Launder, 1989).

2.1.3 Non-Equilibrium Wall Functions

Turbulent flows in the regions close to the walls are affected by the presence of these walls. A rigid boundary exerts many different effects on turbulence, the most important of which are (Launder, 1989):

- It reduces the length scales of the fluctuation raising the dissipation rates;
- It reflects pressure fluctuations, thereby inhibiting the transfer (via the pressure-strain correlation) of turbulence energy into fluctuations normal to the wall;
- The mean velocity field is affected through the no-slip condition that has to be satisfied at the wall. Very close to the wall, turbulence is damped due to the presence of walls, the flow is almost laminar-like, and the (molecular) viscosity plays a dominant role in momentum and heat or mass transfer ("viscous sub-layer"). The effect of this molecular viscosity decreases as the distance from the wall increases and can be neglected in the fully turbulent region.

In the present work, the "non-equilibrium wall function" was used to model the near-wall region. In this approach, the viscosity-affected, inner region is not resolved, saving substantially computational resources. Instead, semi-empirical formulas called "wall functions" are used to "bridge" the viscosity-affected region between the wall and the fully turbulent region. The non-equilibrium wall function effectively relaxes the local equilibrium assumption (the production of turbulent kinetic energy and its dissipation rate are assumed to be equal in the wall-adjacent control volume) which is adopted by the standard "wall function" in computing the budget of the turbulent kinetic energy at wall-neighboring cells. Thus, the non-equilibrium wall functions, in effect, partly account for non-equilibrium effects neglected in the standard wall function.

2.1.4 Reynolds Averaging Approach for Precipitation

Consider the second order, irreversible chemical reaction for precipitation:

$$A + B \rightarrow C + D \tag{2.15}$$

in a turbulent flow and for isothermal conditions. The exact description of the concentration field is given by the equation of continuity for species i:

$$\frac{\partial}{\partial t}\left(C_{s_i}\right) + \frac{\partial}{\partial x_i}\left(u_i C_{s_i}\right) = D_{s_i}\frac{\partial^2 C_{s_i}}{\partial x_i^2} \pm k_R C_A C_B \tag{2.16}$$

where s_i = $-A$, $-B$, $+C$, $+D$

In turbulent regime, similarly to the velocity, u, and pressure, p, C_{si} may be divided into average and fluctuating components, i.e.:

$$C_{s_i} = \overline{C_{s_i}} + C_{s_i}^{'} \tag{2.17}$$

When the equation of continuity for species i is time averaged over a time long compared with the time of turbulent oscillation and the concept of turbulent diffusion is applied (Bird *et al.*, 1960; Rodi, 1984):

$$-\overline{u_i^{'} C_{s_i}^{'}} = D_t \frac{\partial^2 \overline{C_{s_i}}}{\partial x_i^2} \tag{2.18}$$

where D_t is the "turbulent diffusivity" or "eddy diffusivity" (Bird *et al.*, 1960):

$$D_t = \frac{\rho C_\mu}{Sc_t}\frac{k^2}{\varepsilon} \tag{2.19}$$

with $C_\mu = 0.09$ and $Sc_t = 0.7$, one finally obtains:

$$\frac{\partial}{\partial t}\left(\overline{C_{s_i}}\right) + \frac{\partial}{\partial x_i}\left(\overline{u_i}\,\overline{C_{s_i}}\right) = \frac{\partial}{\partial x_i}\left[\left(D_t + D_{s_i}\right)\frac{\partial^2 \overline{C_{s_i}}}{\partial x_i^2}\right] \pm k_R\left(\overline{C_A C_B} + \overline{C_A^{'} C_B^{'}}\right) \tag{2.20}$$

In order to deal with Equation (2.20), it is necessary to have a prediction procedure (closure approximation) for $\overline{C_A' C_B'}$. The balance equation for $\overline{C_A' C_B'}$ of the form similar to Equation (2.20) can easily be generated, but this equation has been shown to be again unclosed, so requires modeling of the third order correlation. The procedure is usually finished by neglecting the third- or fourth-order terms. This procedure is called "moment closure". Of course, the simplest moment closure is to assume that $\overline{C_A' C_B'} = 0$; this is, however, only possible for very slow reactions or steady state CSTR. Recently, the influence of mixing on the product quality in precipitation has been studied using CFD by neglecting the turbulence fluctuations or assuming perfect micromixing (Seckler *et al.*, 1995, Van Leeuwen *et al.*, 1996, Wei and Garside, 1997; Garside and Wei, 1998).

One can also assume the Toor's hypothesis (Toor, 1969), that the $\overline{C_A' C_B'}$ covariance depends only on the hydrodynamics and not on the chemical kinetics, but this can not be applied for fast reactions. This and other moment closures are inaccurate and can led to serious errors. An alternative approach is based on the knowledge of the probability density function (PDF) of the concentration of a chemically inert species and on the interpolation of local concentrations of reactants between the asymptotes of infinitely slow and infinitely fast chemical reactions (Baldyga and Orciuch, 1995). This closure procedure has been applied to simulate the precipitation process (Baldyga and Orciuch, 1997; Baldyga *et al.*, 1997a; Marchisio *et al.*, 2000). Applied to the precipitation of barium sulfate, satisfactory agreement between predicted and observed results was obtained. However, its application to precipitation is limited to tubular reactors. The "closure-CFD" models are presently evolving, and it is expected that in a few years they will be in use.

2.2 Characteristic Times for Mixing

Figure 2.1 shows the different mixing scales, which directly or indirectly affect the precipitation process. These mixing scales will be briefly presented in what follows.

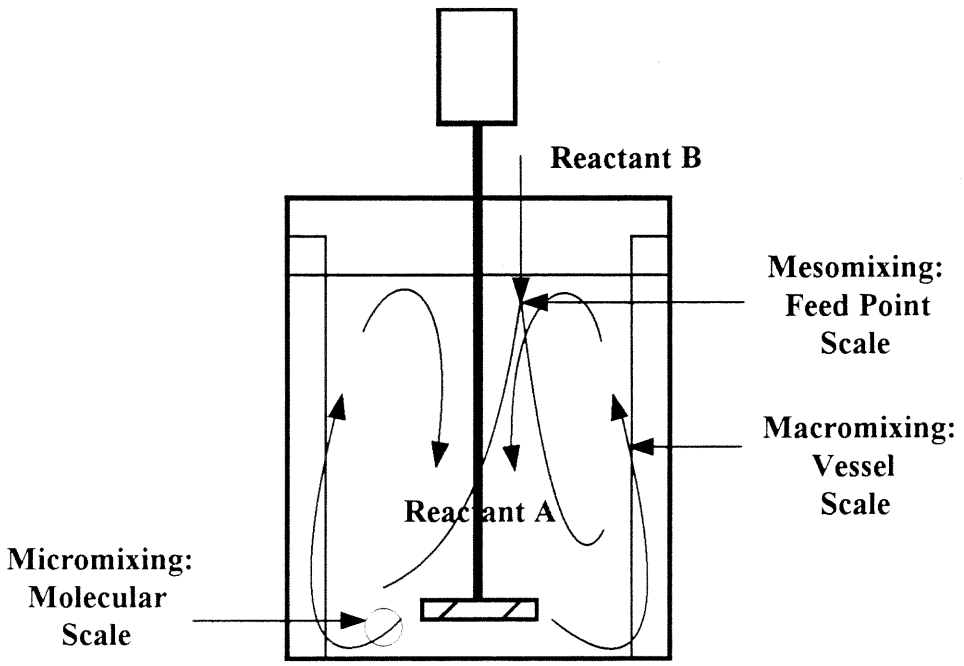

Figure 2.1 Mixing scales in stirred tanks

2.2.1 Macromixing Time

Macromixing is the process of mixing on the scale of the vessel. Macromixing is characterized by the macroscopic flow field and the overall rate of turbulent energy dissipation per unit mass within the reactor. It conveys fluids through environments where the turbulent properties and composition vary. The characteristic macromixing time in a stirred tank can be expressed by the mean circulation time, t_c, which is a function of the total volume of the reactor, $V_{reactor}$, and the circulation capacity, q_c:

$$t_C = \frac{V_{reactor}}{q_c} \tag{2.21}$$

In Equation (2.21), the circulation capacity, q_c, is defined as a function of the :

$$q_c = c_1 c_2 (ND^3) \tag{2.22}$$

c_1 and c_2 are the bulk entrainment and impeller discharge coefficients, respectively. For pitched-blade turbine, c_1 is equal to 2 and c_2 is equal to 0.75 (Oldshue, 1983; Fort, 1986).

2.2.2 Mesomixing Time

Fast reactions are often localized to the region near the feed point, where mesomixing or mixing on a scale larger than micromixing, but smaller than that of macromixing, might be slower. One mesomixing mechanism has been identified as *turbulent diffusion*, which characterizes inhomogeneity of the plume of fresh feed for slow addition. Its characteristic time estimates the period after which the probability of interactions of fluid elements emerging from the feed point becomes negligible (Baldyga and Bourne, 1992):

$$t_D = \frac{q_f}{uD_t} \tag{2.23}$$

where q_f represents the feed addition rate, u the local average velocity, and D_t the turbulent diffusivity.

The other mechanism identified is the *inertial-convective subrange*, which describes a coarse scale segregation of reactants with the scales of inhomogeneity, l, larger than the Kolmogorov microscale, λ_k, and smaller than the integral length scales for concentration fluctuations, L_C:

$$\lambda_k = \left(\frac{\nu^3}{\varepsilon}\right)^{1/4} < l < L_C = \frac{k^{3/2}}{\varepsilon} \tag{2.24}$$

The time constant pertaining to this aspect of mixing, t_{ms} (Corrsin, 1964) is given by:

$$t_{ms} = \frac{3}{2}\left(\frac{5}{\pi}\right)^{2/3}\left(\frac{L_s^2}{\varepsilon}\right)^{1/3} + \frac{1}{2}\left(\frac{\nu}{\varepsilon}\right)^{1/2} \ln Sc \qquad (2.25)$$

where L_s is a segregation macroscale. Assuming that L_s is the length scale of energy containing particles $L_s = L_C = k^{2/3}/\varepsilon$, one obtains (Villermaux and Falk, 1996):

$$t_{ms} = 5.74\left(\frac{k}{\varepsilon}\right) + \frac{1}{2}\left(\frac{\nu}{\varepsilon}\right)^{1/2} \ln Sc \qquad (2.26)$$

The other interpretation given to mesomixing is the *inertial convective disintegration* of large eddies in the course of dispersion, whereby the scale of the concentration fluctuations is reduced by inertial action from the integral scale of concentration fluctuations towards the Kolmogorov scale. The time constant is given by Baldyga *et al.* (1997b) as:

$$t_S = 2\left(\frac{q_f}{\pi u \varepsilon}\right)^{1/3} \qquad (2.27)$$

2.2.4 Micromixing Time

The *viscous-convective subrange* is concerned with fluid elements of size l larger than the Batchelor microscale, λ_B, and smaller than the Kolmogorov microscale, λ_k.:

$$\lambda_B = \left(\frac{D_m^2 \nu}{\varepsilon}\right)^{1/4} < l < \lambda_k = \left(\frac{\nu^3}{\varepsilon}\right)^{1/4} \qquad (2.28)$$

In this region, eddies are subjected to laminar strain and their size is further reduced by viscous deformation. The time t_{DS}, for decreasing the slab thickness from λ_k, to λ_B, (Baldyga and Bourne, 1988) is given by:

$$t_{DS} = 2 \ \text{arcsin h}(0.05Sc)\left(\frac{\nu}{\varepsilon}\right)^{1/2} \qquad (2.29)$$

where the stretching of vortices is accompanied by engulfment of fluid from the environment. The engulfment process causes mixing and segregation decay with the characteristic time constant, t_E (Baldyga and Bourne, 1984):

$$t_E = \frac{12}{\ln 2}\left(\frac{\nu}{\varepsilon}\right)^{0.5} \tag{2.30}$$

The *viscous-diffusive subrange* is concerned with fluid particles of size, l, smaller than the Batchelor microscale, λ_B:

$$l < \lambda_B = \left(\frac{D_m^2 \nu}{\varepsilon}\right)^{1/4} \tag{2.31}$$

which are also so small that molecular diffusion rapidly dissipates the concentration variance. The diffusion time constant t_D, is given by (Baldyga, 1989):

$$t_D = \frac{Sc}{985 + 1.75x10^{-2}\, Sc}\left(\frac{\nu}{\varepsilon}\right)^{1/2} \tag{2.32}$$

For precipitation the controlling mesomixing mechanism has been found to be the eddy breakup, $t_S > t_{ms}$ (Baldyga *et al.*, 1995) and for Schmidt numbers which are not too high ($Sc << 4{,}000$):

$$t_E > t_{DS} > t_D \tag{2.33}$$

Therefore, engulfment would be the rate controlling process.

In the present work, the time of semi-batch operation is much longer than the circulation time; therefore, one can assume uniform composition of the liquid bulk zone contacting the micromixing zone. Equation (2.23) shows that at small values of q_f, the effects of turbulent diffusion are negligible. Similarly, for slow feeding from a nozzle, the fresh feed relaxes to the environment velocity and the continuity relation ($q_f = \pi L_c^2 u$) yields $L_c = [q_f/\pi u]^{1/2}$ for the concentration scale.

Hence, only the *viscous-convective* mechanism of mixing should be employed in this model. One can conclude that the model of a semi-batch precipitation process at low feed addition rate should include mixing on macroscale (history of environments) and the *viscous-convective micromixing* (exchange with the environment).

2.3 Characteristic Times for Precipitation

2.3.1 Nucleation Time

The nucleation time estimated by the induction time t_{ind} (s) (Dirksen and Ring, 1991) is given by:

$$\tau_{ind} = \frac{6 d_m^2 n^*}{D_i \ln S_a} \tag{2.34}$$

where d_m is molecular diameter, n^* the number of ions forming critical nucleus, S_a represent the supersaturation ratio, and D_i the diffusion coefficient of the solute. This induction time is very difficult to calculate since n^* is usually unknown, and the experimental determination is very complicated for times smaller than 1 sec.

2.3.2 Crystal Growth Time

The characteristic time for the crystal growth can be expressed in terms of the product concentration decrease, C_c, resulting from the crystal growth (Baldyga *et al.*, 1995):

$$t_G = \left(\frac{\rho G}{2M} a \right)^{-1} C_c \tag{2.35}$$

in the case of ionic solutions C_c is the concentration of ions consumed during the crystal growth. In the subject literature there are other time constants for precipitation. However, they are useless when the effect of mixing needs to be compared.

At any given operating condition, the nucleation and growth time constants for the barium sulfate precipitation has been found to be at least eight and four order of magnitude smaller, respectively, than the engulfment time constant (Phillips *et al.*, 1999). Baldyga and Bourne (1999) stated that $t_N \approx t_m$. In any case, micromixing by engulfment should be considered.

2.4 Micromixing Model

2.4.1 Engulfment-Deformation-Diffusion Model (EDD Model)

The Engulfment-Deformation-Diffusion (EDD) model (Baldyga and Bourne, 1984) captures the key physical process contributing to turbulent mixing. According to this model, micromixing is described by the process of molecular diffusion and chemical reaction in a shrinking laminated structure within a small energy-dissipating vortex. The development and application of this model can be traced through Baldyga and Bourne (1984, 1988, 1989, 1992), Bourne and Yu (1994), and Baldyga *et al.* (1997b).

Discretized feed addition is used to model the semi-batch operation. In other words, despite the fact that the feed flows continuously, it is treated as a series of discrete feed elements (blobs) entering the reactor sequentially (Samant and Ng, 1999). Each incoming fluid element is rolled up by turbulent vorticity thereby creating multiple layers or slabs of fresh liquid and liquid already in the reactor. This incorporation of liquid from the environment into the deforming vortices is called *engulfment*. The vortices thus formed undergo *deformation* thereby reducing the scale of segregation by elongation and shrinkage of the embedded slabs. *Diffusion* and *chemical reaction* take place until the vortices die out, at which point a fresh burst of vorticity sets the fluid into motion again.

2.4.2 Engulfment Model (E-Model)

For liquids, engulfment is the rate controlling process ($Sc << 4{,}000$). Thus, the EDD Model can be simplified to the E-Model (Baldyga and Rohani, 1987; Baldyga and Bourne, 1989). This model assumes that the volume of the blob or engulfment zone (also referred as the mixing-precipitation zone), V, entering the system at time t_s (measured from the beginning of the semi-batch operation) grows during its residence time in the system t (measured from the blob addition) according to:

$$\frac{dV(t,t_s)}{dt} = E(t,t_s)V(t,t_s)\left[1 - Y(t,t_s)\right] \tag{2.36}$$

where $Y(t,t_s)$ is the self-engulfment factor or local value of the volume fraction. The term in bracket reflects the fact that engulfment within the fluid elements (self-engulfment) does not contribute to the growth of the volume of the engulfment zone (Baldyga and Bourne, 1989). The engulfment rate $E(t,t_s)$ (s^{-1}) is defined as $1/t_E$, Equation (2.30):

$$E(t,t_s) = \frac{\ln 2}{12\left(\nu/\varepsilon(t,t_s)\right)^{1/2}} = 0.058\left(\frac{\varepsilon(t,t_s)}{\nu}\right)^{1/2} \tag{2.37}$$

The blob of feed moves due to the macroscopic pattern to zones of different turbulent levels. Therefore, the local energy dissipation rate and then the engulfment rate are both functions of time or position inside the stirred vessel.

The concentration profiles for all species in the mixing-precipitation zone following the *kth* blob addition can be calculated using the micromixing equations:

$$\begin{aligned}\frac{dC_i(t,t_s)}{dt} &= E(t,t_s)\left(1 - Y(t,t_s)\right)\left(\left\langle C_i(t,t_s)\right\rangle - C_i(t,t_s)\right) \\ &\pm \frac{\rho_{crystal} G\left(L_{avg},t,t_s\right)}{2M_{crystal}} a(t,t_s)\end{aligned} \tag{2.38}$$

Where the crystal growth, G, is assumed to be a function of the average crystal size in the mixing-precipitation zone, L_{avg}. The initial conditions after any blob addition are:

$$C_A(0,t_s)=0, C_B(0,t_s)=C_{Bo}, C_C(0,t_s)=0, C_D(0,t_s)=0 \qquad (2.39)$$

The concentration $<C_i(t,t_s)>$ in the bulk zone is given by:

$$\frac{d\langle C_i(t,t_s)\rangle}{dt}=\pm\frac{\rho_{crystal}\left\langle G\left(\langle L_{avg}\rangle,t,t_s\right)\right\rangle}{2M_{crystal}}\langle a(t,t_s)\rangle \qquad (2.40)$$

The terms in the <> brackets refer to the bulk zone. The initial conditions ($t = 0$) for the bulk concentration after the $(k+1)th$ addition are simply obtained by dividing the residual mass of any species remaining in the mixing-precipitation zone right before the addition of the next blob and the bulk zone by the total reactor volume.

In the present approach, the concentration $<C_i(t,t_s)>$ in the bulk zone was assumed to change with the residence time in the system, t. This situation can arise when the turbulence level is so low resulting in both poor micromixing and poor macromixing. Therefore, there is a slow incorporation of fresh material from the liquid bulk zone to the mixing-precipitation zone as a result of poor micromixing. Poor macromixing keeps this situation for a long period of time. The reactants have no time to be consumed completely and they are diluted in the liquid bulk zone. Therefore, slow heterogeneous nucleation and crystal growth are still carried out in the liquid bulk zone changing the concentration $<C_i(t,t_s)>$ and producing larger crystals. This phenomenon will be used to explain the decrease of the mean crystal size with the increase of the impeller speed observed in the experiments when feeding below the liquid surface. The present approach differs from original E-Model (Baldyga and Rohani, 1987; Baldyga and Bourne, 1989) which considers the concentration in the bulk zone constant (independent of time).

Figure 2.2 shows the visualization of the E-Model (Bourne, 1993). The actual single-feed semi-batch precipitation vessel is represented by the larger reactor. The mixing-precipitation zone originated from the feed point and the liquid bulk zone are represented by the smaller reactors. For both cases, the well-mixing condition is assumed. The mixing-precipitation zone increases its volume by engulfing material from the liquid bulk zone. This engulfment rate is represented by the flow rate from the liquid bulk zone, which contains material with concentration $<C_i(t,t_s)>$ and moment $<m_j(t,t_s)>$ values as indicated in the liquid bulk reactor.

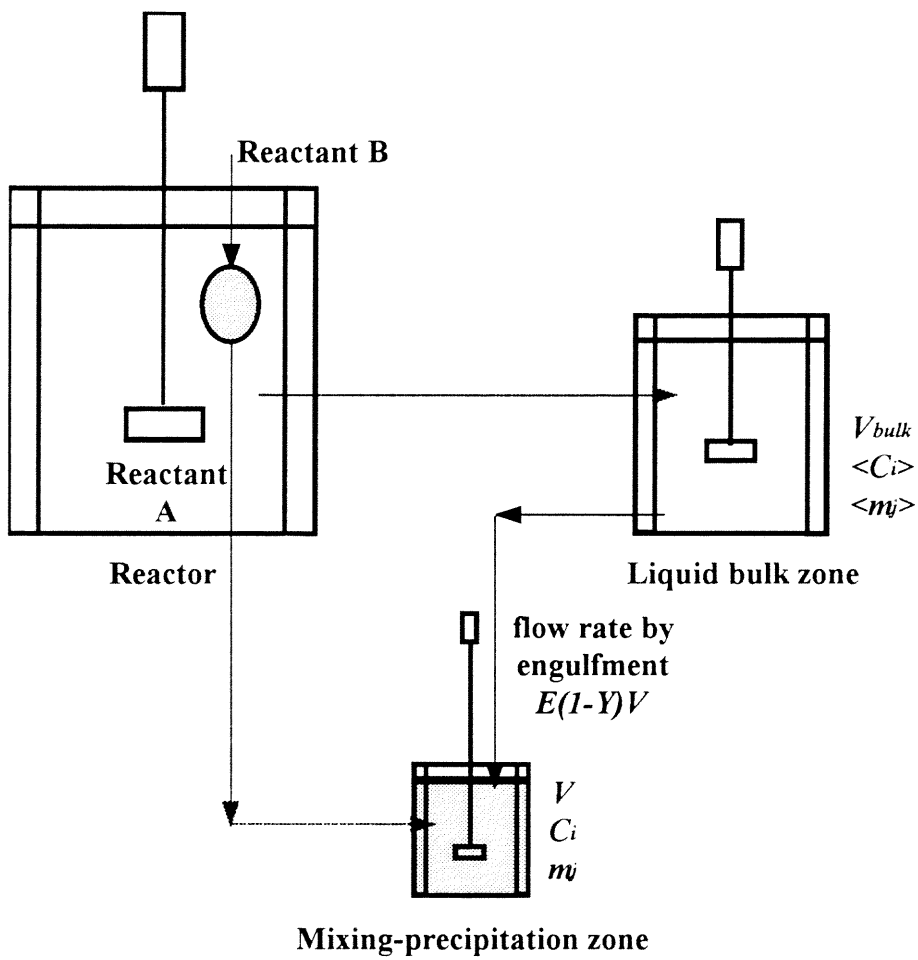

Figure 2.2 Visualization of the E-Model

2.5 Kinetics of Precipitation

2.5.1 Supersaturation

Supersaturation may be expressed in a number of different ways. Among the most common expressions of supersaturation found in the literature are the concentration driving force, or simply supersaturation, ΔC, and the supersaturation ratio, S_a. The thermodynamic supersaturation ratio, S_{at}, and the relative supersaturation, $\Delta C/K_s$, are other forms to express the supersaturation.

The concentration driving force (supersaturation), ΔC, is defined as:

$$\Delta C = \sqrt{C_A C_B} - \sqrt{K_s} \tag{2.41}$$

where C_A and C_B are, respectively, the concentration of barium chloride (A) and sodium sulfate (B) in the engulfment zone, and K_s is the solubility product of the precipitating product. For barium sulfate, the solubility product at room temperature was determined as $pK_s = 9.96$ (Templeton, 1960). The supersaturation ratio, S_a, is defined as:

$$S_a = \sqrt{\frac{C_A C_B}{K_s}} = \frac{\Delta C}{\sqrt{K_s}} \tag{2.42}$$

The thermodynamic supersaturation ratio, S_{at}, is defined as:

$$S_{at} = \sqrt{\frac{C_A C_B}{K_s}}\ \gamma_{\pm A^+B^-} \tag{2.43}$$

where $\gamma_{\pm A^+B^-}$ is the stoichiometric mean activity coefficient expressed in molarities. In solutions of sparingly soluble electrolytes like barium sulfate, especially when they are saturated, the calculation of the thermodynamic supersaturation ratio is difficult and theoretical estimates based on appropriate correlations are needed. Another complication arises since the precipitation of barium sulfate is a multicomponent ionic reaction.

2.5.2 Nucleation Rate

The rate of nucleation (R_N) is usually described by a correlation of the form:

$$R_N = k_n(\Delta C)^n \tag{2.44}$$

This equation is not entirely empirical, and can be derived (Nielsen, 1964; Mullin, 1993) from the classical thermodynamic relationship. From the classical nucleation theory (Dirksen and Ring, 1991), the following equation can be obtained:

$$R_N = k_n \exp\left[-\frac{A_n}{\log^2 S_a}\right] \tag{2.45}$$

2.5.3 Crystal Growth Rate

The growth rate (G) for the case of barium sulfate crystals can be derived using the two step model (Karpinski, 1985). This model considers the surface chemical reaction and the turbulent mass transfer from the bulk to a single particle surface:

$$\begin{aligned} G &= k_\sigma\left[\sqrt{C_{Ai}C_{Bi}} - \sqrt{K_s}\right]^\sigma \\ &= k_{DA}\left[C_A - C_{Ai}\right] = k_{DB}\left[C_B - C_{Bi}\right] \end{aligned} \tag{2.46}$$

where σ and k_σ are the order and rate constant of the reaction, respectively, and $k_{DA} = k_{DB} = k_D$ are coefficients related to the particle-mass-transfer coefficient (k_d) by:

$$k_D = k_d \frac{M}{\rho} \tag{2.47}$$

The measured value of k_D lies between 1.0×10^{-5} and 1.0×10^{-4} (m s^{-1})/(kmol m^{-3}) (Nagata and Nishikawa, 1972). The Armenante and Kirwan (1989) correlation, suited for microparticles ($L < 30$ μm) can be used for the calculations of k_D:

$$Sh = 2 + 0.5 Re_p^{0.52} Sc^{1/3} \tag{2.48}$$

2.6 Population Balance

2.6.1 Crystal Size Distribution

The present analysis of solid phase was based on general population balance derived in the way similar to classical transport equations (Hulbert and Katz, 1964). For the pure precipitation process without agglomeration and breakage, and following the Lagrangian trajectory of the micromixing-precipitation zone, the macroscopic population balance as proposed by Randolph and Larson (1988) can be expressed as:

$$\frac{\partial \Psi(L,t,t_s)}{\partial t} + \frac{\partial G(L,t,t_s)\Psi(L,t,t_s)}{\partial L} = E(t,t_s)\left(1 - Y(t,t_s)\right)\left(\left\langle \Psi(L,t_s)\right\rangle - \Psi(L,t,t_s)\right) \tag{2.49}$$

where $\psi(L,t,t_s)$ represents the size distribution function. The term on the right-hand side of Equation (2.49) represents the exchange with the bulk liquid by engulfment. The initial conditions for Equation (2.49) are:

$$\Psi(L,0,t_s) = 0 \tag{2.50}$$

$$\Psi(0,t,t_s) = \frac{R_N(t,t_s)}{G(0,t,t_s)} \tag{2.51}$$

2.6.2 Moment Transformation of the Population Balance

In many systems of engineering interest, the knowledge of the complete crystal size distribution is unnecessary. Rather some average or total quantities are sufficient to represent the crystal size distribution. One solution method involves the introduction of moments of the crystal size distribution as defined by:

$$m_j(t,t_s) = \int_0^\infty \Psi(L,t,t_s) L^j dL \tag{2.52}$$

The macroscopic population balance given in Equation (2.49) can be written in terms of the moments of the distribution as follows (Randolph and Larson, 1988):

$$\frac{dm_j(t,t_s)}{dt} = jG\left(L_{avg},t,t_s\right)m_{j-1}(t,t_s) + 0^j R_N(t,t_s) + E(t,t_s)\left(1-Y(t,t_s)\right)\left(\left\langle m_j(t_s)\right\rangle - m_j(t,t_s)\right) \tag{2.53}$$

with initial condition:

$$m_j(0,t_s) = 0 \tag{2.54}$$

For the liquid bulk, assuming $\langle m(t,t_s)\rangle$ to be dependent on the residence time, t:

$$\frac{d\left\langle m_j(t,t_s)\right\rangle}{dt} = j\left\langle G\left(\left\langle L_{avg}\right\rangle,t,t_s\right)\right\rangle\left\langle m_{j-1}(t,t_s)\right\rangle + 0^j\left\langle R_N(t,t_s)\right\rangle \tag{2.55}$$

The initial conditions ($t = 0$) for the bulk concentration after the $(k+1)th$ addition are simply obtained by dividing the residual moments remaining in the mixing-precipitation zone and the bulk zone by the total reactor volume.

2.7 Phase Dispersion

2.7.1 Random Walk Model

The engulfment parameter $E(t,t_s)$ which appears in the micromixing model equations must be calculated to solve these equations (Equations 2.36, 2.38, and 2.53). The engulfment parameter is a function of the local energy dissipation $\varepsilon(t,t_s)$ (Equation 2.37). Since the blob undergoes dispersion at time progresses the value of $\varepsilon(t,t_s)$, and hence $E(t,t_s)$, is a function of the position of the growing blob. This position was tracked starting from the feed pipe using the calculated velocities:

$$\frac{dx_{blob,i}}{dt} = u_{blob,i} \tag{2.56}$$

The displacement of the individual blobs was predicted by integrating the trajectory equations using the instantaneous velocity along the blobs path during the integration:

$$u_{blob,i} = \overline{u_i} + u_i' \tag{2.57}$$

where $\overline{u_i}$ is the local average fluid velocity, and u_i' is a random variable defined below.

The stochastic approach of the discrete random walk (MacInnes and Braco, 1992) was adopted here for the evaluation of the instantaneous fluctuating velocity components which appear in the equations of motion of the blob. The values of u_i' which prevail during the lifetime of a fluid eddy that the blob is traversing were sampled by assuming that they obey a Gaussian probability distribution, so that:

$$u_i' = \zeta\left[\left(\overline{u_i'^2}\right)\right]^{1/2} \tag{2.58}$$

In this equation, ζ is a normal distributed random variable and $\left[\left(\overline{u_i'^2}\right)\right]^{1/2}$ is the root mean square value of the velocity fluctuations at the point where the blob becomes engulfed by a particular vortex. The values of these fluctuations can be assumed to remain constant only during the lifetime of the eddy, t_{eddy}, defined by (Fluent, 1995):

$$t_{eddy} = 0.30\frac{k}{\varepsilon} \tag{2.59}$$

when the RSM model is used. As this lifetime depends on the local energy dissipation $\varepsilon(t,t_s)$, it should be updated when a vortex enters a region of different $\varepsilon(t,t_s)$. A vortex ceases to exist after its lifetime. Then, the normal distributed random variable is updated representing a new transporting vortex. When a reacting vortex ceases to exist is by two new ones.

The two new vortices both travel their own way through the turbulent flow field and after their respective lifetimes each vortex produces two new ones. This process continues until all the added substance has reacted. For each vortex individual mass and moment balances should be solved. Bakker and Van Den Akker (1994, 1996) followed this approach for the simulation of chemical reactors on the basis of micromixing models, however, to solve such a large number of equations would require very large computational resources. Baldyga *et al.* (1995) and Phillips *et al.* (1999) for the simulation of double- and single-feed semi-batch precipitation of barium sulfate, respectively, considered only one blob, added sequentially to the reactor, and two regions of different but constant energy dissipation rate.

In the present work, two simplifications were made. First, the values of the fluctuations, Equation (2.58), which prevail only during the lifetime of the eddy, t_{eddy}, were assumed to remain constant in the time interval in which the blobs were tracked (step time in the numerical solution). This assumption holds if this time interval is smaller than the vortex lifetime (Boysan *et al.*, 1982). In the present simulation, using Equation (2.59), the vortex lifetime was determined to be always longer than 1×10^{-4} s. Second, to account for the dispersion each blob was discretized into 10,000 neutrally buoyant, rigid sub-droplets which became dispersed under the action of the fluid flow. The position of each sub-droplet was tracked starting from the feed pipe using the calculated velocities from the computational fluid dynamics simulation. The energy dissipation rate of the entire blob was calculated as the space-averaged, weighed $\varepsilon(t,t_s)$ value of all the sub-droplets constituting the initial blob of added reactant. Figure 2.3 shows a comparison between the different approaches used for the phase dispersion.

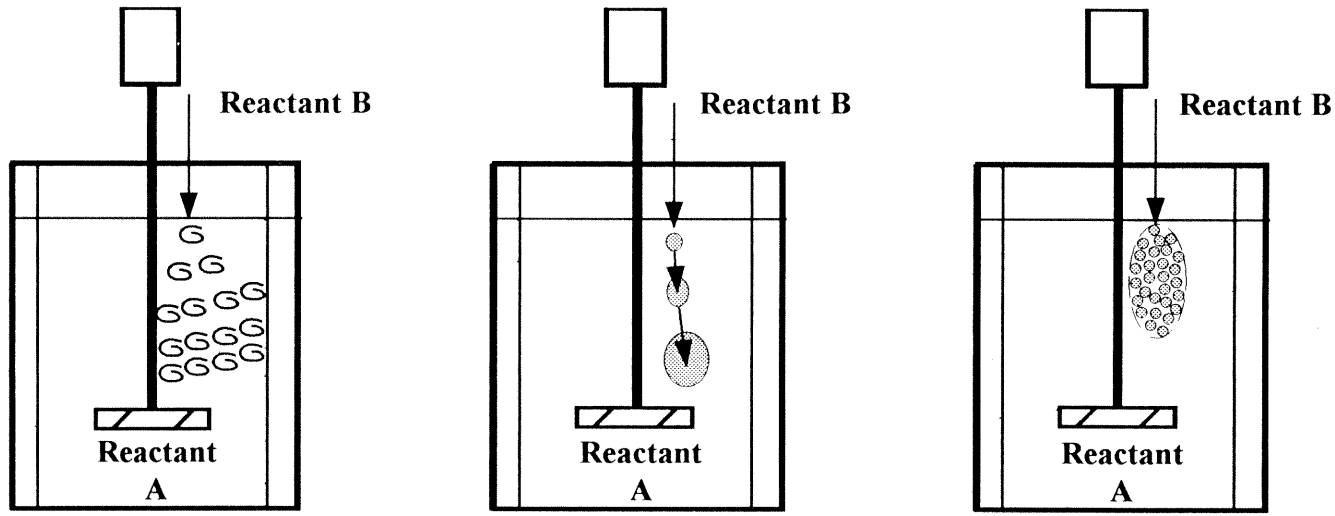

Bakker and Van Den Akker (1994, 1996)

Baldyga, Podgorska and Pohorecki (1995) Phillips, Rohani and Baldyga (1999)

Present approach

Figure 2.3 Different approaches used for feed dispersion

2.7.2 Dispersed Phase Boundary Condition

When a sub-droplet reaches a physical boundary (walls, shaft, impeller blades and baffles), a dispersed phase boundary condition is applied to determine the fate of the trajectory at that boundary. These contingencies can be summarized as follows:

- Reflection: The sub-droplet rebounds off the boundary in question (Figure 2.4) assuming the velocity in the fluid flow (Boysan *et al.*, 1982). This is assumed to occur at the top wall, shaft, impeller blades and baffles.

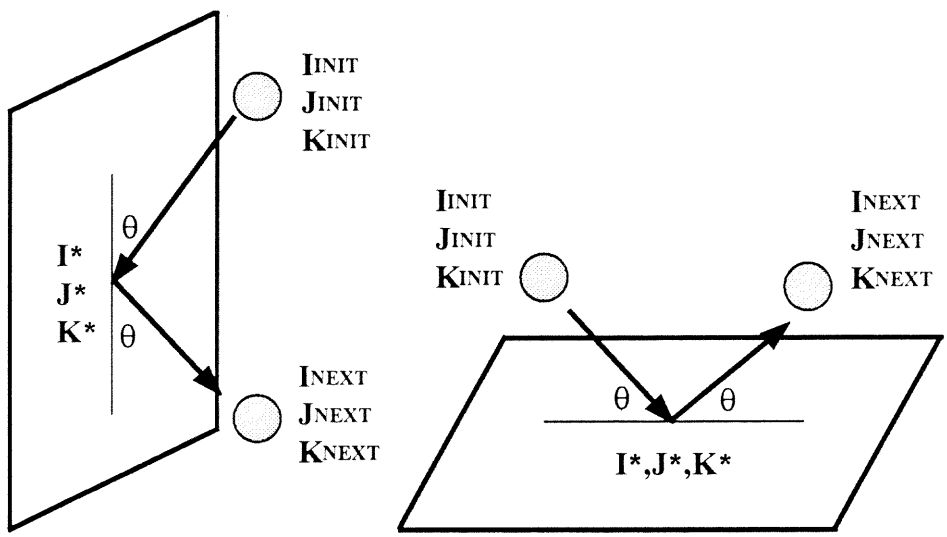

$J_{NEXT} = J_{INIT}$ $\quad K_{NEXT} = K_{INIT}$

$K_{NEXT} = K^* + (K^* - K_{INIT})$ $\quad J_{NEXT} = J^* + (J^* - J_{INIT})$

$I_{NEXT} = I^* + (I^* - I_{INIT})$ $\quad I_{NEX} = I^* + (I^* - I_{INIT})$

Figure 2.4 Dispersed phase boundary condition: reflection

- Saltation: in order to prevent time consuming 'trickling' of a particle down a wall, in some cases the particles is replaced in the flow field a small distance from the wall (Figure 2.5) as though it was 'leaping' back into the flow (Boysan *et al.*, 1982). This is an artificial treatment of the particle intended only to improve the efficiency of the calculation. This boundary condition applies at the side and bottom walls.

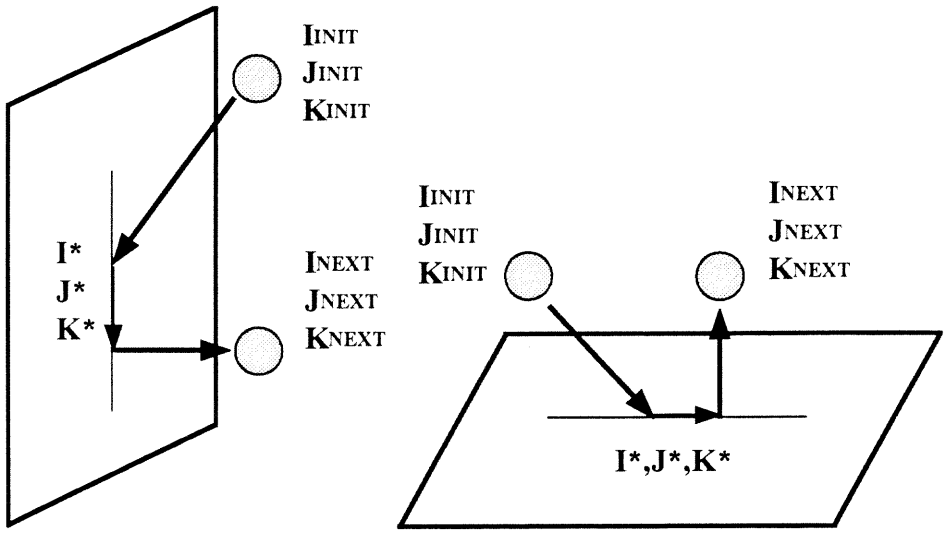

JNEXT = JINIT
KNEXT = K*
INEXT = I*

KNEXT = KINIT
JNEXT = J*
INEX = I*

Figure 2.5 Dispersed phase boundary condition: saltation

2.8 Scale-Up of Semi-Batch Precipitation Processes

For many unit operations in chemical engineering, theoretical or empirical scale-up rules have been established. In precipitation processes, however, where kinetic rates are controlled by the degree of mixing, these simple scale-up criteria often fail due to the fact that it is not only one mixing process that can be limiting. In most situations, we would like to operate in the perfectly mixed regime if possible or, as it will be shown in the present work, in the micromixing-controlled regime. The mixing intensity decreases as the meso- and macromixing effects increase. Thus, the mean crystal size decreases and the coefficient of variation increases. Therefore, if the objective is to obtain larger crystal and smaller coefficient of variation, the micromixing-controlled regime would be preferred on different scales.

Samant and Ng (1999) based on an analysis of the interplay of reaction and mixing at various length scales, showed clearly that the power input (P) per unit volume ($V_{reactor}$) and the feed addition time (t_f) are the only variables that must be manipulated during the scale-up. If these variables change with the reactor volume as:

$$\frac{P}{V_{reactor}} \propto V_{reactor}^{\beta} \tag{2.60}$$

$$t_f \propto V_{reactor}^{\delta} \tag{2.61}$$

The authors established the following conditions for two exponents:

$$\beta \geq 0 \tag{2.62}$$

$$\delta \geq \frac{\beta}{6} + \frac{8}{9} \tag{2.63}$$

Therefore, to operate in the micromixing controlled regime or at constant $P/V_{reactor}$, $\beta = 0$, and δ must be equal or higher than 8/9. These authors also showed in order to preserve the micromixing controlled regime, scale up with "constant impeller tip speed" is not a good scale-up rule since this implies $\beta < 0$, and scale-up with "constant impeller speed" calls for higher power input per unit volume.

Mersmann and Laufhutter (1985) suggested that scale-up with constant specific power input for micromixing-limited processes is a suitable scale-up criterion. Bourne and Dell'Alva (1987) studied micromixing on different scales and excluded any meso- and macromixing effects by feeding the reagents with feed rates much smaller than the circulation rate. Rice and Baud (1990) used constant specific power input as a scale-up criterion and found that this criterion can only be used for certain feed point locations. They state that a localization of the reaction zone with the scale takes place. To avoid this effect, the authors suggest changing the ratio of impeller diameter-to tank diameter.

During scale-up with geometrical similarity (D/T = constant), and assuming constant power number (Po, see Equation 3.3), preservation of power input per unit volume yields (Bourne and Yu, 1994):

$$\frac{P}{\rho V_{reactor}} \propto \frac{PoN^3D^5}{T^3} \propto N^3D^2 \qquad (2.64)$$

Therefore, for a given $P/V_{reactor}$, the larger vessel must operate at a lower impeller speed. Since the circulation time in a stirred vessel is inversely proportional to the impeller speed, the larger vessel would have a longer circulation time than the smaller vessels. This means that on a dimensionless basis the mixing-precipitation zone after injection will travel through a smaller fraction of the vessel volume in the larger scale.

In most of the studies, the feed addition time has been kept constant. Only few authors (Bourne and Yu, 1994) considered the effect of changes in feed addition time, although it was not explicitly included in the proposed scale-up rules. In many situations, it may not be possible to increase the feed addition time due to the operating constraints. However, scale-up with "constant power input per unit volume" and constant feed addition time may not improve or preserve the performance of the precipitator in the micromixing-controlled regime (Bourne and Hilber, 1990).

CHAPTER 3

DEVELOPMENT OF MIXING-PRECIPITATION MODEL

3.1 Modeling Approach Developed in This Work

In this work, a novel method was developed to quantitatively describe the single-feed semi-batch precipitation process of barium sulfate according to the following reaction:

$$\begin{array}{ccccccc} BaCl_2 & + & Na_2SO_4 & \rightarrow & 2\,NaCl & + & BaSO_4 \\ \textit{Barium} & & \textit{Sodium} & & \textit{Sodium} & & \textit{Barium} \\ \textit{Chloride} & & \textit{Sulfate} & & \textit{Chloride} & & \textit{Sulfate} \\ A & + & B & \rightarrow & C & + & D \end{array} \qquad (3.1)$$

A conceptual diagram of the modeling approach is shown in Figure 3.1. The model integrates together different components (CFD, phase dispersion, micromixing model, precipitation kinetics) in order to predict the final crystal size distribution as a function of all the operating and geometric variables of importance. Accordingly, the model was based on the following steps:

1. The velocity profile and energy dissipation rate distributions in the reactor were predicted using CFD (no experimental input was needed). The CFD predictions were experimentally validated via LDV measurements;
2. The feed containing sodium sulfate was discretized in individual blobs, each blob added individually and sequentially to the reactor;
3. The engulfment model (E-Model) was used to simulate the rate of incorporation (engulfment) of fluid from the liquid bulk to the expanding blob;
4. Differential mass balance equations were written for each reacting species; the rates of material engulfment and precipitation were included in the mass balances;
5. Appropriate expressions for the precipitation kinetics and species transfer (nucleation rate, crystal growth rate, and solid-liquid mass transfer coefficient) were also utilized;

6. A moment transformation of the crystal population balance was used to determine the mean crystal size and the coefficient of variation of the crystal size distribution, as a function of time;
7. In order to determine the local energy dissipation rate required by the E-Model, each blob was numerically decomposed into 10,000 sub-droplets becoming dispersed in the reactor over time under the action of the fluid flow. The trajectory of each sub-droplet was computed using the fluid velocity profiles obtained via CFD. The average energy dissipation rate of all sub-droplets was calculated as a function of time;
8. Steps 3-7 were repeated for each new blob addition, until the feed was exhausted. The final mean crystal size and the coefficient of variation were determined, and compared with experimental results.

In setting up the modeling approach, the following assumptions were made:

- The presence of solid phase did not affect the flow field;
- The solid phase was assumed to follow the flow field because the crystals (typically less than 10 μm) were very small and the solids concentration was low. Sedimentation of the solids can thus be neglected;
- Aggregation and breakage, as well as dissolution of the particles in any regions of undersaturation were neglected;
- Only primary nucleation (homogeneous and heterogeneous) was considered.

The first two assumptions have been verified experimentally using three-dimensional phase-Doppler anemometer (Pettersson and Rasmuson, 1997, 1998). Breakage and Ostwald ripening have been shown to be not important in barium sulfate precipitation (Fitchett and Tarbell, 1990; Tavare and Garside, 1990; Åslund and Rasmuson, 1992).

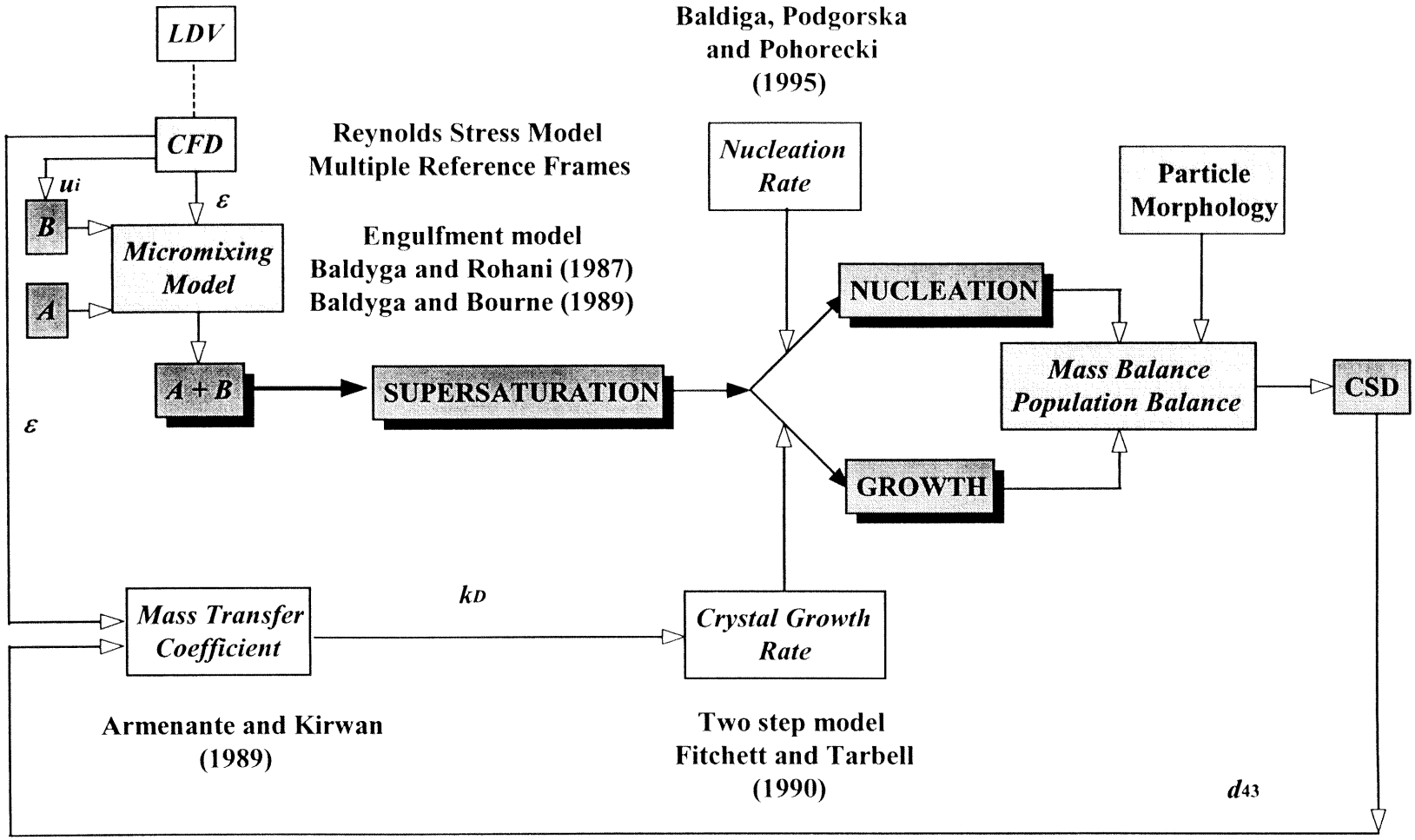

Figure 3.1 Modeling approach for single-feed semi-batch precipitation process

3.2 Fluid Field Simulation

In the present work, six-blade 45° pitched blade turbines were used to agitate the precipitation vessels. Several works on fluid fields simulation in stirred tanks using these turbines are found in the literature. Of interest are those which make a comparison between different modeling approaches (Brucato *et al.*, 1998, Armenante and Chou, 1996; Daskopoulos and Harris, 1996, Sahu and Joshi, 1995), show the effect of different parameters (Zhou and Kresta, 1996a; Fokema and Kresta, 1994; Kresta and Woods, 1993a), and present experimental data (Ranade and Joshi, 1989; Ranade *et al.*, 1992).

3.2.1 Grid Generation

The conservation equations were solved using a control volume technique. The computational domain was divided into discrete control volume by means of a grid. The conservation equations were integrated on the individual control volumes to construct algebraic equations for the unknowns, which were solved using algebraic techniques.

The flow field was simulated using FLUENT v4.5.2. A three-dimensional, single-block, hexahedral element grid were automatically generated using MIXSIM v1.5. The full 360° tank was modeled in this work. Often situations arise in which the swirl component of velocity is in direction opposite of the impeller. In order to eliminate this reverse swirl, the grid was refined in the near impeller region, and adjacent to the walls (Oshinowo *et al.*, 2000). Figure 3.2 shows the grid generated. This grid consisted of 146, 35 and 68 cells in the tangential, radial and axial direction, respectively, and was obtained by refining the normal grid density generated by MIXSIM in the impeller, baffle and tank wall regions.

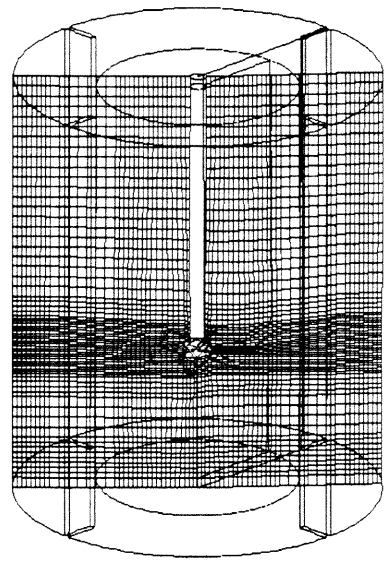

Figure 3.2 Grid generation for stirred tanks

3.2.2 Boundary conditions

The boundary conditions imposed on the systems were as follows. The condition of no slip was applied at the impeller shaft and at the vessel cylindrical wall, baffles, and bottom. The shear stress near the solid surfaces was specified using the "non-equilibrium wall function" with no assumption of equilibrium between the generation and dissipation of turbulent kinetic energy, k. This relaxes the assumption of equilibrium of the "standard wall function". The boundary conditions at the top liquid surface (free surface) were of zero-gradient, zero-flux type, which is equivalent to a frictionless impenetrable wall. The vessel was assumed to be symmetric along its axis and the impeller centerline. This implied that at the vessel axis (except for the region where the shaft was present), the radial and tangential velocities and the gradients of the axial velocity and k were all imposed to be zero in the fluid.

Table 3.1 summarizes the boundary conditions used in the numerical simulations. In this table, u, v, w are the mean axial, radial, and tangential components of velocity, respectively, and k and ε represent the turbulent kinetic energy and the energy dissipation rate, respectively. The origin of the cylindrical coordinate system was located at the axis of symmetry in the bottom vessel, and the angular position $\theta = 0°$ coincided with one of the baffles. The axial, radial, and tangential coordinates were assumed to be positive upward to the vessel bottom, outward to the vessel wall, and clockwise, respectively.

Table 3.1 Boundary conditions for fluid field simulation

At the axis of symmetry:

$r = r_s;\ 0 < z < H - C;$ $\forall\theta$	$v = 0;\ w = w_s$ $\frac{\partial u}{\partial r} = 0; \frac{\partial k}{\partial r} = 0;\ \frac{\partial \varepsilon}{\partial r} = 0$
$r = 0;\ H - C < z < H;$ $\forall\theta$	$v = 0;\ w = 0$ $\frac{\partial u}{\partial r} = 0; \frac{\partial k}{\partial r} = 0;\ \frac{\partial \varepsilon}{\partial r} = 0$

At the vessel wall:

$r = \frac{T}{2};\ \forall z;\ \forall\theta$	$u = v = w = 0$ $k = \varepsilon = 0$

At the vessel bottom:

$\forall r;\ z = H;\ \forall\theta$	$u = v = w = 0$ $k = \varepsilon = 0$

At the liquid surface:

$\forall r;\ z = 0;\ \forall\theta$	$v = 0;$ $\frac{\partial u}{\partial r} = 0;\ \frac{\partial w}{\partial r} = 0; \frac{\partial k}{\partial r} = 0;\ \frac{\partial \varepsilon}{\partial r} = 0$

3.2.3 Impeller Region

In the past, the impeller region has often been excluded from the computational domain. Experimental informational has been used to prescribe the flow field near the impeller as a stationary boundary condition for the remainder of the computational domain ("black box" method). This model has been applied extensively (Ranade and Joshi, 1989; Kresta and Woods, 1991; Bakker and Van den Akker, 1994b; Bakker *et al.*, 1996; Armenante and Chou, 1996) with good results. As an alternative, the impeller has been modeled as a momentum source (Xu and McGrath, 1996). The main limitation of these approaches is their lack of generality; experimental data which require extensive experimental work are needed for each specific case under investigation, while such data are actually available only for a few vessel-impeller geometry.

Fully predictive models reported in the literature are: the sliding mesh model (Murthy *et al.*, 1994), the inner-outer model (Brucato *et al.*, 1994), and the multiple reference frames model (Luo *et al.*, 1993, 1994). The sliding mesh model offers the advantage of modeling the transient behavior of the fluid motion in the tank but with a penalty of computational expense due to the time-dependent formulation. The inner-outer model divides the tank into two partially overlapping zones, one in a rotating frame, and the other in the stationary frame. An iterative matching of the solution obtained on the boundaries of the overlapping zones is required. The multiple reference frames (MRF) is the simplest being a steady-state approximation. It requires least computational effort since the inner and outer frames are implicitly matched at the interface, requiring no additional iterative calculations. MRF can achieve a solution with a computer processing time one tenth of that require for the sliding mesh method (Lane, 2000).

The MRF model (Luo *et al.*, 1993, 1994) was used to model the impeller motion. In this model approach, two fluid regions are allowed to rotate relative to each other in a non-moving grid. Figure 3.3 shows the rotating and stationary frames of reference. The flow in the rotating region of the modeled geometry is solved in a rotating reference frame. A stationary reference frame is used in the non-rotating part of the geometry. This results in an approximate steady-state solution, because the relative position of the impeller and the baffle remain unchanged in the grid during the calculation. The MRF interface was set from the vessel bottom and all the way to the liquid surface above the impeller, midway between the impeller blade tips and the baffle edges furthest away from the wall.

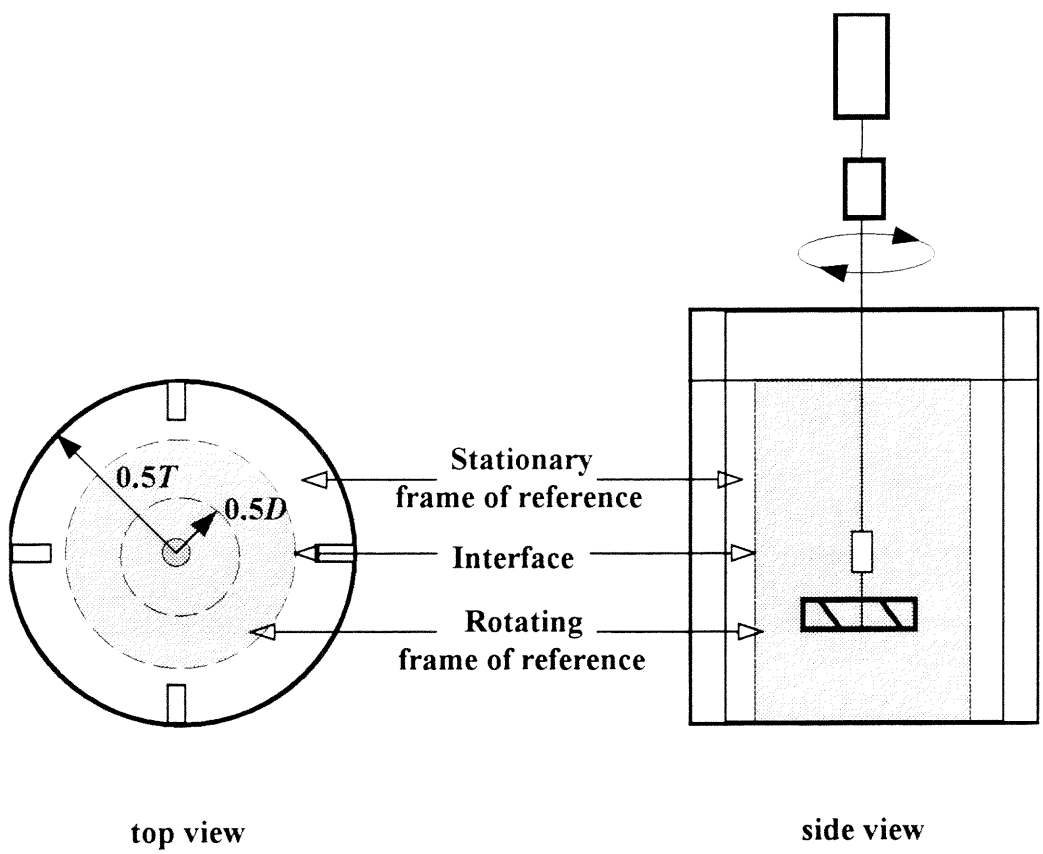

Figure 3.3 Frames of reference for MRF model

3.2.4 Numerical Method of Solution

Since the MRF model is not available with higher order schemes in the FLUENT code, power law interpolation scheme was used for the space discretization of the convection terms in momentum and turbulence equations in all simulations. Power law scheme has been shown to be more appropriate for the numerical simulation of axial flow impellers (Sahu *et al.*, 1998). A standard interpolation scheme was used to interpolate the cell face values of pressure in the momentum equations. The pressure-velocity coupling was solved using the SIMPLE algorithm. All simulations were performed first with the standard k-ε model before switching to the RSM model. When the results from the k-ε model were used as initial guess values for the simulation with the RSM model the number of iterations to obtain the converged solution was reduced. Initial guesses have a great influence on the success of the iterative process (Sahu and Joshi, 1995).

The under-relaxation parameters for flow variables were adjusted very carefully to obtain a converged solution. Early simulations were conducted with under-relaxation values taken from the work of Sahu *et al.* (1998). These values were 0.75, 0.45, 0.35, 0.45, 0.25 and 0.30, for pressure, radial, axial and tangential velocities, turbulent kinetic energy, and turbulent energy dissipation rate, respectively. The value for the turbulent energy dissipation rate (0.3) was also used as initial values for the Reynolds stresses. These values were changed until the set of parameters attained an optimal value for which convergence was obtained with an optimum number of iterations and computational time. It was observed that these optimal values were 0.6, 0.30-0.40, 0.20-0.30 and 0.10-0.20, for pressure, velocities, turbulent kinetic energy, and Reynolds stresses, respectively. These values were used in all subsequent simulations

In the iterative process, the algebraic equations for a given unknown variable were treated as linear. These linear equations were solved iteratively using the Gauss-Seidel line-by-line method. In this method, the equations were solved simultaneously for small groups of lines of cells (either a complete row or a complete column), one at a time. For velocity, 3-5 internal iterations were sufficient to obtain a converged solution. However, for the turbulent kinetic energy, a minimum of 10-15 internal iterations was required, and 10-20 internal iterations were needed for the Reynolds stresses.

A refined grid near the impeller, and wall and baffles in the discharge stream help to eliminate reverse swirl (Oshinowo et al., 2000) and obtain accurate calculations of integral quantities, such as power number. However, the convergence of the solution, i.e., minimization of errors in variable equations, must be also sufficient deep. Typically, 30,000-36,000 iterations were sufficient for a converged solution. The solutions were considered converged when the sum of the residuals was $< 5\times10^{-4}$, and the residuals and variables were unchanging.

3.2.5 Power Number

The design of mixing equipment requires an estimation of the impeller power consumption (P). P is utilized to generate circulation flow and turbulence, by imparting kinetic energy to the liquid. Turbulence is produced due to the sharp velocity changes (both in magnitude and direction) behind the blades, which depend on the geometry of the impeller. Depending on the starting point different liquid elements will have different velocities and will follow certain pattern having certain direction changes. As a result, eddies of different sizes and energy are produced (Rewatkar *et al.*, 1990).

P is usually reported in terms of the dimensionless power number (Po). Using dimensionless analysis, a general functional relationship can be found between Po and physical and geometrical parameters:

$$Po = \frac{P}{\rho N^3 D^5} = k\left(\frac{ND^2}{\nu}\right)^a \left(\frac{N^2 D}{g}\right)^b \left(\frac{T}{D}\right)^c \left(\frac{H}{D}\right)^d \left(\frac{C}{D}\right)^e \left(\frac{W_b}{D}\right)^f \left(\frac{k_b}{D}\right)^g \tag{3.2}$$

The first group on the right hand is known as the impeller Reynolds number, Re, and describes the hydrodynamic effect in the system. The second group is known as the Foude number, Fr, and accounts for the effect of vortex in swirling systems. The remaining terms account for the effects of the tank geometry and impeller configuration. However, the full form is seldom used in practical power calculation. If the mixing process is carried out in a fully baffled turbulent region at a given geometry of configuration, the general functional relationship reduces to:

$$Po = \frac{P}{\rho N^3 D^5} = constant \tag{3.3}$$

FLUENT code calculates the power number. The cross product of the radius vector (originated on the shaft axis) and the force vector at all nodes on the impeller surface are summed and the resulting torque (τ) is directed along the shaft axis. The forces on the impeller include both shear forces and normal forces. Shear forces are computed from tangential velocity gradients at the surface, and the normal forces are computed from the surface pressure and cell area. The product of the torque and impeller speed allows the calculation of P:

$$P = 2\pi N\tau \tag{3.4}$$

and Po is obtained using Equation (3.3).

3.3 Feed Discretization

Upon addition of the reacting feed to the reactor a mixing-precipitation zone is generated. This zone moves away from the feed point while the mixing-precipitation takes place as a result of bulk motion and macromixing (Bourne *et al.*, 1995). For computational purposes, in this work the feed solution was discretized, with each blob being fed into the system in sequence. Following each blob addition, the micromixing equations were solved. Then, another blob was added and the calculations repeated until the feed was completely exhausted.

Two approaches are reported in the literature for the feed discretization. In the first approach, the feed stream is discretized into parts of volume $q_f \times t_c$, where q_f is the feed flow rate of the second reactant and t_c the circulation time (Baldyga *et al.*, 1995; Phillips *et al.*, 1999). This discretization results from the macromixing pattern, the concentration of environment changes with frequency $1/t_c$ due to circulation. This method differs from the second approach described by Baldyga and Bourne (1984) and David and Marcant (1994) where the feed is discretized into drops growing independently of each other in the tank and is rather similar to the method of Baldyga and Bourne (1989), developed for the pipe flow with self-engulfment.

The first approach often used for the simulation of the precipitation process requires a large number of blobs. In this work, the second approach was used and the number of blobs was increased until the final solution (mean crystal size and coefficient of variation, *C.V.*) appeared to be independent of the number of blobs. As shown in Figure 3.4, 100 blobs were determined to be sufficient for the solution to be independent, i. e., the mean crystal size and *C.V.* remain practically constant.

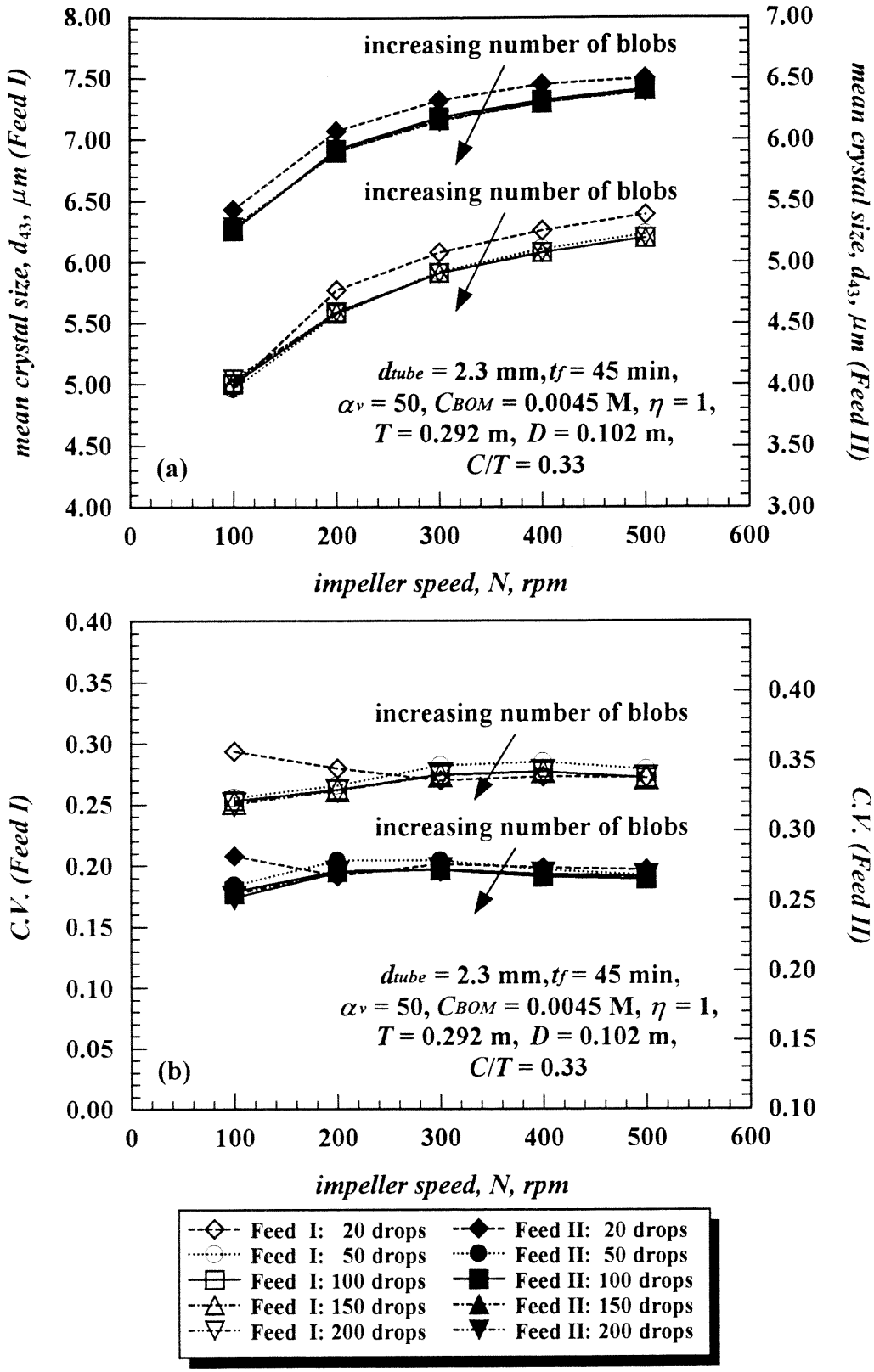

Figure 3.4 Effect of feed discretization on: (a) mean crystal size; and (b) *C.V.*

3.4 Engulfment Rate

The rate of growth of the mixing-precipitation volume due to engulfment was expressed in Equation (2.36). However, a more useful expression would be obtained if this equation is expressed in dimensionless form. The change of the local value of the volume fraction, Y, of the mixing-precipitation zone (also referred as the engulfment zone in this system) for the *kth* blob addition can be obtained from Equation (2.36) by dividing both sides of this equation by the total reactor volume, $V_{reactor}$:

$$\frac{dY_k(t,t_s)}{dt} = E_k(t,t_s)\left(1 - Y_k(t,t_s)\right)Y_k(t,t_s) \tag{3.5}$$

Since the volume of the blob entering the reactor (@ $t = 0$) is known, the initial condition of Equation (3.5) is as follows:

$$Y_k(0,t_s) = \frac{V_{kth\ blob}(t=0)}{V_{reactor}(0,t_s)} \tag{3.6}$$

3.5 Differential Mass Balance Equations

The concentration profiles for all the species in the mixing-precipitation zone following the *kth* blob addition can be calculated using Equation (2.38):

$$\begin{aligned}\frac{dC_{A,k}(t,t_s)}{dt} &= E_k(t,t_s)\left(1 - Y_k(t,t_s)\right)\left(\left\langle C_{A,k}(t,t_s)\right\rangle - C_{A,k}(t,t_s)\right) \\ &\quad - \frac{\rho_{crystal} G_k\left(L_{avg},t,t_s\right)}{2M_{crystal}} k_a m_{2,k}(t,t_s)\end{aligned} \tag{3.7}$$

$$\begin{aligned}\frac{dC_{B,k}(t,t_s)}{dt} &= E_k(t,t_s)\left(1 - Y_k(t,t_s)\right)\left(\left\langle C_{B,k}(t,t_s)\right\rangle - C_{B,k}(t,t_s)\right) \\ &\quad - \frac{\rho_{crystal} G_k\left(L_{avg},t,t_s\right)}{2M_{crystal}} k_a m_{2,k}(t,t_s)\end{aligned} \tag{3.8}$$

$$\frac{dC_{C,k}(t,t_s)}{dt} = E_k(t,t_s)\left(1 - Y_k(t,t_s)\right)\left(\left\langle C_{C,k}(t,t_s)\right\rangle - C_{C,k}(t,t_s)\right) + \frac{\rho_{crystal} G_k\left(L_{avg},t,t_s\right)}{2M_{crystal}} k_a m_{2,k}(t,t_s) \tag{3.9}$$

$$\frac{dC_{D,k}(t,t_s)}{dt} = E_k(t,t_s)\left(1 - Y_k(t,t_s)\right)\left(\left\langle C_{D,k}(t,t_s)\right\rangle - C_{D,k}(t,t_s)\right) + \frac{\rho_{crystal} G_k\left(L_{avg},t,t_s\right)}{2M_{crystal}} k_a m_{2,k}(t,t_s) \tag{3.10}$$

with initial conditions:

$$C_{A,k}(0,t_s) = 0,\ C_{B,k}(0,t_s) = C_{BO},\quad C_{C,k}(0,t_s) = 0,\ C_{D,k}(0,t_s) = 0 \tag{3.11}$$

Similarly, for the bulk zone, by using Equation (2.40):

$$\frac{d\left\langle C_{A,k}(t,t_s)\right\rangle}{dt} = -\frac{\rho_{crystal}\left\langle G_k\left(\left\langle L_{avg}\right\rangle,t,t_s\right)\right\rangle}{2M_{crystal}} k_a \left\langle m_{2,k}(t,t_s)\right\rangle \tag{3.12}$$

$$\frac{d\left\langle C_{B,k}(t,t_s)\right\rangle}{dt} = -\frac{\rho_{crystal}\left\langle G_k\left(\left\langle L_{avg}\right\rangle,t,t_s\right)\right\rangle}{2M_{crystal}} k_a \left\langle m_{2,k}(t,t_s)\right\rangle \tag{3.13}$$

$$\frac{d\left\langle C_{C,k}(t,t_s)\right\rangle}{dt} = \frac{\rho_{crystal}\left\langle G_k\left(\left\langle L_{avg}\right\rangle,t,t_s\right)\right\rangle}{2M_{crystal}} k_a \left\langle m_{2,k}(t,t_s)\right\rangle \tag{3.14}$$

$$\frac{d\left\langle C_{D,k}(t,t_s)\right\rangle}{dt} = \frac{\rho_{crystal}\left\langle G_k\left(\left\langle L_{avg}\right\rangle,t,t_s\right)\right\rangle}{2M_{crystal}} k_a \left\langle m_{2,k}(t,t_s)\right\rangle \tag{3.15}$$

The initial conditions ($t = 0$) for the bulk concentration after the *(k+1)th* addition are simply obtained by dividing the residual mass of any species remaining in the mixing-precipitation zone and the bulk zone by the total reactor volume.

$$\left\langle C_{A,k+1}(0,t_s)\right\rangle = \left\langle C_{A,k}(t_{end},t_s)\right\rangle\left[1 - Y_k(t_{end},t_s)\right] + C_{A,k}(t_{end},t_s)Y_k(t_{end},t_s) \tag{3.16}$$

$$\left\langle C_{B,k+1}(0,t_s)\right\rangle = \left\langle C_{B,k}\left(t_{end,},t_s\right)\right\rangle\left[1-Y_k\left(t_{end},t_s\right)\right]+ C_{B,k}\left(t_{end},t_s\right)Y_k\left(t_{end},t_s\right) \tag{3.17}$$

$$\left\langle C_{C,k+1}(0,t_s)\right\rangle = \left\langle C_{C,k}\left(t_{end,},t_s\right)\right\rangle\left[1-Y_k\left(t_{end},t_s\right)\right]+ C_{C,k}\left(t_{end},t_s\right)Y_k\left(t_{end},t_s\right) \tag{3.18}$$

$$\left\langle C_{D,k+1}(0,t_s)\right\rangle = \left\langle C_{D,k}\left(t_{end,},t_s\right)\right\rangle\left[1-Y_k\left(t_{end},t_s\right)\right]+ C_{D,k}\left(t_{end},t_s\right)Y_k\left(t_{end},t_s\right) \tag{3.19}$$

where t_{end} is the total time the *kth* blob remains in the system before the addition of the next blob $(k+1)th$ and equal to the total feed addition time divided by the number of blobs assumed in the feed discretization.

3.6 Kinetics of Precipitation

The precipitation of barium sulfate was chosen for the present work. This system has been widely used to validate micromixing and precipitation models (Pohorecki and Baldyga, 1983, 1988; Fitchett and Tarbell, 1990, Baldyga *et al.*, 1995, Kim and Tarbell, 1996; Baldyga *et al.* 1997a; Phillips *et al.*, 1999). The precipitation kinetics for barium sulfate is well known, and can be obtained from published nucleation and crystal growth kinetics expressions calculated from extensive experimental data (Nielsen, 1957, 1958, 1961, 1964; Gunn and Murthy, 1972; Aoun *et al.*, 1996).

Barium sulfate crystals do not present polymorphism, which is common among organic substances and can confuse the interpretation of the experimental results. Particle breakage (Fitchett and Tarbell, 1990) and Ostwald ripening (Tavare and Garside, 1990; Åslund and Rasmuson, 1992) are not considered to be important effects in this system. Agglomeration can be eliminated by keeping a suitable level of the local supersaturation.

3.6.1 Nucleation Rate

For the case of barium sulfate, using the experimental data by Nielsen (1964), Baldyga *et al.* (1995) obtained the following expressions from the semi-empirical correlation, Equation (2.44):

$$R_N = 6.00\times10^{15}(\Delta C)^{1.775} \qquad (\text{for } \Delta C < 0.01 \text{ kmol/m}^3) \quad (3.20)$$

$$R_N = 2.53\times10^{42}(\Delta C)^{15.0} \qquad (\text{for } \Delta C > 0.01 \text{ kmol/m}^3) \quad (3.21)$$

Using the same set of experimental data, regarded in the subject literature as the most reliable one for barium sulfate, Dirksen and Ring (1991) estimated from the classical nucleation theory, Equation (2.45):

$$R_N = 1.00\times10^{11}\exp\left[-\frac{2}{\log^2 S_a}\right] \quad (\text{for } S_a < 1000) \qquad (3.22)$$

$$R_N = 1.00\times10^{3}\exp\left[-\frac{200}{\log^2 S_a}\right] \quad (\text{for } S_a > 1000) \qquad (3.23)$$

Wei and Garside (1997) and Garside and Wei (1998) also represented the experimental nucleation data for barium sulfate obtained by Nielsen (1964) by the classical primary nucleation rate equation:

$$R_N = 1.42\times10^{12}\exp\left[-\frac{67.3}{\ln^2 S_{at}}\right] \quad (\text{for } S_{at} < 1000) \qquad (3.24)$$

$$R_N = 1.00\times10^{36}\exp\left[-\frac{2686}{\ln^2 S_{at}}\right] \quad (\text{for } S_{at} > 1000) \qquad (3.25)$$

In these correlations, the driving force is defined as the thermodynamic supersaturation ratio, S_{at}. Wei and Garside (1997) used the Bromley (1973) method to estimate the activity coefficient and presented the relevant equations.

Figure 3.5 shows the comparison of the different nucleation rate correlations. The correlation proposed by Aoun *et al.* (1996) under both stoichiometric and non-stoichiometric conditions is also shown in this figure. However, these authors proposed the correlation only for the heterogeneous nucleation. The fit to Nielsen's experimental data in the most important region of homogeneous nucleation is better when the Equations (3.20) and (3.21) are applied. An interesting phenomenon of changing the order of nucleation from 1.775 to 15 measured by Nielsen (1964) is related to the change of mechanism from heterogeneous to homogeneous. Any dilution of the supersaturation level will practically stop the nucleation rate.

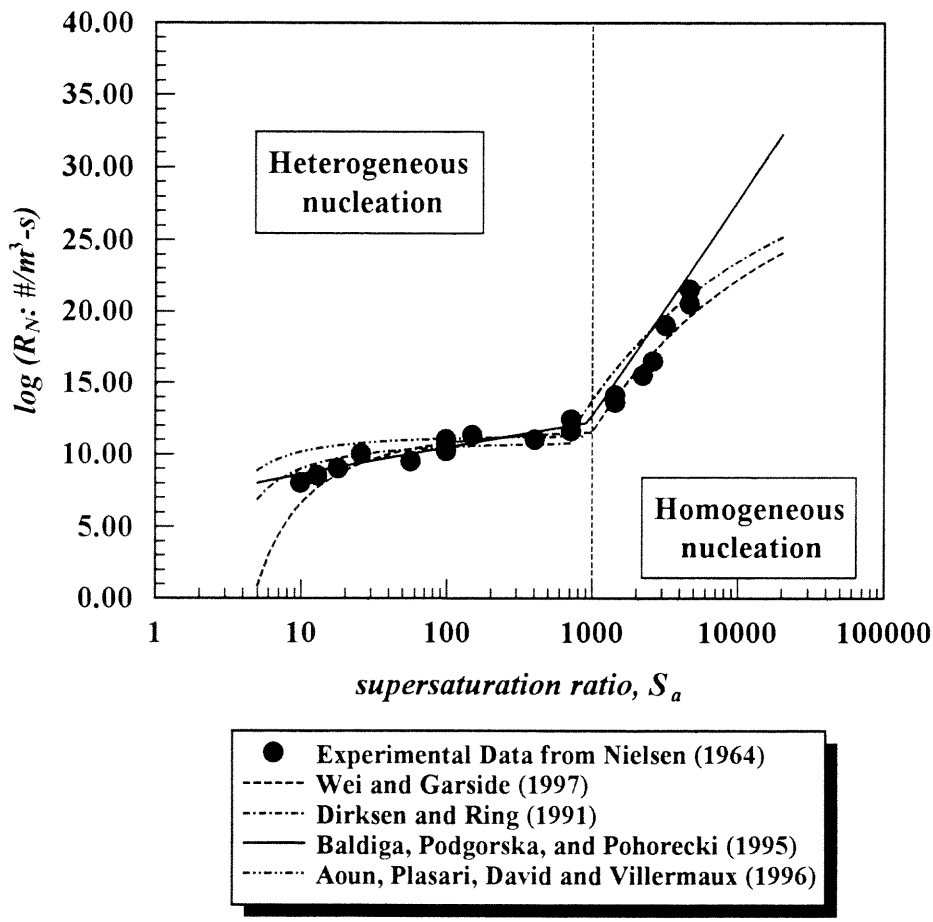

Figure 3.5 Comparison between nucleation rate correlations

3.6.2 Crystal Growth Rate

Elimination of the interfacial concentrations (C_{Ai} and C_{Bi}) from Equation (2.46) lead to a nonlinear equation for the calculation of crystal growth rate (Fitchett and Tarbell, 1990):

$$\Delta C = \frac{3k_v G}{k_a k_D} + \left(\frac{3k_v G}{k_a k_\sigma}\right)^{1/\sigma} \tag{3.26}$$

The measured value of k_D lies between 1.0×10^{-5} and 1.0×10^{-4} (m s^{-1})/(kmol m^{-3}) and assumes no dependence of mass transfer coefficient on the size of crystals (Nagata and Nishikawa, 1972). However, Nagata and Nishikawa's (1972) data for the dissolution of 0.9 μm barium sulfate crystals in water appear suspicious since they indirectly measured the solute concentration. Therefore, k_D was determined using the Armenante and Kirwan (1989) correlation which is based on extensive experimental measurements and supported by semi-theoretical analysis. By definition of the Sherwood (Sh), particle Reynolds (Re_p) and Schmidt (Sc) numbers, Equation (2.48) can be written as:

$$\frac{k_D d_{43}}{D_{crystal}} = 2 + 0.52\left(\frac{\varepsilon^{1/3} d_{43}^{4/3}}{\nu}\right)^{0.52}\left(\frac{\nu}{D_{crystal}}\right)^{1/3} \tag{3.27}$$

Different values have been reported for the surface reaction order, σ, and for the corresponding value of the rate constant k_σ. G was calculated using either a second order reaction, i.e., $\sigma = 2$ and $k_\sigma = 0.058$ (m s^{-1})/(kmol^2 m^{-6}) (Nielsen, 1984) or a fourth order reaction, i.e., $\sigma = 4$ and $k_\sigma = 6.3\text{x}10^5$ (m s^{-1})/(kmol^4 m^{-12}) (Nielsen, 1958). Figure 3.6 shows the comparison between these two calculations. For simplicity in the numerical calculations, k_D was first assumed to be constant and equal to 4.0×10^{-5} (m s^{-1})/(kmol m^{-3}) for both reaction orders. To investigate the effect of k_D, this coefficient was varied between 1.0×10^{-5} and 1.0×10^{-4} (m s^{-1})/(kmol m^{-3}) assuming the fourth order reaction.

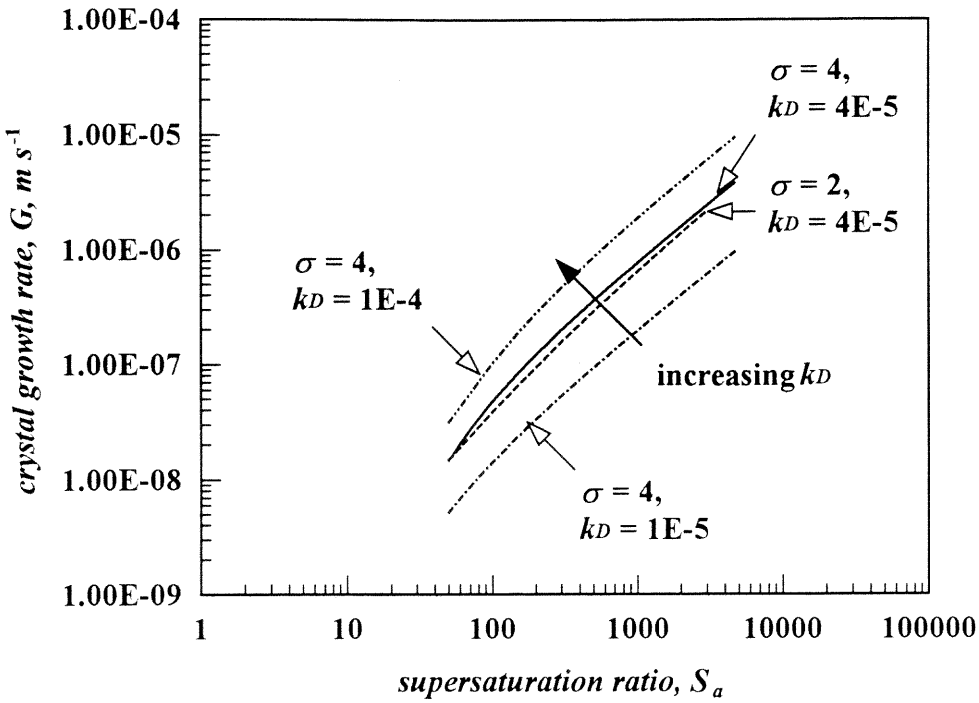

Figure 3.6 Comparison between crystal growth rates

As observed in Figure 3.6, the crystal growth rate slightly increases with the increase of the surface reaction order. This increase would have little effect on the final numerical solution of the mean crystal size and *C.V.*. Therefore, the growth kinetics of Nielsen (1958) was incorporated in the present simulation ($\sigma = 4$, $k_\sigma = 6.3\times10^5$ (m s^{-1})/(kmol^4 m^{-12})). Fitchett and Tarbell (1990) and Phillips *et al.* (1999) used the fourth order reaction in the simulation of the barium sulfate precipitation process, while Baldyga *et al.* (1995) and Baldyga and Orciuch (1995) used the second order reaction. Figure 3.6 also shows the increase of the crystal growth rate with the increase of the mass transfer coefficient. As explained before, instead of using a constant k_D value, this coefficient was calculated from Equation (3.27). For $\varepsilon = 0.1$ m^2 s^{-3} ($T = 0.292$ m, $D/T = 0.34$, $N = 300$ rpm, $C/T = 0.33$), k_D varies between $1.1\text{x}10^{-4}$ and $1.8\text{x}10^{-5}$ (m s^{-1})/(kmol m^{-3}) for a range of mean crystal size, d_{43}, between 1 to 10 μm, respectively.

3.6.3 Shape Factors

The area (k_a) and volume (k_v) shape factors are defined respectively as:

$$A_{crystal} = k_a L^2 \tag{3.28}$$

$$V_{crystal} = k_v L^3 \tag{3.29}$$

where $A_{crystal}$ and $V_{crystal}$ are the area and the volume of the crystal, respectively, and L the characteristic length. The characteristic length is related to the diameter of a sphere of the same volume, d, through the sphericity factor, ϕ_v:

$$L = \left(\frac{\pi}{6k_v}\right)^{1/3} d = \phi_v d \tag{3.30}$$

There is a considerable diversity in the reported k_a and k_v values for barium sulfate. Different values have been reported in the literature depending on the type of reactor: $k_a = 8.17$ for semi-batch reactor (Chen *et al.*, 1995, Phillips *et al.*, 1999) and $k_a = 348$ for tubular reactor (Baldyga *et al.*, 1997b), and depending on the addition mode: $k_a = 47.2$ near the impeller and $k_a = 348$ below the liquid surface (Baldyga *et al.*, 1995).

The shape factors depend on the crystal morphology. It has been established that the prevailing morphology is strongly affected by the supersaturation level (Pagliolico *et al.*, 1999). At high supersaturation, dendritic crystals are formed as a consequence of the bulk diffusion control in the crystal growth (Gunn and Murthy, 1972; Fitchett and Tarbell, 1990; Baldyga and Orciuch, 1997). At lower supersaturation, well-formed rectangular crystals are obtained due to the slow and then, more orderly incorporation by surface reaction (Gunn and Murthy, 1972; Liu *et al.*, 1975; Baldyga *et al.*, 1995; Phillips *et al.*, 1999). For barium sulfate crystals with structures developed by bulk diffusion $k_a = 348$, and for well-formed rectangular crystals $k_a = 8.17$ (Baldyga *et al.*, 1995).

For $\sigma = 4$, Equation (3.26) can be arranged in the following way:

$$\Delta C = \left[\frac{3k_v}{k_a k_D} + \left(\frac{3k_v}{k_a k_\sigma} \right)^{1/4} G^{-3/4} \right] G \qquad (3.31)$$

The first term in brackets [] represents the mass transfer resistance and the second term represents the resistance due to the surface reaction. Figure 3.7 shows the plot of these two resistances against the supersaturation ratio in the range used in this work. At low supersaturation ratio the crystal growth rate is mostly controlled by the surface reaction step. At high supersaturation ratio, the mass transfer would control, however, at this level of supersaturation, homogeneous nucleation also becomes dominant hiding the effect of crystal growth. Therefore, well-formed rectangular crystals were expected to be predominant in this work. This was supported from observations of the crystal photographs when agglomeration was not present.

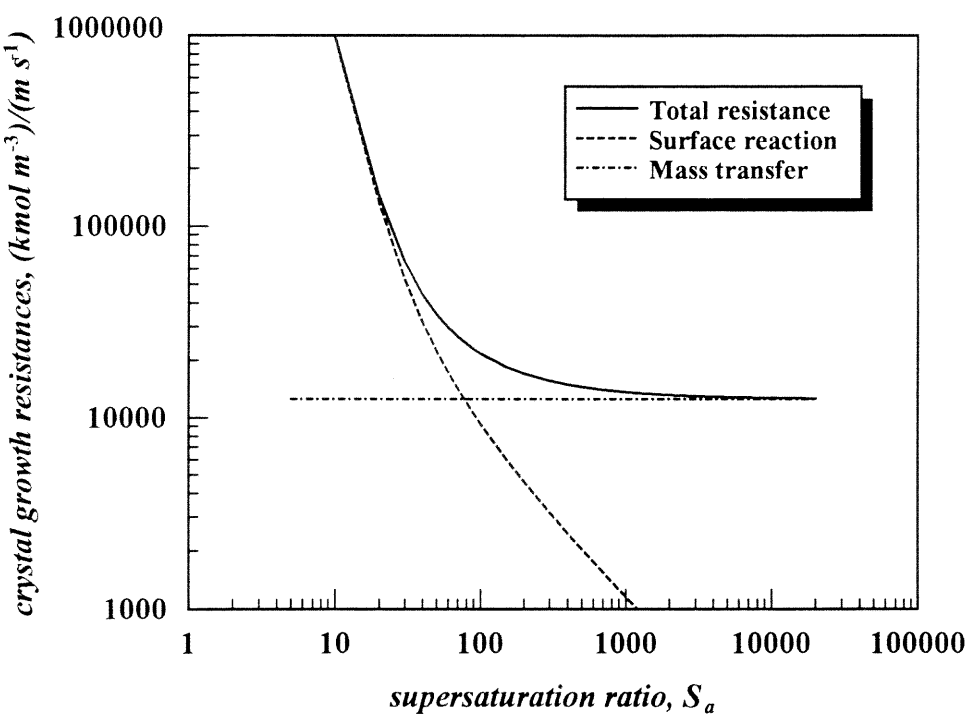

Figure 3.7 Crystal growth resistances

As will be explained in Section 5.2.6 (Crystal Morphology), an attempt to obtain experimentally the crystal shape factor was made using an environmental scanning electron microscope. The geometry and the dimensions were determined from one sample obtained from the precipitation experiments at the reference conditions. This is only an approximate approach, a more accurate quantification would require sophisticated techniques like image analysis (Bernard *et al.*, 1997, 1999). The large variation in the values reported is due to differences in definition and uncertainty in the choice of the characteristic crystal dimension. The characteristic length was assumed to be the second largest dimension of the crystal (Paglioco *et al.*, 1999). An average value of 4.50 ± 0.56 and 5.02 ± 0.70 were determined for the characteristic length and the area shape factor, respectively. This estimation required the measurement of the three dimensions of the crystals. The measurement of the depth of the crystals from the 2D images was difficult and must be considered approximate.

To investigate the effect of the shape factor value in the numerical solution, simulations with different values of k_a were carried out. Usually, the ratio $k_a/k_v = 6$ which corresponds to cube and sphere geometries has been reported in the literature (Phillips *et al.*, 1999; Wei and Garside, 1997; Baldyga *et al.*, 1995; Seckler *et al.*, 1995; Chen *et al.*, 1995), and was used in the simulation. Figure 3.8 shows the effect of k_a on the mean crystal size and *C.V.* for different values of volume ratio. As shown in this figure, the mean crystal size increases with the increase of the shape factor value. However, for low values of k_a this increase is very small and can be neglected in the simulation. *C.V.* is not affected for this factor. Therefore, $k_a = 8.17$ as determined for well rectangular crystal (Baldyga *et al.*, 1995) was used in the present simulation.

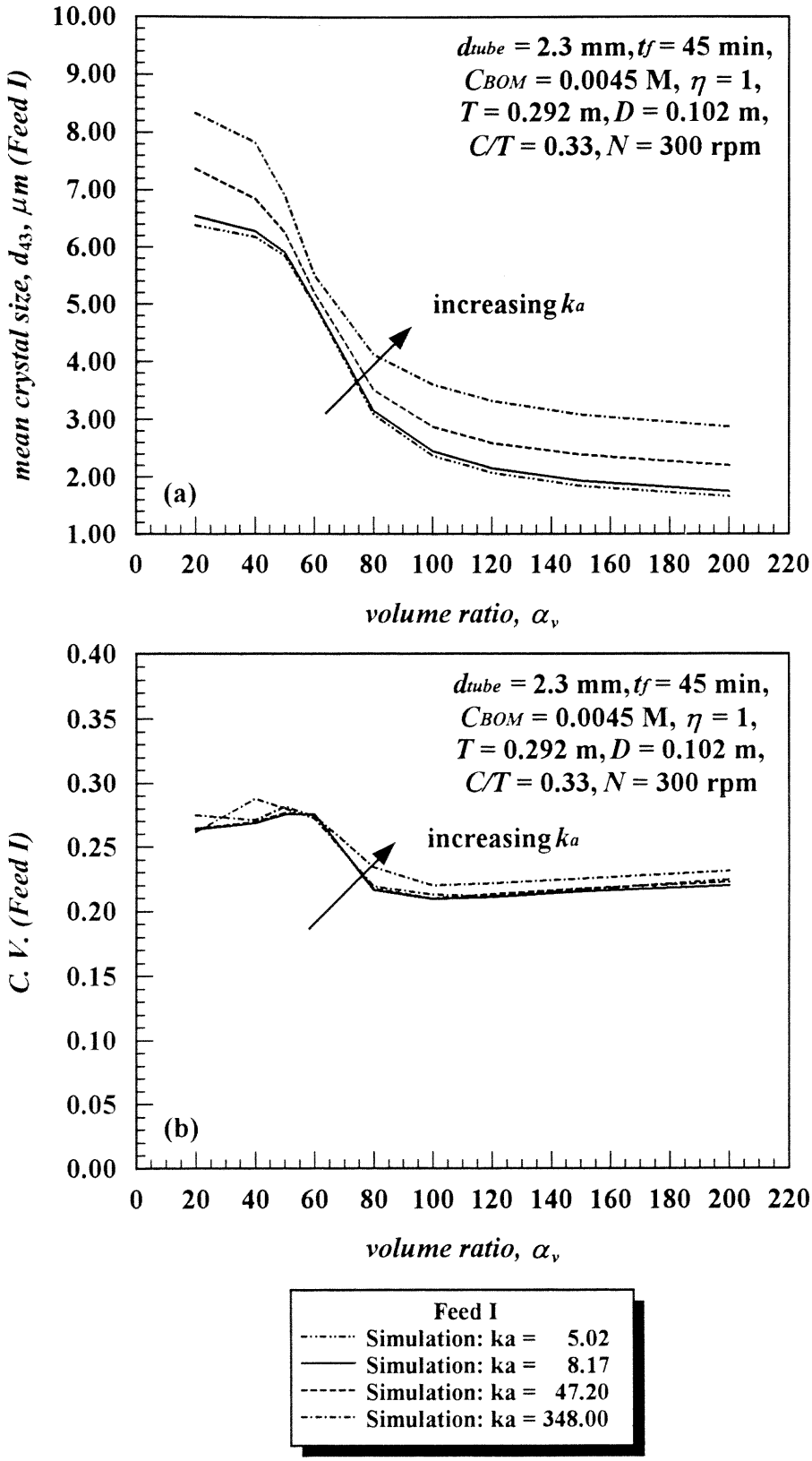

Figure 3.8 Effect of shape factor on: (a) mean crystal size; and (b) *C.V.*

Table 3.2 summarizes the parameter values used in the numerical simulations. The density and viscosity of the dilute solution were assumed to be equal to those of pure water. All the crystal properties were obtained from the literature, the density ($\rho_{crystal}$) and diffusivity ($D_{crystal}$) of the barium sulfate crystals vary from 4,480 to 4,500 kg m^{-3} and $9.5x10^{-10}$ to $9.55x10^{-10}$ m^2 s^{-1}, respectively. The variation of the values reported is small; therefore, the values reported by Mullin (1993), $\rho_{crystal} = 4{,}500$ kg m^{-3}, and Nielsen (1969), $D_{crystal} = 9.5x10^{-10}$ m^2 s^{-1}, were used in the present simulation.

Table 3.2 Parameters used in the numerical simulation

Parameter	Value	Units
ρ	1000	kg m^{-3}
ν	10^{-6}	m^2 s^{-1}
$\rho_{crystal}$	4500	kg m^{-3}
$D_{crystal}$	9.5×10^{-10}	m^2 s^{-1}
$M_{crystal}$	233.386	kg $kmol^{-1}$
M_{BaCl}	208.236	kg $kmol^{-1}$
M_{Na2SO4}	142.036	kg $kmol^{-1}$
M_{NaCl}	58.443	kg $kmol^{-1}$
K_s	1.096×10^{-10}	$kmol^2$ m^{-6}
σ	4	--
k_σ	6.3×10^5	$(m\ s^{-1})/(kmol^4\ m^{-12})$
k_a	8.17	--
k_v	1.36	--

3.7 Differential Moment Equations

The 0^{th} to 5^{th} moments in the mixing-precipitation zone following the *kth* blob addition can be calculated from Equation (2.53):

$$\frac{dm_0(t,t_s)}{dt} = R_N(t,t_s) + E(t,t_s)\left(1 - Y(t,t_s)\right)\left(\langle m_0(t_s)\rangle - m_0(t,t_s)\right) \tag{3.32}$$

$$\frac{dm_1(t,t_s)}{dt} = G\left(L_{avg},t,t_s\right)m_0(t,t_s) + E(t,t_s)\left(1 - Y(t,t_s)\right)\left(\langle m_1(t_s)\rangle - m_1(t,t_s)\right) \tag{3.33}$$

$$\frac{dm_2(t,t_s)}{dt} = 2G\left(L_{avg},t,t_s\right)m_1(t,t_s) + E(t,t_s)\left(1 - Y(t,t_s)\right)\left(\langle m_2(t_s)\rangle - m_2(t,t_s)\right) \tag{3.34}$$

$$\frac{dm_3(t,t_s)}{dt} = 3G\left(L_{avg},t,t_s\right)m_2(t,t_s) + E(t,t_s)\left(1 - Y(t,t_s)\right)\left(\langle m_3(t_s)\rangle - m_3(t,t_s)\right) \tag{3.35}$$

$$\frac{dm_4(t,t_s)}{dt} = 4G\left(L_{avg},t,t_s\right)m_3(t,t_s) + E(t,t_s)\left(1 - Y(t,t_s)\right)\left(\langle m_3(t_s)\rangle - m_3(t,t_s)\right) \tag{3.36}$$

$$\frac{dm_5(t,t_s)}{dt} = 5G\left(L_{avg},t,t_s\right)m_4(t,t_s) + E(t,t_s)\left(1 - Y(t,t_s)\right)\left(\langle m_4(t_s)\rangle - m_4(t,t_s)\right) \tag{3.37}$$

L_{avg} represents the average crystal length in the mixing-precipitation zone. The initial conditions for the 0^{th} to 5^{th} moment differential equations are, respectively:

$$\begin{aligned} &m_0(0,t_s) = 0,\ m_1(0,t_s) = 0, \\ &m_2(0,t_s) = 0,\ m_3(0,t_s) = 0, \\ &m_4(0,t_s) = 0,\ m_5(0,t_s) = 0 \end{aligned} \tag{3.38}$$

For the bulk liquid, the 0^{th} to 5^{th} moments can be calculated from Equation (2.55):

$$\frac{d\langle m_{0,k}(t,t_s)\rangle}{dt} = \langle R_{N,k}(t,t_s)\rangle \tag{3.39}$$

$$\frac{d\langle m_{1,k}(t,t_s)\rangle}{dt} = \langle G_k(\langle L_{avg}\rangle,t,t_s)\rangle\ \langle m_{0,k}(t,t_s)\rangle \tag{3.40}$$

$$\frac{d\langle m_{2,k}(t,t_s)\rangle}{dt} = 2\langle G_k(\langle L_{avg}\rangle,t,t_s)\rangle\ \langle m_{1,k}(t,t_s)\rangle \tag{3.41}$$

$$\frac{d\langle m_{3,k}(t,t_s)\rangle}{dt} = 3\langle G_k(\langle L_{avg}\rangle,t,t_s)\rangle\ \langle m_{2,k}(t,t_s)\rangle \tag{3.42}$$

$$\frac{d\langle m_{4,k}(t,t_s)\rangle}{dt} = 4\langle G_k(\langle L_{avg}\rangle,t,t_s)\rangle\ \langle m_{3,k}(t,t_s)\rangle \tag{3.43}$$

$$\frac{d\langle m_{5,k}(t,t_s)\rangle}{dt} = 5\langle G_k(\langle L_{avg}\rangle,t,t_s)\rangle\ \langle m_{4,k}(t,t_s)\rangle \tag{3.44}$$

For the *(k+1)th* blob addition the initial conditions for the 0^{th} to 5^{th} moment differential equations are, respectively:

$$\langle m_{0,k+1}(0,t_s)\rangle = \langle m_{0,k}(t_{end},t_s)\rangle[1-Y_k(t_{end},t_s)] + m_{0,k}(t_{end},t_s)Y_k(t_{end},t_s) \tag{3.45}$$

$$\langle m_{1,k+1}(0,t_s)\rangle = \langle m_{1,k}(t_{end},t_s)\rangle[1-Y_k(t_{end},t_s)] + m_{1,k}(t_{end},t_s)Y_k(t_{end},t_s) \tag{3.46}$$

$$\langle m_{2,k+1}(0,t_s)\rangle = \langle m_{2,k}(t_{end},t_s)\rangle[1-Y_k(t_{end},t_s)] + m_{2,k}(t_{end},t_s)Y_k(t_{end},t_s) \tag{3.47}$$

$$\langle m_{3,k+1}(0,t_s)\rangle = \langle m_{3,k}(t_{end},t_s)\rangle[1-Y_k(t_{end},t_s)] + m_{3,k}(t_{end},t_s)Y_k(t_{end},t_s) \tag{3.48}$$

$$\left\langle m_{4,k+1}(0,t_s)\right\rangle = \left\langle m_{4,k}(t_{end},t_s)\right\rangle\left[1-Y_k(t_{end},t_s)\right] + m_{4,k}(t_{end},t_s)Y_k(t_{end},t_s) \tag{3.49}$$

$$\left\langle m_{5,k+1}(0,t_s)\right\rangle = \left\langle m_{5,k}(t_{end},t_s)\right\rangle\left[1-Y_k(t_{end},t_s)\right] + m_{5,k}(t_{end},t_s)Y_k(t_{end},t_s) \tag{3.50}$$

The calculation of the mean size and *C.V.* can be simplified in terms of moments (Randolph and Larson, 1988). The moments of the particle size distribution are directly related to the properties of the particle size distribution, such as the total number concentration (N_T), i.e., for the mixing-precipitation zone:

$$N_T = m_0 \tag{3.51}$$

specific or characteristic length per unit volume of suspension (L_{spec}):

$$L_{spec} = m_1 \tag{3.52}$$

mean specific surface area per unit volume of suspension (a):

$$a = k_a m_2 \tag{3.53}$$

mass fraction of particles ($X_{crystal}$):

$$X_{crystal} = \frac{k_v \rho_{crystal} m_3}{\rho} \tag{3.54}$$

The mass weighted mean size (L_{43}) is given by the ratio of the fourth moment to the third moment of particle population density:

$$L_{43} = \frac{m_4}{m_3} \tag{3.55}$$

Using the definition of sphericity, ϕ_v, given in Equation (3.30), L_{43} can be compared to the mass weighed mean size or average crystal size (d_{43}) measured during laboratory experiments by the Coulter-Counter (which assumes spherical particles):

$$d_{43} = \frac{L_{43}}{\phi_v} \tag{3.56}$$

Another important parameter characterizing the CSD is the coefficient of variation, $C.V.$:

$$C.V. = \sqrt{\frac{m_3 m_5}{m_4^2} - 1} \tag{3.57}$$

3.8 Engulfment Parameter

In this work, the energy dissipation rate of the entire blob was calculated as the space-averaged, weighed $\varepsilon(t,t_s)$ value of all the sub-droplets constituting the initial blob of added reactant. This value is a function of time, since the sub-droplets move within the reactor. This function, termed $\varepsilon_{blob}(t,t_s)$, was used to calculate the instantaneous value of the engulfment parameter, $E(t,t_s)$, which appears in the micromixing model equations.

$$\varepsilon_{blob}(t,t_s) = \frac{\sum \varepsilon_n(t,t_s)}{N_{sub}} \tag{3.58}$$

The number of sub-droplets (N_{sub}) was determined by following the energy dissipation profile during the residence time of the blob. Figure 3.9 shows that for $N_{sub} <$ 1,000, this profile is very erratic. For $N_{sub} \geq$ 10,000, the energy dissipation profile follows the expected trajectory of the flow field. For feeding below the liquid surface, Feed I, $\varepsilon_{blob}(t,t_s)$ starts from the low value found near the liquid surface, increases as the sub-droplets approach the impeller, reaches a maximum close to the impeller, decreases and then attains a constant value when the sub-droplets disperse all over the vessel. For feeding above the impeller, Feed II, $\varepsilon_{blob}(t,t_s)$ starts from a higher value as compared with Feed I, increases as the sub-droplet cross the high turbulent impeller region, decreases and then attains a constant value when the sub-droplets disperse all over the vessel.

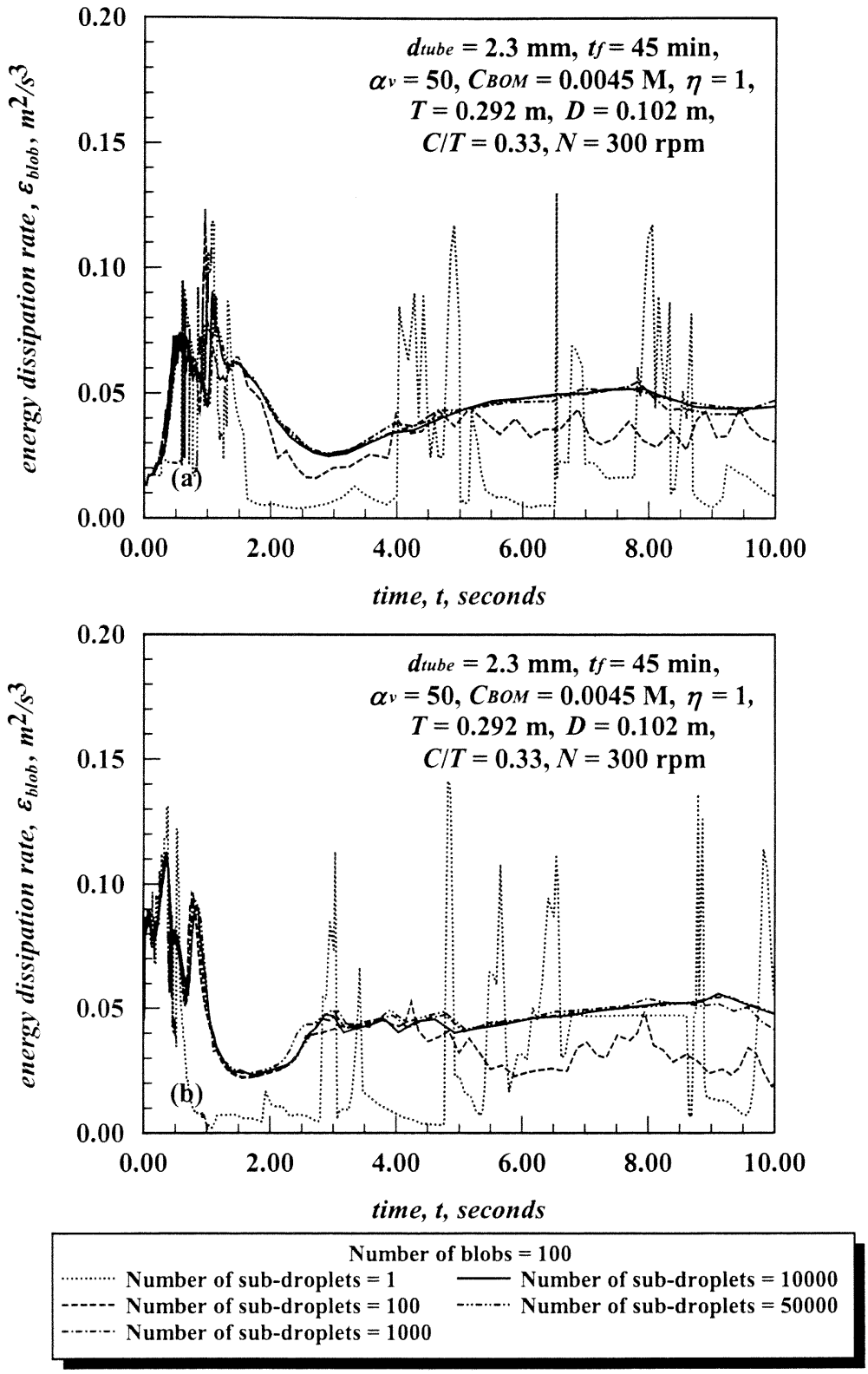

Figure 3.9 Effect of feed sub-discretization on energy dissipation rate profile: (a) Feed I; and (b) Feed II

3.9 Numerical Solution

The self-engulfment factor, mass balance and moment equations presented above were simultaneous integrated. This set of ordinary differential equations included eleven equations in the mixing-precipitation zone, i.e., the volume fraction Y (Equation 3.5), the concentrations of A, B, C, and D (Equations 3.7, 3.8, 3.9 and 3.10, respectively), and the 0^{th} to 5^{th} moments (Equations 3.32 to 3.37, respectively), and ten equations in the bulk zone, i.e., the concentrations of A, B, C, and D (Equations 3.12, 3.13, 3.14 and 3.15, respectively), and the 0^{th} to 5^{th} moments (Equations 3.39 to 3.44, respectively).

The equations were solved using FORTRAN 77 programming and the Subroutine GERK which uses the fifth order Fehlberg's method with error control and time-step of integration adjustment. The subroutine was obtained from the online numerical library *Netlib repository*. The equation for growth rate was solved using a combination of Newton-Raphson's convergence scheme with bisection step. The code was obtained from *Numerical Recipes* (Press *et al.*, 1992). The normally distributed random variables for the evaluation of the instantaneous velocity, Equation (2.58), were generated from a uniformly distributed random variables using the Box-Muller transformation (Rubinstein, 1981), based upon the fundamental transformation law of probabilities.

Integration of these equations resulted in the time-dependent determination of all the variables of relevance to the precipitation process, including the species concentration and moment values, from which the local level of supersaturation ratio and the crystal size distribution were determined as a function of time. Therefore, the history of the supersaturation, which determines the CSD and the crystal morphology, could be followed. At the end of the integration, mean crystal size and $C.V.$ were determined.

Two criteria were used to verify the correctness of the final numerical solution. First, the amount of products and reactants at the end of the simulation were compared with the initial amount of reactants. The difference between these values was always found to be < 0.05%. Second, the final value of the mass fraction of particles (calculated from the third moment) was compared with the amount of barium sulfate produced. Also in this case, the difference between these values was always found to be < 0.05%. The actual percent conversion at the end of the simulation was also compared to the theoretical conversion (99.7%). However, this value was always found between 96%-97%. This was due to the slow precipitation rate predicted by the nucleation and crystal growth rate for $S_a < 12$.

CHAPTER 4

EXPERIMENTAL SECTION

4.1 Laser Doppler Velocimetry (LDV)

4.1.1 General Principles

Laser Doppler Velocimetry (LDV) has been used extensively for the characterization of the flow field generated by pitched blade turbines (Ranade and Joshi, 1989; Jaworski *et al.*, 1991; Ranade *et al.*, 1992; Kresta and Woods, 1993a, 1993b; Sturesson *et al.*, 1995; Armenante and Chou, 1996; Bakker *et al.*, 1996; Jaworski *et al.*, 1996; Zhou and Kresta, 1996b; Schafer *et al.*, 1998). Accurate velocity measurements can be performed one point at a time. LDV offers unique advantages in comparison with other fluid flow instrumentation: it is a non-intrusive optical measurement, no calibration is required, presents a well-defined directional response, and high spatial and temporal resolution.

When two laser beams of the same wavelength cross, an interference pattern of bright and dark fringes is formed. If the beams intersect in their respective beam waists, the wave fronts are nearly plane and subsequently the interference fringes will be parallel. This is of practical importance in LDV since it means a uniform velocity-frequency relationship over the entire intersection volume. As a single particle passes through the intersection, it reflects light at certain frequencies which depends only on the velocity of the particle and the fringe spacing. Since the frequency is not dependent on the sign of the direction of the velocity, the frequency of one of the two crossing beams is shifted. Therefore, a particle travelling against the fringes will produce Doppler bursts of a higher frequency than the shift and a particle travelling in the same direction as the fringes will produce a lower frequency than the shift.

4.1.2 LDV System

Figure 4.1 shows the experimental set-up for the LDV system. The mixing vessel, geometrically similar to the mixing-precipitation vessel, was a fully baffled, cylindrical, flat-bottomed, Plexiglas tank of diameter 0.292 m. The vessel was filled with tap water up to a height equals to the tank diameter and placed in a square tank, also filled with tap water, to minimize the effect of diffraction on LDV measurements. The agitation system consisted of six-blade 45° pitched-blade turbines mounted on a centrally located shaft (12.5 mm OD), and with a diameter either of 0.076 m or 0.102 m. The characteristics of these impeller were also similar to those used in the precipitation experiments. A 1/8-HP motor controlled by an external controller (G. K. Heller Corp., Model 202P6518) was used to rotate the impeller at different speeds. The agitation speed was measured by an optical tachometer. The off-bottom clearance of the impeller (measured from the center of the impeller) was changed by moving vertically the impeller, shaft and the motor assembly. The average and fluctuating velocities at different heights and radial distances in the vessel were experimentally obtained using a three-dimensional mechanical traversing apparatus on which the vessel assembly was mounted.

LDV measurement of the flow field velocities and turbulence characteristics were made using a DANTEC 55X modular series (Dantec Measurement Technology USA, Mahwah, NJ) in forward scatter mode. The laser, transmitting optics, receiving optics, and the signal processor were mounted on a bench. A 300-mW Argon-Ion laser (Ion Laser Technology, Salt City, Utah, Model 5500A-00) was used as the light source. The light beam from the source was filtered to retain all the component colors except for the green light.

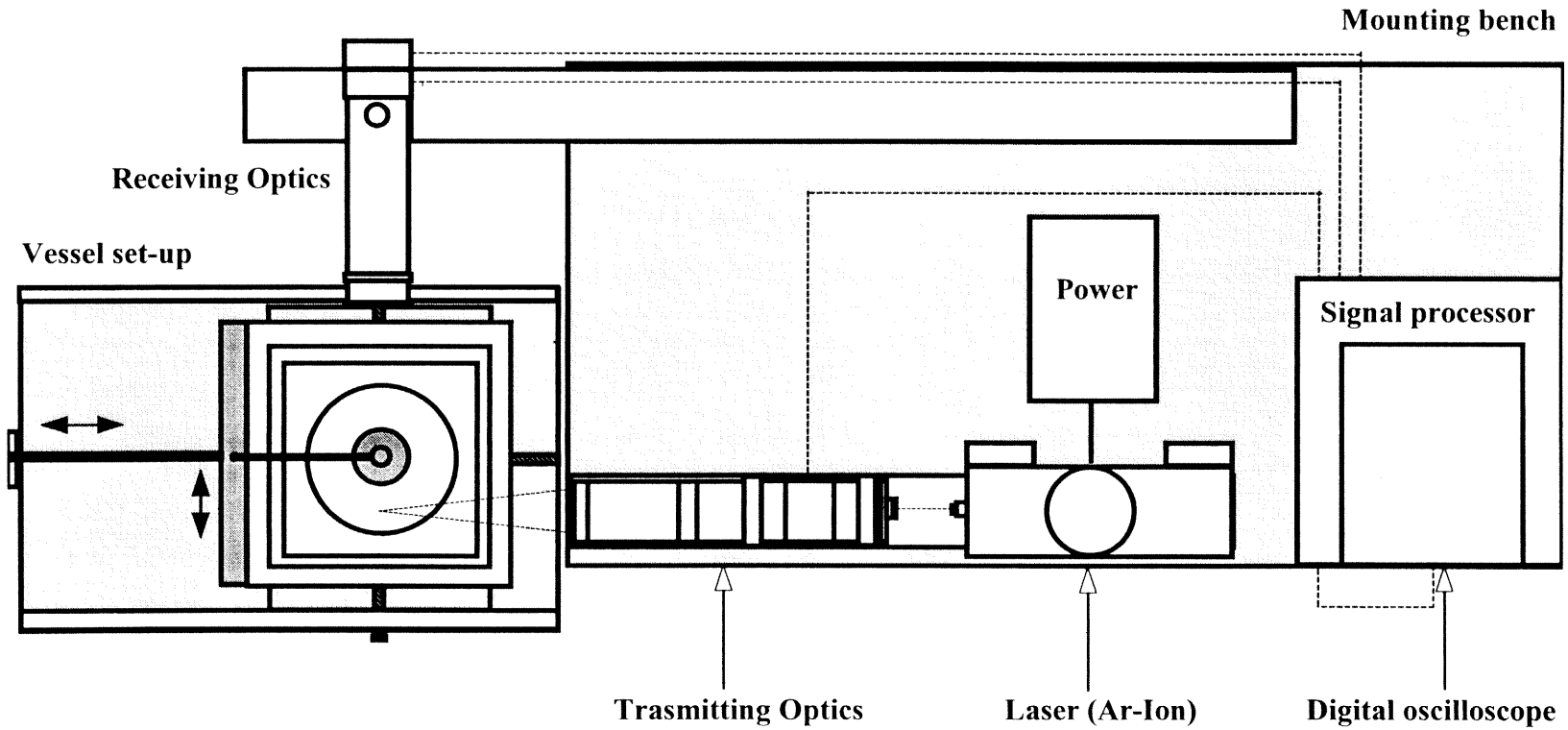

Figure 4.1 Laser-Doppler velocimeter system: (a) top view

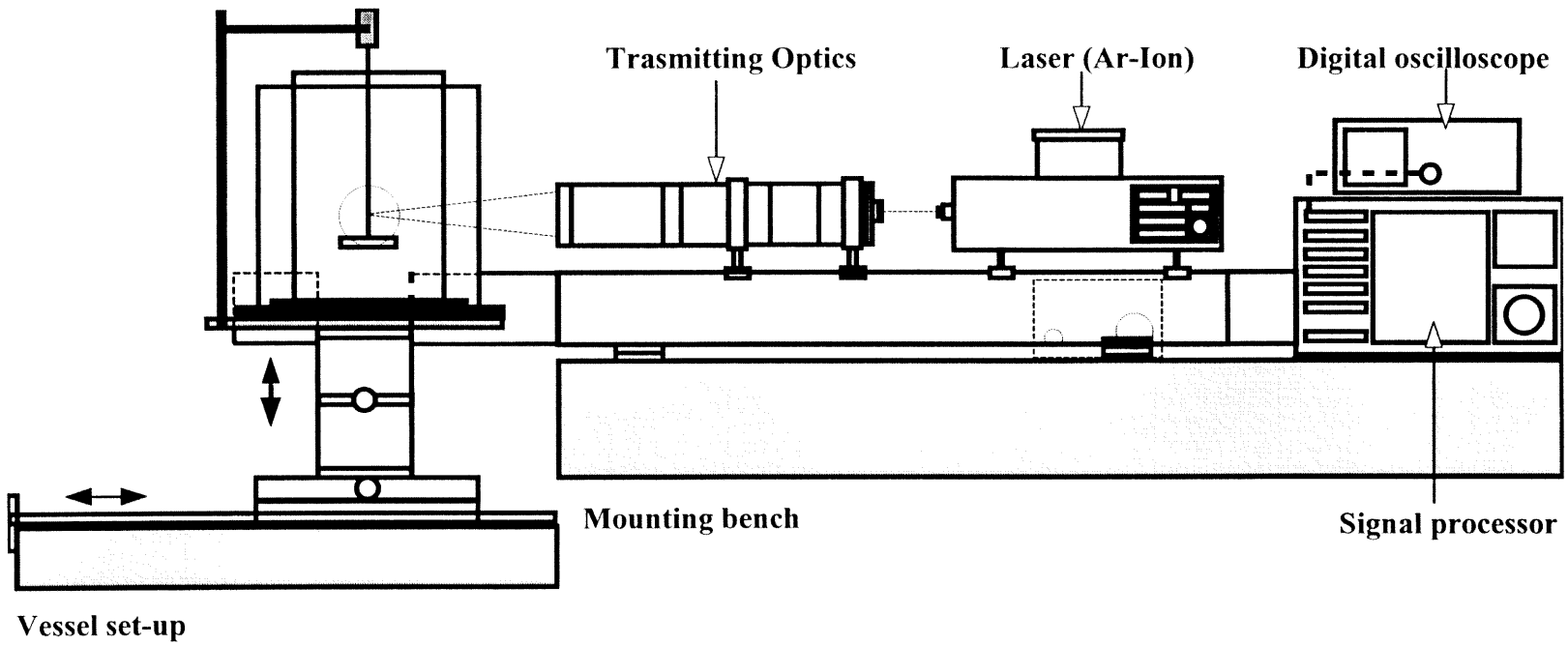

Figure 4.1 (Continued): (b) side view

The green light beam was then split in two by a neutral beam splitter. To identify flow reversals correctly, a frequent shift of 40 MHz was given to one of the beam by means of a Bragg cell while the other part was passed through a glass rod to compensate for the optical path length in the Bragg cell. The shifted and the direct beams were then focused by a front lens to intersect in a small elliptical control volume 310 mm from the focusing lens. The water in the vessel was seeded with 1.5 μm silicon carbide particles capable of scattering light as they traveled through the volume control. The scattered light was collected by the receiving optical assembly composed of a variable focus lens and a photomultiplier. The quality of the signal was monitored during the experiment using a 2201 Digital Storage Oscilloscope (Tektronix, Inc., Beaverton, Oregon, USA). Data validation and signal processing was carried out with the help of DANTEC 58N10 Doppler signal processor or "counter". The Doppler signal analyzer uses frequency domain burst detection to convert the analog signal from the receiving optics to instantaneous velocity measurements. Dantec's software program SIZEware™, installed in a computer, acquired, processed and presented the data.

Figure 4.2 shows the arrangement of the LDV system and the vessel assembly for the measurement of the different velocities components. The measurements of axial and radial components of velocities were carried out in a vertical center plane of the vessel perpendicular to the optical axis of beams. For the axial component, the two laser beams intersected in a horizontal plane (Figure 4.2a), while for the radial component, the plane of intersection was vertical (Figure 4.2b). The tangential components of velocities were measured in a vertical center plane passing through the optical axis of the beams with the two laser beams intersection in a vertical plane (Figure 4.2c).

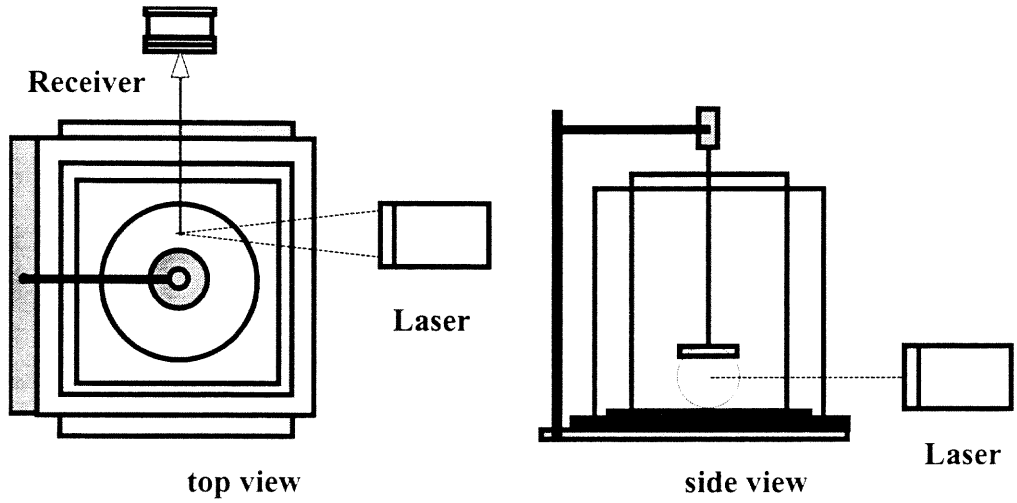

(a) axial velocity

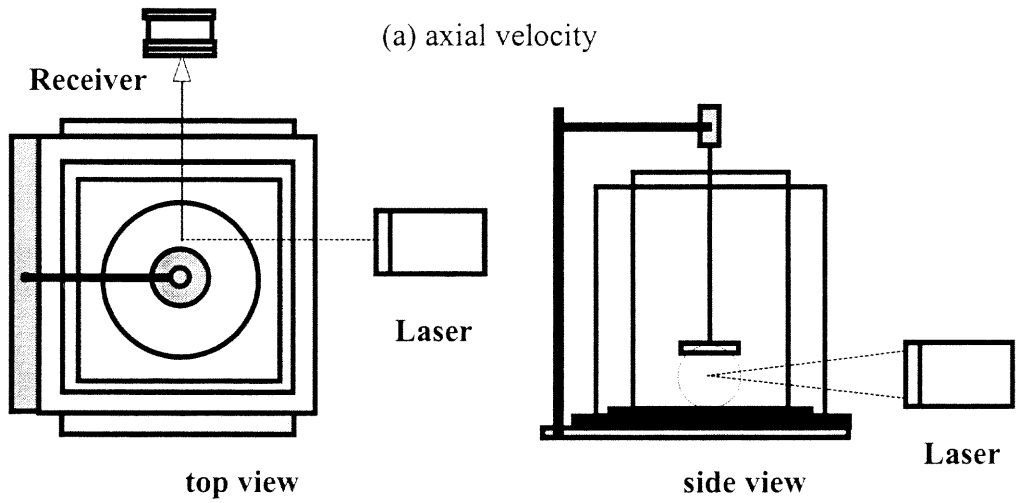

(b) radial velocity

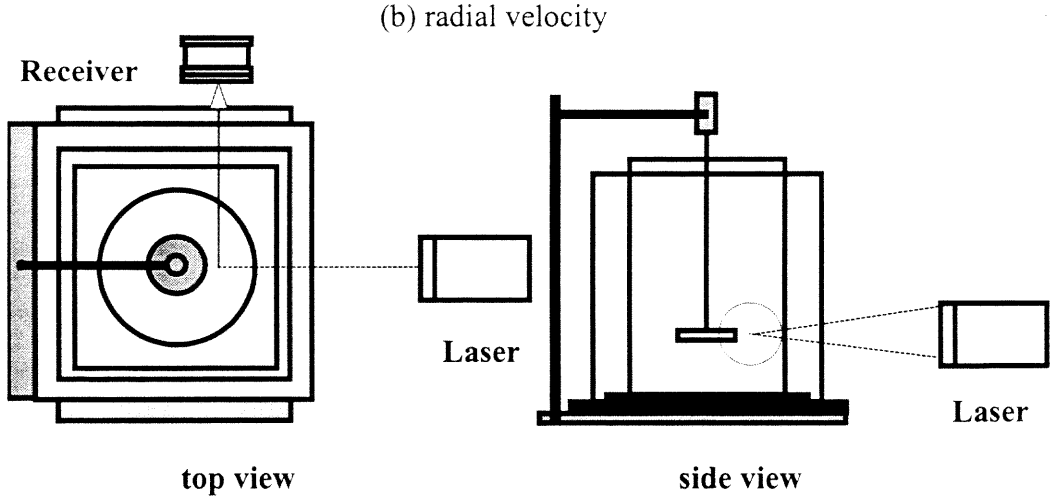

(c) tangential velocity

Figure 4.2 Measurement of the velocity components

4.2 Experimental Mixing-Precipitation Equipment

4.2.1 Mixing-Precipitation Apparatus

To investigate the effect of the process variables and operating conditions, the precipitation experiments were carried out in a 19-L, open, flat-bottomed, transparent cylindrical tank provided with four equally spaced baffles and having a diameter, T, equal to 0.292 m. The baffle thickness was 5 mm, and the baffle width-to-tank diameter was 0.1. Both Plexiglas and glass tanks with identical geometries were used in the preliminary experiments, and no difference in the CSD and morphology was observed. The effect of micromixing on scale-up was investigated using a similar experimental setup. The precipitation experiments were carried out in 8-L and 160-L Plexiglas cylindrical vessels with diameters equal to 0.219 m and 0.584 m, respectively. The vessels used in these experiments were geometrically similar. The dimensions of the vessels are shown in Table 4.1. The vessels were mounted on a traversing system, which allowed to change the impeller off-bottom clearance, C (measured from the impeller middle plane). A 2-HP variable speed motor (G. K. Heller Corp., Model 202P6518) was used to rotate the six-blade 45° pitched-blade turbines (PBT).

Table 4.1 Vessel dimensions

Vessel diameter, T m	**Vessel height, H' m**	**Liquid height, H m**	**Baffle width, B mm**	**Baffle thickness, b mm**
0.219	0.420	0.219	21.9	3
0.292	0.400	0.292	29.2	5
0.584	0.623	0.584	58.4	5

For the effect of process variables and operating conditions, the impeller diameter used, D, was equal to either 0.076 m or 0.102 m in the 0.292 m vessel. For the effect of micromixing on scale-up, the ratio of the impeller diameter-to-vessel diameter was equal to 0.348. Figure 4.3 shows the shape and characteristic dimensions of the PBT impellers used in this work. The dimensions are shown in Table 4.2.

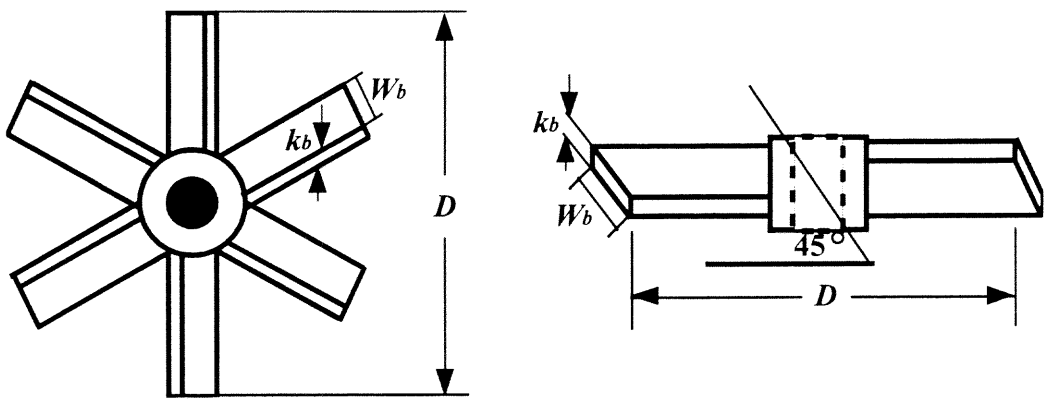

Figure 4.3 Impeller geometry

Table 4.2 Impeller dimensions

D m	W_b m	k_b mm	∠
0.076	0.017	1.6	45°
0.102	0.012	2.0	45°
0.204	0.024	4.0	45°

Figure 4.4 shows the components of the mixing-precipitation system: feeding system (constant head burette and feed pump), mixing-precipitation vessel (Plexiglas vessel, impeller, motor, controller and tachometer), power measurement (strain gages, slip ring and conditioner), reaction monitoring (electrode, conductivity board and thermocouple), and data acquisition system.

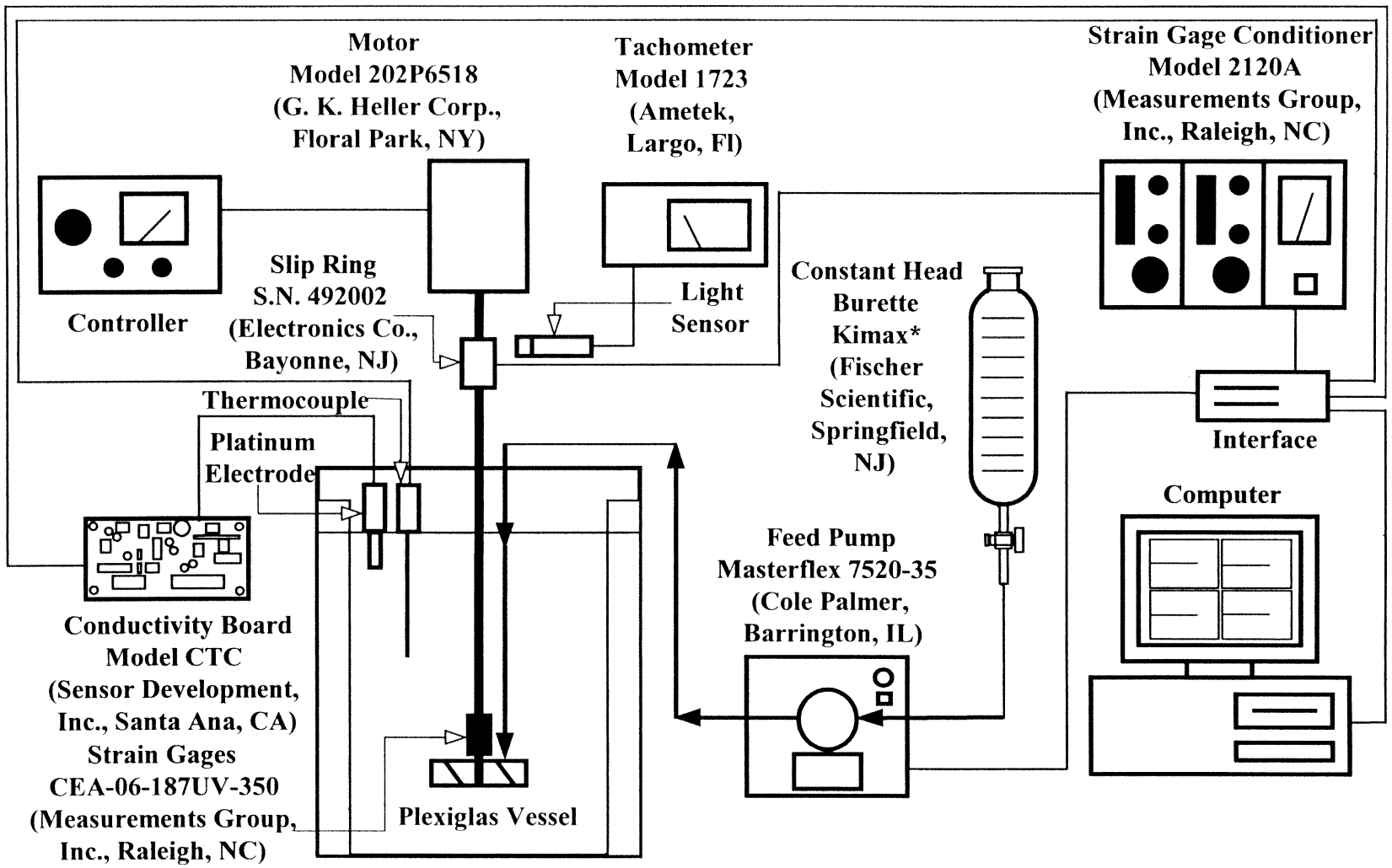

Figure 4.4 Experimental equipment: mixing-precipitation system

Barium chloride and sodium sulfate, both certified ACS grade (Fischer Scientific) were used to prepare the aqueous solutions. Single-distillate water was determined to be of sufficient purity for all experiments (preliminary tests using water of greater purity showed no difference in the CSD). The sodium sulfate solution was added to a stirred solution of barium chloride, with a Masterflex® peristaltic pump (Cole Parmer). The feed passed through PharMed® tubes of 1.6 mm ID (Cole Palmer) connected at the end to a small glass tube. To ensure a constant flow rate, a constant head burette was used.

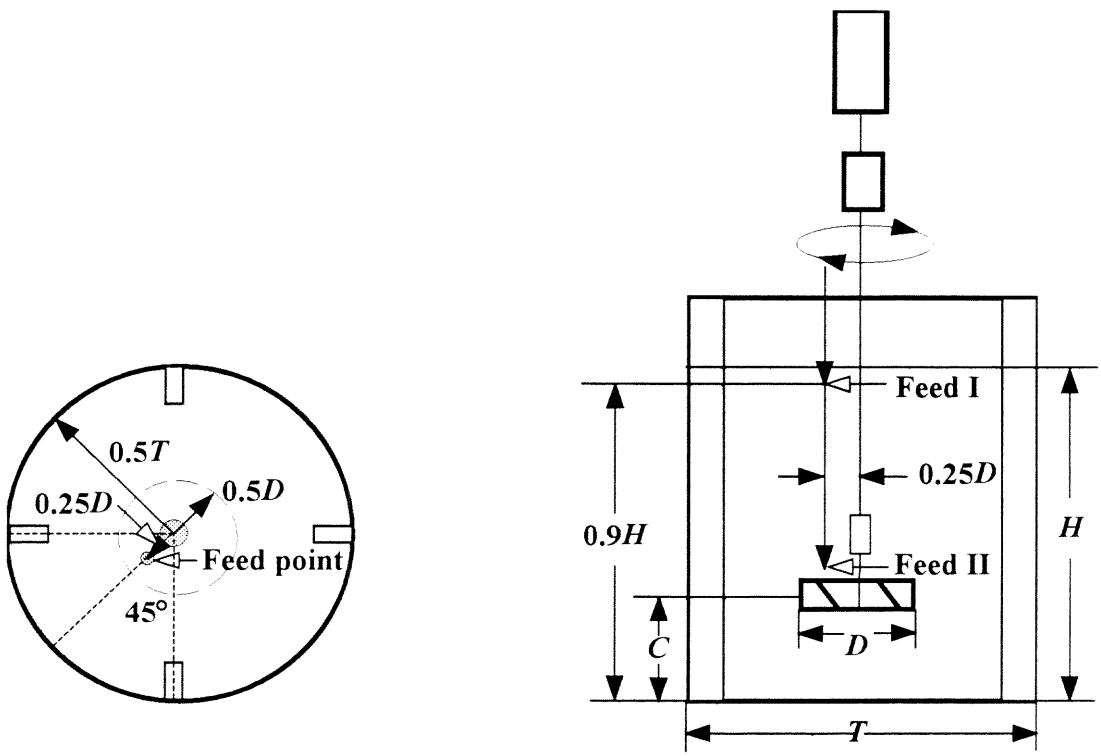

Figure 4.5 Feed point locations

As shown in Figure 4.5, the feed was located at one of two possible locations, one near the liquid surface ($Z = 0.9\ H$; Feed I), and another directly above the impeller ($Z = 0.05H+0.95C$; Feed II), where Z is the vertical distance from the tank bottom. In both cases, the feed was 0.25 D from the tank centerline, midway between two baffles.

4.2.2 Power Measurement

The power number, *Po*, predicted by the FLUENT code was validated experimentally by measuring the power consumption, *P*, and using Equation (3.3). To measure *P*, 1000 ohm foil strain gages (Measurement Group Co., Raleigh, NC, CEA-06-187UV-350) were mounted on the outside of the hollow shaft (length of 0.838 m). The strain gages were attached to the shaft and coated for complete water resistance using a variety of compounds from the company's M-line. Since the impeller for the larger vessel was too heavy to be held by the hollow shaft, *P* could not be measured for the larger vessel.

The resistance change was determined by using a Wheatstone bridge circuit connected up to a slip ring assemble (Electronics Co., Bayonne, NJ). The latter essentially consists of a transmitter unit, mounted on the rotating shaft, which generates a square wave oscillation whose frequency is proportional to the change in resistance of the strain gage. A receiver unit (Measurement Group, Co., Raleigh, NC, 2120A system) converts the transmitted frequency back to a voltage and amplifies it so that it can be sent to a data collection system (Labtech Notebook, Ver. 9.0). Each value of *Po* was determined by averaging 10 readings per second sampling time over 300 seconds.

The system was calibrated periodically to assure reliability and accuracy of the strain gage response. The calibration was performed by torsional measurements under static conditions, by using a system of weights. The signals from the strain gages were sent to the same data acquisition system used in the actual experiments. This system has been previously used for the measurement of *P* and determination of *Po* in solids suspension experiments (Armenante and Uehara, 1998 and Armenante *et al.*, 1998) and agitated vessels provided with multiple impellers (Armenante and Chang, 1998).

4.2.3 Reaction Monitoring

The rotational speed was measured with an optical tachometer with a light sensor (Cole Parmer Instrument Co.), accurate within ±1 rpm. The progress of the reaction was monitored with a platinum conductivity electrode to avoid polarization (Khang and Fitzgerald, 1975) connected to a conductivity board (Sensor Development Inc., Model CTC). The temperature in the tank (20.5±0.5°C) was measured with a thermocouple type J. No temperature changes occurred during the course of the reaction. A digital data acquisition system (Labtech Notebook, Ver. 9.0) was used to analyze the signals (mV) from the tachometer, conductivity meter, thermocouple, strain gages and feed pump.

4.2.4 Particle Characterization

Figure 4.6 shows the components of the analytical system used for particle characterization. The crystal size distribution was determined using the Coulter® Multisizer (Beckman Coulter, Model TA). The Coulter® Multisizer is a microprocessor-controlled, broad range analyzer. It counts and sizes up to 5,000 particles per second from 0.4 to 1,200 μm in diameter. The instrument reports data as volume percent, population or surface area distribution in cumulative or differential form on linear or log scales.

The crystal morphology was analyzed with an Environmental Scanning Electron Microscope (Philips Electro Scan 2020). Scanning Electron Microscope has been widely used to examine precipitated barium sulfate in crystallization studies (Gunn and Murphy, 1972; Liu *et al.*, 1976; Houcine *et al.*, 1997). The solutions used for preparation of samples for the crystal were purified using Millipore® sterifil aseptic filter and filtering through 0.22 um Millipore® membrane filters (Fischer Scientific).

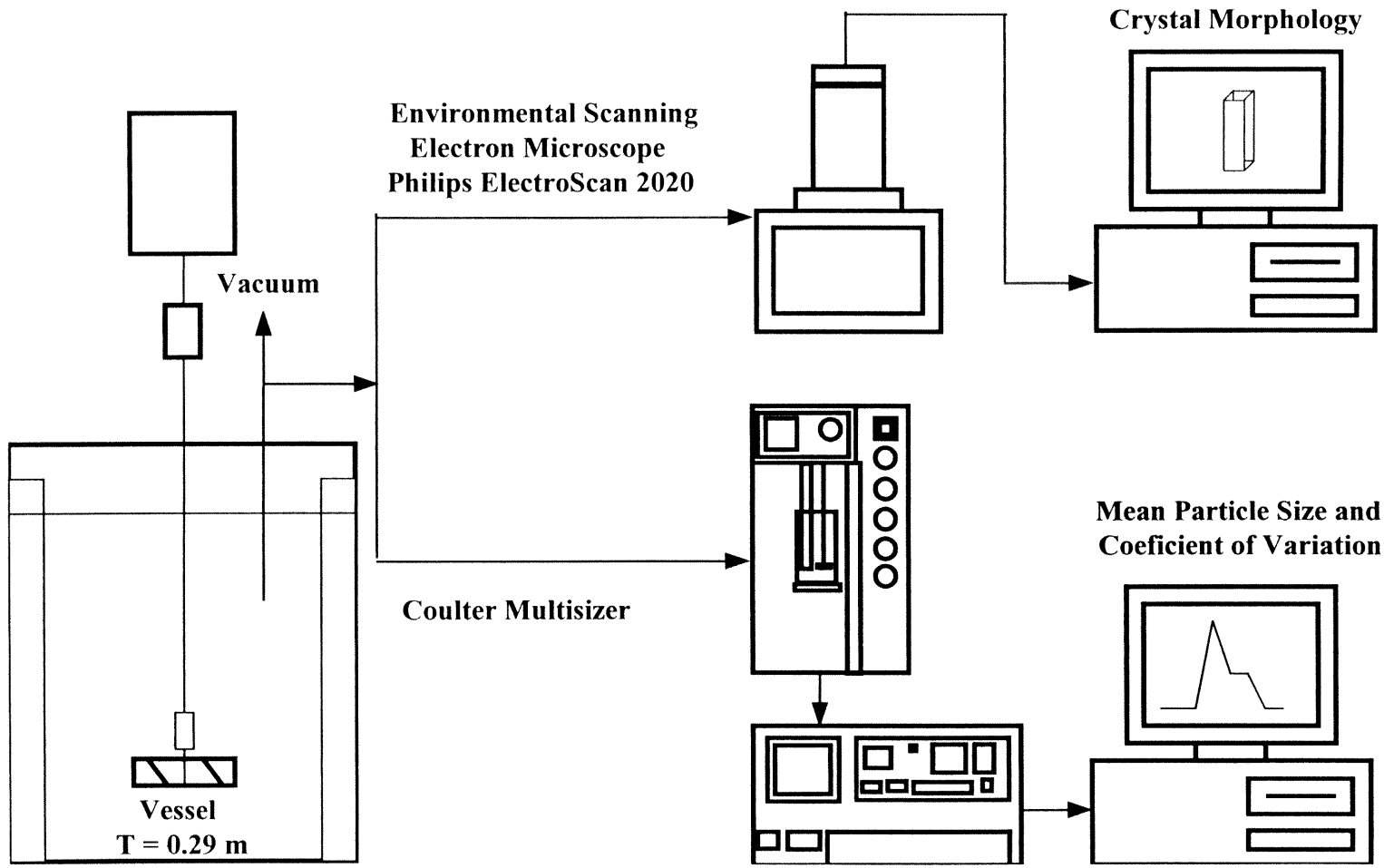

Figure 4.6 Experimental equipment: particle characterization

4.3 Experimental Procedure

4.3.1 LDV Validation

The LDV system was used in the forward scatter mode. The characteristics of the optical probe volume were a diameter of 0.20 mm, a length of 3.32 mm, a fringe spacing of 4.21 μm, and a number of fringes of 48. The angle of intersection (in the air) of the two laser beams was 14.03°. The mean velocity and turbulence intensities were determined from a population with a sample size set at 10,000 data (<300 sec). The data rate varied between 3 and 8 kHz. The validation rate (the percentage of validated samples out of a block of 1,000 calculated frequencies) never fell below 60%. The probe volume was positioned at the desired point with the help of traversing mechanism described earlier. Corrections for deflection of the laser beams due to changes in the refractive indices were based on the laws of refraction (Durst *et al.*, 1978).

The measurements of mean and fluctuating velocities were made at eight radial locations ($2r/T$ = 0.1, 0.2, 0.3, 0.4, 0.5, 0.6, 0.7, 0.8) for each axial location. To study the effects of impeller speed and diameter on the flow field, the measurements were made at four axial locations (z/H = 0.10, 0.25, 0.50, 0.67). The effect of impeller off-bottom clearance was investigated by measuring velocities and turbulent kinetic energy at a plane 15 mm below the bottom surface of the impeller and at a plane in the upper part of the vessel (z/H = 0.67). In all the cases, the impeller Reynolds number was above 10,000 (turbulent regime). To assess the repeatability of the LDV data, two series of velocity measurements at the plane z/H = 0.25 were undertaken. Mean axial, radial, and tangential velocities as well as the corresponding fluctuating velocities, were measured first, with increasing radial distance and second, by reducing it.

4.3.2 General Procedure for Precipitation Experiments

All glassware and the mixing vessel were cleaned with a freshly prepared, diluted sulfuric acid-potassium dichromate cleaning solution after each run. The cleaning solution was left in the glassware for at least 30 minutes before it was rinsed out. Since the cleaning solution can be easily saturated with barium sulfate new cleaning solution was prepared quite often. Also, the glassware and tank were given a final washing with distilled water after adding the cleaning solution. The tank was filled with distilled water. A concentrated barium chloride solution was separately prepared and added to the tank to obtain the desired initial concentration and initial liquid level (equals to the tank diameter, $H = T$). Sodium sulfate feed solution with the concentration and volume required was prepared and added to the constant head burette. This solution was pumped into the tank until complete exhaustion. Then, the samples for the particle characterization were collected and the system was shut off for cleaning.

In any crystallization study, sampling is a very important procedure and many factors affect the accuracy of solids sampling (MacTaggart *et al.*, 1993; Nasr-EL-Din, *et al.*, 1996). Slurry samples were immediately collected at the end of the experiments to eliminate settling effects, using a 5-mL pipette connected to vacuum. In order to obtain representative crystal samples from the tank, the sampling velocity in the pipette was always larger than 1 m/sec (Nasr-El-Din *et al.*, 1996). Samples from at least three vertical locations in the tanks were considered representative of the experiments. Even though accurate values cannot be obtained easily, it does not greatly affect the analysis of the results obtained because the errors for samples from different locations have the same magnitude and same tendency (Sha and Palosaari, 2000).

The combined samples were dispersed in 200 ml of Isoton II solution and the CSD was determined using the Coulter Multisizer. The mass-weighted mean size and the corresponding coefficient of variation, *C.V.*, were then calculated from the CSD measurements. The sample was then filtered through a 0.22 μm membrane Millipore® filter. The filter was dried in an oven at 105°C overnight, and the crystals were dispersed over an aluminum paper. These crystals were observed and photographed with the Environmental Scanning Electron Microscope (ESEM).

4.3.3 Effect of Process Variables

Preliminary experiments were carried out to eliminate the effects of backmixing and mesomixing. To avoid backmixing, the effect of the feed tube internal diameter, d_{tube}, on the CSD was investigated. The effect the feed addition time, t_f, was also investigated to assure slow addition rate and eliminate mesomixing effect. The effect on the final CSD of a number of process variables was then investigated. These variables were: volume ratio, α_v, *mean* initial concentration of sodium sulfate, C_{BOM}, and stoichiometry ratio, η.

The volume ratio and the stoichiometry ratio are defined, respectively, as:

$$\alpha_v = \frac{V_{AO}}{V_{BO}} \tag{4.1}$$

$$\eta = \frac{C_{AOM}}{C_{BOM}} = \frac{C_{AO}V_{AO}}{C_{BO}V_{BO}} \tag{4.2}$$

where V_{AO} and V_{BO}, are, respectively, the initial volume of barium chloride (A) in the tank and the initial volume of sodium sulfate (B) in the burette, and C_{AO} and C_{BO} are the corresponding *actual* initial concentrations of A (in the tank) and B (in the burette).

The *mean* initial concentrations of barium chloride (C_{AOM}) and sodium sulfate (C_{BOM}) are defined as:

$$C_{AOM} = \frac{C_{AO}V_{AO}}{\left(V_{AO}+V_{BO}\right)} = \frac{C_{AO}}{\left(1+\frac{1}{\alpha_v}\right)} \tag{4.3}$$

and:

$$C_{BOM} = \frac{C_{BO}V_{BO}}{\left(V_{AO}+V_{BO}\right)} = \frac{C_{BO}}{\left(1+\alpha_v\right)} \tag{4.4}$$

Whenever a variable was varied the other variables were kept at reference values which were: d_{tube} = 2.3 mm, t_f = 45 min (q_f = 0.51 L/h), α_v = 50, C_{BOM} = 0.0045 M, η = 1.0. All experiments were conducted at the two feed locations. The experiments for each variable were carried out randomly and repeated twice.

Table 4.3 shows the preliminary experiments carried out. First, the effect of backmixing in the feed tube was investigated using different tube internal diameters (d_{tube} = 1.2 mm, 1.8 mm, 2.3 mm, 2.7 mm, 3.8 mm, and 5.0 mm) at the highest impeller speed (N = 500 rpm). Second, the effect of mesomixing was investigated by decreasing the feed addition time (82 min ≥ t_f ≥ 12 min) at a very low impeller speed (N = 100 rpm), corresponding to the worst-case scenario. Since macromixing and agglomeration effects were present, the mesomixing effect was also investigated at a higher impeller speed (N = 300 rpm). Finally, the effects of α_v, C_{BOM}, and η were studied individually at N = 300 rpm and using d_{tube} and t_f determined previously to avoid backmixing and mesomixing, respectively. α_v was varied in the range 20-200, and C_{BOM} in the range 0.002-0.02 M. The range of η explored was from 0.5-3.0 in 0.5 increments.

Table 4.3 Experiments for effect of process variables
(a) Feed tube diameter

Run	D m	C/T	N rpm	d_{tube} mm	t_f min	α_v	C_{BOM} M	η
TD 1	0.102	0.33	500	1.2	45	50	0.0045	1.0
TD 2	0.102	0.33	500	1.8	45	50	0.0045	1.0
TD 3	0.102	0.33	500	2.3	45	50	0.0045	1.0
TD 4	0.102	0.33	500	2.7	45	50	0.0045	1.0
TD 5	0.102	0.33	500	3.8	45	50	0.0045	1.0
TD 6	0.102	0.33	500	5.0	45	50	0.0045	1.0

(b) Feed time addition

Run	D m	C/T	N rpm	d_{tube} mm	t_f min	α_v	C_{BOM} M	η
TF 1	0.076	0.33	100/300	2.3	82	50	0.0045	1.0
TF 2	0.076	0.33	100/300	2.3	60	50	0.0045	1.0
TF 3	0.076	0.33	100/300	2.3	45	50	0.0045	1.0
TF 4	0.076	0.33	100/300	2.3	40	50	0.0045	1.0
TF 5	0.076	0.33	100/300	2.3	30	50	0.0045	1.0
TF 6	0.076	0.33	100/300	2.3	25	50	0.0045	1.0
TF 7	0.076	0.33	100/300	2.3	18	50	0.0045	1.0
TF 8	0.076	0.33	100/300	2.3	12	50	0.0045	1.0

Table 4.3 (Continued)
(c) Volume ratio of reactants

Run	D m	C/T	N rpm	d_{tube} mm	t_f* min	α_v	C_{BOM} M	η
VR 1	0.102	0.33	300	2.3	113	20	0.0045	1.0
VR 2	0.102	0.33	300	2.3	56	40	0.0045	1.0
VR 3	0.102	0.33	300	2.3	45	50	0.0045	1.0
VR 4	0.102	0.33	300	2.3	38	60	0.0045	1.0
VR 5	0.102	0.33	300	2.3	28	80	0.0045	1.0
VR 6	0.102	0.33	300	2.3	23	100	0.0045	1.0
VR 7	0.102	0.33	300	2.3	19	120	0.0045	1.0
VR 8	0.102	0.33	300	2.3	11	200	0.0045	1.0

* q_f = 0.51 L/h

(d) Mean initial concentration of sodium sulfate

Run	D m	C/T	N rpm	d_{tube} mm	t_f min	α_v	C_{BOM} M	η
MC 1	0.102	0.33	300	2.3	45	50	0.0020	1.0
MC 2	0.102	0.33	300	2.3	45	50	0.0040	1.0
MC 3	0.102	0.33	300	2.3	45	50	0.0045	1.0
MC 4	0.102	0.33	300	2.3	45	50	0.0060	1.0
MC 5	0.102	0.33	300	2.3	45	50	0.0080	1.0
MC 6	0.102	0.33	300	2.3	45	50	0.0100	1.0
MC 7	0.102	0.33	300	2.3	45	50	0.0120	1.0
MC 8	0.102	0.33	300	2.3	45	50	0.0200	1.0

Table 4.3 (Continued)
(e) Stoichiometry ratio of reactants

Run	D m	C/T	N rpm	d_{tube} mm	t_f min	α_v	C_{BOM} M	η
SR 1	0.102	0.33	300	2.3	45	50	0.0045	0.5
SR 2	0.102	0.33	300	2.3	45	50	0.0045	1.0
SR 3	0.102	0.33	300	2.3	45	50	0.0045	1.5
SR 4	0.102	0.33	300	2.3	45	50	0.0045	2.0
SR 5	0.102	0.33	300	2.3	45	50	0.0045	2.5
SR 6	0.102	0.33	300	2.3	45	50	0.0045	3.0

4.3.4 Effect of Operating Conditions

To investigate the effect of the impeller speed, N, diameter, D, and off-bottom clearance, C/T, on mean crystal size and coefficient of variation, $C.V.$, experiments based on a factorial design with these three variables at two levels were performed. The two levels for N were 100 rpm (-, low level) and 500 rpm (+, high level). The low level was chosen to assure turbulent flow ($Re > 10^4$), and the high level was the limit for air entrainment. For D two available sizes were used, namely, 0.076 m (-) and 0.102 m (+). For C a low clearance (-), $T/5$, and a high clearance (+), $T/3$, were selected. Table 4.4 shows the two-level factorial experimental design. During these experiments, the process variables were kept at the reference values. The experiments were carried out in random order to keep consistent bias error from being confused with the real effects of the variables. To increase the precision in the estimate of the experimental error, each one of the factorial experiments was repeated three times.

Table 4.4 Experiments for effect of operating conditions

d_{tube} = 2.3 mm, t_f = 45 min, α_v = 50, C_{BOM} = 0.0045 M, η = 1.0

Run	*N* **100 rpm (-)** **500 rpm (+)**	*D* **0.076 m (-)** **0.102 m (+)**	*C* **T/5 (-)** **T/3 (+)**
1	100 rpm (-)	0.076 m (-)	T/5 (-)
2	500 rpm (+)	0.076 m (-)	T/5 (-)
3	100 rpm (-)	0.102 m (+)	T/5 (-)
4	500 rpm (+)	0.102 m (+)	T/5 (-)
5	100 rpm (-)	0.076 m (-)	T/3 (+)
6	500 rpm (+)	0.076 m (-)	T/3 (+)
7	100 rpm (-)	0.102 m (+)	T/3 (+)
8	500 rpm (+)	0.102 m (+)	T/3 (+)

In order to complement the analysis of the two-level factorial design, experimental runs at one more level of the impeller speed (N = 300 rpm, intermediate between 100 rpm and 500 rpm), were carried out. The differences between experimental runs were evaluated using these extended data. The effect of operating conditions on the flow field generated by PBT has been also studied using the ratio of the impeller off-bottom clearance-to-impeller diameter (C/D) instead of C/T (Kresta and Woods, 1993a, 1993b). In particular, Kresta and Woods (1993b) reported a transition between two flow patterns (with and without a secondary circulation loop near the vessel bottom) at C/D = 0.6. Therefore, additional experiments were carried out at two levels of C/D. The two levels for C/D used were 0.50 and 0.96.

4.3.5 Scale-Up Experiments

The effect of vessel scale on mean crystal size and *C.V.* was investigated in three geometrically-similar vessels under micromixing conditions ($D/T = 0.34$, $C/T = 0.33$). The process variables at the reference conditions were the same for all three vessels except for t_f. To avoid mesomixing effects, t_f was scaled according to Equation (2.61) and using $\delta = 1$ (> 8/9). N for the smaller scales varied between 100 rpm to 500 rpm. However for the larger scale, N was increased only up to 300 rpm. Higher N produced excessive breakage of crystals and air entrainment into the vessel. The experiments for each variable were carried out randomly and repeated twice. Table 4.5 shows the operating conditions for the scale-up experiments.

Table 4.5 Operating conditions for scale-up experiments

$d_{tube} = 2.3$ mm, $\alpha_v = 50$, $C_{BOM} = 0.0045$ M, $\eta = 1.0$

T **m**	V **liter**	t_f **min**	N **rpm**
0.219	8.3	20	100-500
0.292	19.6	45	100-500
0.584	156.4	360	100-300

CHAPTER 5

RESULTS AND DISCUSSION

5.1 Flow Field Generated by Six-Blade 45° Pitched-Blade Turbines (PBT)

5.1.1 General Description of the Flow Field

Figure 5.1 shows the CFD prediction of the velocity distribution generated by the PBT in the stirred vessel. PBT produces a strong axially downward flowing jet below the impeller. The velocity decreases as the jet approaches the tank bottom. The fluid strikes the tank bottom and then moves along the bottom up to the wall. At the wall, the fluid turns upward. In the upper part of the impeller, the up-flowing liquid takes a 'U' turn and returns to the impeller from the impeller top surface. Some part of the up-flowing fluid return to the impeller through the vertical periphery of the impeller swept surface after making a short circulation leading to radially inward flow. Below the impeller hub, a distinct cone shaped region expanding towards the vessel base is found. In this region, a low intensity recirculation loop is developed. There is an intense turbulent flow zone between the impeller and the vessel bottom. The maximum of the velocity is found at the bottom surface of the impeller at approximately $0.28(T/2)$ from the axis of symmetry, and the value is of the order of 0.6 times the impeller tip speed (U_{tip}). In the region above the impeller top surface, fluid velocities and turbulence level are very low.

CFD predictions of velocity components and turbulent quantities were compared with LDV measurements using the 0.292 m vessel. Since it is a very common practice, the comparisons were made in dimensionless form. The dimensionless velocities were obtained by dividing each velocity component by U_{tip}. The turbulent kinetic energy was divided by $(U_{tip})^2$ to obtain the respective dimensionless value.

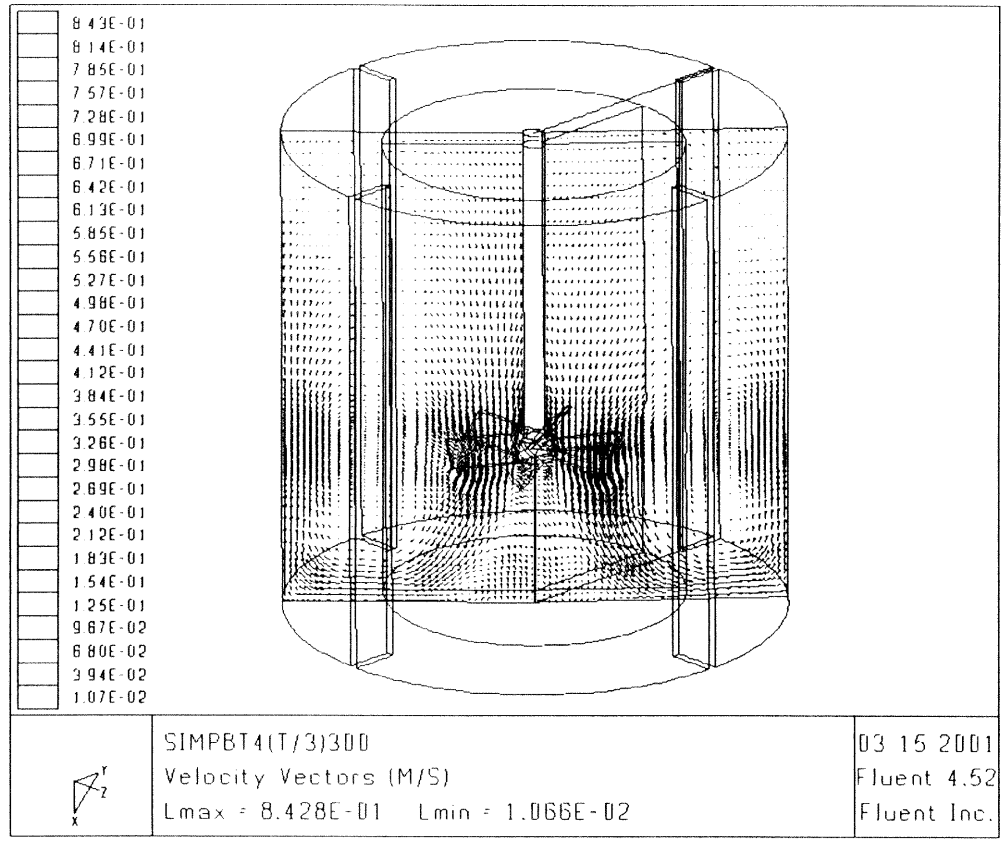

Figure 5.1 Velocity distribution in the stirred tank

The general comparison between experimental LDV measurements and CFD predictions was carried out with the 0.102 m impeller size located one-third of the liquid height from the vessel bottom. The dimensionless axial, radial, and tangential velocities, and turbulent kinetic energy are shown in Figure 5.2, Figure 5.3, Figure 5.4, and Figure 5.5, respectively. The two sets of experiments carried out for the assessment of the LDV data reproducibility are shown at the plane below the impeller (z/H = 0.25). The maximum standard deviations were 13.62%, 14.33%, 14.67% and 18.13% for the axial, radial, tangential velocities, and turbulent kinetic energy, respectively.

As shown in Figure 5.2, below the bottom surface of the impeller (z/H = 0.25), the axial component of the velocity is mostly downward. Near the symmetry axis and the vessel wall, the axial velocity turns upward. The maximum in the radial profile of the axial velocity occurs in this vertical plane at about 0.28(T/2), and the value is about $0.45U_{tip}$. Ranade and Joshi (1989) and Jaworski *et al.* (1991) reported a maximum axial velocity of $0.47U_{tip}$ and $0.44U_{tip}$, respectively, located at 0.28(T/2). The maximum axial velocity in the wall stream is close to $0.25U_{tip}$. Near the vessel bottom (z/H = 0.10), there is a reduction in the magnitude of the axial velocity. The maximum value in the radial profile is shifted toward the vessel wall. Above the impeller (z/H = 0.50), the radial profile of the axial velocity shows a large decrease in magnitude. This decrease continues as the distance above the impeller increases (z/H = 0.67). There is a good agreement between LDV measurements and CFD predictions.

Figure 5.3 shows a maximum in the radial profile of the radial component of the velocity near the tank bottom (z/H = 0.10). This maximum value is of the order of $0.16U_{tip}$ and occurs at about 0.42(T/2). Ranade and Joshi (1989) found a maximum axial

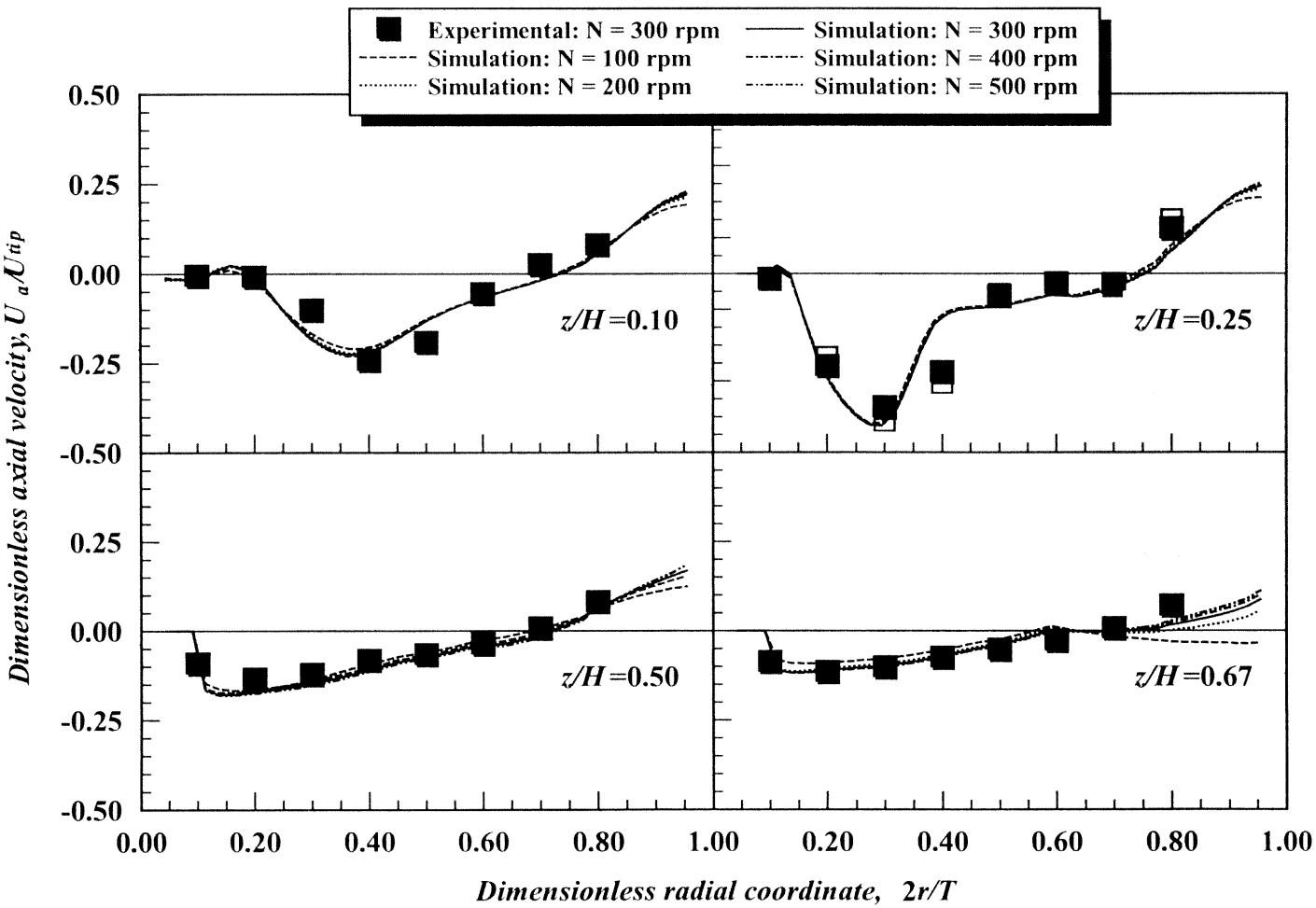

Figure 5.2 Comparison between LDV measurements and CFD predictions: Effect of impeller speed-Dimensionless axial velocity

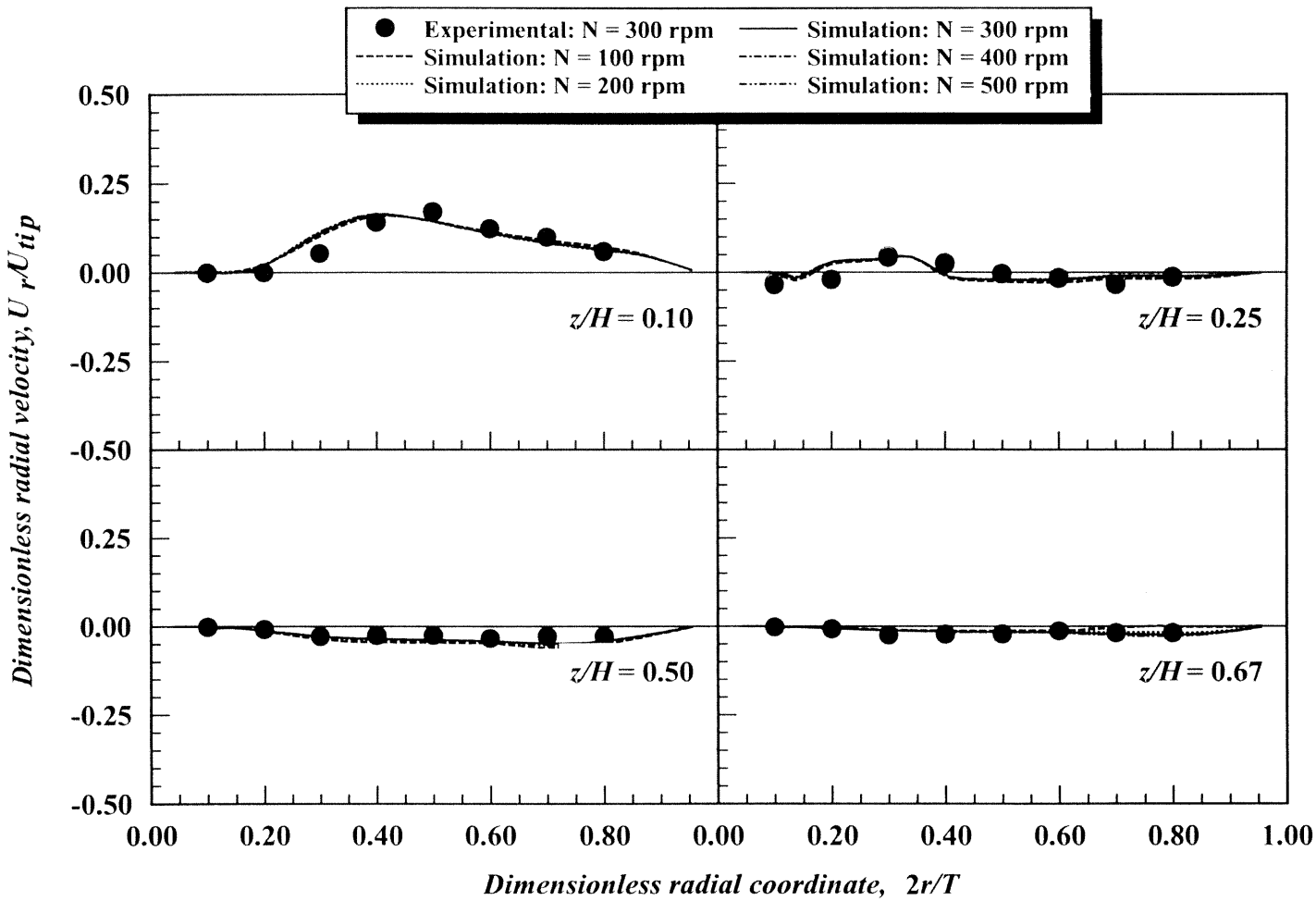

Figure 5.3 Comparison between LDV measurements and CFD predictions: Effect of impeller speed-Dimensionless radial velocity

velocity of $0.25U_{tip}$ near to the tank vessel. In this vertical location, the radial velocity is mostly outward towards the vessel wall. Below the impeller (z/H = 0.25), the radial velocity is lower than $0.1U_{tip}$. This agrees with observations by Ranade and Joshi (1989) and Kresta and Woods (1993b). There is some short circulation of fluid, leading to the radially inward flow through the vertical periphery of the impeller swept surface. Above the impeller (z/H = 0.50, 0.67), the radial velocity is inward indicating that the liquid returns to the impeller from the impeller top surface. Similarly to the axial velocity, there is a good agreement between LDV measurements and CFD predictions.

Figure 5.4 shows the tangential component of velocity. Similarly to the axial component of velocity, the maximum value occurs below the bottom surface of the impeller (z/H = 0.25). This peak velocity appears close to the blade tips, 0.35(T/2) or 0.5D, with a magnitude $0.35U_{tip}$. This component decays smoothly with the axial distance towards to the bottom vessel (z/H = 0.10). Above the impeller, the magnitude of the tangential component of velocity decays very rapidly (z/H = 0.50, 0.67). For this case, the tangential component is less well predicted than the axial and radial velocities.

Figure 5.5 shows that the maximum of the turbulence kinetic energy occurs below the bottom surface of the impeller (z/H = 0.25). The position of this maximum is almost the same as that of the axial component of velocity. CFD simulation under-predicts the maximum value by a factor of 3. Near the vessel bottom (z/H = 0.10), the maximum is not as pronounced as below the impeller. There is a large decrease in the magnitude of the turbulent kinetic energy as the distance above the impeller increases (z/H = 0.50, 0.67). Except for the region around the maximum value (z/H = 0.25), the agreement between LDV measurements and CFD predictions is quite satisfactory.

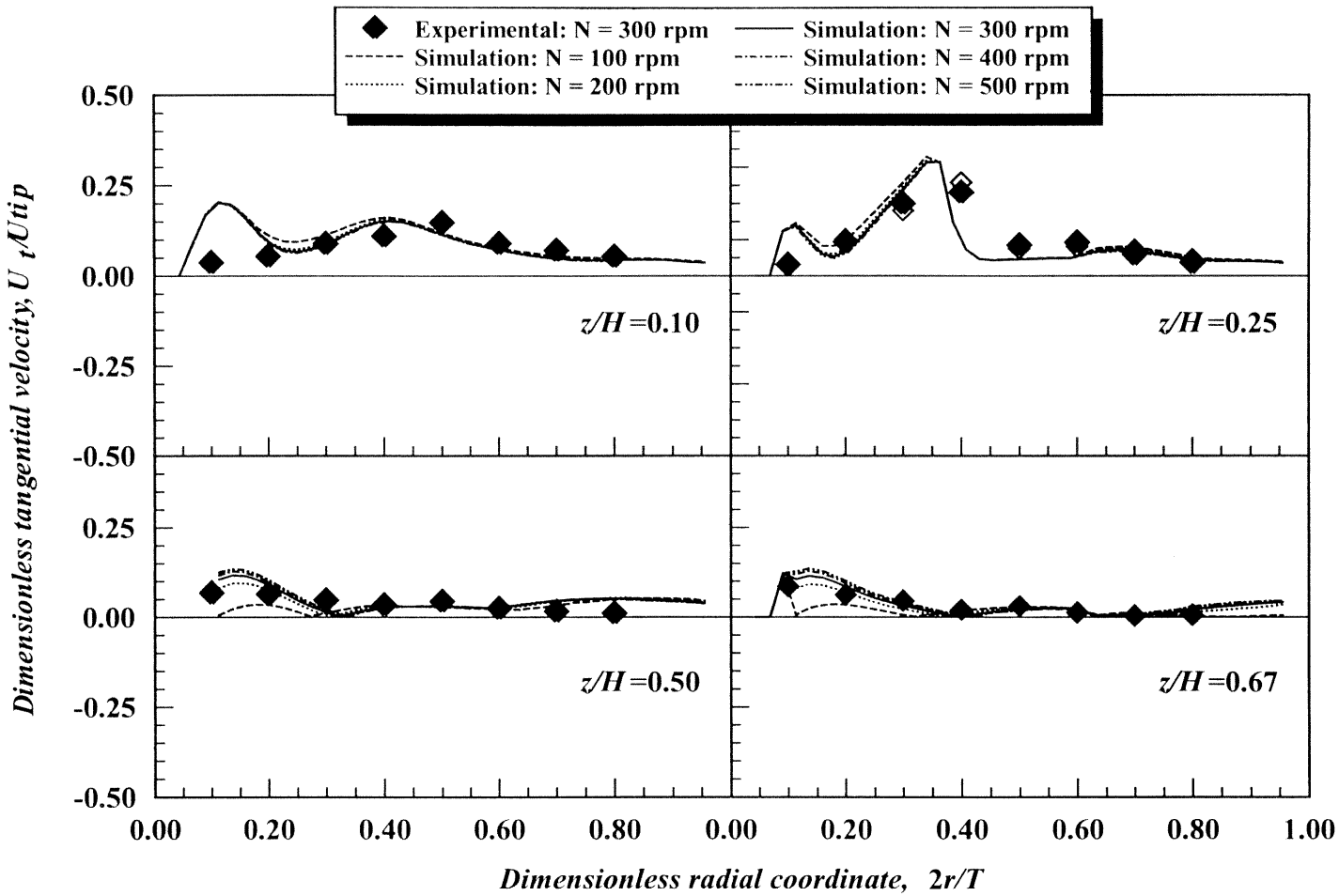

Figure 5.4 Comparison between LDV measurements and CFD predictions: Effect of impeller speed-Dimensionless tangential velocity

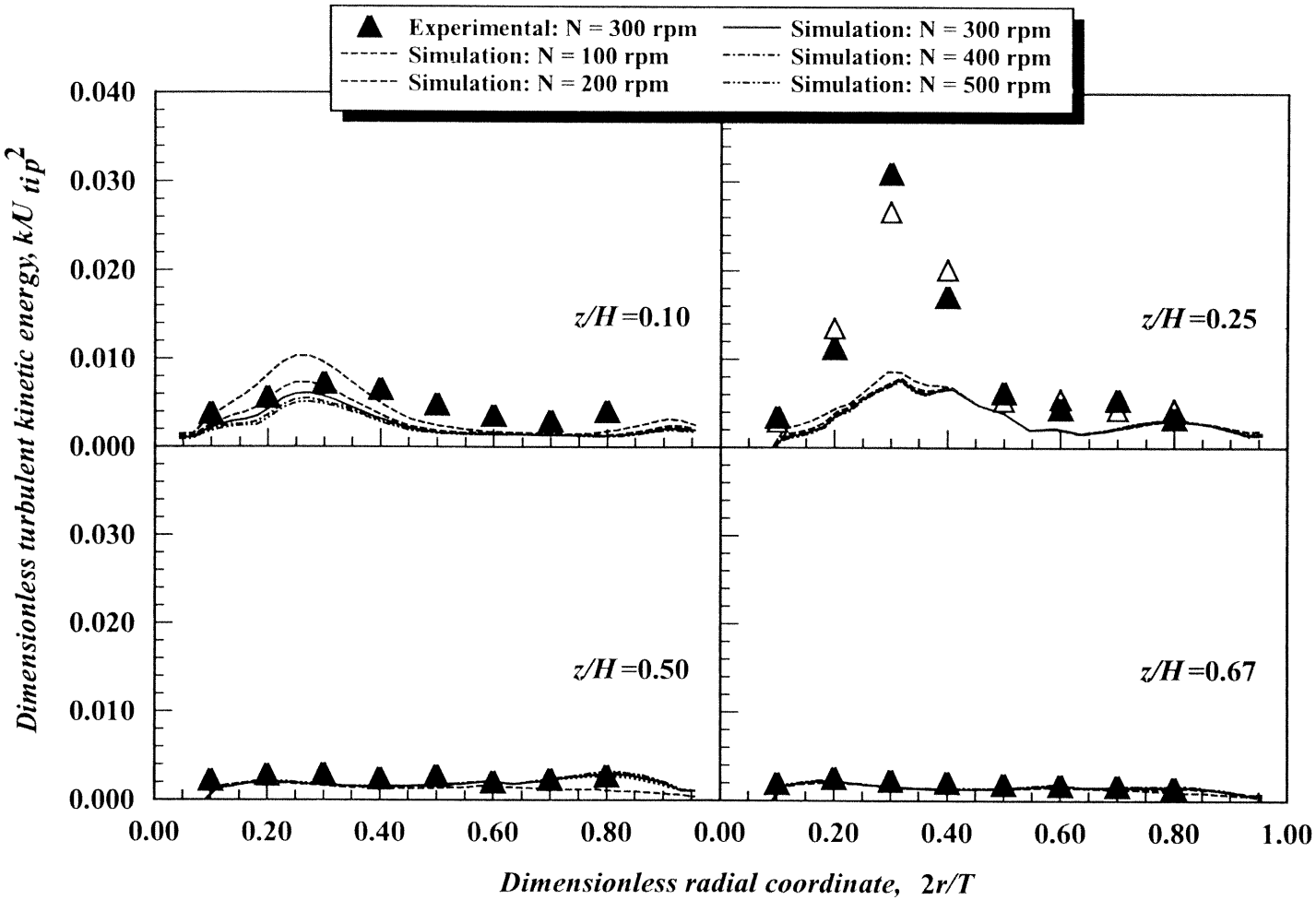

Figure 5.5 Comparison between LDV measurements and CFD predictions: Effect of impeller speed-Dimensionless turbulent kinetic energy

5.1.2 Effect of Impeller Speed on Flow Field

As shown in Figure 5.2, Figure 5.3, and Figure 5.4, respectively, the axial, radial, and tangential components of the fluid velocity are proportional to the impeller tip speed. This agrees with observations by Pettersson and Rasmuson (1998). For $N > 200$ rpm, Figure 5.5 shows that the turbulent kinetic energy scales with the impeller speed raised to the power two. Near the tank bottom ($z/H = 0.1$) and for $N < 200$ rpm, Figure 5.5 also shows that CFD predicts an increase of the dimensionless turbulent kinetic energy with the decrease of the impeller speed.

5.1.3 Effect of Impeller Diameter on Flow Field

The flow field generated by the 0.076 m impeller diameter and the 0.102 m impeller diameter in the 0.292 m vessel were compared at $N = 300$ rpm, and for a location one-third of the liquid height from the bottom vessel. The dimensionless axial, radial, and tangential velocities, and dimensionless turbulent energy rate are shown in Figure 5.6, Figure 5.7, Figure 5.8, and Figure 5.9, respectively.

In general, the comparison shows that the flow field generated by the smaller impeller is qualitatively similar to that of the larger size. The position of maxima of the axial, radial, and tangential component of velocity for the 0.076 m impeller size are located in the same vertical plane as occurs for the 0.102 m impeller size with slightly less magnitude and shifted towards to the symmetry axis. The profile of turbulent kinetic energy is also qualitatively similar. Simulation under-predicts the turbulent kinetic energy below the impeller surface. Except for the region around the maximum turbulent kinetic energy value, LDV measurements and CFD predictions are in good agreement.

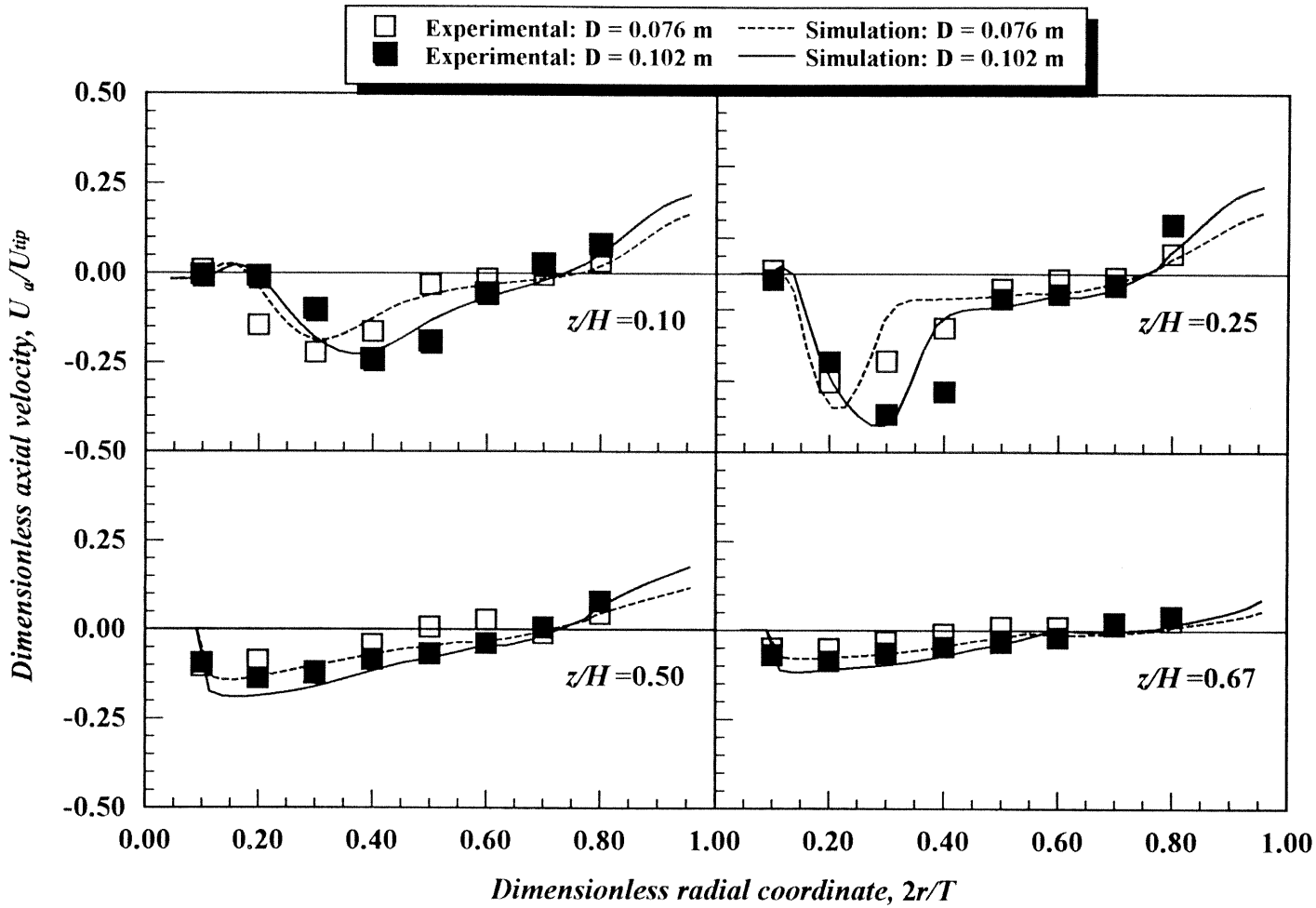

Figure 5.6 Comparison between LDV measurements and CFD predictions: Effect of impeller diameter-Dimensionless axial velocity

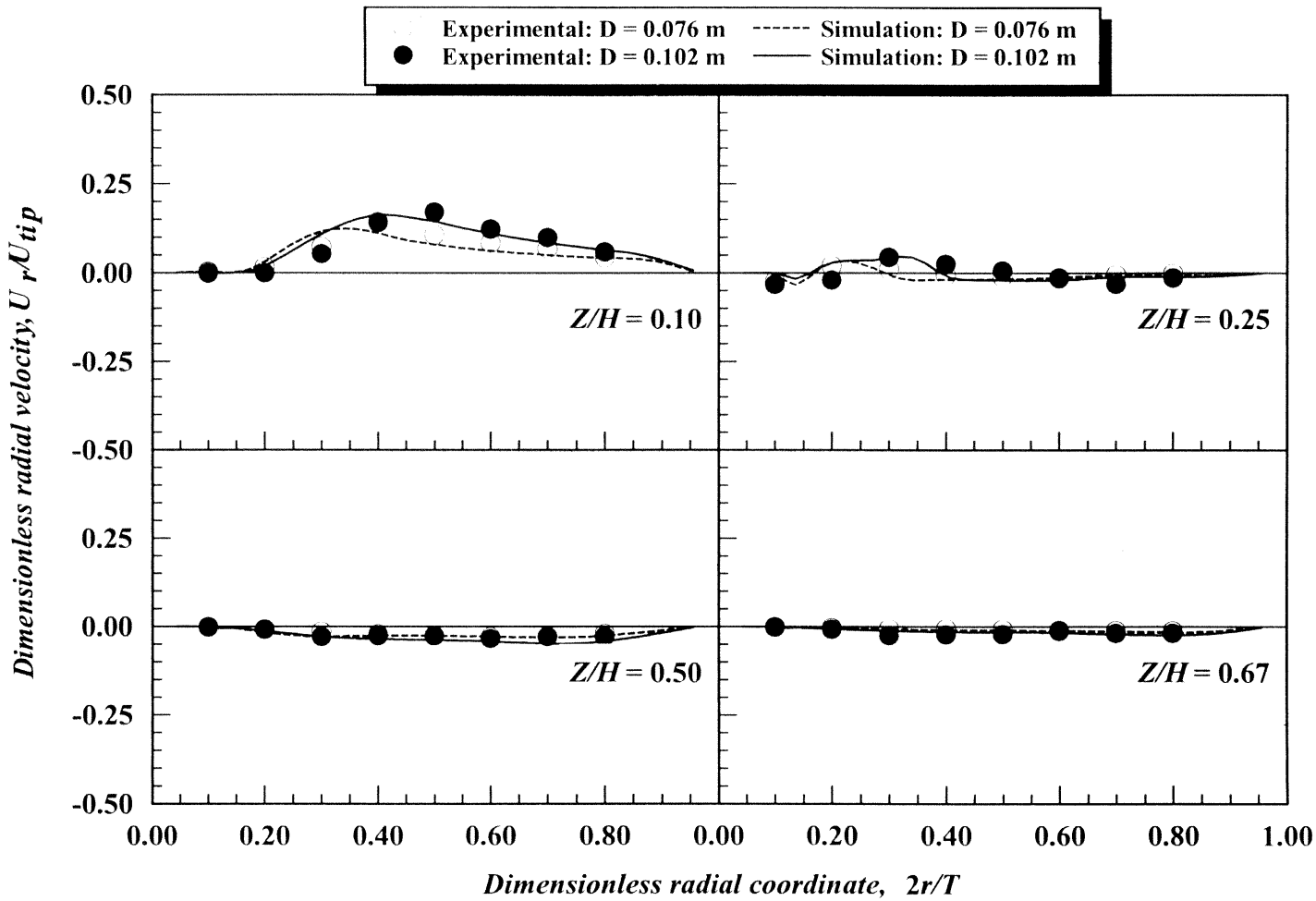

Figure 5.7 Comparison between LDV measurements and CFD predictions: Effect of impeller diameter-Dimensionless radial velocity

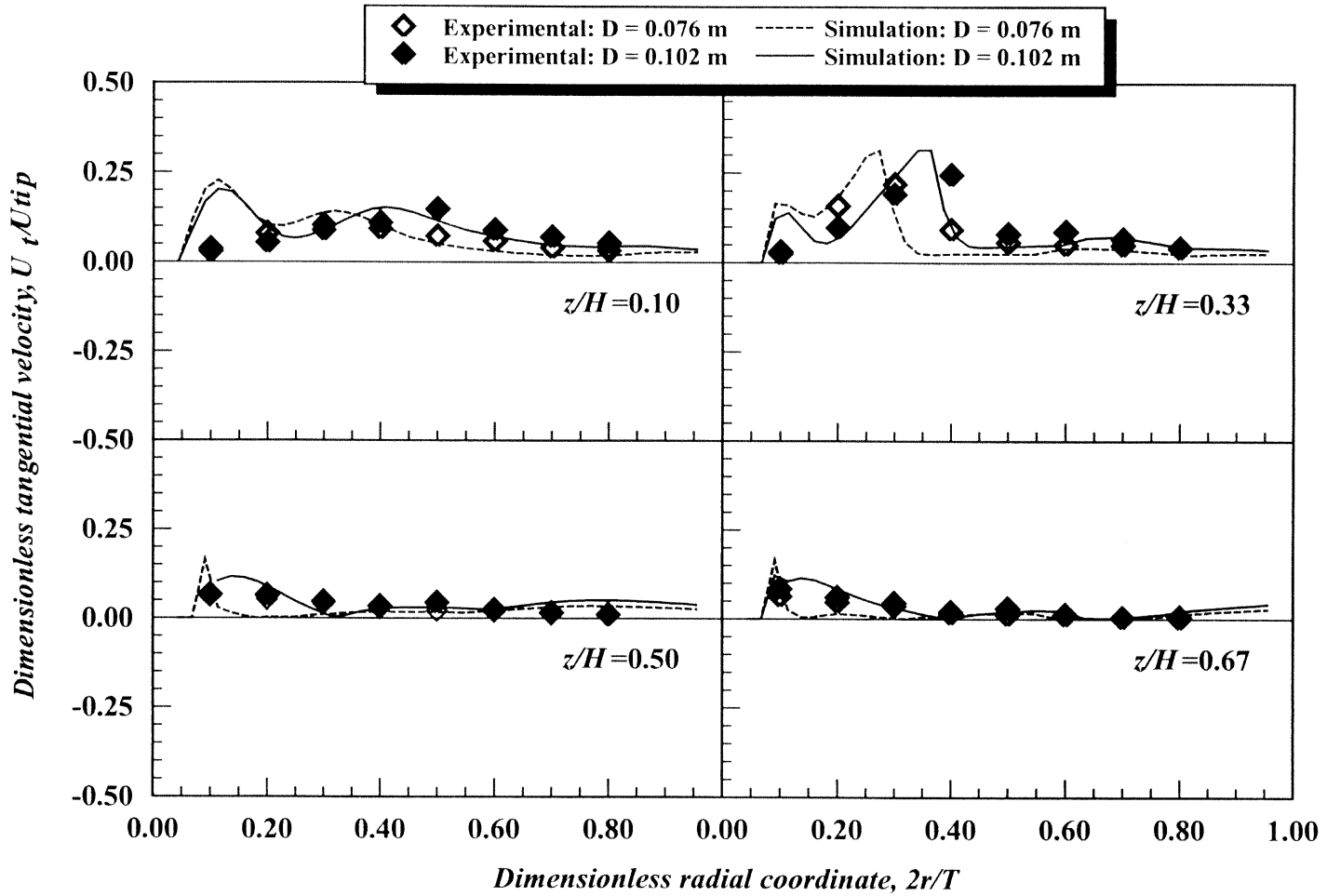

Figure 5.8 Comparison between LDV measurements and CFD predictions: Effect of impeller diameter-Dimensionless tangential velocity

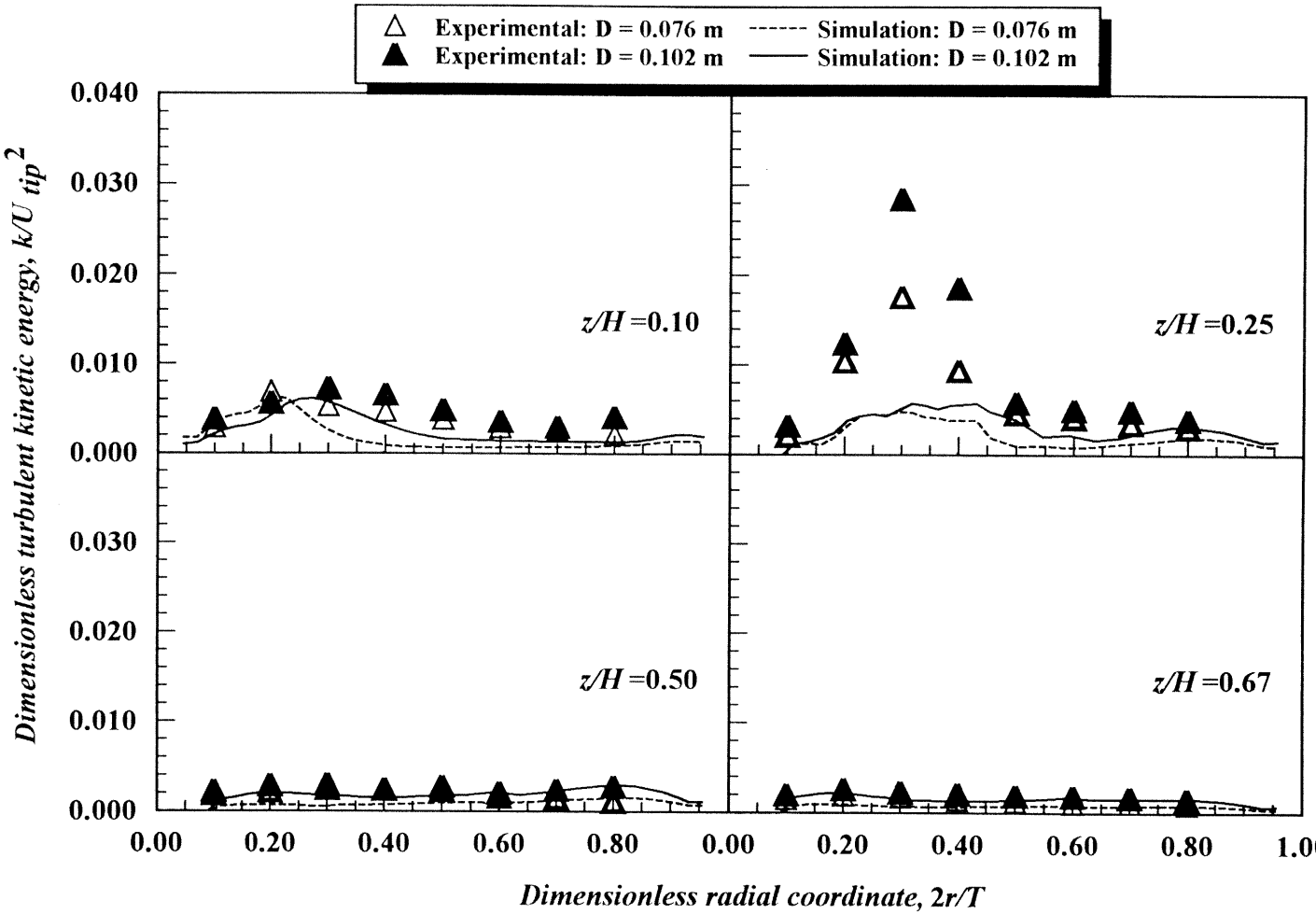

Figure 5.9 Comparison between LDV measurements and CFD predictions: Effect of impeller diameter-Dimensionless turbulent kinetic energy

5.1.4 Effect of Impeller Off-Bottom Clearance on Flow Field

The experimental results and numerical predictions were compared for the 0.102 m impeller size in the 0.292 m vessel at N = 300 rpm, located at one-third and one-fifth of the liquid height from the bottom vessel. The dimensionless axial, radial, and tangential velocities, and dimensionless turbulent energy rate are shown in Figure 5.10, Figure 5.11, Figure 5.12, and Figure 5.13, respectively.

At a plane immediately below the impeller (0.15D below the impeller bottom surface), there is a reduction in the axial component of velocity with a decrease of the distance from the bottom (Figure 5.10), while the radial component of velocity increases (Figure 5.11). Similarly to the axial component, the tangential component of velocity decreases with a decrease of the distance from the bottom (Figure 5.12). When the PBT impeller is away from the base, the downward liquid flows continuously changing its axial direction to radial direction, so that the liquid flows along the base in the horizontal direction before it rises along the wall. As the impeller clearance decreases, the change in direction becomes sharper decreasing the axial velocity and increasing the radial velocity. At a plane far above the impeller (z/H = 0.67), the magnitude of the components of velocity become independent of the distance of the impeller to the vessel bottom.

Similarly to C/T = 0.33, the maximum value of the turbulent kinetic energy is observed below the impeller plane (0.15D below the impeller bottom surface), but shifted to the axis of symmetry (Figure 5.13). The decrease of the distance from the vessel bottom increases the turbulent kinetic energy below the hub of the impeller. Except for the region around the maximum turbulent kinetic energy value, LDV measurements and CFD predictions are in good agreement.

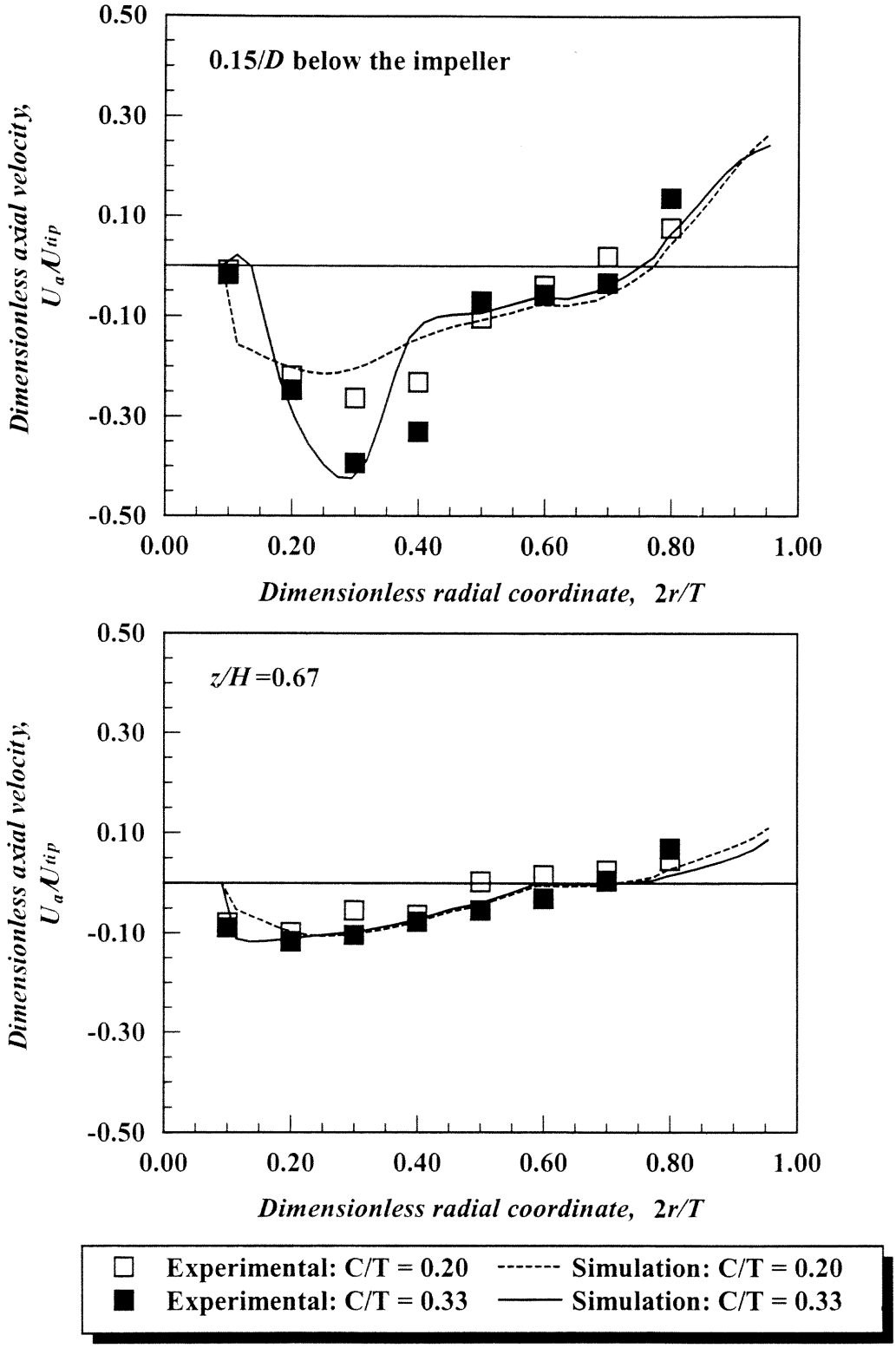

Figure 5.10 Comparison between LDV measurements and CFD predictions: Effect of impeller off-bottom clearance-Dimensionless axial velocity

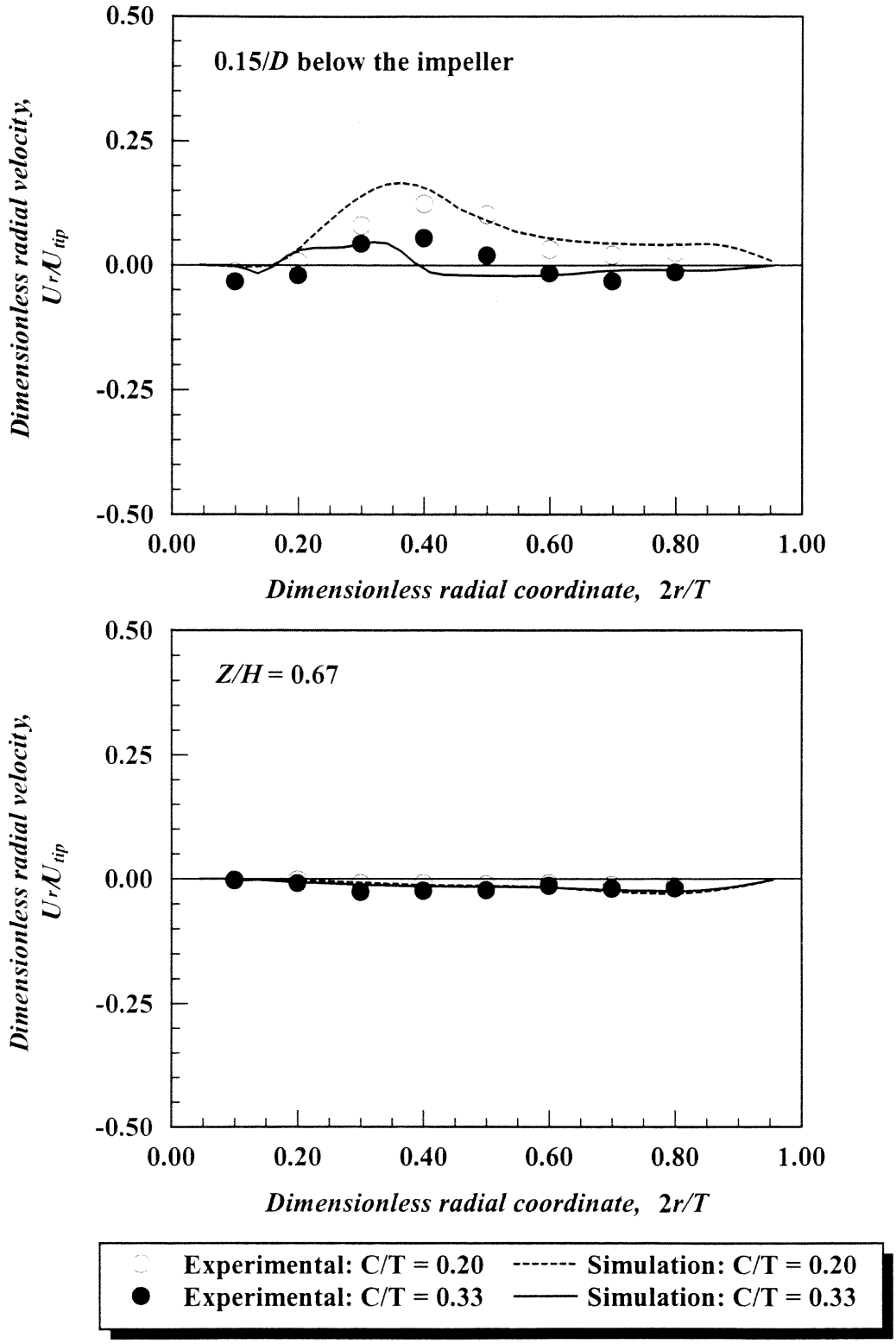

Figure 5.11 Comparison between LDV measurements and CFD predictions: Effect of impeller off-bottom clearance-Dimensionless radial velocity

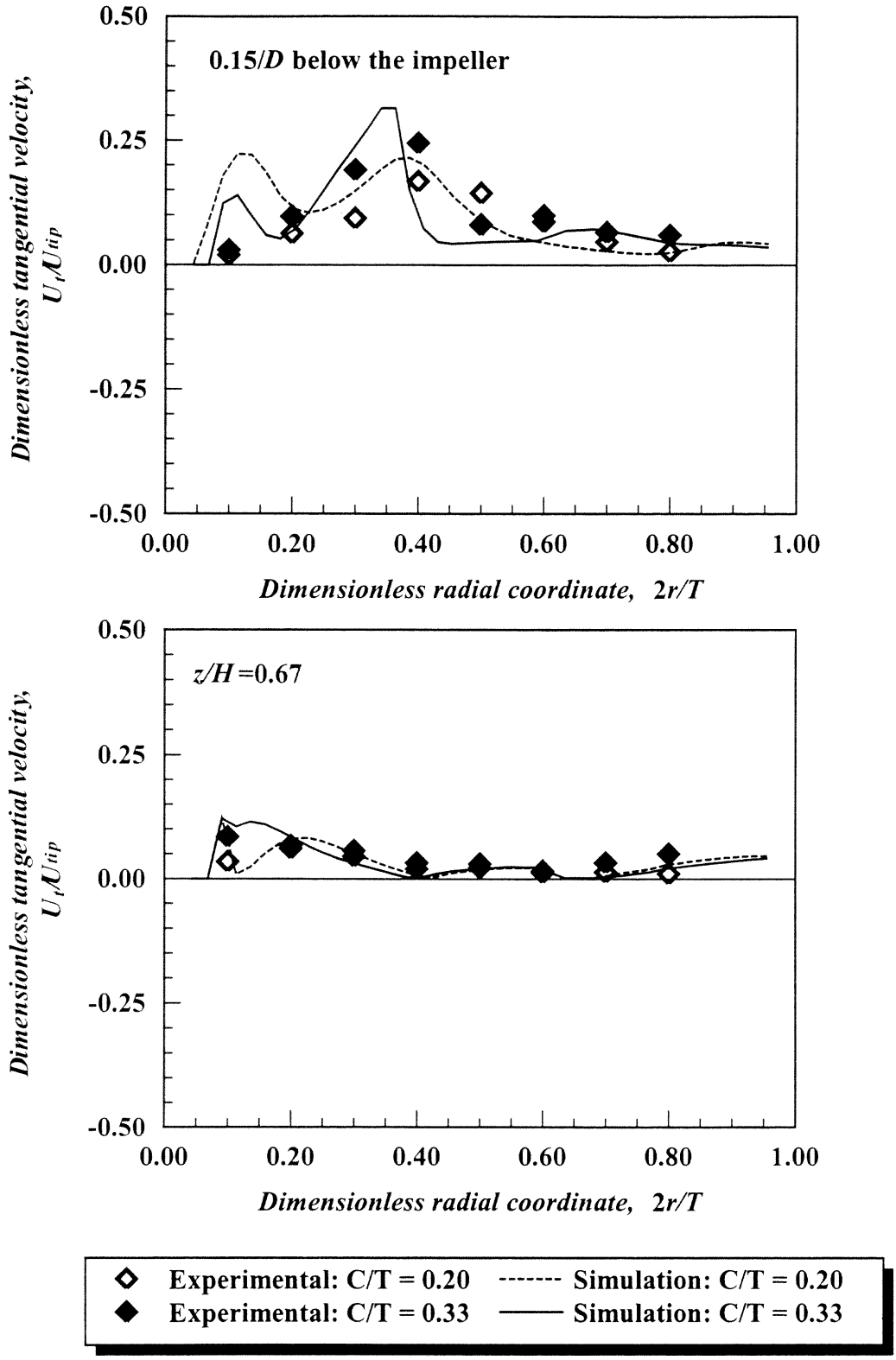

Figure 5.12 Comparison between LDV measurements and CFD predictions: Effect of impeller off-bottom clearance-Dimensionless tangential velocity

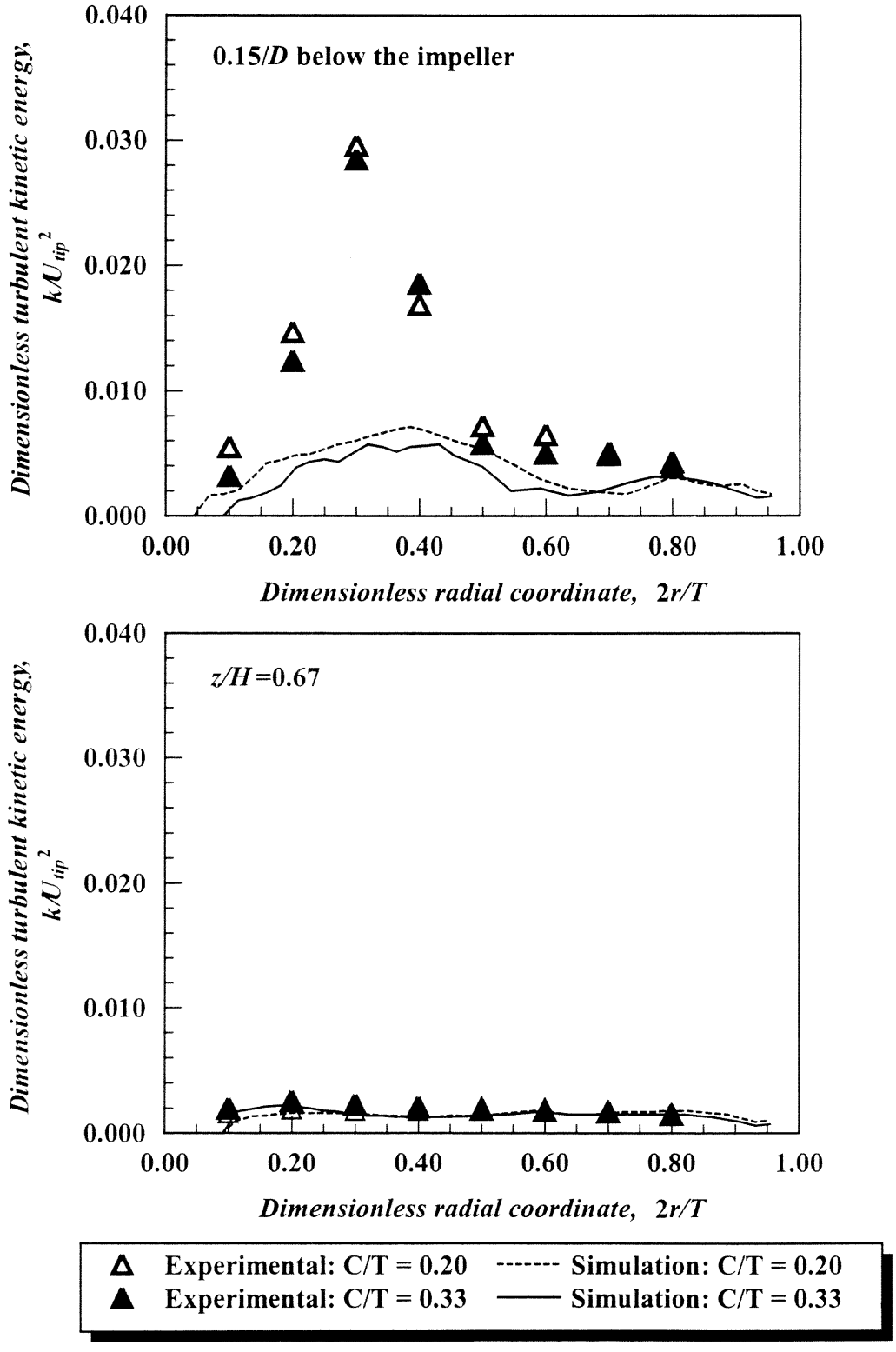

Figure 5.13 Comparison between LDV measurements and CFD predictions: Effect of impeller off-bottom clearance-Dimensionless turbulent kinetic energy

5.1.5 Energy Dissipation Rate Distribution

From the CFD simulations, the ratio of the volume averaged ε values (ε_{zone})-to-the average dissipation rate in the tank (ε_{avg}) for four different zones in the stirred vessel were estimated ($D/T = 0.34$, $C/T = 0.33$). Figure 5.14 shows the four zones: zone I, region below the impeller; zone II, impeller region; zone III, annular space between the impeller region and the vessel wall; and zone IV, rest of the liquid bulk.

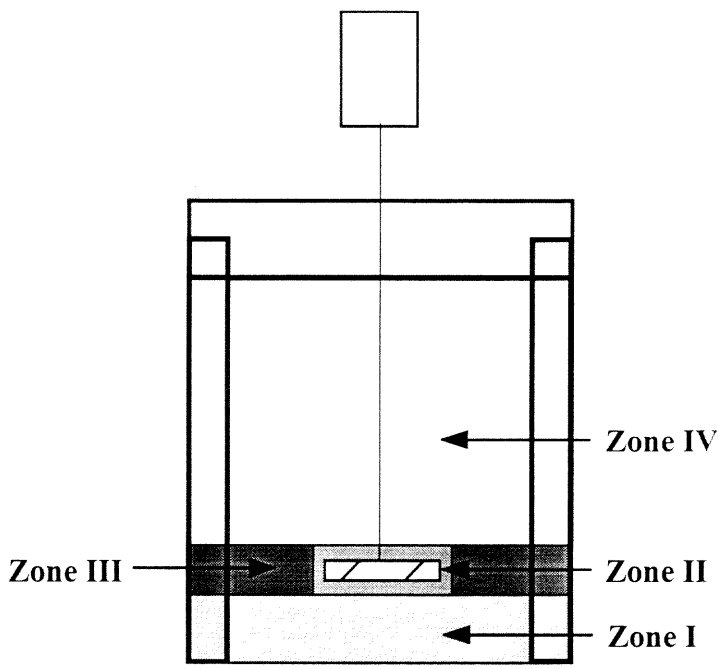

Figure 5.14 Energy dissipation rate zones in stirred tanks

Table 5.1 shows the ratio $\varepsilon_{zone}/\varepsilon_{avg}$ obtained from this calculation. By comparison, the ratios experimentally estimated by Jaworski and Fort (1991) are also shown ($D/T = 0.33$, 0.25 and 0.2, $C/T = 0.25$). Except for the under-prediction in the impeller region, the distribution of ε is in agreement with the experimental values of Jaworski and Fort (1991). Fokema and Kresta (1994) found that the ratio ($\varepsilon_{zone}/\varepsilon_{avg}$) in the impeller region varies between 5.3 for high clearance to 5.9 for low clearance.

Table 5.1 Distribution of energy dissipation rate

	Present work		Jaworski and Fort (1991)	
Zone	$\varepsilon_{zone}/\varepsilon_{avg}$	*%V*	$\varepsilon_{zone}/\varepsilon_{avg}$	*%V*
I	2.2	28.1	2.7	20.7
II	3.3	2.6	6.0	2.6
III	0.6	7.7	0.4	7.8
IV	0.4	61.6	0.2	69.0

There are three factors that lead to the under-prediction of the energy dissipation rate in the impeller region. First, a single trailing vortex is formed behind each blade from the interaction of the fluid streams issuing from the side, upper, and lower edges of the blades. These vortices provide the primary source of turbulence generation in the vessel, but are dissipated into the bulk flow (Schäfer *et al.*, 1998). The energy dissipated through these trailing vortices and through shear at the impeller blades are not accounted by the CFD simulation. To seriously capture the trailing vortex, the grid in the impeller swept volume would have to be considerably denser (Syrjänen and Manninen, 2000).

Second, CFD simulation assumed that the flow is steady. However, semi-instantaneous full flow field measurement using digital particle image velocimetry shows large scales unstable flow structures (Bakker *et al.*, 1996). Energy dissipated through these large scale instabilities is therefore unaccounted for. To obtain correct predictions of the turbulent energy dissipation rate, it may be necessary to perform time dependent calculations for the impeller (Murthy *et al.*, 1994) or use another alternative as Large Eddy Simulations (Eggels, 1995) which accounts for the large scale instabilities.

Finally, RSM model are not so restricted as the k-ε turbulent models, however, the model parameters are not universal (i.e., the models should be calibrated for different classes of problems). RSM model parameters have been estimated from simple configurations, such as the flow field inside the pipes, and should be calibrated for the application to stirred vessels. The performance of the turbulent models may be improved with the optimization of the parameters (Sahu *et al.*, 1998). Furthermore, since RSM was built for fully developed turbulent flows, the model could present some shortcomings when handling mixed laminar and turbulent flows.

In conclusion, better prediction of the energy dissipation rate in the impeller region would require refine the grids in this region, take into account the large scale instabilities, and optimize the performance of the RSM model. However, considering the functional relationship of the engulfment parameter rate with the local energy dissipation rate as shown in Equation (2.37): $E(t,t_s) \propto \varepsilon(t,t_s)^{1/2}$, and the kinetic term included in the mixing-precipitation model equations, the under-prediction of ε would cause the underestimation of the mean crystal size by a much lower percentage.

5.1.6 Power Number

Table 5.2 shows the comparison between the experimental and CFD predicted power numbers. For each value of C/T, the experimental Po values were calculated from P measurements and using Equation (3.3). Experimental values obtained from measurements at different impeller speeds in the turbulent regime (Re > 10,000) were averaged. Experimental Po ranged from 1.46 to 1.62 which agree with published values. The maximum standard deviation for the experimental Po was 5.84%.

Table 5.2 shows an increase of *Po* with a decrease in *C/T*. This agrees with observation found in previous works (Raghava Rao and Joshi, 1988; Armenante and Uehara, 1998; Armenante *et al.*, 1999). As *C/T* decreases, the change in direction becomes sharper and more energy is dissipated. For the smallest *C/T*, the liquid flow almost hits the base so that practically all the kinetic energy is dissipated. *Po* appears to be independent of the impeller diameter, *D*. Rewatkar *et al.* (1990) found that PBT shows a minimum value with respect to *D*. These authors also found that depending on the impeller diameter different flow patterns are generated by the impeller. They correlated this unique effect of *D* on *Po* and found a very weak relationship: $Po \propto D^{-0.11}$, this represents a 4% difference in *Po* between the two impeller sizes used here. When the power drawn by the impeller is calculated from the pressure distribution, *Po* predicted by CFD simulation is 15% average low compared with the experimental value. However, the simulation also predicts the increase of *Po* with the decrease on *C/T* and the weak dependence on *D*.

Table 5.2 Comparison between experimental and predicted power number

	Experimental		**Simulation**	
C/T	**0.076 m**	**0.102 m**	**0.076 m**	**0.102 m**
0.33	1.46±0.07	1.46±0.06	1.24	1.24
0.25	1.49±0.04	--	1.27	--
0.20	1.54±0.09	1.52±0.08	1.31	1.29
0.17	--	1.55±0.06	--	1.32
0.13	1.62±0.05	--	1.38	--

5.2 Effect of Process Variables

In these experiments, the effect of a number of process variables on the CSD was determined. The experimental mean crystal size ranged from 1.75 μm to 6.76 μm, and *C.V.* from 0.17 to 0.39. The experimental crystal size distribution were unimodal and similar to the Gaussian distribution. All experiments were duplicated. The standard deviation for the experimental mean crystal size and *C.V.* are shown in Table 5.3. The maximum standard deviations were 15.79% and 15.73%, respectively. The standard deviation was somewhat larger due to the agglomeration effect. When the experiments that showed the presence of agglomeration were discarded, the maximum standard deviations were 5.14% and 11.40% for the mean crystal size and *C.V.*, respectively.

Table 5.3 Reproducibility of experiments for effect of process variables

Process variable	Feed	Standard deviation	
		Mean crystal size	*C.V.*
Feed tube diameter	I	3.18%	7.64%
	II	4.52%	11.82%
Feed addition time	I	3.47%	7.99%
	II	4.81%	13.78%
Volume ratio of reactants	I	6.02%	15.73%
	II	9.14%	7.30%
Mean initial concentration of sodium sulfate	I	13.13%	6.17%
	II	15.79%	10.27%
Stoichiometry ratio of reactants	I	6.75%	9.03%
	II	12.96%	9.01%

5.2.1 Effect of Feed Tube Diameter

Figure 5.15 shows the effect of feed tube diameter on the CSD. The mean crystal size was not affected by d_{tube}, but only if $d_{tube} < 2.3$ mm (Figure 5.15a). As shown in Figure 5.15b, no effect on *C.V.* was observed. Since the flow rate was constant in these experiments the velocity in the feed tube decreased with increasing d_{tube}, leading to backmixing inside the tube. This had an impact on the mean crystal size (Figure 5.15a) which became smaller because of the high level of local supersaturation in the tube due to poorer mixing conditions (Baldyga *et al.*, 1993). The backmixing effect was more pronounced when the feed was above the impeller than when it was below the liquid surface, probably because of the higher liquid velocity in the zone in the former case. Backmixing is a very complex phenomenon and is very difficult to predict. Since the simulation did not include backmixing, the predictions are shown as constant values for both the mean crystal size and *C.V.*

Fasano and Penney (1991b) proposed that for $u_{tube} > 0.09\pi ND$ no feedpipe backmixing should occur for feed locations above the impeller. This criterion gives a value for d_{tube} of 0.8 mm for the system used here. However, their correlation applies only to turbulent regimes inside the tube, whereas the regime here was laminar. It has been reported that feedpipe backmixing is more pronounced under turbulent rather than laminar conditions in the tube flow (Jo *et al.*, 1994). Zauner and Jones (2000a) also investigated the effect of d_{tube} in the semi-batch precipitation of calcium oxalate, and attributed the results obtained to mesomixing effects. However, a careful examination of their data indicates that backmixing is a more likely explanation, because of their long feed time, which would ensure that micromixing conditions dominate.

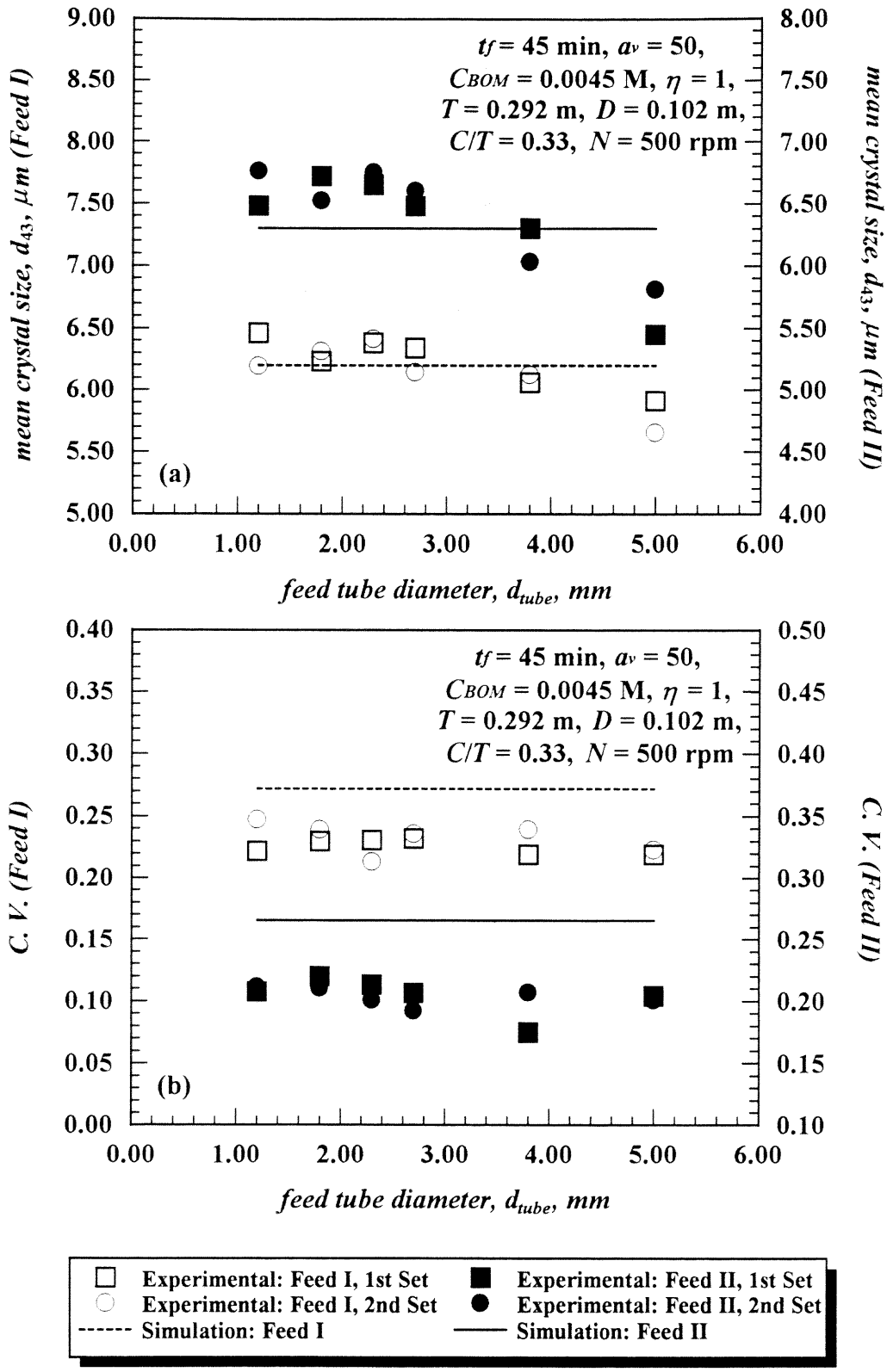

Figure 5.15 Effect of feed tube diameter on: (a) mean crystal size; and (b) *C.V.*

5.2.2 Effect of Feed Addition Time

The effect of addition time is shown in Figure 5.16. When the feed was positioned above the impeller (Feed II) and the agitation speed was low (100 rpm) the mean crystal size increased with t_f, and then became independent for $t_f > 35$ min (Figure 5.16a). t_f did not affect *C.V.* (Figure 5.16b). By increasing t_f at constant impeller speed, the effect of mesomixing decreased. This agrees with observations found by Bourne and Dell'Alva (1987) and Bourne and Hilber (1990). The decrease of mesomixing increases the intensity of mixing and decreases the local supersaturation level and hence the nucleation rate. Consequently, a smaller number of larger crystals are produced. Similar results to those reported in Figure 5.16a were presented by Åslund and Rasmuson (1992) for benzoic acid, Baldyga *et al.* (1995) and Phillips *et al.* (1999) for barium sulfate, and Zauner and Jones (2000a) for calcium oxalate. When the agitation speed was increased at 300 rpm the mesomixing effects were still noticeable (Figure 5.16a) but disappeared at a lower t_f value (30 min). This is consistent with the hypothesis that increasing level of turbulence decreases the importance of mesomixing (Bourne and Thomas, 1991).

The situation is more complex for feeding below the liquid surface (Feed I). No typical evidence of mesomixing was observed when the agitation speed was low (100 rpm; Figure 5.16a). Furthermore, the mean crystal size was significantly larger than when Feed II was used, which is the reverse of what was observed in all the experiments described later, and difficult to explain using only micromixing theory. However, when the impeller speed was increased to 300 rpm, a trend similar to that obtained with Feed II (Figure 5.16a) was observed (with mesomixing effects becoming apparent for $t_f < 42$ min), and the crystal size was smaller compared to Feed II, as expected.

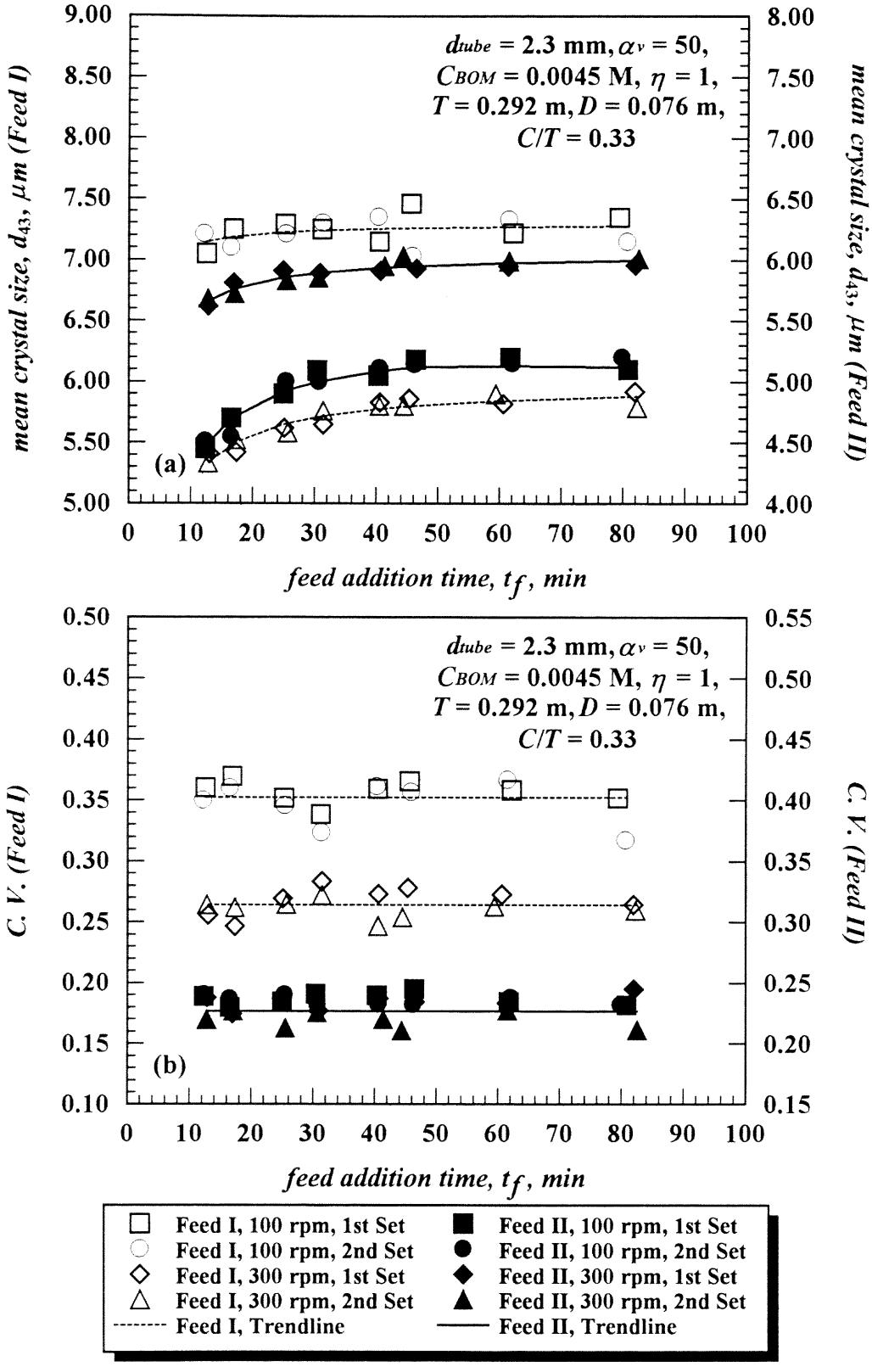

Figure 5.16 Effect of feed addition time on: (a) mean crystal size; and (b) *C.V.*

The phenomenon observed for Feed I is difficult to explain if only micro- and mesomixing effects are considered. Two other effects must be taken into consideration. First, at 100 rpm the turbulence level near the surface is so low resulting in both poor micromixing and poor macromixing. The former effect produces slow incorporation of fresh material in the reaction zone; the latter ensures that the reaction zone is kept in this state for a relatively long period of time. The net result is a prolonged low supersaturation in the reaction zone (with heterogeneous nucleation dominating), resulting in low nucleation rate and low consumption of reagents. When the blob finally reaches the higher turbulent level in the impeller region, the increase in mixing dilutes the supersaturation ratio, thus the blob simply dissolves in the bulk, where crystal growth dominates, producing large crystals. Second, the low turbulence level found promotes agglomeration (Kuboi *et al.*, 1985) contributing to the unusual larger crystal size for Feed I (Figure A.3, agglomerated crystals) as compared with Feed II (Figure A.4, well-formed crystals). Thus, increasing the impeller speed reduces agglomeration and increases the micromixing until becomes controlling.

The simulation considered the macromixing effect as explained in Section 2.4.2. Mesomixing was not included in the simulation. For precipitation processes, the controlling mesomixing mechanism has been found to be the eddy breakup (Baldyga *et al.*, 1995). A comparison between Equation (2.27) and Equation (2.30) shows that increasing the turbulence level, ε, would increase the mesomixing effect contrary to what was observed here and by other authors (Bourne and Thomas, 1991). Furthermore, the theory developed for mesomixing (Baldyga *et al.*, 1997b) suggests that the mesomixing zone can grow without limit. The mesomixing theory still needs more development.

5.2.3 Effect of Volume Ratio of Reactants

The effect of volume ratio on mean crystal size and *C.V.* is shown in Figure 5.17. The first and second set of experiments were carried out with a Plexiglas and glass vessel of identical geometries, respectively. No difference in the CSD and morphology was observed. Plexiglas tank was considered to be adequate for the precipitation experiments.

The mean crystal size decreased with the volume ratio (Figure 5.17a), especially for $\alpha_v = 60$. Figure 5.17b also indicates that *C.V.* decreased at $\alpha_v = 60$. Increasing the volume ratio implies that a higher amount of sodium sulfate is added at the same flow rate, resulting in an increase in the local supersaturation, and leading to higher nucleation rates and smaller crystal sizes. For $\alpha_v > 80$ crystal agglomeration became apparent from the ESEM photographs (Figure A.5 and Figure A.6). This had two effects, i.e., a less steep decline in the mean crystal size with increasing volume ratios, and a marked *C.V.* increase at high volume ratios. Previous investigators (Baldyga *et al.*, 1995; Phillips *et al.*, 1999) also observed similar variations of the mean crystal size with the volume ratio.

Figure 5.17 also shows the predicted simulation results. The mean crystal size (Figure 5.17a) and *C.V.* (Figure 5.17b) were correctly predicted to decrease with the volume ratio. Since the simulation did not account for agglomeration (typically observed at high volume ratio), the simulation under-predicted the mean crystal size for $\alpha_v > 80$. *C.V.* was overestimated in the simulation. An explanation of this result is that *C.V.* is very sensitive to the value of the 5^{th} moment and the order of magnitude of the 0^{th} moment ($\sim 10^{12}$) and the 5^{th} moment ($\sim 10^{-16}$) were very large, thus making the solution of the moment differential equations very stiff. Multiplying the value of the 5^{th} moment by a factor of 0.97, produced a much-improved agreement for *C.V.* (Figure 5.17b).

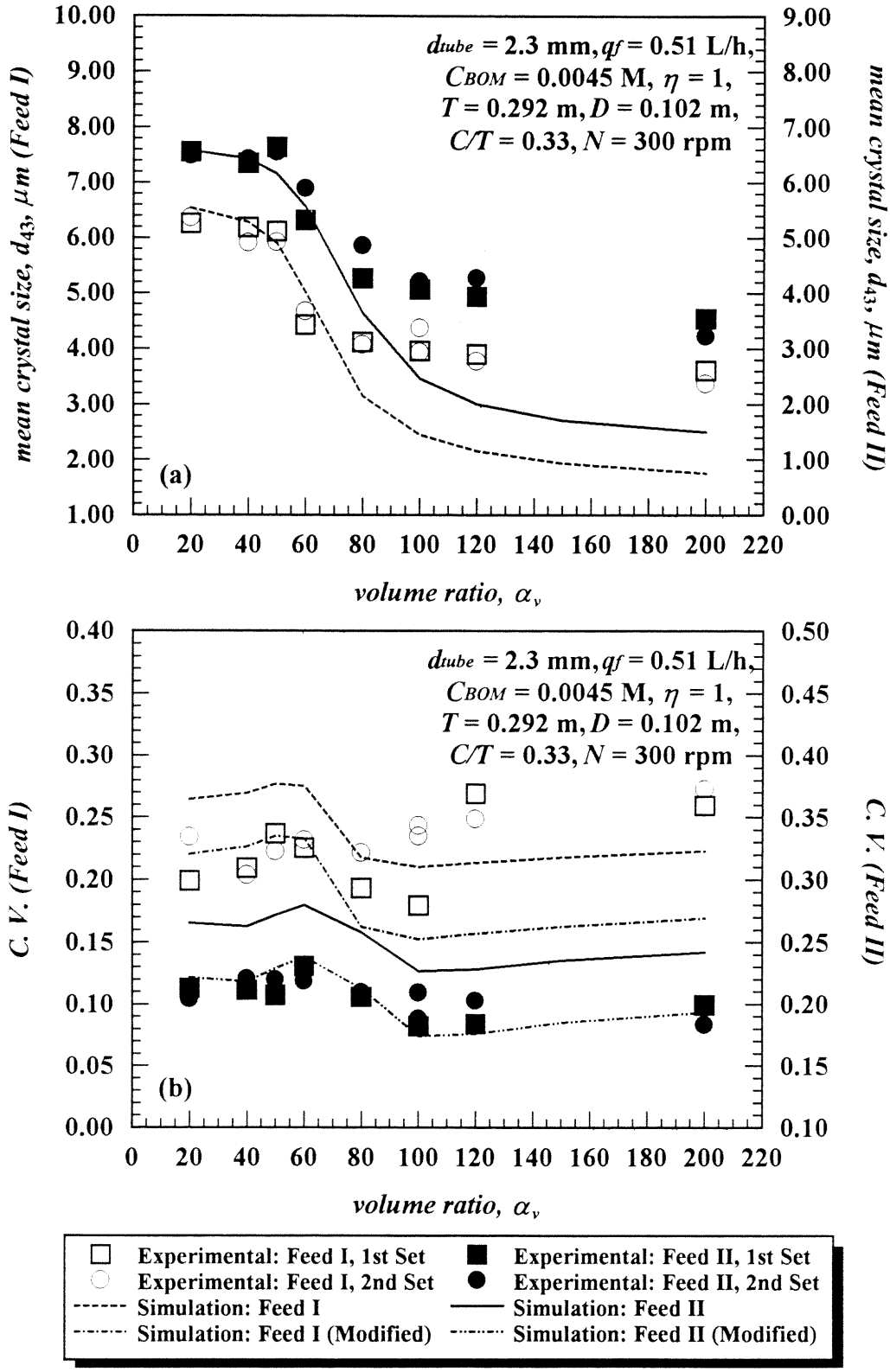

Figure 5.17 Effect of volume ratio on: (a) mean crystal size; and (b) *C.V.*

5.2.4 Effect of Mean Initial Concentration of Sodium Sulfate

The effect of mean initial concentration is shown in Figure 5.18. Single-distillate and Milli-Q water were used in the first and second set of experiments, respectively. Similarly to the previous experiments, no difference in the CSD and morphology was observed. Hence, single-distillate water was determined to be of adequate purity.

Both the experimental results and the simulation predictions show a maximum in the mean crystal size at approximately $C_{BOM} = 0.0045$ M (Figure 5.18a). Figure 5.18b shows that a change in slope for *C.V.* occurred at approximately the same C_{BOM} value. Again, experimental results and simulation predictions follow the same trend. This non-monotonic functionality can be explained in terms of competition between nucleation (heterogeneous or homogeneous) and crystal growth. Depending on the controlling step (mass transfer or chemical reaction), Equation (3.26) shows that the rate of crystal growth is proportional to ΔC raised to an exponent between 1 to 4. At low C_{BOM} values (low supersaturation levels), crystal growth is typically proportional to ΔC^4 which is a stronger function of C_{BOM} than the heterogeneous nucleation rate ($\propto \Delta C^{1.775}$). However, the reverse is true at higher supersaturation values since the homogeneous nucleation rate ($\propto \Delta C^{15}$) is now a stronger function of C_{BOM}. As in the volume ratio experiments, agglomeration was observed through ESEM photographs for $C_{BOM} > 0.006$ M (Figure A.7 and Figure A.8). Tosun (1988), Åslund and Rasmuson (1992), Baldyga *et al.* (1995), Phillips *et al.* (1999), and Zauner and Jones (2000a) also found that a decrease in the mean concentration of the added reactant significantly increased the mean crystal size. Similar behavior found in this work for *C.V.* was experimentally observed and predicted for a tubular reactor (Baldyga and Orciuch, 1997).

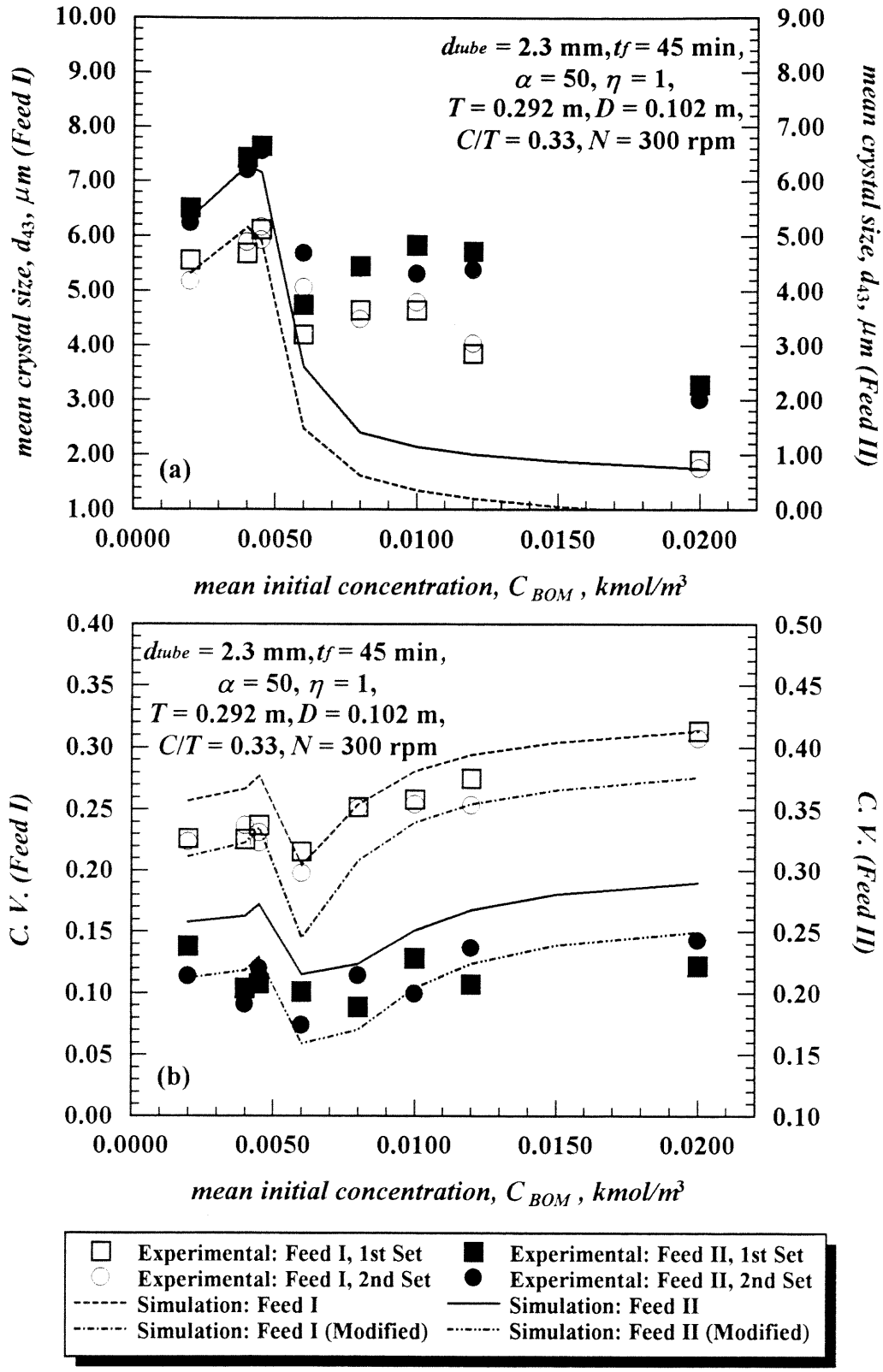

Figure 5.18 Effect of mean initial concentration on: (a) mean crystal size; and (b) *C.V.*

5.2.5 Effect of Stoichiometry Ratio of Reactants

Figure 5.19 shows the experimental results and the simulation predictions for the effect of the stoichiometry ratio on the CSD. When sodium sulfate was fed in excess of barium chloride ($\eta < 1$), the mean crystal size increased with η (Figure 5.19a), reaching a maximum for $\eta = 1$. However, when barium chloride was in excess of sodium sulfate ($\eta > 1$) the reverse was observed. The explanation for this behavior resides, as in the previous case, in the competition between nucleation and crystal growth rates, and their varying dependence on the independent variable under study. As in the variable volume ratio experiments, agglomeration was observed in ESEM photographs for $\eta > 1.5$ (Figure A.9 and Figure A.10). Figure 5.19b shows the effect of η on *C.V.* No clear pattern emerges. However, agglomeration could be responsible for the phenomenon.

5.2.6 Crystal Morphology

The crystal morphology was analyzed with the Environmental Scanning Electron Microscope (Philips Electro Scan 2020). The ESEM photographs are shown in the Appendix A (ESEM Photographs). At the reference conditions: $d_{tube} = 2.3$ mm, $t_f = 45$ min, $\alpha_v = 50$, $C_{BOM} = 0.0045$ M, $\eta = 1$, $D = 0.102$ m, $N = 300$ rpm, and $C/T = 0.33$, well-formed rectangular crystals were obtained for Feed I (Figure A.1) and Feed II (Figure A.2). At $N = 100$ rpm and $D = 0.076$ m, amorphous crystals and well-formed rectangular crystals were obtained for Feed I (Figure A.3) and Feed II (Figure A.4), respectively. These occurred independently of t_f. For Feed I, low turbulence level promoted agglomeration producing the amorphous crystals. However, at $N = 300$ rpm and $D = 0.076$ m, well-formed rectangular crystals were obtained independently of t_f.

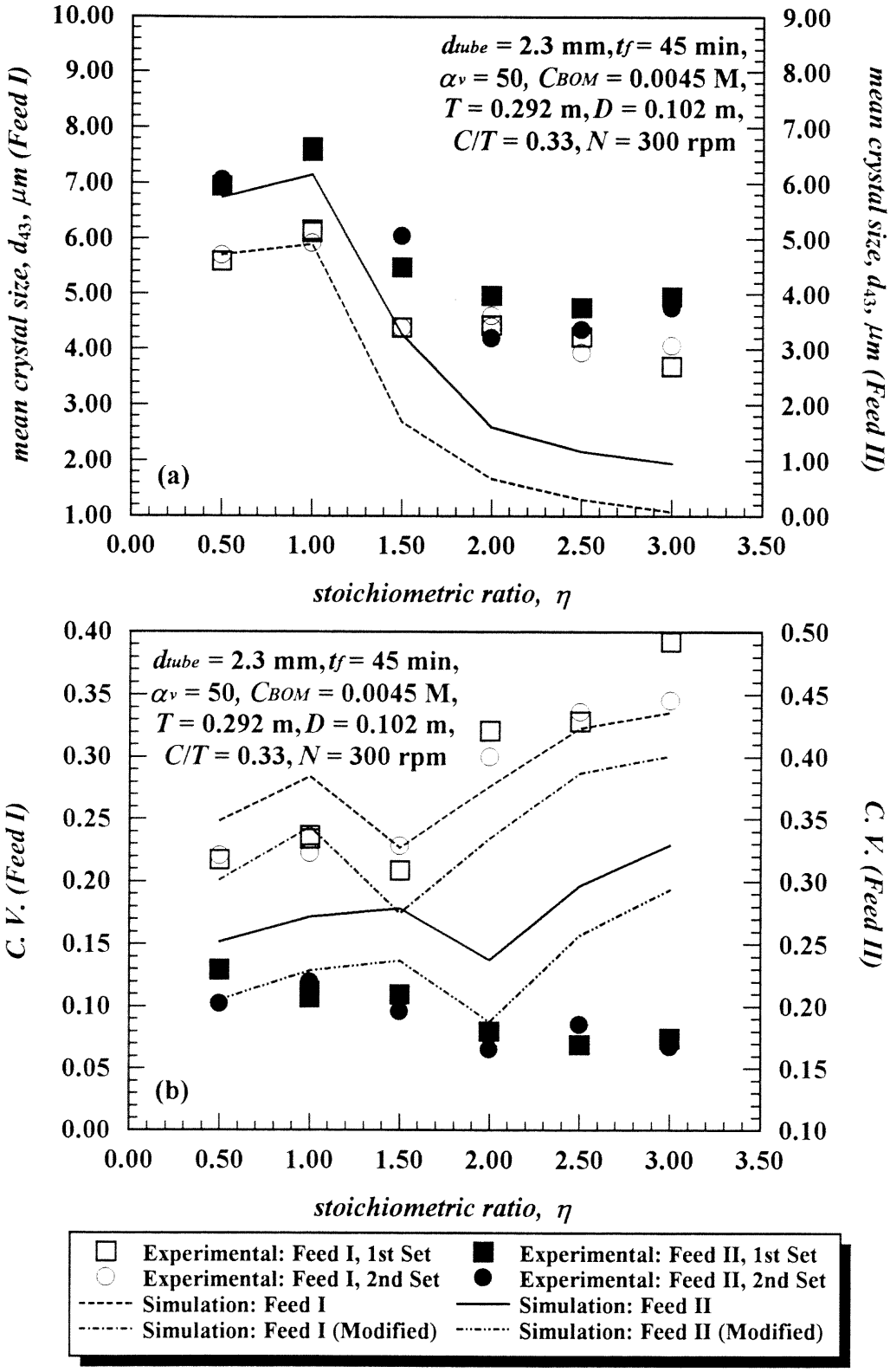

Figure 5.19 Effect of stoichiometry ratio on: (a) mean crystal size; and (b) *C.V.*

At high values of volume ratio, $\alpha_v \geq 80$ (Figure A.5 and Figure A.6, for Feed I and Feed II, respectively), mean initial concentration, $C_{BOM} \geq 0.006$ M (Figure A.7 and Figure A.8, for Feed I and Feed II, respectively), or stoichiometry ratio, $\eta \geq 1.5$ (Figure A.9 and Figure A.10, for Feed I and Feed II, respectively), agglomeration occurred and the crystals obtained were amorphous. Below these values, well-formed rectangular crystals were observed. During the agglomeration process, small crystals in the liquid suspension cluster together. In this process, the aggregates increase the mean crystal size and broaden the CSD. The dendritic forms, usually produced at high level of supersaturation (Gunn and Murthy, 1972; Fitchett and Tarbell, 1990; Baldyga *et al.*, 1995; Barresi *et al.*, 1999), were not observed in this work.

An attempt to obtain the crystal shape factor was made using the environmental scanning electron microscope. The geometry and the dimensions were determined from one sample (20 crystals from this sample) at the reference conditions. It should be notice, that the result of such a calculation would be prone to significant error (Mullin, 1997). The dimensions and the superficial area of the well-formed rectangular crystals analyzed are shown in Table 5.4. Paglioco *et al.* (2000) have recently evaluated the average size of thin platelets of barium sulfate crystals from scanning electron microscope photographs. Comparison with the average value determined by a Malvern particle sizer (3600 D) showed that this average value is very close to the second largest dimension of the crystal (*i.e.*, the width). Using this dimension, an average value of $k_a = 5.02 \pm 0.70$ from Equation (3.28) was calculated in this work from the ESEM photographs. Considering the difficulty of measuring the depth of the crystals from the 2D images, this value is in agreement with $k_a = 8.17$ reported by Baldyga *et al.* (1995).

Table 5.4 Dimensions of crystals

N°	Length μm	Width μm	Depth μm	Area μm^2	ka	ϕ_v
1	9.1	4.5	0.5	95.5	4.72	0.87
2	10.0	4.8	0.4	107.8	4.68	0.88
3	9.5	4.9	0.6	110.4	4.60	0.88
4	10.3	5.1	0.4	117.4	4.51	0.89
5	9.8	5.0	0.5	112.8	4.51	0.89
6	9.0	4.3	0.6	93.4	5.05	0.85
7	8.4	3.9	0.5	77.8	5.12	0.85
8	9.0	3.2	0.4	67.4	6.58	0.78
9	11.7	5.2	0.4	135.2	5.00	0.86
10	8.0	3.8	0.6	75.0	5.19	0.85
11	9.6	4.1	0.4	89.7	5.33	0.84
12	8.9	4.0	0.5	84.1	5.26	0.84
13	9.1	3.1	0.5	68.6	7.14	0.76
14	10.1	5.0	0.4	113.1	4.52	0.89
15	9.5	4.5	0.5	99.5	4.91	0.86
16	9.1	4.2	0.5	89.7	5.09	0.85
17	9.8	4.4	0.3	94.8	4.89	0.86
18	8.1	4.0	0.4	74.5	4.66	0.88
19	8.0	4.3	0.5	81.1	4.39	0.89
20	9.2	5.0	0.5	106.2	4.25	0.90

The weigh averaged characteristic length, L_{43}, was obtained as a weigh average of the second largest dimension. This value was estimated as $L_{43} = 4.50 \pm 0.56$ μm. Using the ratio $k_a/k_v = 6$ and Equation (3.30), the sphericity, ϕ_v, was also calculated for each individual crystal analyzed. A weigh average value of $\phi_v = 0.86+0.04$ was estimated from the individual values. By using Equation (3.56), the mean crystal size was determined as $d_{43} = 5.23$ μm. The experimental value obtained for this sample was $d_{43} = 6.64$ μm. This value is 21.23% higher compared with the estimated value from the ESEM photographs. During the sample preparation for the ESEM, in order to disperse the crystals over the aluminum paper, shear stress was applied between the filter and the aluminum paper causing the breakage of some crystals. From the experimental mean crystal size and the estimated L_{43}, $k_a = 7.27$ was calculated, which is very close to the value reported by Baldyga *et al.* (1985), $k_a = 8.17$, for well-formed rectangular crystals.

5.2.7 Final Remarks

In these preliminary experiments, $d_{tube} = 2.3$ mm was determined to be small enough to eliminate the backmixing effect. For Feed II, $t_f = 45$ min was determined to be long enough to eliminate the mesomixing effect. For Feed I, this was also true for impeller speed higher than 200 rpm. However, poor macromixing and agglomeration effects found at low impeller speed made difficult to give a final conclusion about the presence of mesomixing. For $\alpha_v = 50$, $C_{BOM} = 0.0045$ M, and $\eta = 1$, agglomeration effect was not observed. However, this effect was difficult to eliminate at low impeller speed for Feed I. Plexiglas vessel and distillate water were determined to be satisfactory for the precipitation experiments.

5.3 Effect of Operating Conditions

In these experiments, the effect of impeller speed, diameter, and off-bottom clearance on the CSD was determined. The experimental mean crystal size ranged from 5.11 μm to 7.46 μm, and *C.V.* from 0.19 to 0.38. The experimental crystal size distributions observed were unimodal and similar to the Gaussian distribution. All the experiments were carried out in triplicate. The maximum standard deviations were 5.46% and 7.50% for the mean crystal size and *C. V.*, respectively.

5.3.1 Statistical Analysis

The statistical significance of the effects of the two-level factorial design was analyzed to distinguish whether the effects were caused by chance occurrences or were real effects. Three criteria were used to assess the significance of effects: the *95% confidence interval*, *normal probability plot*, and an *evaluation of the extended data*. These criteria are described elsewhere (Box *et al.*, 1978; Zhou and Kresta, 1996a).

Each experiment was replicated three times providing an estimate of the error. These estimates were checked for homogeneity and pooled to provide an overall estimate. All the effects (main effects or interactions) were calculated using the Yate's algorithm (Box *et al.*, 1978). The familiar *Student's t statistic* was used to calculate the 95% confidence interval (95% C.I.) on each effect based on 16 degrees of freedom. When normal probability plots are used, effects that do not fall on a straight line may be considered significant. Using the 95% C.I. and normal probability plot as guides, the differences between experimental runs were evaluated using an extended data obtained by adding one more level to the impeller speed (intermediate level of 300 rpm).

5.3.2 Evaluation of Effects

Figure 5.20 shows the effects of impeller speed (N), diameter (D), and off-bottom clearance-tank diameter ratio (C/T) on mean crystal size when the feed was positioned below the liquid surface, Feed I. Figure 5.20a shows that the effect of N is greater than the 95% C.I. and fall above the normal probability plot regression line. The effect of D is also greater than the 95% confidence interval and fall slightly above the regression line (Figure 5.20a). However, this effect cannot be interpreted separately of N because of the large $N \times D$ interaction. The extended data (Figure 5.20b) show a decrease of the mean crystal size with an increase of impeller speed for $N < 300$ rpm, then increases at high impeller speed. Figure 5.20b also shows that at $N < 300$ rpm, the mean crystal size decreases with an increase of D. For $N > 300$ rpm, the reverse is true, the mean crystal size is higher for the larger impeller size. The 95% C.I., the normal probability plot, and the evaluation of the extended data all show a slight effect of C/T. Except for the low impeller speed, numerical predictions slightly under-predict the experimental mean crystal size values.

Figure 5.21a shows the normal probability plot of the effects of N, D, and C/T on $C.V.$, and Figure 5.21b shows the extended experimental results for Feed I. As deduced from the 95% C.I., the normal probability plot (Figure 5.21a), and the evaluation of the extended data (Figure 5.21b), only the effect of the impeller speed, N, on $C.V.$ is significant. At $N < 300$, $C.V.$ decreases significantly with an increase of N, and at higher impeller speed, $C.V.$ remains almost constant. Similarly to the preliminary experiments, except for the low impeller speed, numerical predictions overestimate the experimental values. This was attributed to the sensitivity of $C.V.$ to the value of the 5^{th} moment.

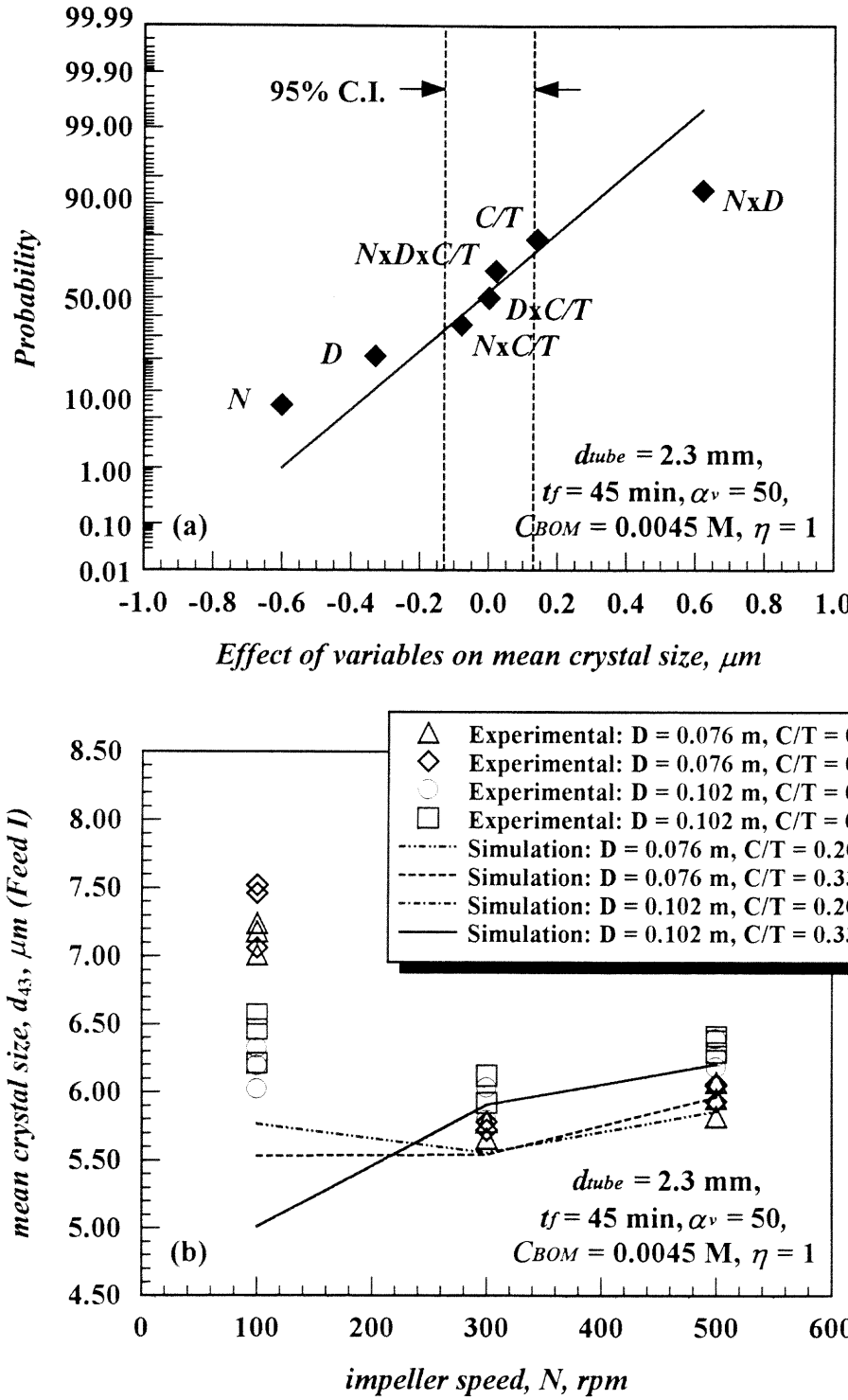

Figure 5.20 Effect of N, D, and C/T (Feed I) on mean crystal size: (a) normal probability plot; and (b) evaluation of extended data

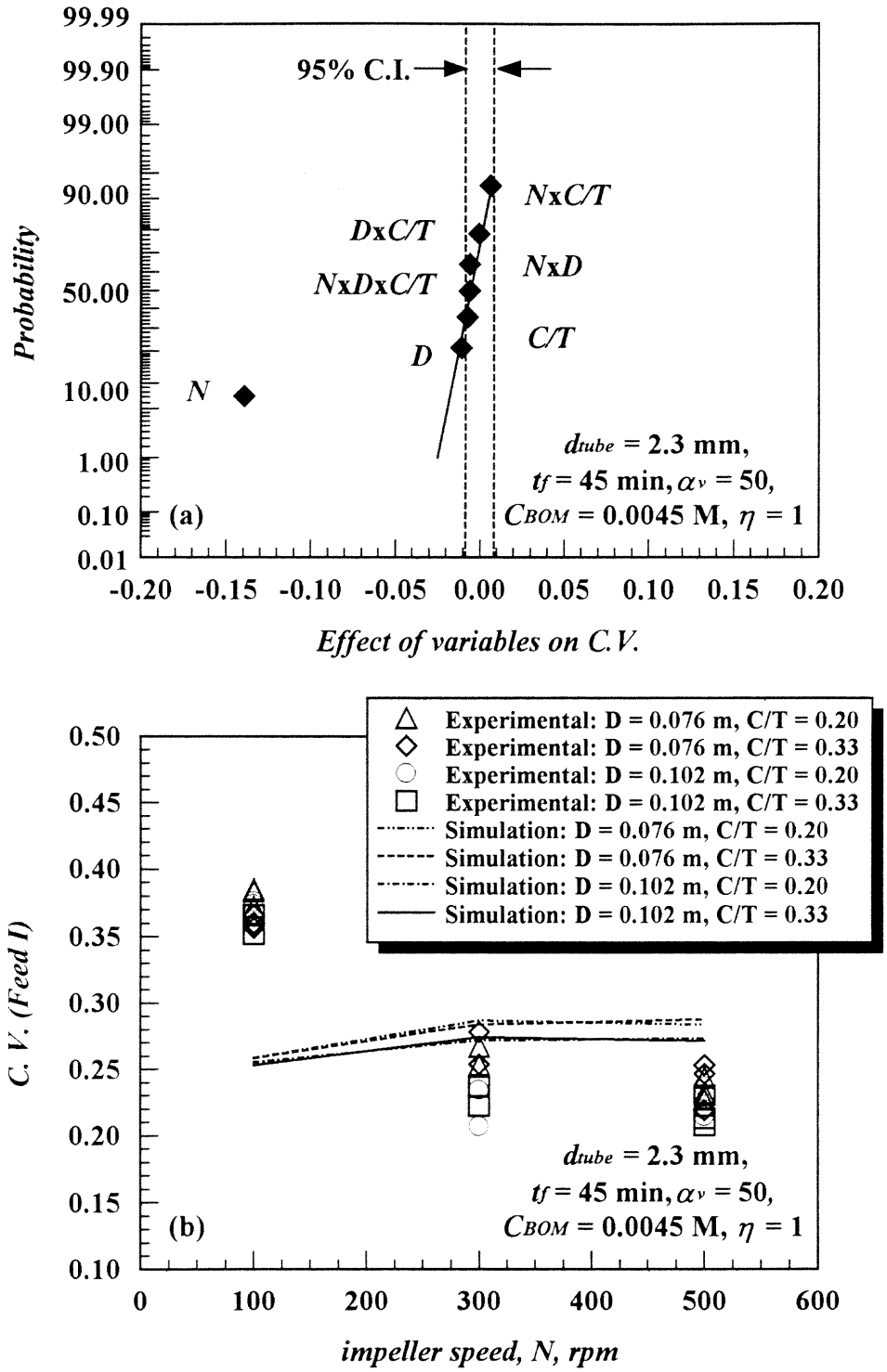

Figure 5.21 Effect of N, D, and C/T (Feed I) on $C.V.$:
(a) normal probability plot; and (b) evaluation of extended data

Figure 5.22 shows the effects of N, D, and C/T on mean crystal size when the feed was positioned above the impeller, Feed II. The 95% C.I. and the normal probability plot (Figure 5.22a), and the evaluation of the extended data (Figure 5.22b), all show that N has a significant effect on the mean crystal size followed by the effect of D. The effect of D is slightly greater than the 95% C.I. and falls slightly below the regression line. In both cases, the mean crystal size increases with N or with D. The evaluation of the extended data shows a slight increase of the mean crystal size when the off-bottom impeller clearance decreases, however, the 95% C.I. and the normal probability plot both show that there is no significant effect of C/T. Due to the underestimation of ε, numerical predictions under-predict the experimental mean crystal size values.

Figure 5.23 shows the effects of N, D, and C/T on $C.V.$ for Feed II. The effect on $C.V.$ of both N and D are smaller than the 95 C.I. but fall in the regression line (Figure 5.23a). An inspection of the extended data (Figure 5.23b) shows an increase of the $C.V.$, at low speed (100 rpm), for the smaller impeller size. Therefore, there is an interaction between these two variables, $N \times D$. The effect of the interaction $N \times D$ is slightly greater than the 95% C.I. and falls slightly above the regression line. $C.V.$ decreases with the increase of N for the small D, and remains constant for the large size. Again, numerical predictions overestimate the experimental $C.V.$ values.

Appendix A (ESEM Photographs) shows the photographs of the crystals produced in the two-level factorial design experiments (Figure A.11-Figure A.26). For Feed I and N = 100 rpm, the crystals produced were amorphous, some dendritic crystals could be observed (Figure A.11, Figure A.15, Figure A.19 and Figure A.23). For the other experiments, well-formed rectangular crystals were produced.

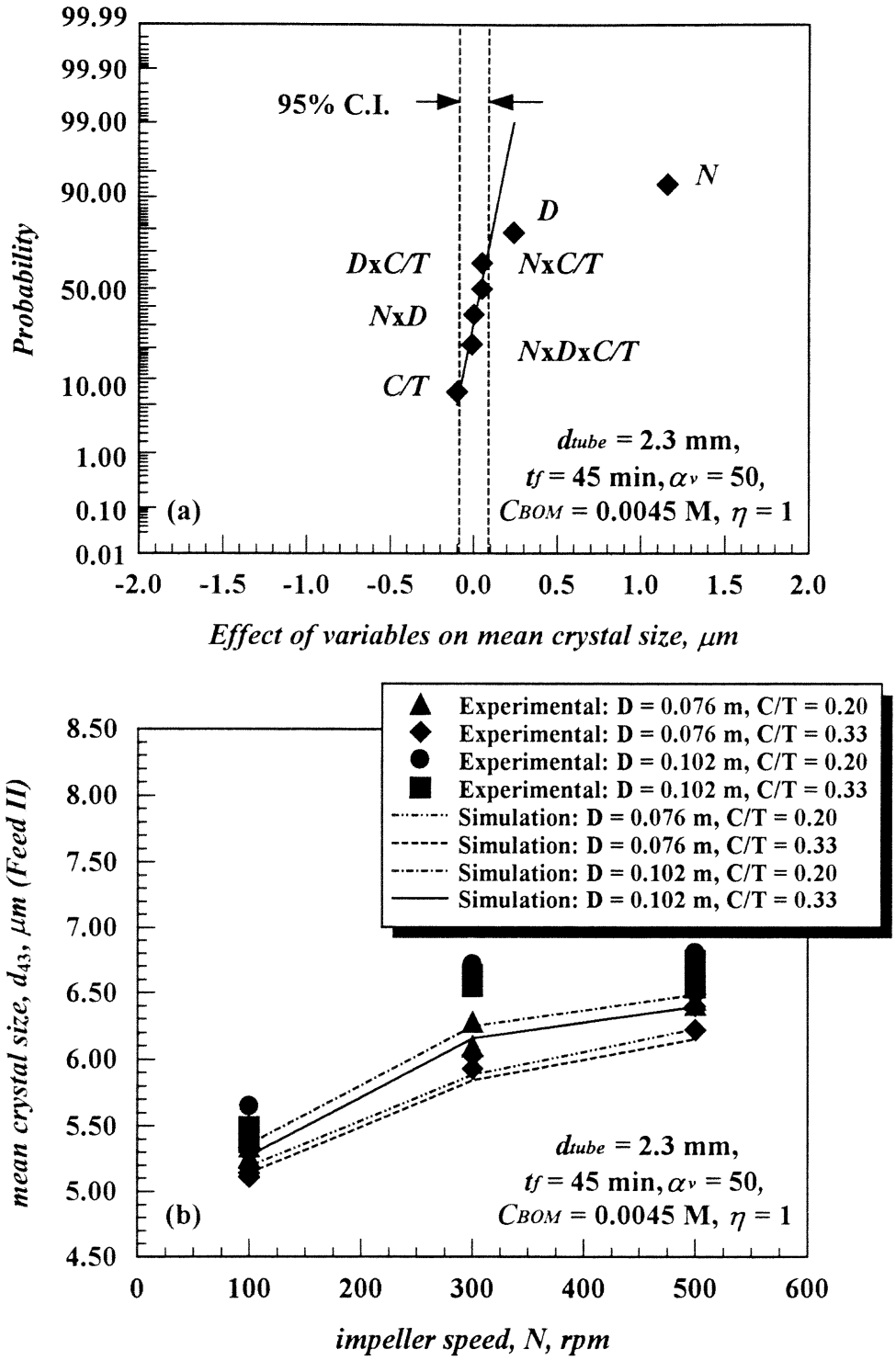

Figure 5.22 Effect of N, D, and C/T (Feed II) on mean crystal size: (a) normal probability plot; and (b) evaluation of extended data

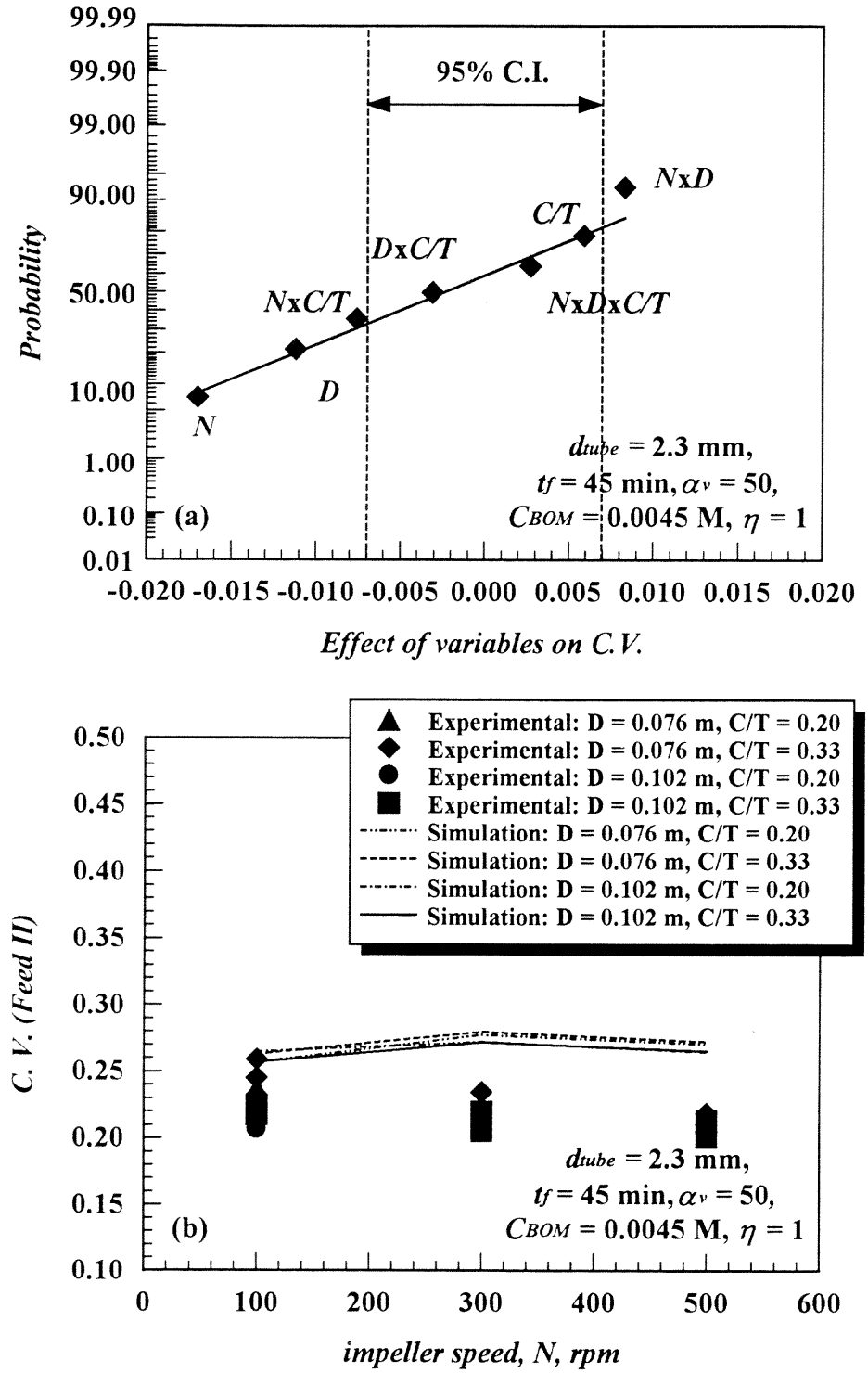

Figure 5.23 Effect of N, D, and C/T (Feed II) on $C.V.$:
(a) normal probability plot; and (b) evaluation of extended data

5.3.3 Effect of Impeller Speed

The effect of N is shown in Figure 5.24 for the 0.076 m and 0.102 m impeller sizes in the 0.292 m vessel. When the feed was located above the impeller, Feed II, experimental results and simulation prediction show that the mean crystal size increased monotonically with N. This can be easily explained by the micromixing model: since the turbulence energy dissipation rate is proportional to the impeller speed to the third power (Zhou and Kresta, 1996a), then increasing N also increases the engulfment rate, diluting the local supersaturation level and producing larger mean crystal sizes, as experimentally observed here (Figure 5.24a). Baldyga *et al.* (1995) and Phillips *et al.* (1999) also observed the same experimental behavior. Åslund and Rasmuson (1992) and Zauner and Jones (2000a) observed a maximum in the mean crystal size plotted against impeller speed. The decrease at higher speed was attributed to secondary nucleation and breakage not detected in the present work at this scale (T = 0.292 m). *C.V.* was found to be independent of N for the Feed II case (Figure 5.24b).

When the feed was located below the liquid surface, Feed I, a minimum in the mean crystal size appeared. The location of the minimum point of this experimentally observed phenomenon was corrected predicted by the model, at least for the 0.076 m impeller case. This behavior cannot be rationalized through micromixing alone. Tosun (1988) and Chen *et al.* (1996) obtained similar experimental results. Chen *et al.* (1996) attributed their results as well as Tosun (1988) results to the complex interaction between macromixing and micromixing. For Feed I and at 100 rpm, *C.V.* was much higher than at higher speeds, indicating that a different phenomenon was taking place as discussed above (i.e., agglomeration). Similar experimental results were obtained by Tosun (1988).

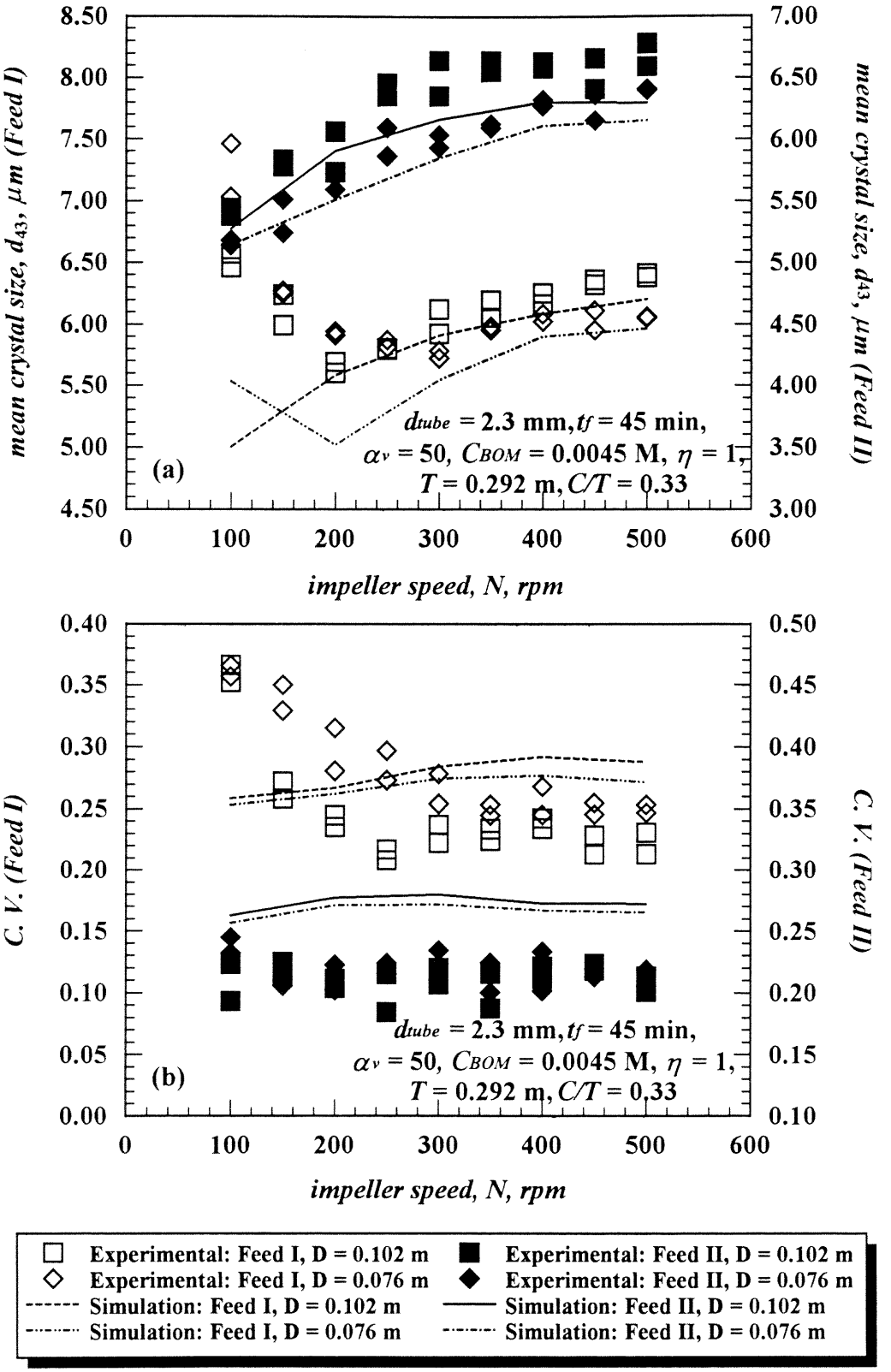

Figure 5.24 Effect of N at constant C/T and different D values on: (a) mean crystal size; and (b) $C.V.$

5.3.4 Effect of Impeller Diameter

The effect of the impeller diameter, D, is also shows in Figure 5.24. When the feed was located above the impeller, the mean crystal size increased with D. This can also be easily explained by the micromixing model: since the turbulence energy dissipation rate is proportional to the impeller diameter to the fifth power (Zhou and Kresta; 1996a), then increasing D also increases the engulfment rate, diluting the local supersaturation level and producing larger mean crystal sizes, as experimentally observed here.

When the feed was located below the liquid surface, a similar trend was observed, at least for $N > 200$ rpm. At lower N values, the mean crystal size increased with decreasing of D. This can be attributed to the lower turbulence level produced and the increase of the macromixing and agglomeration effects.

5.3.5 Effect of Impeller Off-Bottom Clearance

Figures 5.25 and 5.26 report the effect of impeller clearance, expressed in terms of C/T and C/D, respectively. For Feed II, the mean crystal size slightly increased with decreasing the off-bottom impeller clearances. $C.V.$ was not affected. When the PBT impeller is away from the base, as already mentioned, the downward liquid flows continuously changing its direction, so that the liquid flows along the base in the horizontal direction before it rises along the wall. As the impeller clearance decreases, the change in direction becomes sharper and more energy is locally dissipated. The increase in the turbulent energy dissipation rate may cause the slight increase in the mean crystal size observed. However, the small difference observed requires further investigation. The results obtained for C/T and C/D are qualitatively similar.

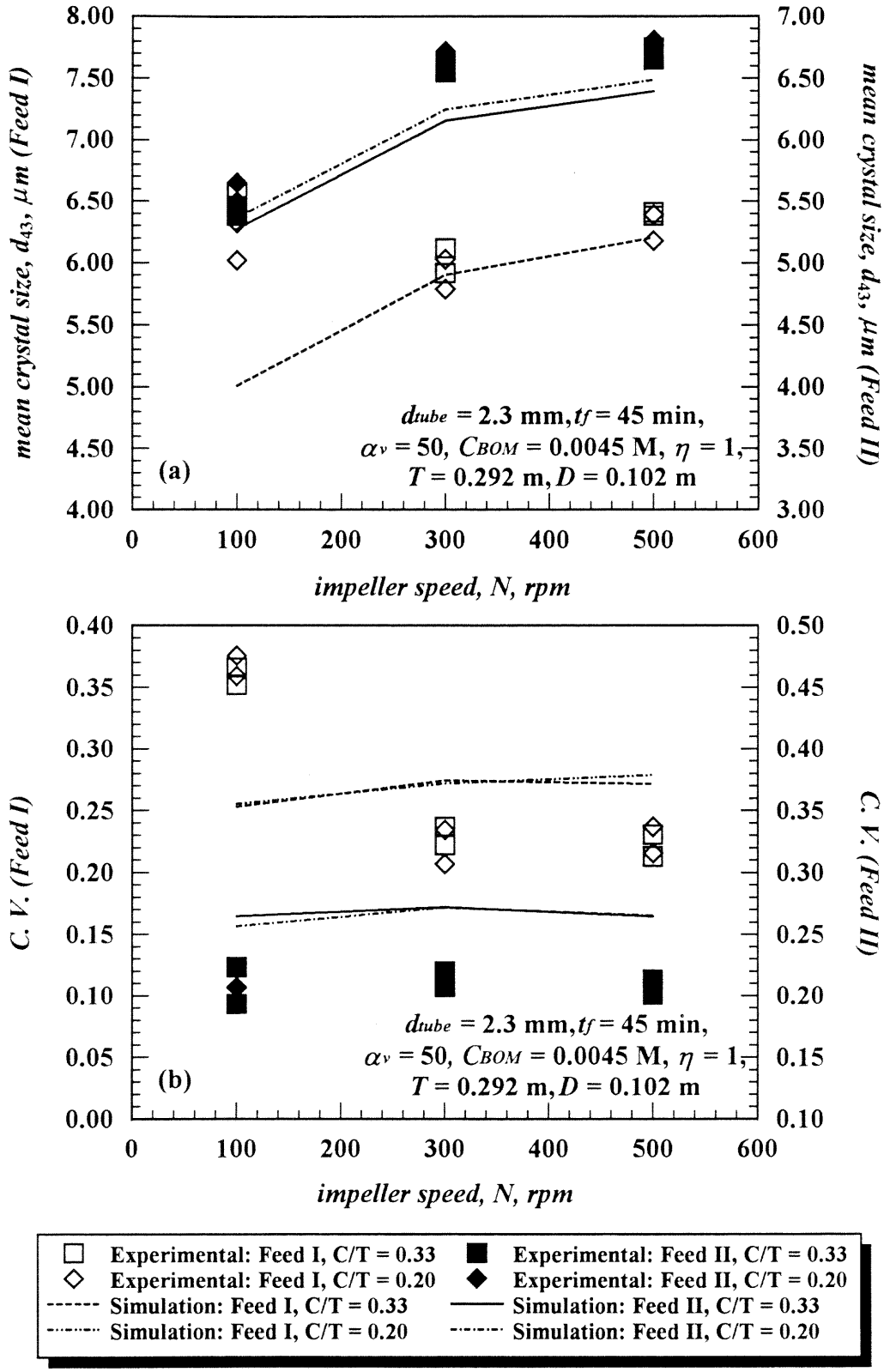

Figure 5.25 Effect of N at constant D and different C/T values on: (a) mean crystal size; and (b) $C.V.$

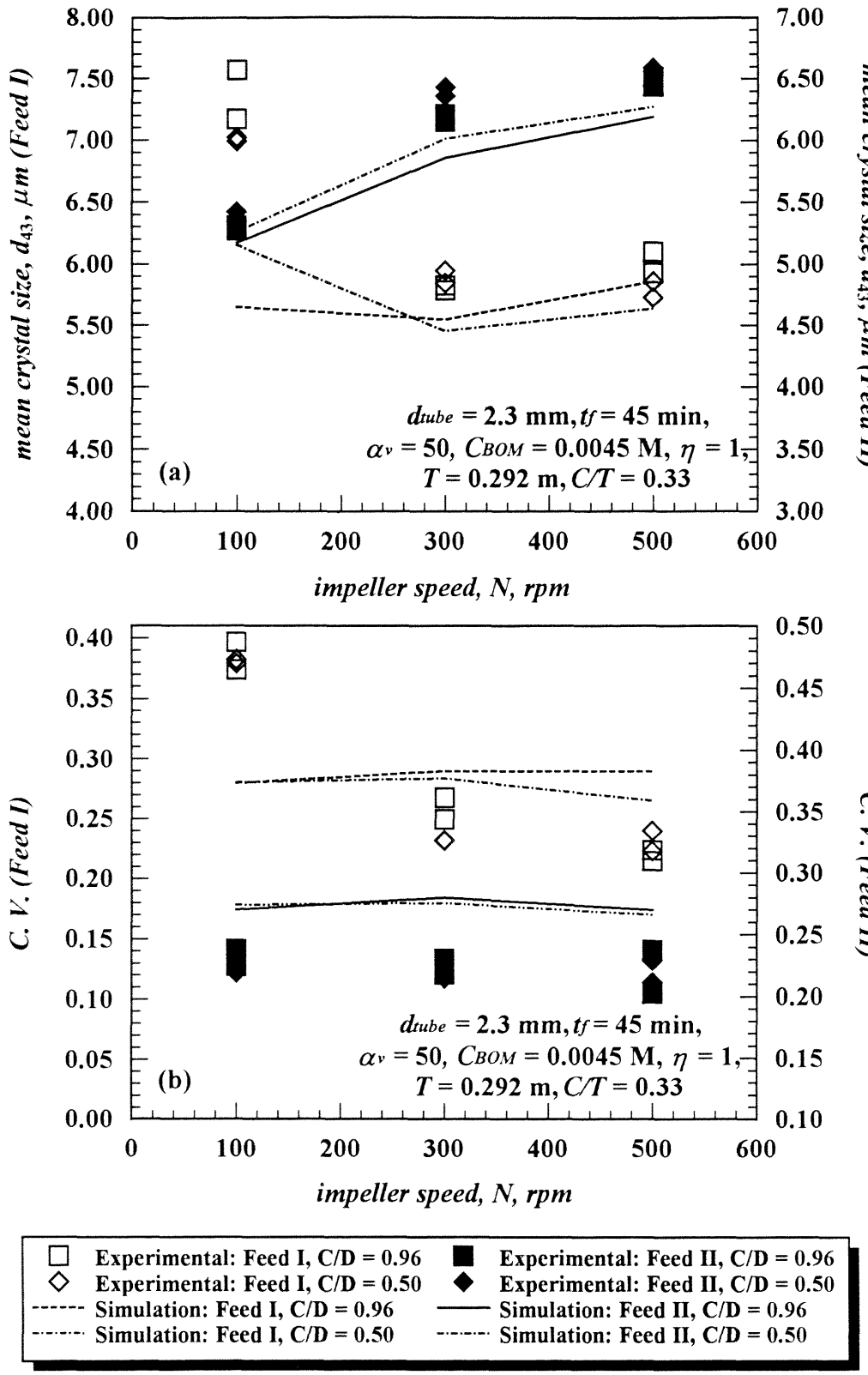

Figure 5.26 Effect of N at constant D and different C/D values on: (a) mean crystal size; and (b) $C.V.$

The situation for Feed I is more complex, since the recirculation in the upper portion of the reactor (where the feed was located) also plays an important role. The net result is the complex behavior observed experimentally, which is also partially predicted by the model (Figure 5.25a). Similarly to Feed II, the results obtained at the two levels of *C/D* are qualitatively similar to the results obtained at the two levels of *C/T*. Therefore, there is no difference, as far as the effect of the impeller off-bottom clearance on the CSD is considered, to define this variable as *C/T* or *C/D*.

5.3.6 Effect of Feed Position

Except for the results obtained at $N < 200$ rpm, all the results show that placing the feed in the impeller region produced mean crystal sizes some 10% larger than when the feed was below the liquid (all other things being equal), as well as resulting in a more homogeneous CSD, as indicated by lower *C.V.* values. Feeding near the impeller increases the turbulent intensity and reduces the time to incorporate (engulf) material from the surrounding liquid into the reacting zone. This, in turn, contributes to reduce more rapidly the local level of supersaturation (ΔC), which determines the type of nucleation (Equations 3.20 and 3.21). Therefore, the faster the supersaturation level drops, the faster homogeneous nucleation is replaced by the much slower heterogeneous nucleation process. Hence, fewer and larger crystals are produced before the crystals are exposed to a lower ΔC value where crystal growth dominates, as experimentally observed here when the feed location is moved from the liquid surface to the impeller region. The decrease in *C.V.* has been related to shorter periods of fast nucleation, which can be achieved by increasing N and/or changing the feed position (Phillips *et al.*, 1999).

5.4 Supersaturation Ratio Profiles

As explained before, the supersaturation ratio in the blob region was numerically calculated as a function of time, as the sub-droplets initially constituting the blob became dispersed through out the reactor. Such supersaturation ratio profiles can be used to elucidate the results observed under different operating conditions.

Figure 5.27 shows the predicted supersaturation ratio profiles for different volume ratios. In general, these curve show that the supersaturation ratio rapidly increased with time, reached a maximum, and then decreased more or less slowly. The horizontal line delimitates the regions of homogeneous and heterogeneous nucleation. For both feed additions (Figure 5.27a and 5.27b, for Feed I and II, respectively), increasing the volume ratio up to $\alpha_v = 60$ resulted in a more prolonged time period during which the conditions for homogeneous nucleation predominated, thus producing smaller crystals. The supersaturation curves for $\alpha_v > 60$ showed very high maxima ($S_a > 1600$), corresponding to the formation of very high number of nuclei, and hence a rapid drop in the final crystal size, as confirmed by the data and model predictions of Figure 5.17. It is important to notice that the comparison of the effect of volume ratio on supersaturation profile was made by keeping constant the mean initial concentrations and stoichiometry ratio.

The effect of mean initial concentration on the supersaturation ratio profiles is shown in Figure 5.28. The same pattern for the volume ratio is observed for the mean initial concentration. However, the same interpretation can not be made, since the different profiles correspond to different amount of reactants (different mean initial concentration). Figure 5.28a and 5.28b, for Feed I and Feed II, respectively, show that increasing the mean initial concentration up to $C_{BOM} = 0.006$ M increased the value of the

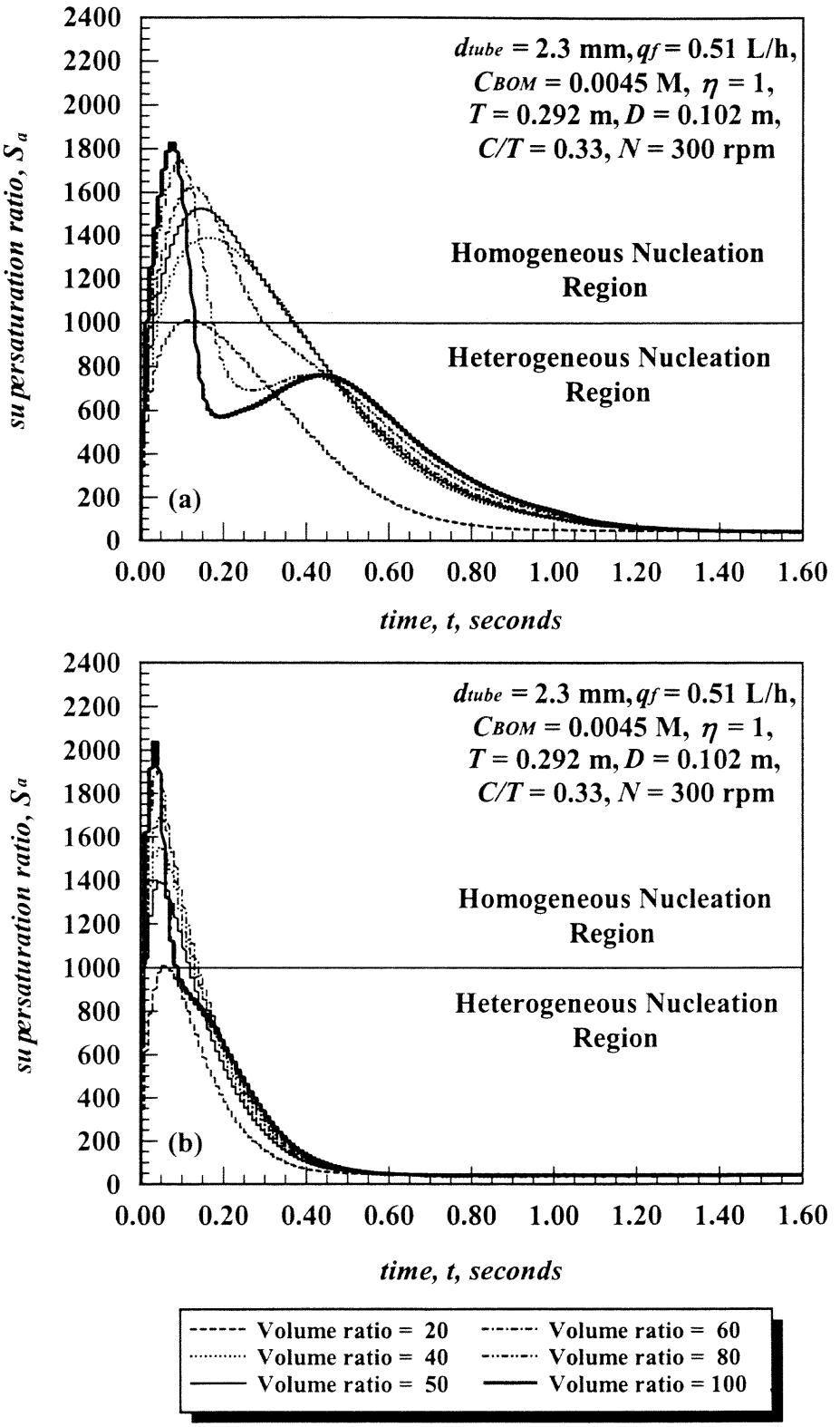

Figure 5.27 Effect of volume ratio on supersaturation ratio profile: (a) Feed I; and (b) Feed II

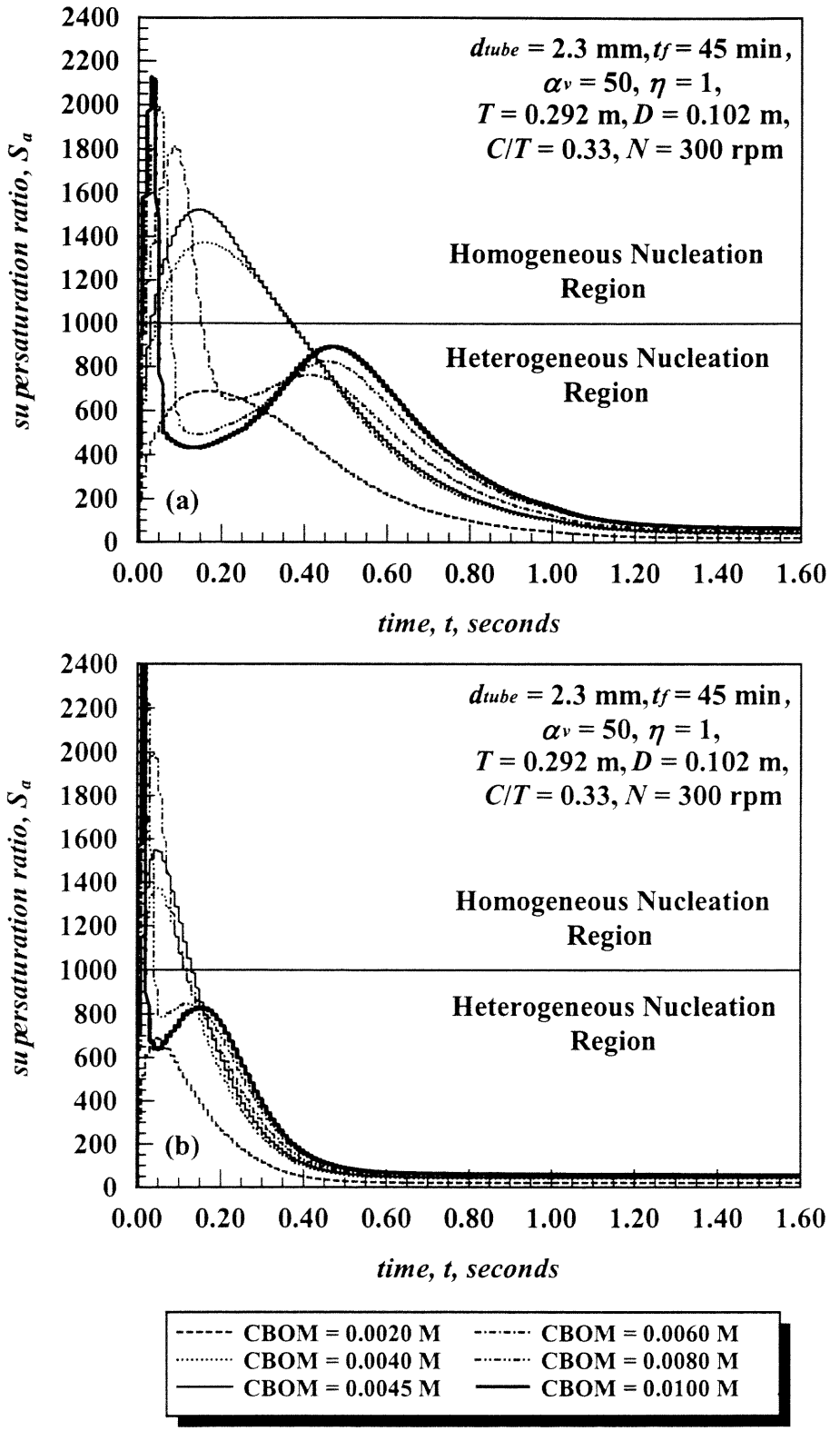

Figure 5.28 Effect of mean initial concentration on supersaturation ratio profile: (a) Feed I; and (b) Feed II

maxima in the supersaturation ratio. This increase in the supersaturation ratio increases the rate of crystal growth more than the nucleation rate, producing larger crystal sizes. For $C_{BOM} > 0.006$ M, the supersaturation curves showed very high maxima ($S_a > 1600$), resulting in a significant increase in the nucleation rate and reducing significantly the mean crystal size. The supersaturation level over which the mean crystal size is reduced significantly is not necessarily the critical value in which the mechanism of heterogeneous nucleation changes to homogeneous nucleation ($S_a = 1000$).

Figure 5.29 shows the effect of the stoichiometry ratio on the supersaturation ratio profiles. Since the amount of reactant changes, a similar interpretation as the effect of mean initial concentration can be applied to this case. For both Feed I and Feed II, Figure 5.29a and 5.29b, respectively, increasing the stoichiometry ratio up to $\eta = 1.0$ increased the maxima in the supersaturation ratio, increasing the rate of crystal growth more than the nucleation rate and producing larger crystal sizes. For $\eta > 1.0$ the supersaturation curves showed very high maxima ($S_a > 1600$), resulting in a high increase of the nucleation rate and reducing significantly the mean crystal size.

Figure 5.30 shows the supersaturation ratio profiles for different impeller speeds. Any of the supersaturation curves shows a relative high maxima ($S_a < 1600$), therefore the significantly decrease in size observed in previous cases was not observed here. For both Feed I and Feed II, Figure 5.30a and 5.30b, respectively, increasing the impeller speed decreased the period of fast nucleation producing larger mean crystal sizes. A comparison between the two feed positions also shows that increasing the turbulence level by moving the feed position from liquid surface to the impeller decreased the period of fast nucleation producing larger mean crystal sizes.

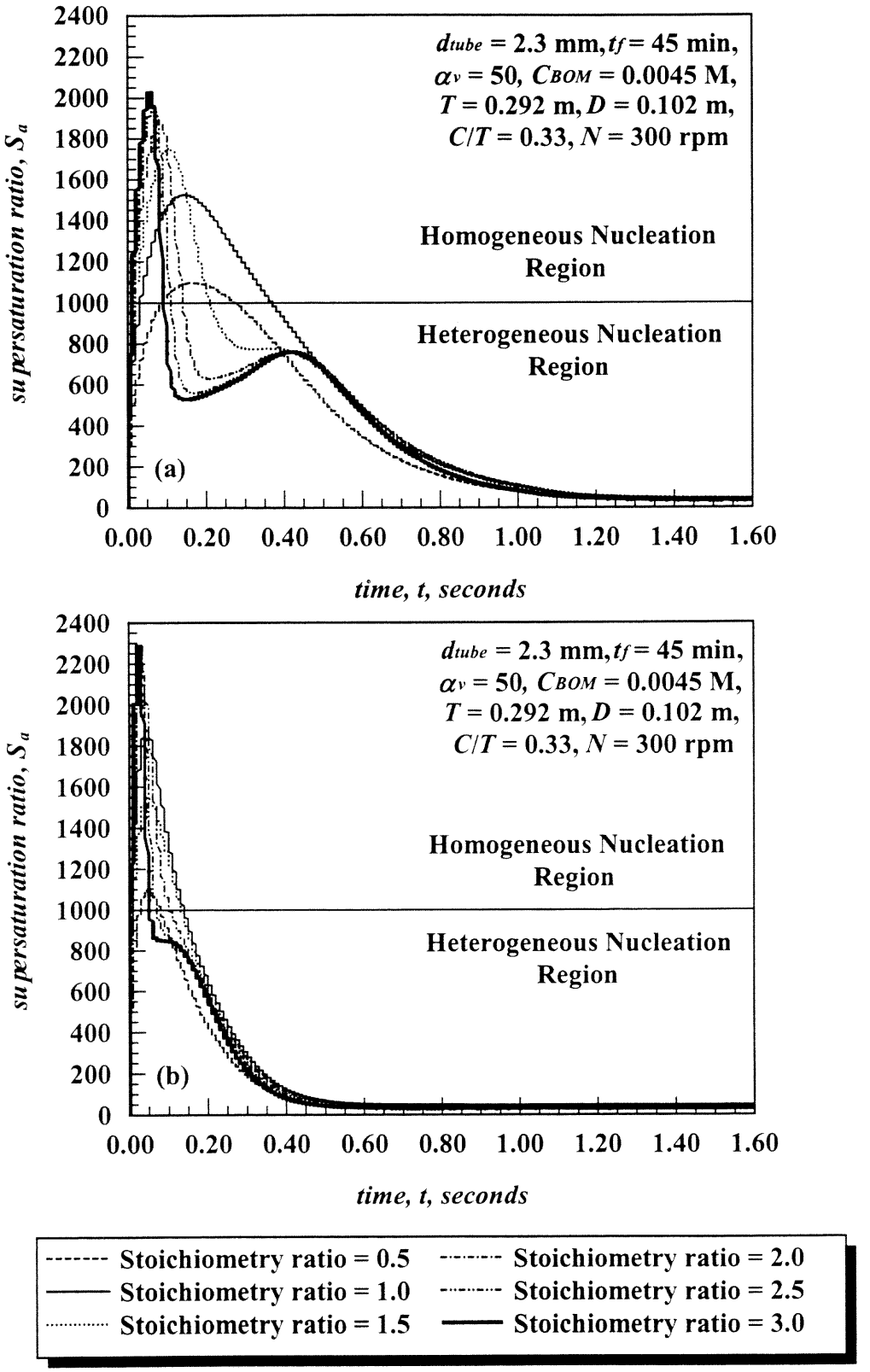

Figure 5.29 Effect of stoichiometry ratio on supersaturation ratio profile: (a) Feed I; and (b) Feed II

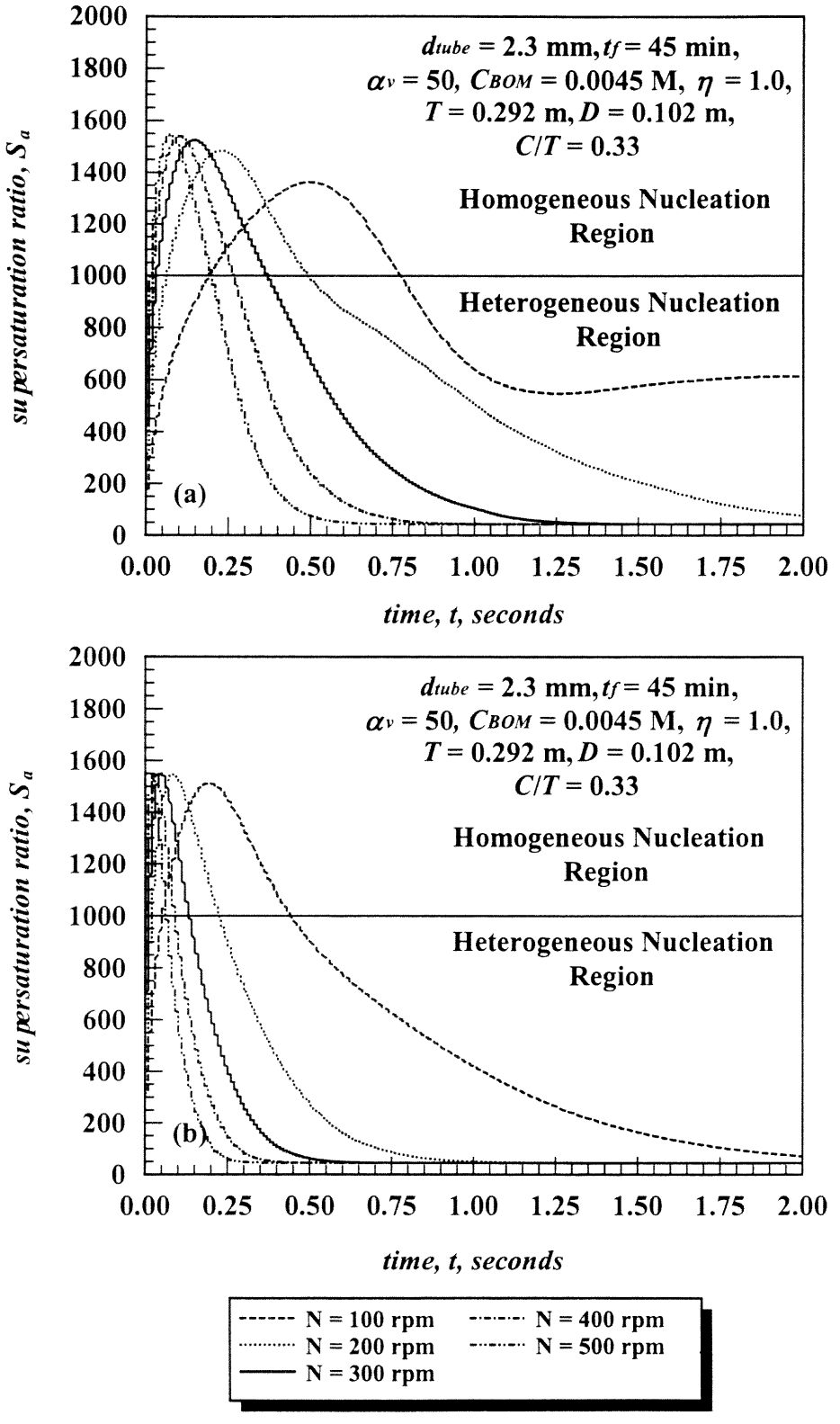

Figure 5.30 Effect of impeller speed on supersaturation ratio profile: (a) Feed I; and (b) Feed II

5.5 Effect of Vessel Scale

Figure 5.31 and Figure 5.32 show the effect of vessel scale on mean crystal size and *C.V.* for Feed I and Feed II, respectively. Since the larger scale (T = 0.584m) requires additional explanation, the following discussion will consider only the smaller vessel scales (T = 0.219 m and T = 0.292 m). For Feed I, Figure 5.31a shows an increase in the mean crystal size with the vessel scale for $N \geq 200$ rpm. At $N < 200$ rpm, the inverse is true, the mean crystal size decreases with the vessel scale. The conditions of operation were chosen to operate in the micromixing controlled regime. However, as explained before, low energy dissipation rates obtained at low impeller speed when feeding below the liquid surface, promote macromixing and agglomeration effects increasing the mean crystal size. Figure 5.31b shows that *C.V.* is not affected for the increase in vessel capacity for the smaller scales. For Feed II, Figure 5.32a shows an increase of the mean crystal size with the vessel capacity. Figure 5.32b shows that *C.V.* was not affected by the increase in vessel scale. Appendix A shows the effect of vessel scale on crystal morphology. For T = 0.219 m, well-formed rectangular crystals were observed for Feed I (Figure A.27) and Feed II (Figure A.28) when agglomeration effect was not present.

For T = 0.584 m and both feed positions, the mean crystal size increases with the increase of the impeller speed up to N = 200 rpm and then decreases. Analysis of ESEM photographs shows that the decrease is due to the breakage of crystals. *C.V.* decreases with the impeller speed. This also gives indication of the breakage of crystals which narrows the CSD leading to smaller *C.V.* ESEM photographs (Appendix A) show that at the larger scales, well-formed rectangular crystals were produced but the breakage of the crystals was observed for both Feed I (Figure A.29) and Feed II (Figure A.30).

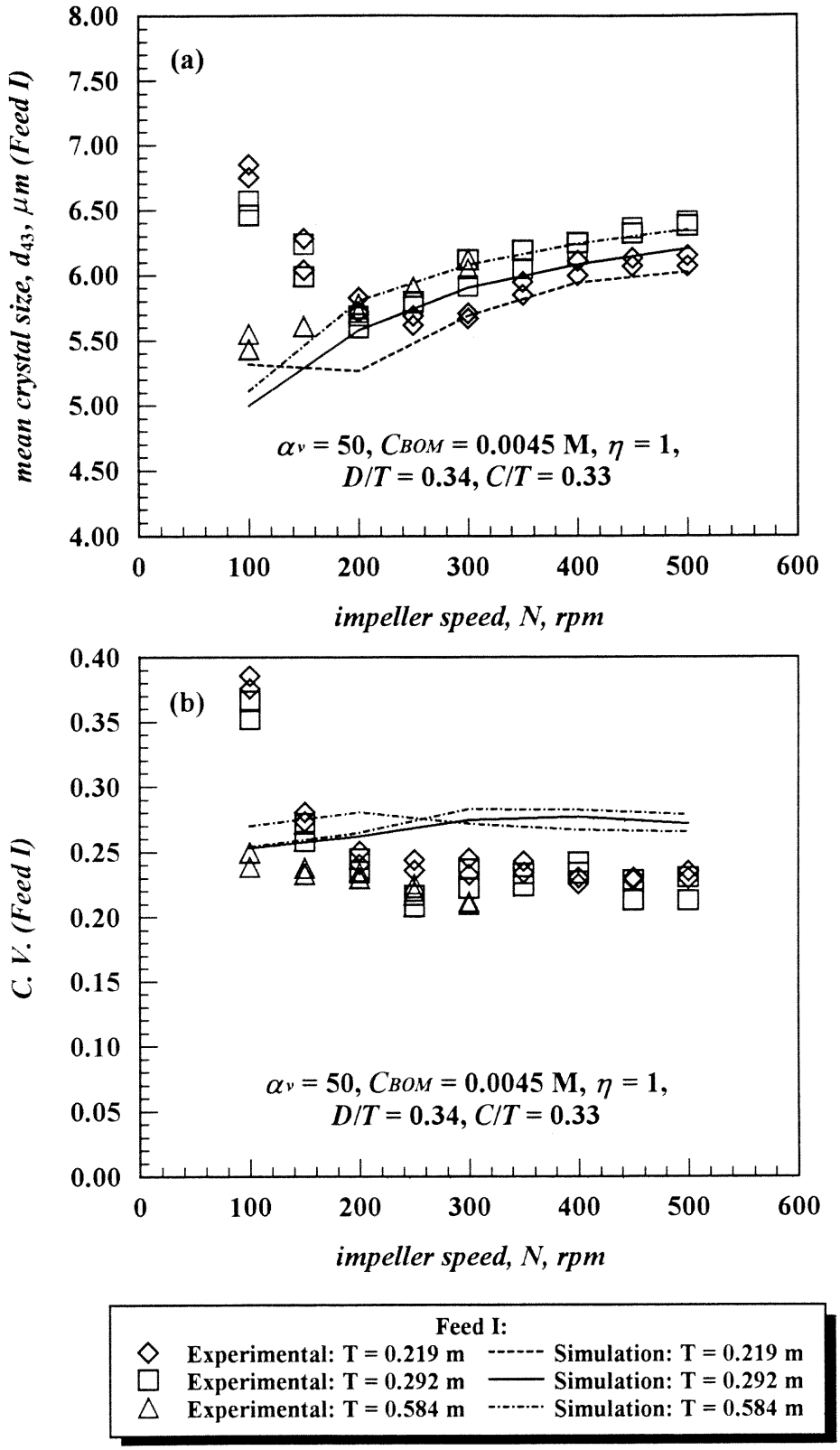

Figure 5.31 Effect of impeller speed at different vessel scales (Feed I) on: (a) mean crystal size; and (b) *C.V.*

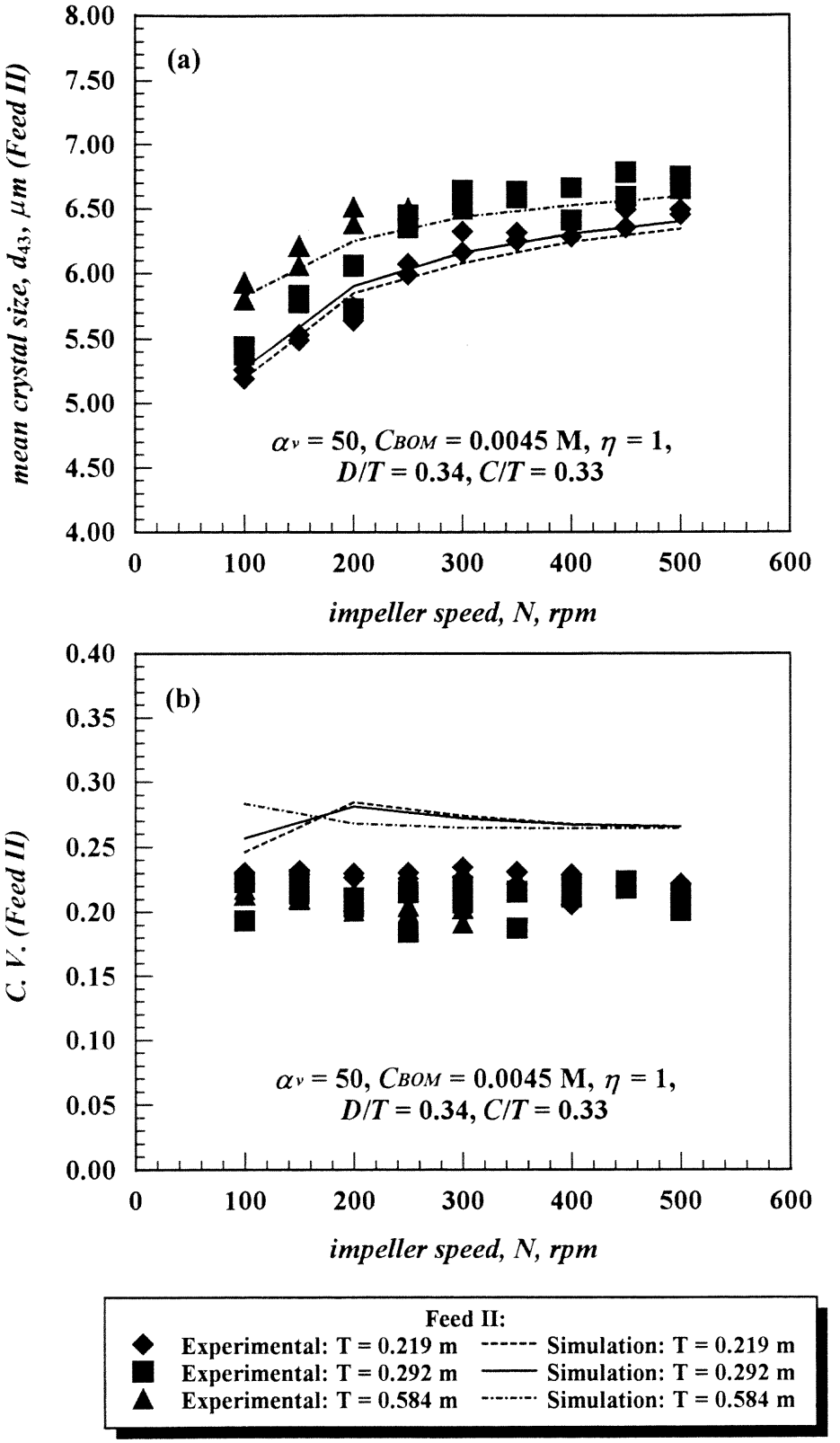

Figure 5.32 Effect of impeller speed at different vessel scales (Feed II) on: (a) mean crystal size; and (b) *C.V.*

Since scale-up with constant $P/V_{reactor}$ is equivalent to scale-up with constant N^3D^2 (Equation 2.64), the predicted and experimental mean crystal sizes were plotted against N^3D^2 in Figure 5.33. For Feed I (Figure 5.33a), scale-up with constant power input per unit volume seems to be appropriate for the smaller scales, $T = 0.219$ m and $T = 0.292$ m. For the larger scale, numerical simulation and experimental results show that smaller crystals were obtained. A likely explanation for the reduction in the mean crystal size at the larger scale is related to what was termed "further localization" of the reaction zone in the larger vessels (Rice and Baud, 1990; Falk *et al.*, 1994, Bourne and Yu, 1994). For a given $P/V_{reactor}$, the larger vessel was operated at lower speeds and had a longer circulation time than the smaller vessels. The mixing-precipitation zone after injection traveled through a smaller fraction of the vessel volume in the larger scale and remained in the zone of lower values of ε longer than in the case of the smaller vessel scales. For Feed II (Figure 5.33b), numerical simulation and experimental results show that scale-up with constant power input per unit volume seems to be appropriate for all the scales. The "further localization" of the reaction was not observed when the mixing-precipitation zone dispersed through a region where ε was large (Bourne and Yu, 1994).

The classical scale-up rule of constant $P/V_{reactor}$ may be applied to scale-up of micromixing only for the case of feeding above the impeller plane. For feeding below the liquid surface, identical crystal size distributions will not generally be obtained during scale-up by applying the rule of constant $P/V_{reactor}$ because of the spatial inhomogeneity of ε and the variation of the trajectory of the mixing-precipitation zone during scale up even using homologous feed positions for different scales. However, the numerical simulation correctly predicts the reduction of the mean crystal size for the larger scale.

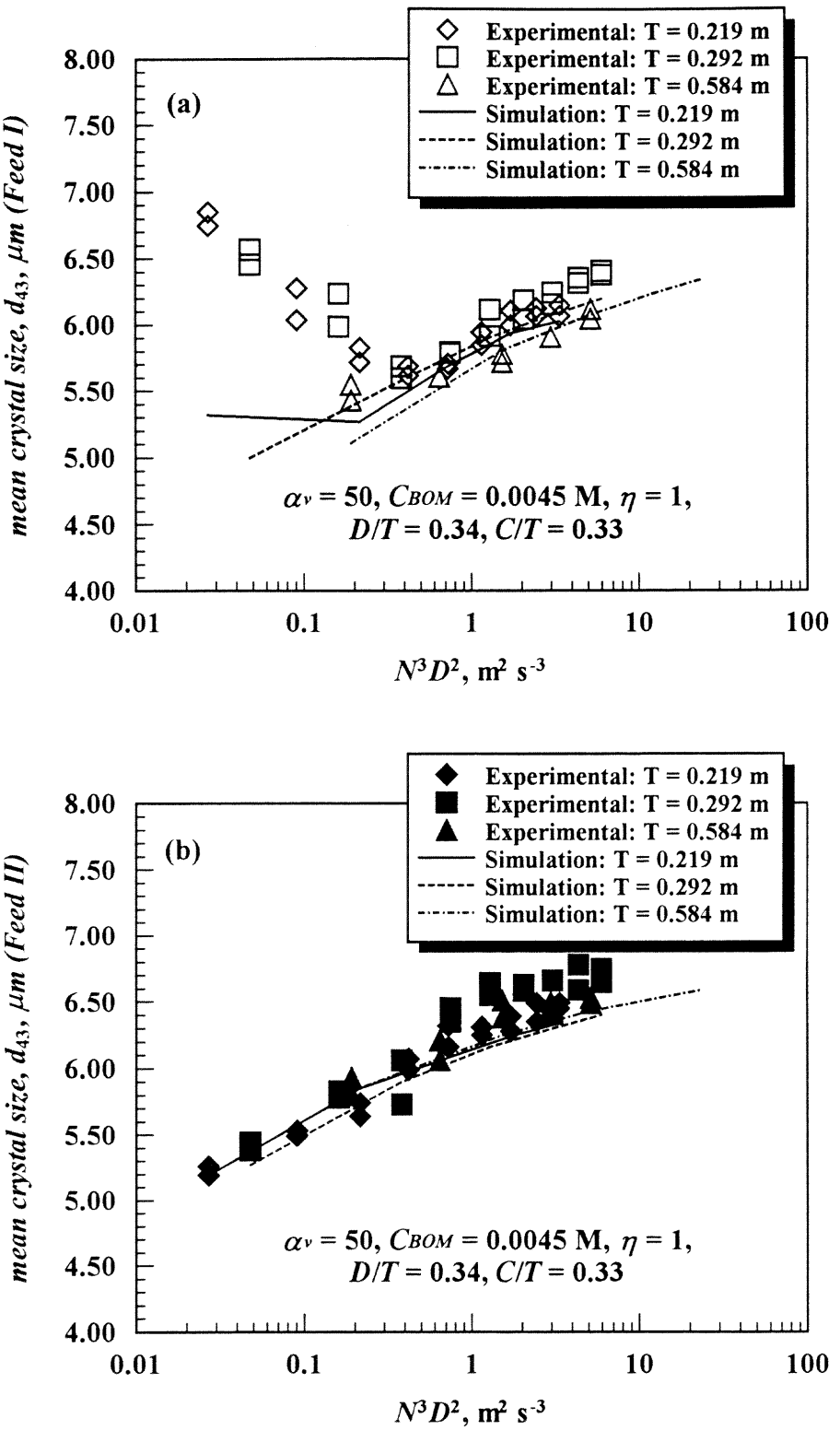

Figure 5.33 Scale-up with constant power input per unit volume: (a) Feed I and; (b) Feed II

5.5 Discussion

Based on the micromixing controlling mechanism, on the competition between nucleation (heterogeneous and homogeneous) and crystal growth, and with the knowledge of the flow field developed by the six-blade 45° pitched-blade turbine in the tank, the experimental results obtained can be interpreted as follows.

A blob of sodium sulfate fed from the feeding point rapidly reaches the velocity of the bulk and follow the circulation path, flowing through environments where the turbulence properties (scale of turbulence, energy dissipation rate) vary. The blob incorporates (by engulfment) the environment liquid with the barium chloride initially present in the reactor. The rate of incorporation is proportional to the engulfment rate defined in Equation (2.37). This parameter varies with time (or position) inside the tank. The sulfate and barium ions present in the blob (mixing-precipitation zone) build the supersaturation level, and nucleation and growth compete for the material. Initially the supersaturation level starts to increase until it reaches a maximum value, then decreases with the consumption of sulfate ions in the mixing-precipitation zone. In the initial stages growth dominates against the heterogeneous nucleation until a certain level of supersaturation ratio is reached. From this level, the very fast homogeneous nucleation dominates. This level of supersaturation is not necessarily the critical value at which the mechanism of heterogeneous nucleation changes to homogeneous nucleation (S_a = 1000). Micromixing rate increases with the increase of the turbulent energy dissipation (feeding above the impeller plane, increasing the impeller speed, etc.). However, intense micromixing rate can dilute the supersaturation built in the mixing-precipitation zone, i.e., the time in which the mixing precipitation zone is exposed to the high levels of

supersaturation in the homogeneous nucleation regime decreases, producing larger crystals. This means that in incomplete mixing situations, very high intermediate local supersaturation may be achieved (Marcant and David, 1991). The order of the nucleation step is usually so high that even small dilution of the supersaturated solution often practically stops the nucleation process (Baldyga *et al.* 1995). During the process, as the nuclei are formed, the mean ionic concentration drops quickly and the available surface area rises, and growth predominates eventually.

For feeding above the impeller, increasing the impeller speed and the impeller diameter increases the energy dissipation rate, and then the local micromixing rate, reducing the nucleation and producing larger crystals. Decreasing the off-bottom impeller clearance, also increases the energy dissipation rate; however, the difference in crystal size observed with different impeller clearances falls within the experimental error. *C.V.* does not seem to be affected by any of these variables. For feeding below the liquid surface, at low impeller speeds, the mean crystal size and *C.V.* significantly decrease with impeller speed and impeller diameter. This is contrary to the effect found for feeding above the impeller. Less turbulent flow regime and macromixing and agglomeration effects present in the bulk below the liquid surface change the pattern found before. Low supersaturation in the engulfment zone results in low nuclei density and poor mixing with the bulk produces a broad distribution. Figure 5.34 shows the comparison between experimental data and numerical prediction of the mean crystal size. The numerical prediction underestimates the experimental mean crystal size due to the under-prediction of the local energy dissipation rate. At low impeller speed, there is a large disagreement due to the macromixing and agglomeration effects.

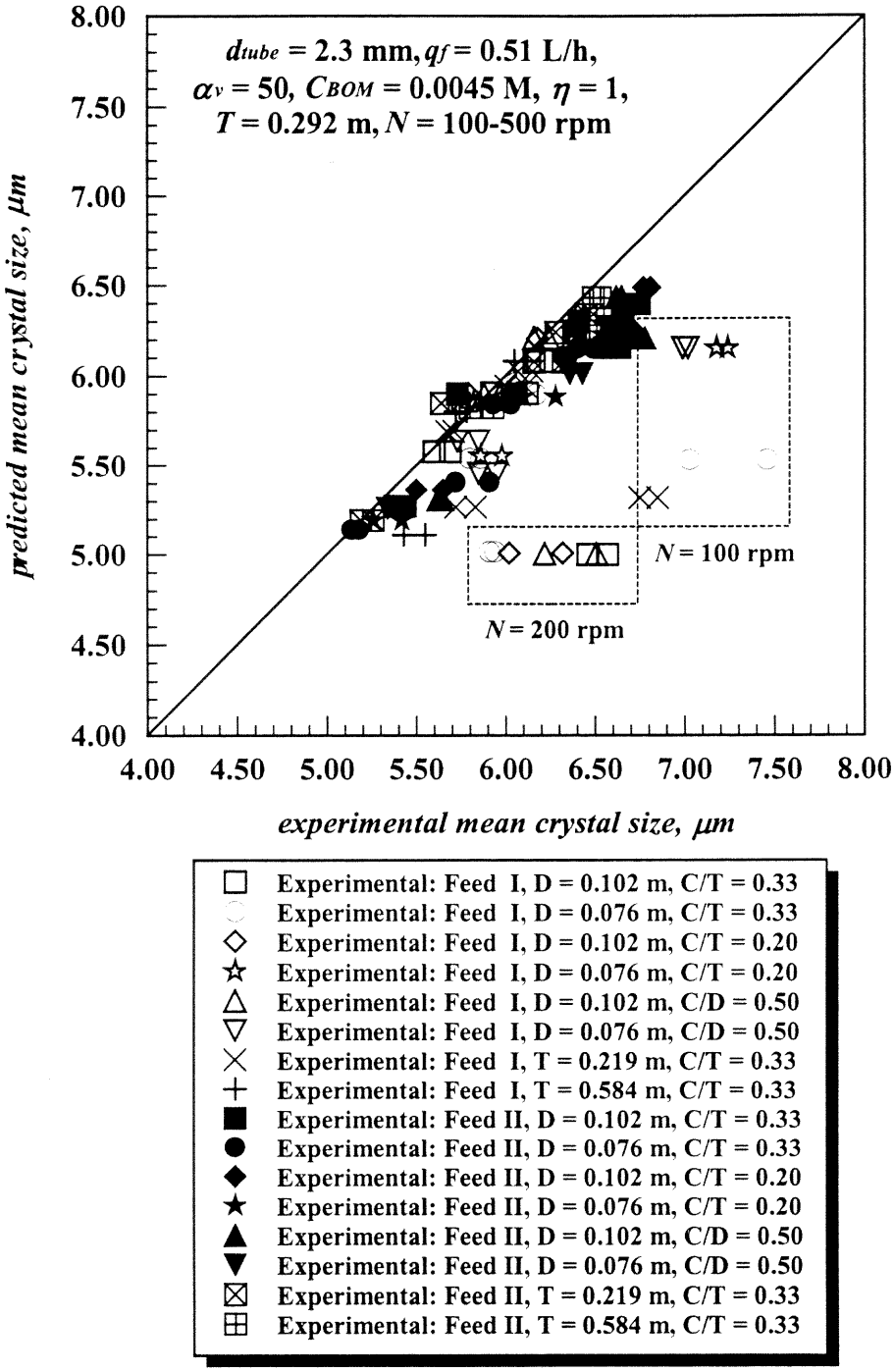

Figure 5.34 Comparison between experimental and predicted mean crystal size

CHAPTER 6

CONCLUSIONS

- In this work, a numerical method was developed which quantitatively combines the description of the macroflow (through Computational Fluid Dynamics) with the precipitation phenomena occurring at the microscale level (through a micromixing model), coupled via a random walk model simulating the dispersion-mixing-precipitation phenomena.
- The experimental data obtained in this work clearly show that the effect on the crystal size distribution of a number of operating and geometric variables is quite complex, often resulting in a non-monotonic dependence of the final crystal size on the variable under study.
- Despite the complexity of the problem, the mathematical model proposed here is able to capture all the essential features of such dependencies (including the non-monotonic behaviors) on all the variables examined in this work. Furthermore, these predictions often quantitatively match the experimental results, thus indicating that the essential characteristics of the process have been captured.
- Since agglomeration effect was not included in the present model, experimental data and numerical prediction show disagreement at high values of volume ratio, mean initial concentration, and stoichiometry ratio.
- In general, the results obtained here and those of other investigators can be interpreted on the basis of competition between nucleation (heterogeneous or homogeneous) and crystal growth in the region where precipitation takes place.

- The rate of engulfment (micromixing) of material from the liquid bulk into the region where one of the reactants is fed appears to be especially critical. Micromixing increases with the increasing turbulent energy dissipation rates (generated, for example, by feeding in the impeller region or increasing the impeller speed), producing a rapid decrease of the level of supersaturation in the engulfment region, and reducing the time during which high levels of supersaturation are maintained. Lowering supersaturation results in slow heterogeneous nucleation, allowing crystal growth to dominate, and generating larger crystals. In general, increasing the volume ratio of reactants increases supersaturation, promoting homogeneous nucleation and the formation of smaller crystals. However, at low values of the mean initial concentration or stoichiometry ratio the reverse is true, and increasing these variables results in larger crystal sizes, since the rate of crystal growth dominates over heterogeneous nucleation.
- Numerical predictions of the supersaturation profiles were obtained; such profiles provide an explanation of the effect of process variables and operating conditions on the crystal size distribution.
- Larger mean crystal size and narrow size distribution, characterized by a coefficient of variation of 0.20-0.25, can be obtained by increasing the turbulence level (i.e., increasing the impeller speed, increasing the impeller diameter and/or feeding above the impeller).
- Under unusual conditions (low impeller speeds, feed point located in a low turbulence zone, low feed pipe velocity), other mixing phenomena other than micromixing, such as macromixing, can become relevant and affect the crystal size distribution.

- As the blob initially comes in contact with the bulk liquid non stoichiometric conditions prevail during the first periods of mixing of reactive fluids generating the supersaturation. The agreement between experimental data and numerical prediction would improve by using more reliable precipitation kinetics for both stoichiometric and non stoichiometric conditions (Aoun *et al.*, 1996). Unfortunately, very limited information is available on this subject.
- The under-prediction of turbulent quantities (*i.e.*, maximum value of the turbulent kinetic energy) requires more accurate modeling of turbulence. One alternative would be to increase the grid density around the impeller. Another promising alternative would be to use Large Eddy Simulations (LES) using the lattice Boltzmann method (Eggels, 1995). LES can be effectively employed to explicitly resolve the phenomena directly related to the unsteady boundaries created by the movement of the impeller blades.
- This conceptual approach proposed here and the simulation method has the potential to be extended to double-feed semi-batch precipitation process.
- It is expected that the proposed modeling approach will be successfully implemented in the prediction of the performance of industrial crystallization processes.

APPENDIX A

ESEM PHOTOGRAPHS

This appendix includes the Environmental Scanning Electron Microscope photographs of the barium sulfate crystals discussed in Chapter 5 (Results and Discussion). The scanning electron microscope (Philips Electro Scan 2020) is located in the Geo-Environmental Lab, Civil Engineering Department, NJIT. The magnification was between ×2700 to ×3500. The photographs were selected to show the well-formed rectangular crystals produced during most of the experiments and the effect of agglomeration on the crystal morphology. The mean crystal size, d_{43}, and the coefficient of variation, *C.V.*, measured with the Coulter® Multisizer are also reported with the photographs.

For the preliminary experiments: effect of time feed addition, volume ratio of reactants, mean initial concentration of sodium sulfate, and stoichiometry ratio of reactants, these photographs include:

Figure A.1 Crystal shape for reference conditions-Feed I

Figure A.2 Crystal shape for reference conditions-Feed II

Figure A.3 Crystal shape for preliminary experiment TF 6-Feed I

Figure A.4 Crystal shape for preliminary experiment TF 6-Feed II

Figure A.5 Crystal shape for preliminary experiment VR 5-Feed I

Figure A.6 Crystal shape for preliminary experiment VR 5-Feed II

Figure A.7 Crystal shape for preliminary experiment MC 4-Feed I

Figure A.8 Crystal shape for preliminary experiment MC 4-Feed II

Figure A.9 Crystal shape for preliminary experiment SR 3-Feed I

Figure A.10 Crystal shape for preliminary experiment SR 3-Feed II

For the two-level factorial design: effect of impeller speed, impeller diameter, and impeller off-bottom clearance, these photographs include:

Figure A.11 Crystal shape for experimental design EDA1-Feed I

Figure A.12 Crystal shape for experimental design EDA1-Feed II

Figure A.13 Crystal shape for experimental design EDA2-Feed I

Figure A.14 Crystal shape for experimental design EDA2-Feed II

Figure A.15 Crystal shape for experimental design EDA3-Feed I

Figure A.16 Crystal shape for experimental design EDA3-Feed II

Figure A.17 Crystal shape for experimental design EDA4-Feed I

Figure A.18 Crystal shape for experimental design EDA4-Feed II

Figure A.19 Crystal shape for experimental design EDA5-Feed I

Figure A.20 Crystal shape for experimental design EDA5-Feed II

Figure A.21 Crystal shape for experimental design EDA6-Feed I

Figure A.22 Crystal shape for experimental design EDA6-Feed II

Figure A.23 Crystal shape for experimental design EDA7-Feed I

Figure A.24 Crystal shape for experimental design EDA7-Feed II

Figure A.25 Crystal shape for experimental design EDA8-Feed I

Figure A.26 Crystal shape for experimental design EDA8-Feed II

For the effect of vessel scale, these photographs include:

Figure A.27 Crystal shape for small vessel, $T = 0.219$ m-Feed I

Figure A.28 Crystal shape for small vessel, $T = 0.219$ m-Feed II

Figure A.29 Crystal shape for large vessel, $T = 0.584$ m-Feed I

Figure A.30 Crystal shape for large vessel, $T = 0.584$ m-Feed II

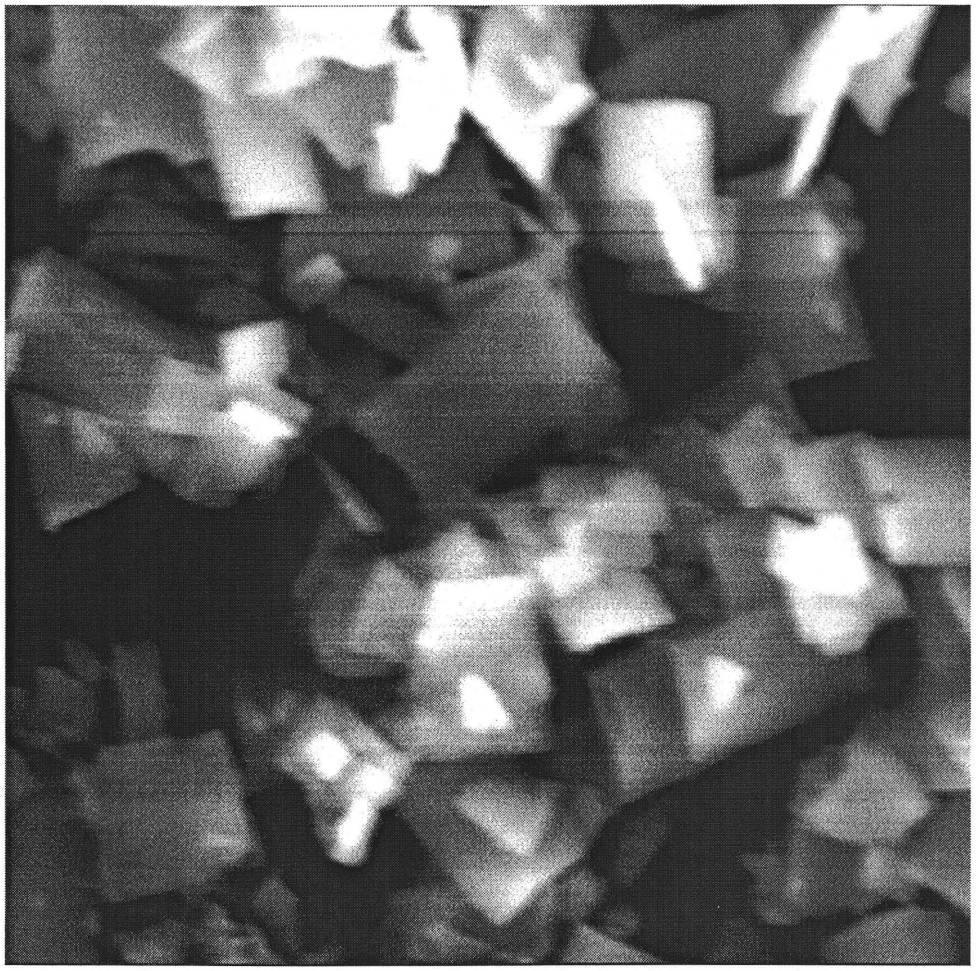

Figure A.1 Crystal shape for reference conditions-Feed I
t_f = 45 min, α_v = 50, C_{BOM} = 0.0045 kmol/m^3, η = 1, D = 0.102 m, C/T = 0.33, N = 300 rpm:
d_{43} = 6.12 μm, $C.V.$ = 0.2369

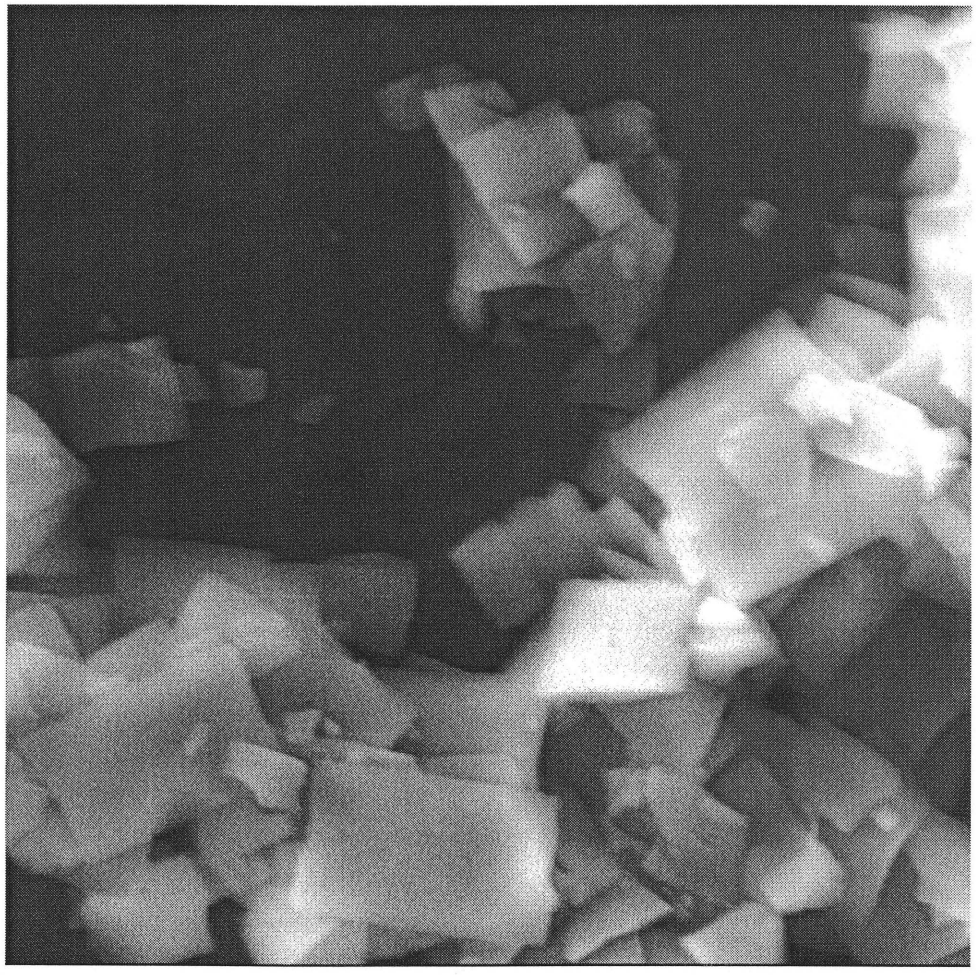

Figure A.2 Crystal shape for reference conditions-Feed II
t_f = 45 min, α_v = 50, C_{BOM} = 0.0045 kmol/m^3, η = 1, D = 0.102 m, C/T = 0.33, N = 300 rpm:
d_{43} = 6.64 μm, $C.V.$ = 0.2073

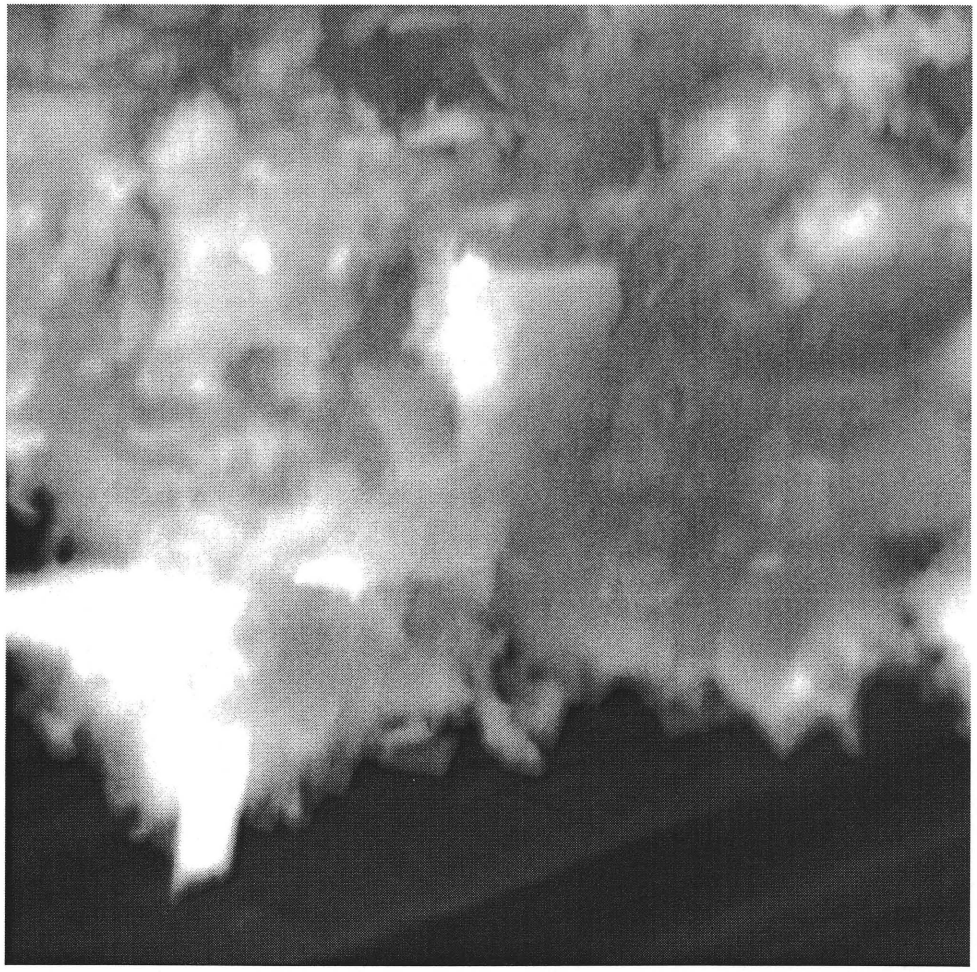

Figure A.3 Crystal shape for preliminary experiments TF 6-Feed I
t_f = 25 min, α_v = 50, C_{BOM} = 0.0045 kmol/m^3, η = 1, D = 0.102 m, C/T = 0.33, N = 300 rpm:
d_{43} = 6.55 μm, $C.V.$ = 0.3839

Figure A.4 Crystal shape for preliminary experiments TF 6-Feed II
t_f = 25 min, α_v = 50, C_{BOM} = 0.0045 kmol/m^3, η = 1, D = 0.102 m, C/T = 0.33, N = 300 rpm:
d_{43} = 5.17 μm, $C.V.$ = 0.2467

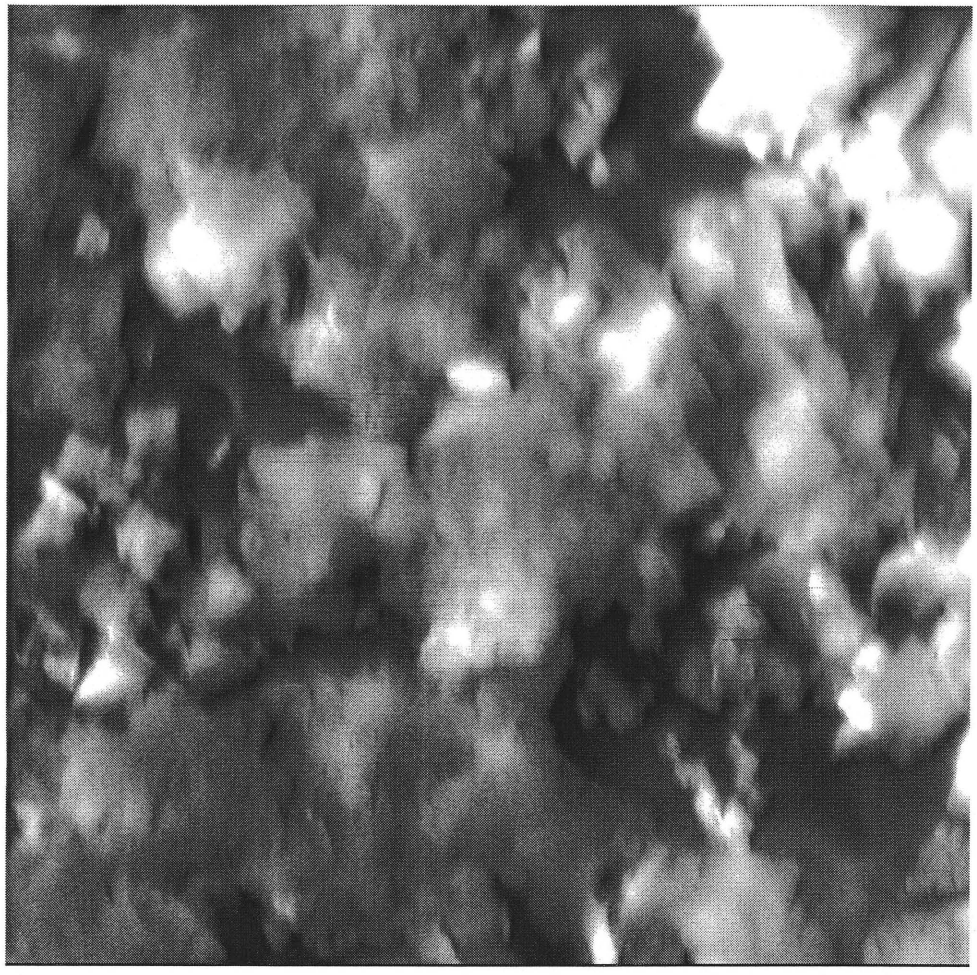

Figure A.5 Crystal shape for experiment VR5-Feed I
t_f = 45 min, α_v = 80, C_{BOM} = 0.0045 kmol/m^3, η = 1, D = 0.102 m, C/T = 0.33, N = 100 rpm:
d_{43} = 4.12 μm, $C.V.$ = 0.1932

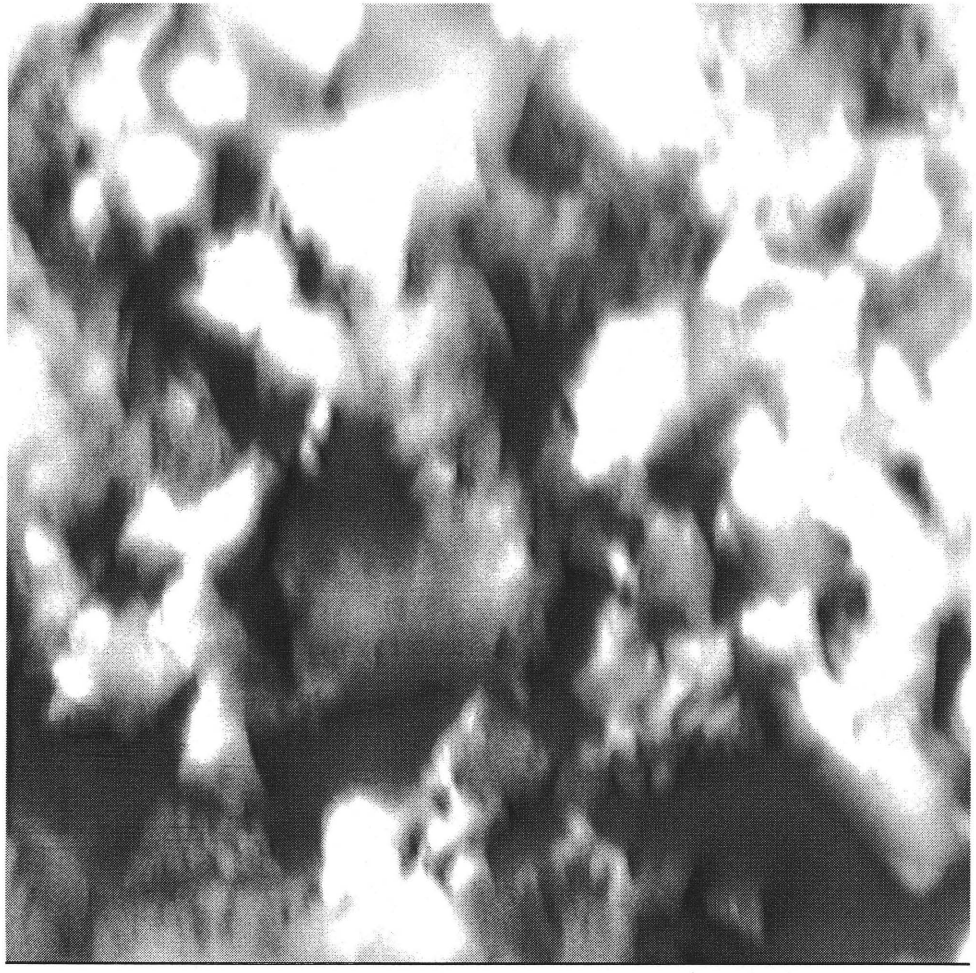

Figure A.6 Crystal shape for experiment VR5-Feed II
t_f = 45 min, α_v = 80, C_{BOM} = 0.0045 kmol/m^3, η = 1, D = 0.102 m, C/T = 0.33, N = 100 rpm:
d_{43} = 4.27 μm, $C.V.$ = 0.2056

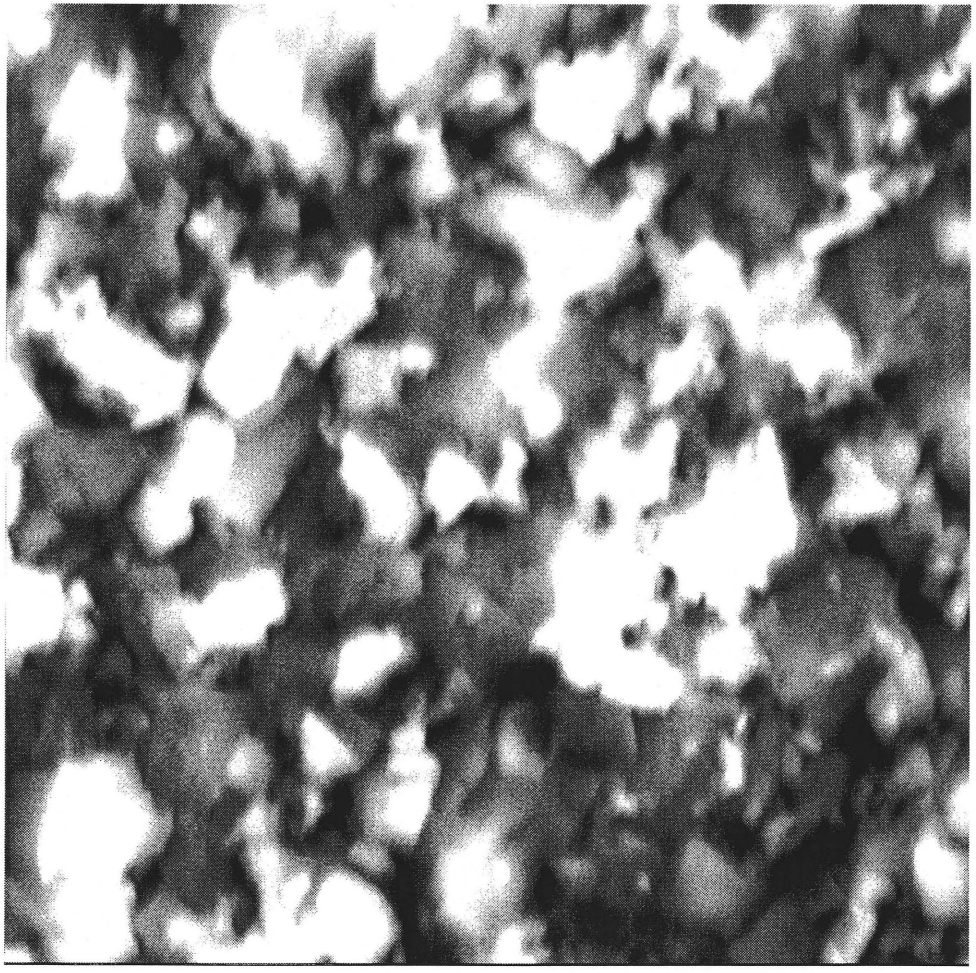

Figure A.7 Crystal shape for experiment MC4-Feed I
t_f = 45 min, α_v = 50, C_{BOM} = 0.0060 kmol/m^3, η = 1, D = 0.102 m, C/T = 0.33, N = 300 rpm:
d_{43} = 4.20 μm, $C.V.$ = 0.2154

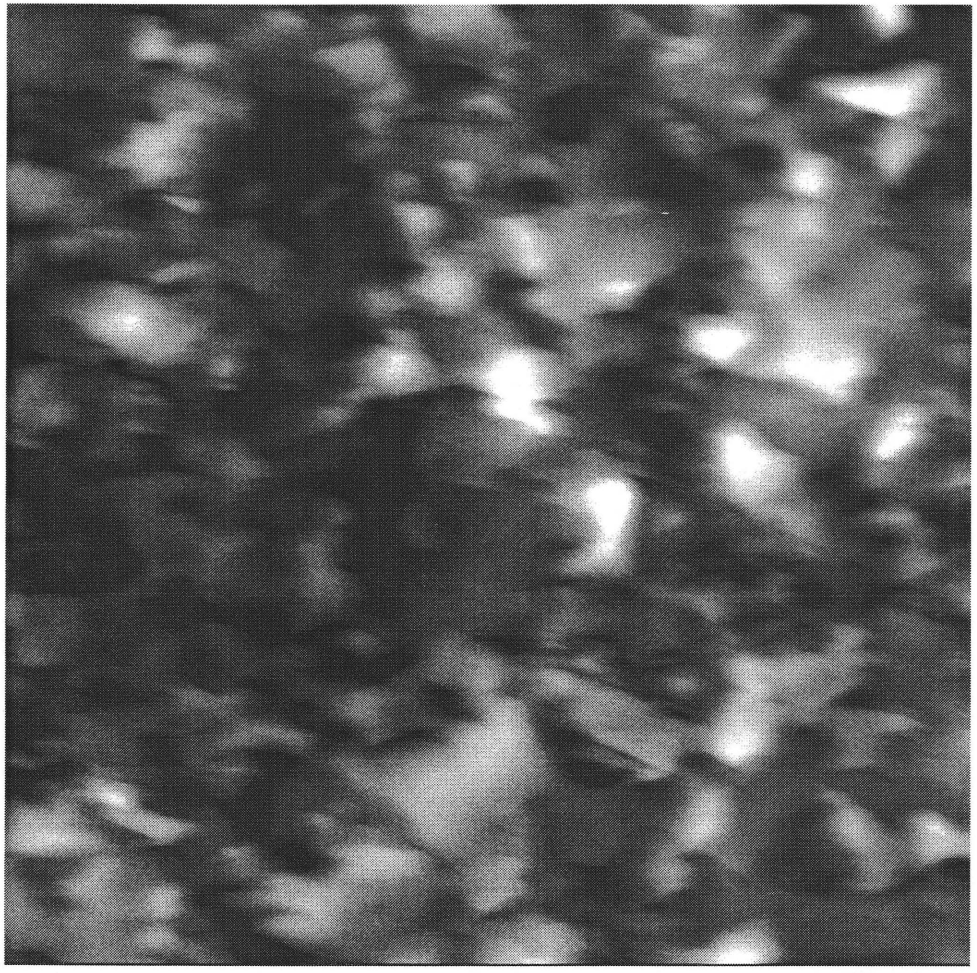

Figure A.8 Crystal shape for experimental design MC4-Feed II
t_f = 45 min, α_v = 50, C_{BOM} = 0.0060 kmol/m^3, η = 1, D = 0.102 m, C/T = 0.33, N = 500 rpm:
d_{43} = 3.74 μm, $C.V.$ = 0.2009

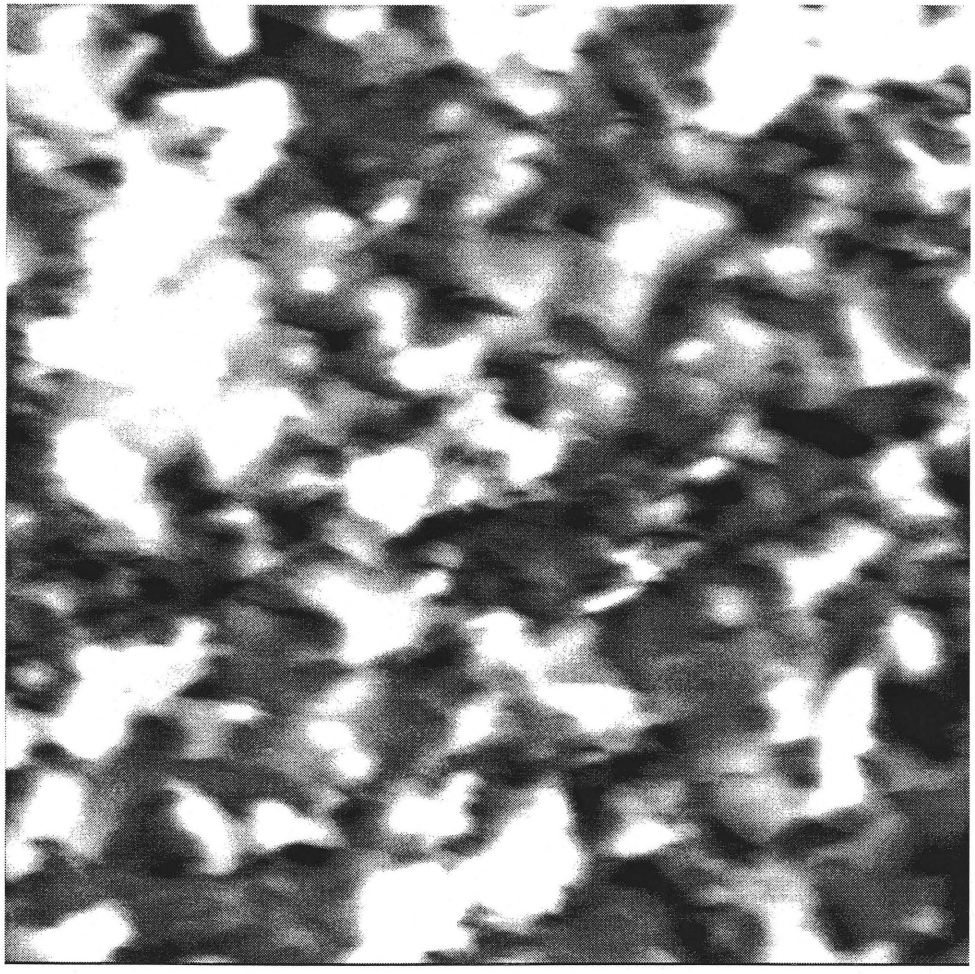

Figure A.9 Crystal shape for experiment SR3-Feed I
t_f = 45 min, α_v = 50, C_{BOM} = 0.0045 kmol/m^3, η = 1.5, D = 0.102 m, C/T = 0.33, N = 300 rpm:
d_{43} = 4.39 μm, $C.V.$ = 0.2088

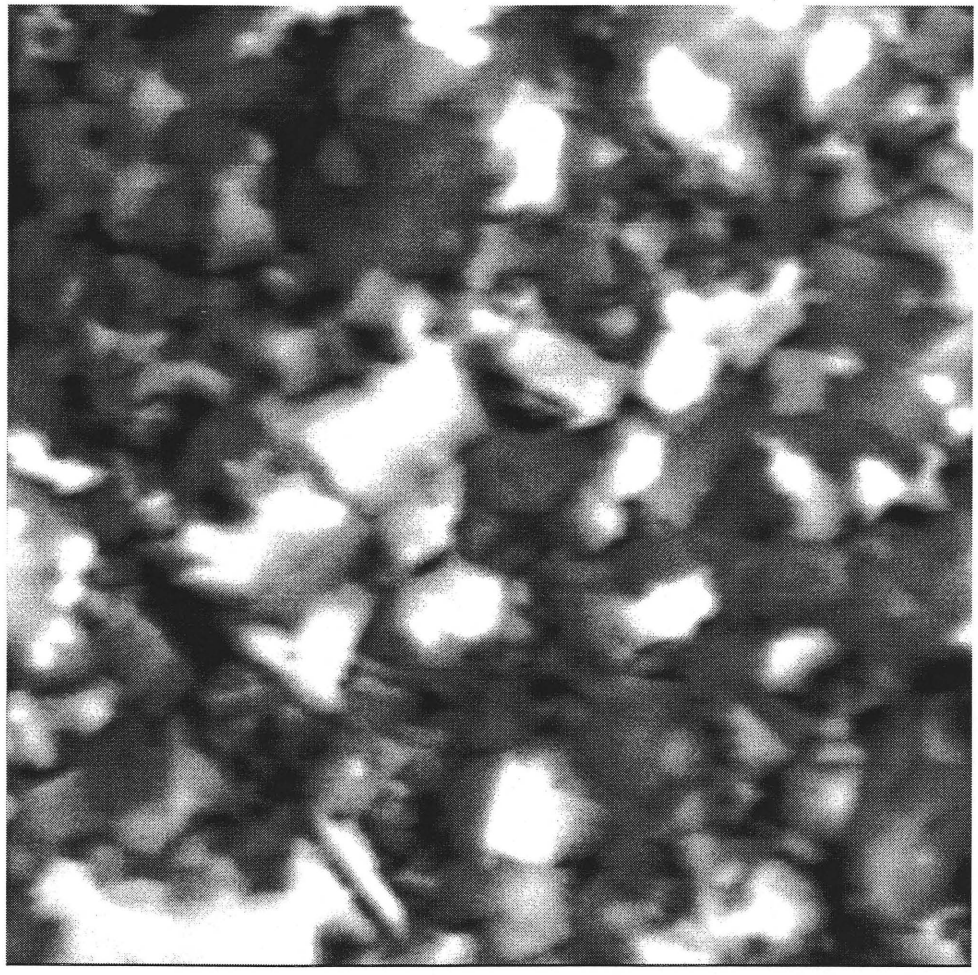

Figure A.10 Crystal shape for experimental SR3-Feed II
t_f = 45 min, α_v = 50, C_{BOM} = 0.0045 kmol/m^3, η = 1.5, D = 0.102 m, C/T = 0.33, N = 300 rpm:
d_{43} = 4.48 μm, $C.V.$ = 0.2097

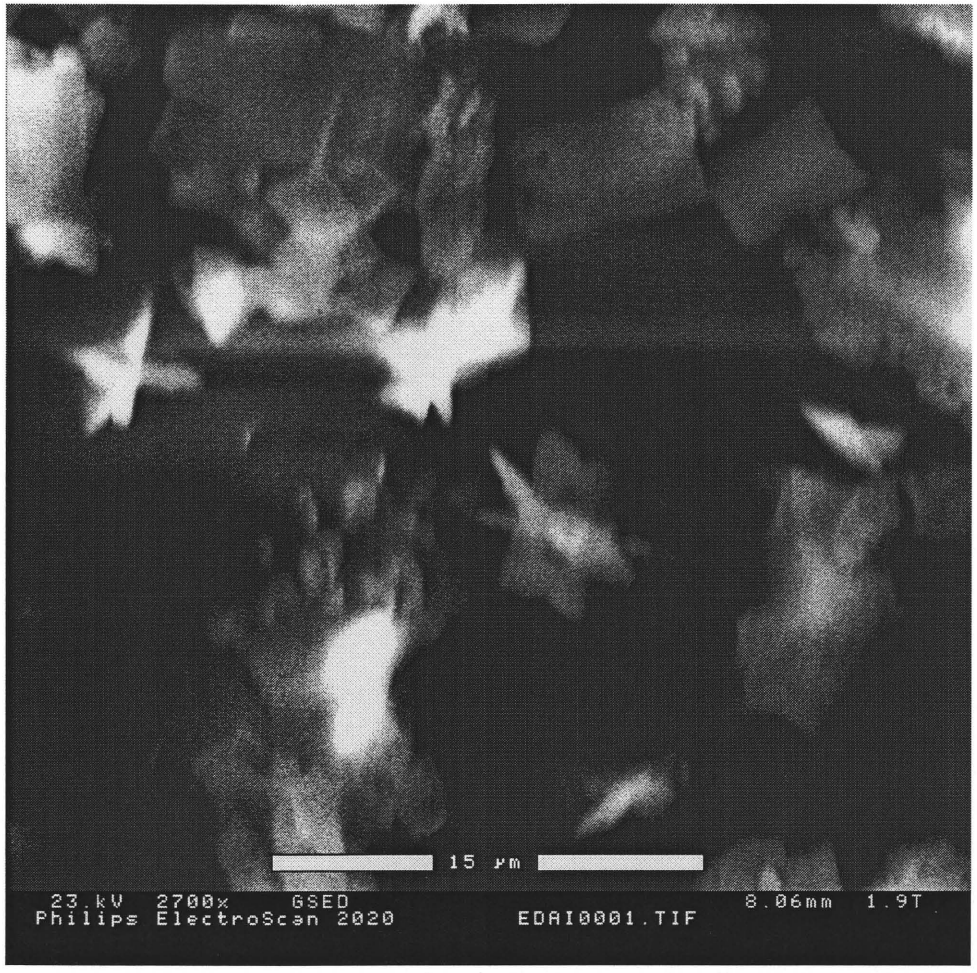

Figure A.11 Crystal shape for experimental design EDA1-Feed I
t_f = 45 min, α_v = 50, C_{BOM} = 0.0045 kmol/m^3, η = 1, D = 0.076 m, C/T = 0.20, N = 100 rpm:
d_{43} = 7.18 µm, $C.V.$ = 0.3719

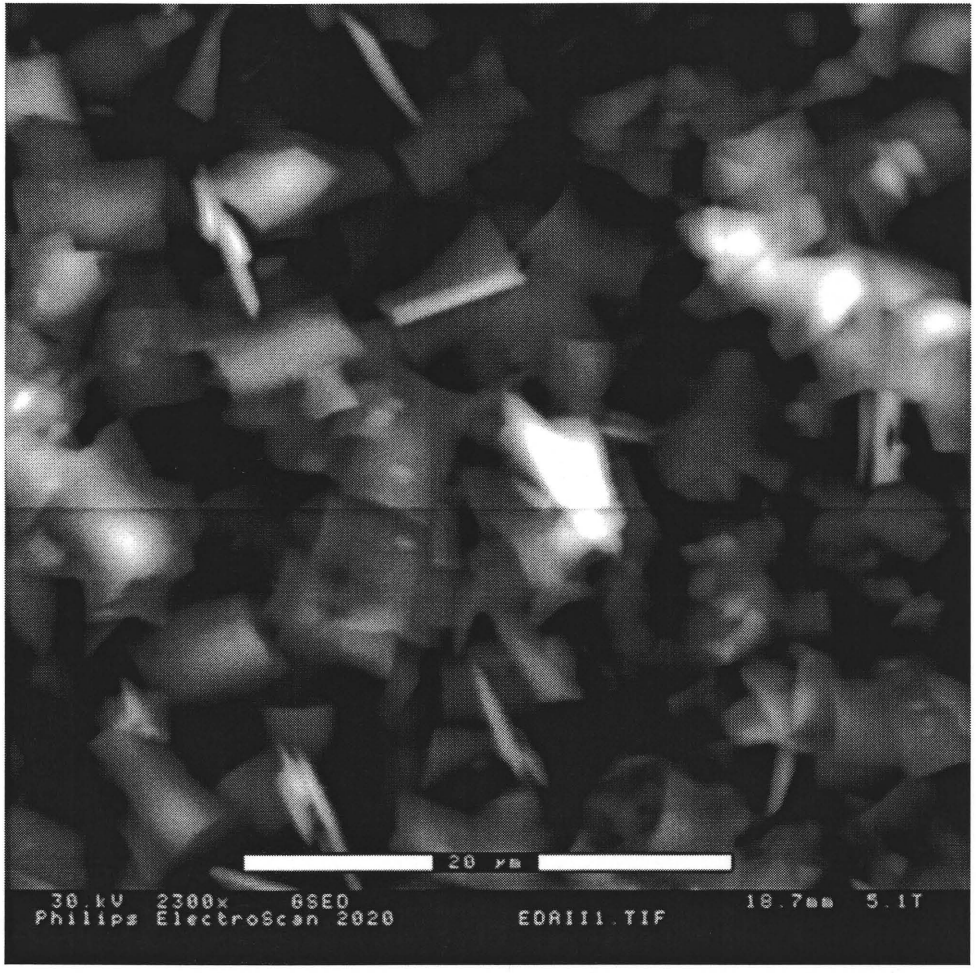

Figure A.12 Crystal shape for experimental design EDA1-Feed II
t_f = 45 min, α_v = 50, C_{BOM} = 0.0045 kmol/m^3, η = 1, D = 0.076 m, C/T = 0.20, N = 100 rpm:
d_{43} = 5.26 µm, $C.V.$ = 0.2170

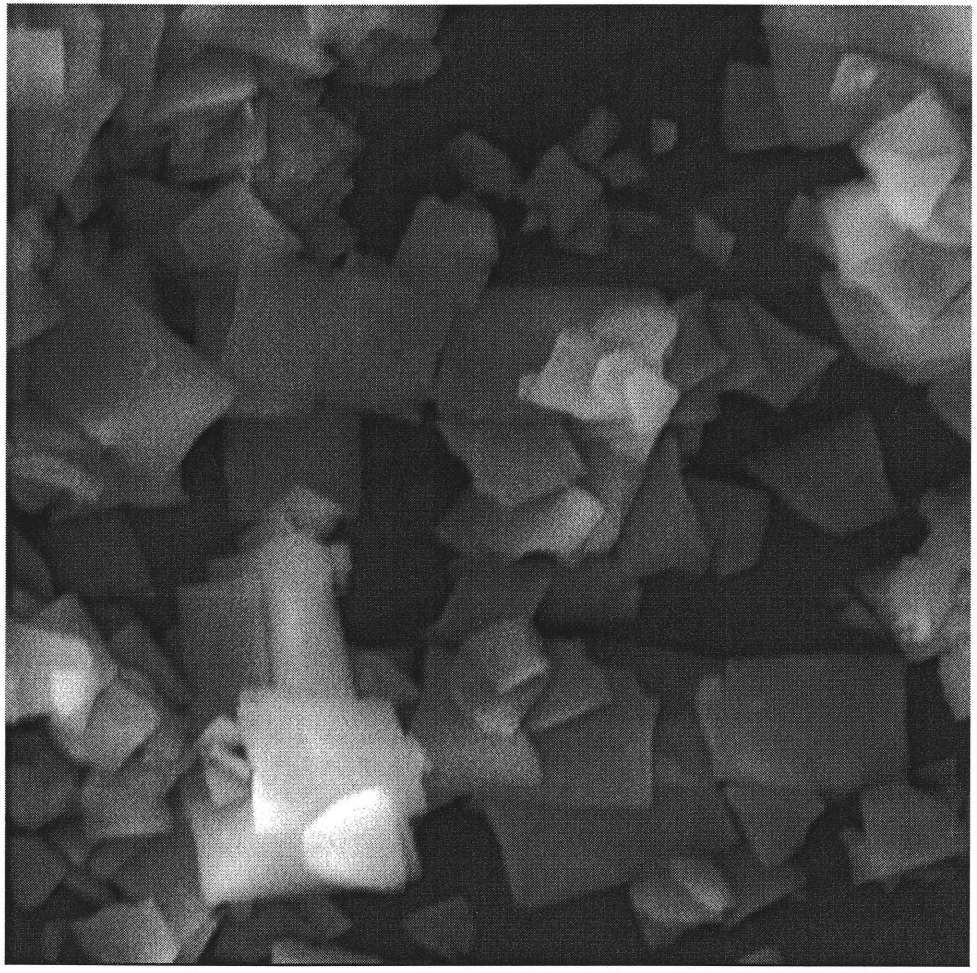

Figure A.13 Crystal shape for experimental design EDA2-Feed I
t_f = 45 min, α_v = 50, C_{BOM} = 0.0045 kmol/m^3, η = 1, D = 0.076 m, C/T = 0.50, N = 500 rpm:
d_{43} = 5.95 μm, $C.V.$ = 0.2317

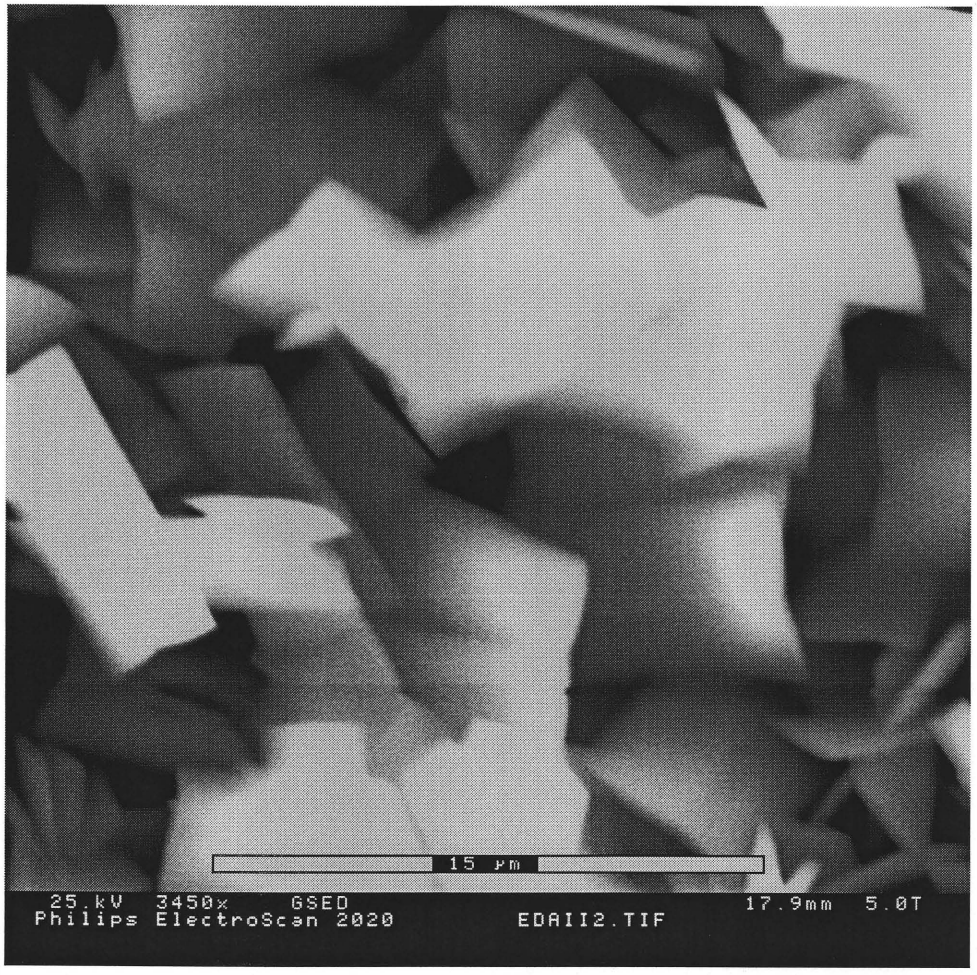

Figure A.14 Crystal shape for experimental design EDA2-Feed II
t_f = 45 min, α_v = 50, C_{BOM} = 0.0045 kmol/m^3, η = 1, D = 0.076 m, C/T = 0.50, N = 500 rpm:
d_{43} = 6.54 µm, $C.V.$ = 0.2131

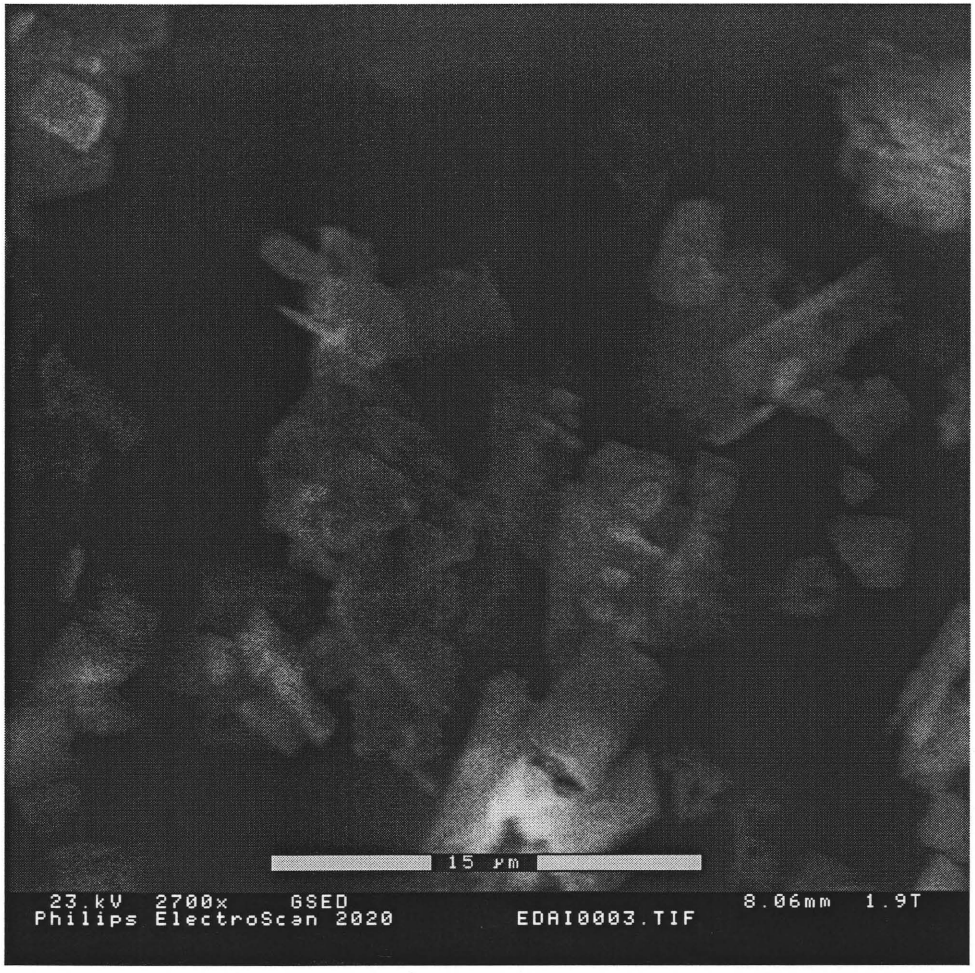

Figure A.15 Crystal shape for experimental design EDA3-Feed I
t_f = 45 min, α_v = 50, C_{BOM} = 0.0045 kmol/m^3, η = 1, D = 0.102 m, C/T = 0.20, N = 100 rpm:
d_{43} = 6.32 µm, $C.V.$ = 0.3757

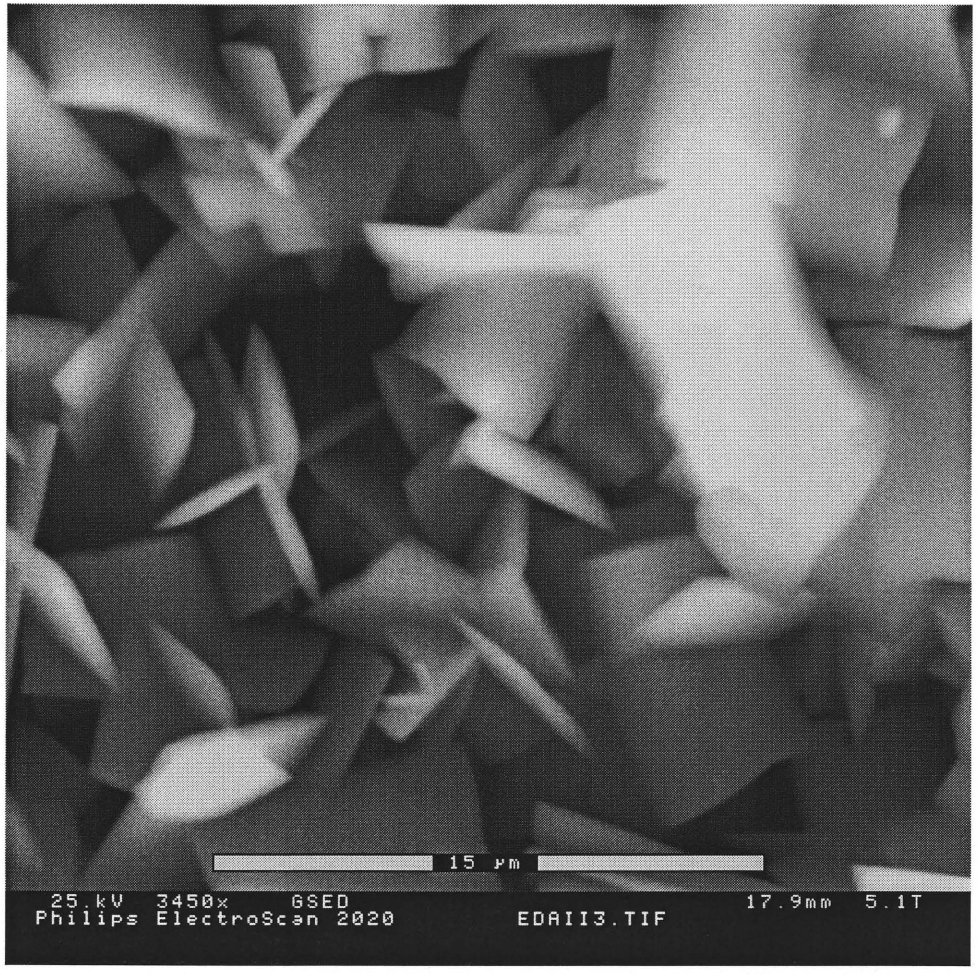

Figure A.16 Crystal shape for experimental design EDA3-Feed II
t_f = 45 min, α_v = 50, C_{BOM} = 0.0045 kmol/m^3, η = 1, D = 0.102 m, C/T = 0.20, N = 100 rpm:
d_{43} = 5.50 µm, $C.V.$ = 0.2065

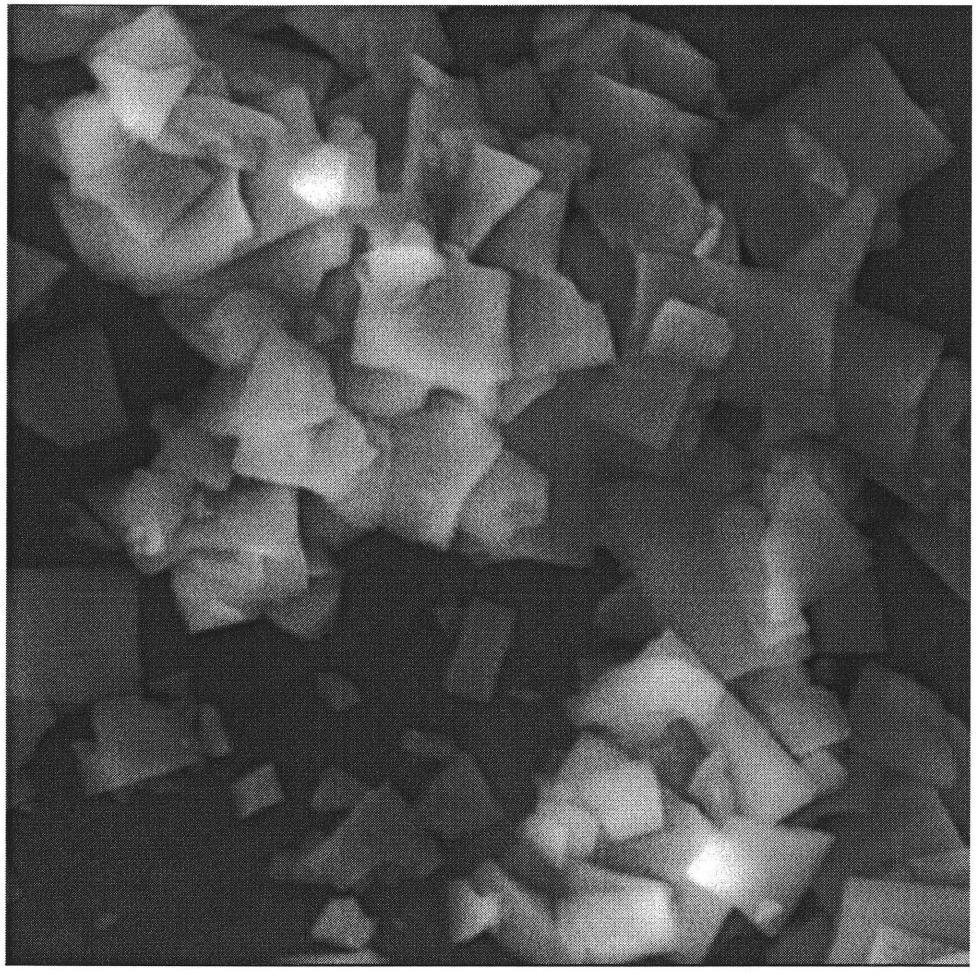

Figure A.17 Crystal shape for experimental design EDA4-Feed I
t_f = 45 min, α_v = 50, C_{BOM} = 0.0045 kmol/m^3, η = 1, D = 0.102 m, C/T = 0.50, N = 500 rpm:
d_{43} = 6.39 μm, $C.V.$ = 0.2370

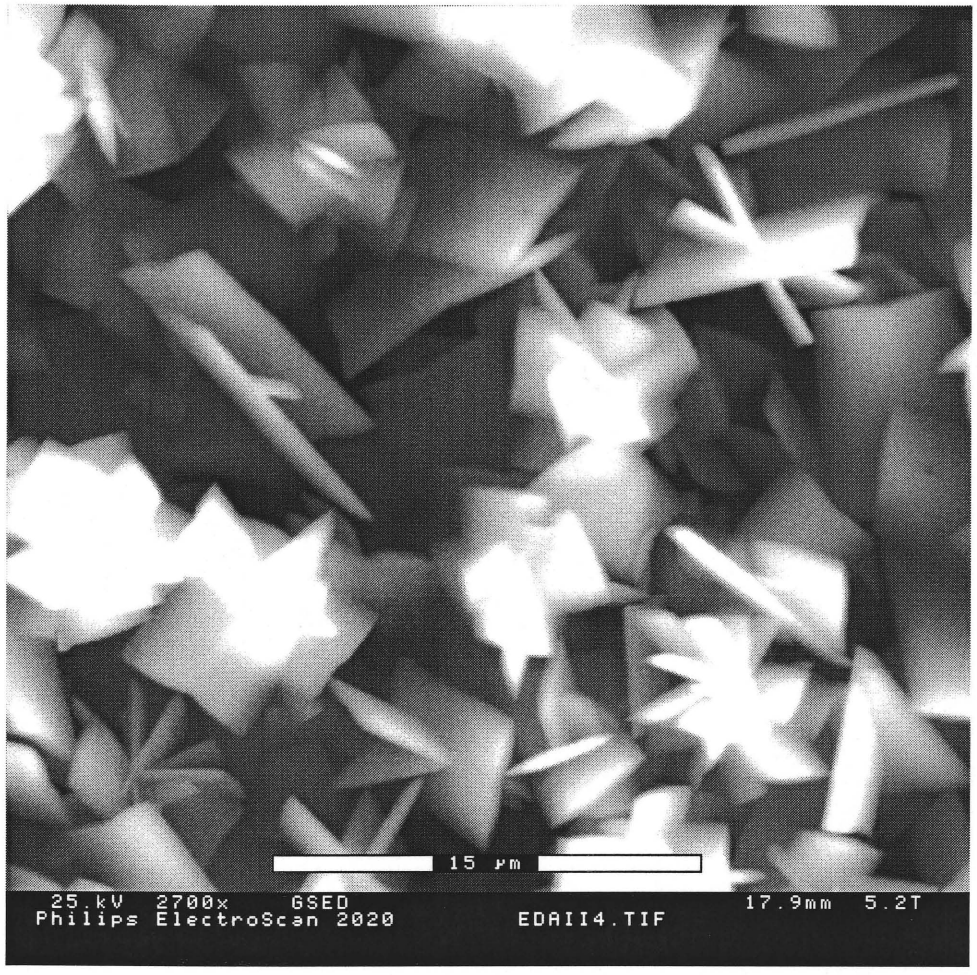

Figure A.18 Crystal shape for experimental design EDA4-Feed II
t_f = 45 min, α_v = 50, C_{BOM} = 0.0045 kmol/m^3, η = 1, D = 0.102 m, C/T = 0.50, N = 500 rpm:
d_{43} = 6.81 µm, $C.V.$ = 0.2107

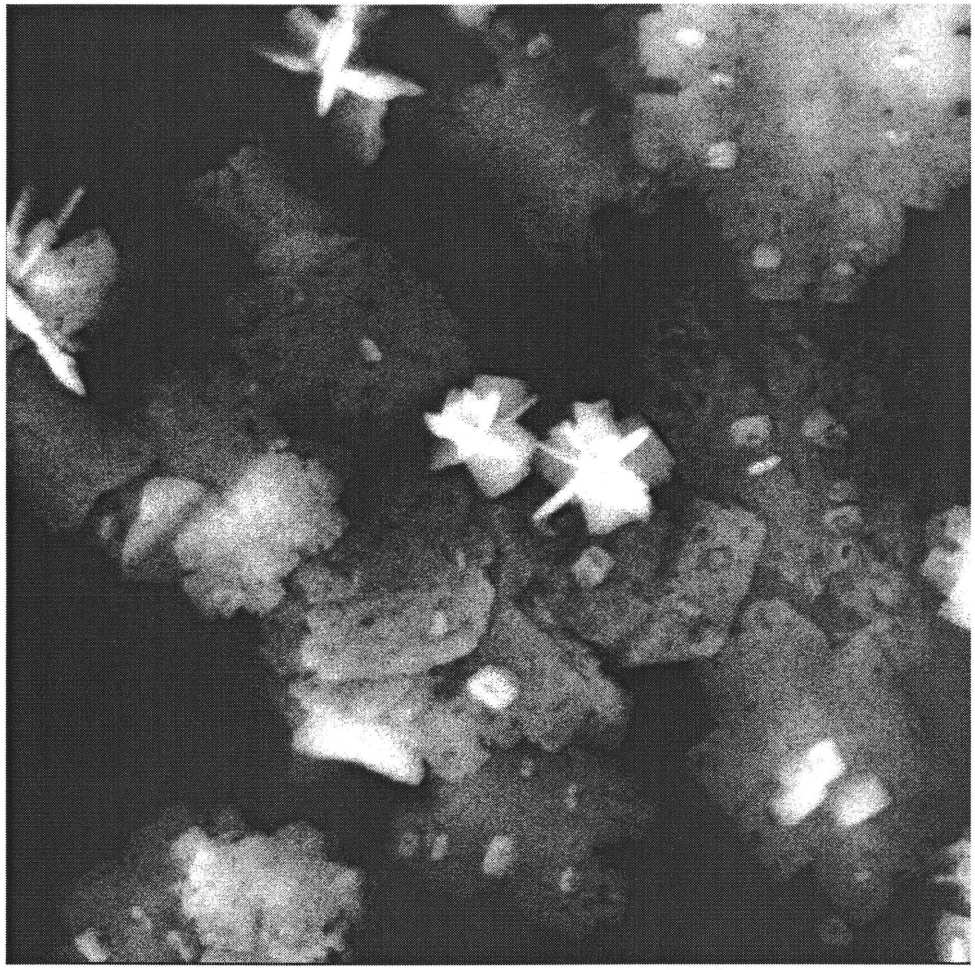

Figure A.19 Crystal shape for experimental design EDA5-Feed I
t_f = 45 min, α_v = 50, C_{BOM} = 0.0045 kmol/m^3, η = 1, D = 0.076 m, C/T = 0.33, N = 100 rpm:
d_{43} = 7.46 μm, $C.V.$ = 0.3656

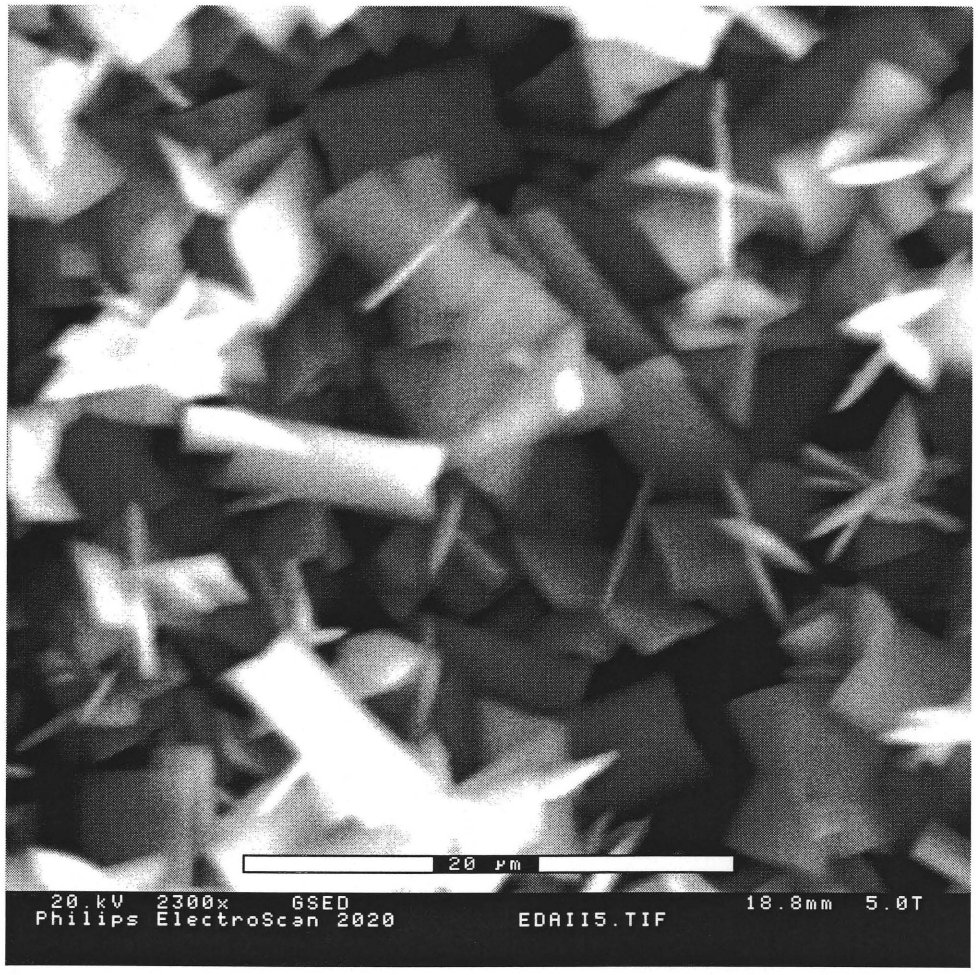

Figure A.20 Crystal shape for experimental design EDA5-Feed II
t_f = 45 min, α_v = 50, C_{BOM} = 0.0045 kmol/m^3, η = 1, D = 0.076 m, C/T = 0.33, N = 100 rpm:
d_{43} = 5.18 µm, $C.V.$ = 0.2450

Figure A.21 Crystal shape for experimental design EDA6-Feed I
t_f = 45 min, α_v = 50, C_{BOM} = 0.0045 kmol/m^3, η = 1, D = 0.076 m, C/T = 0.33, N = 500 rpm:
d_{43} = 6.05 μm, $C.V.$ = 0.2567

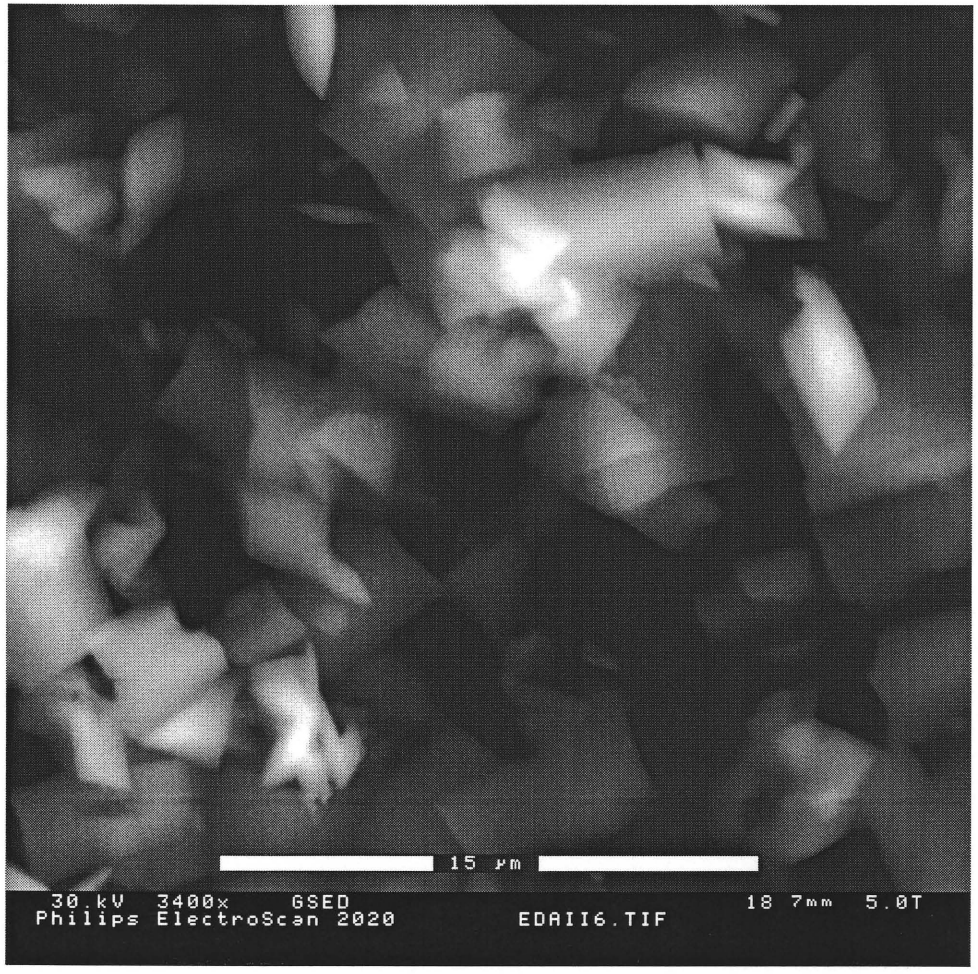

Figure A.22 Crystal shape for experimental design EDA6-Feed II
t_f = 45 min, α_v = 50, C_{BOM} = 0.0045 kmol/m^3, η = 1, D = 0.076 m, C/T = 0.33, N = 500 rpm:
d_{43} = 6.40 µm, $C.V.$ = 0.2187

Figure A.23 Crystal shape for experimental design EDA7-Feed I
t_f = 45 min, α_v = 50, C_{BOM} = 0.0045 kmol/m^3, η = 1, D = 0.102 m, C/T = 0.33, N = 100 rpm:
d_{43} = 6.46 μm, $C.V.$ = 0.3660

Figure A.24 Crystal shape for experimental design EDA7-Feed II
t_f = 45 min, α_v = 50, C_{BOM} = 0.0045 kmol/m^3, η = 1, D = 0.102 m, C/T = 0.33, N = 100 rpm:
d_{43} = 5.38 μm, $C.V.$ = 0.2232

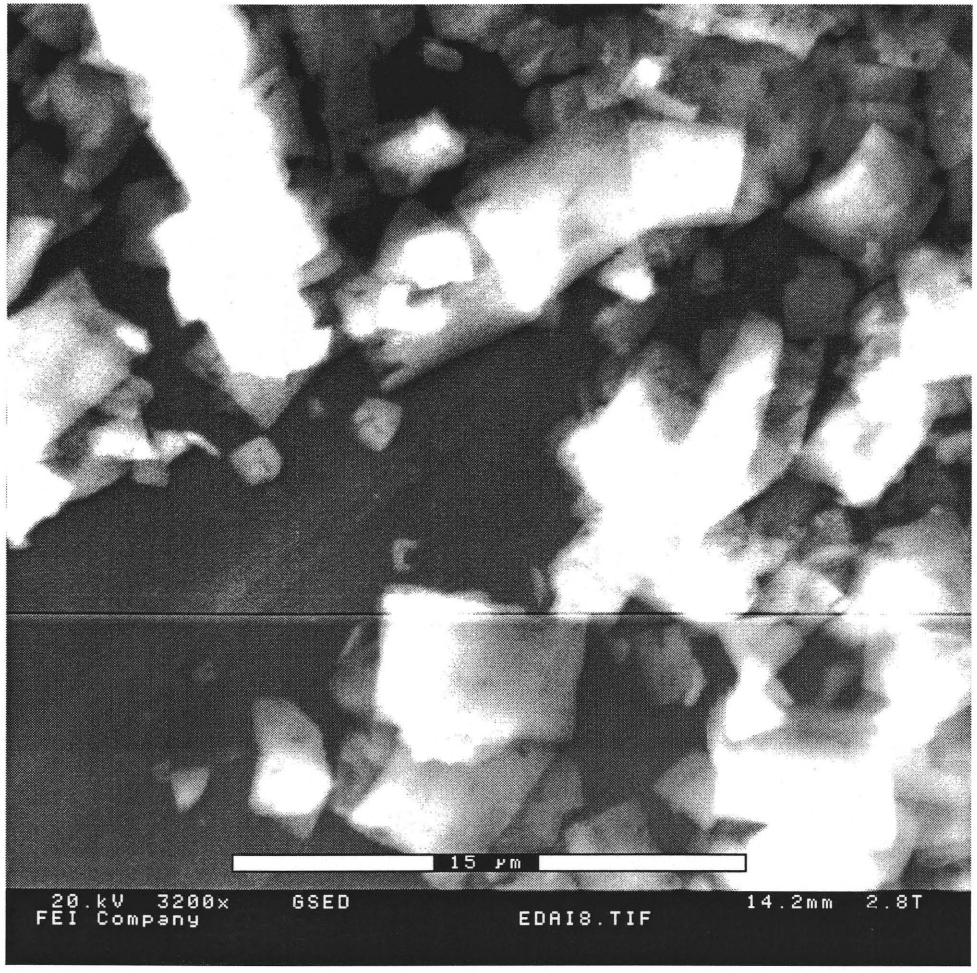

Figure A.25 Crystal shape for experimental design EDA8-Feed I
t_f = 45 min, α_v = 50, C_{BOM} = 0.0045 kmol/m^3, η = 1, D = 0.102 m, C/T = 0.33, N = 500 rpm:
d_{43} = 6.38 µm, $C.V.$ = 0.2306

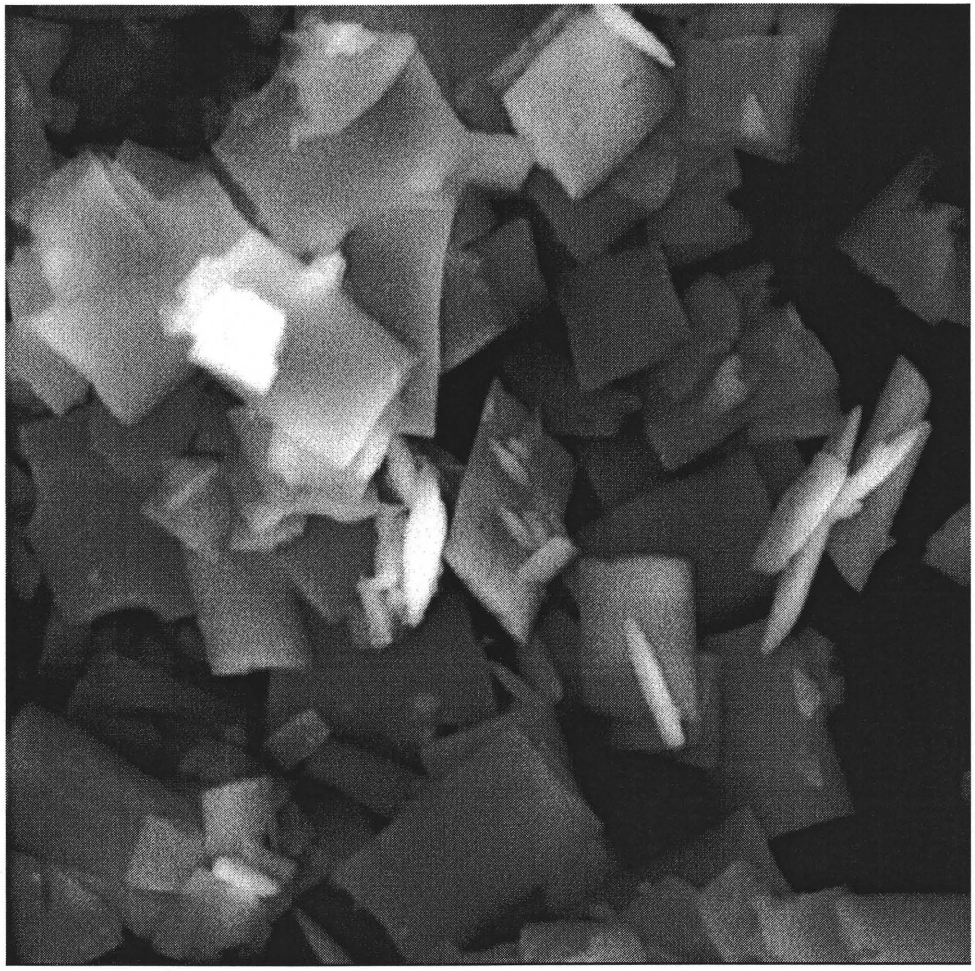

Figure A.26 Crystal shape for experimental design EDA8-Feed II
t_f = 45 min, α_v = 50, C_{BOM} = 0.0045 kmol/m^3, η = 1, D = 0.102 m, C/T = 0.33, N = 500 rpm:
d_{43} = 6.65 μm, $C.V.$ = 0.2134

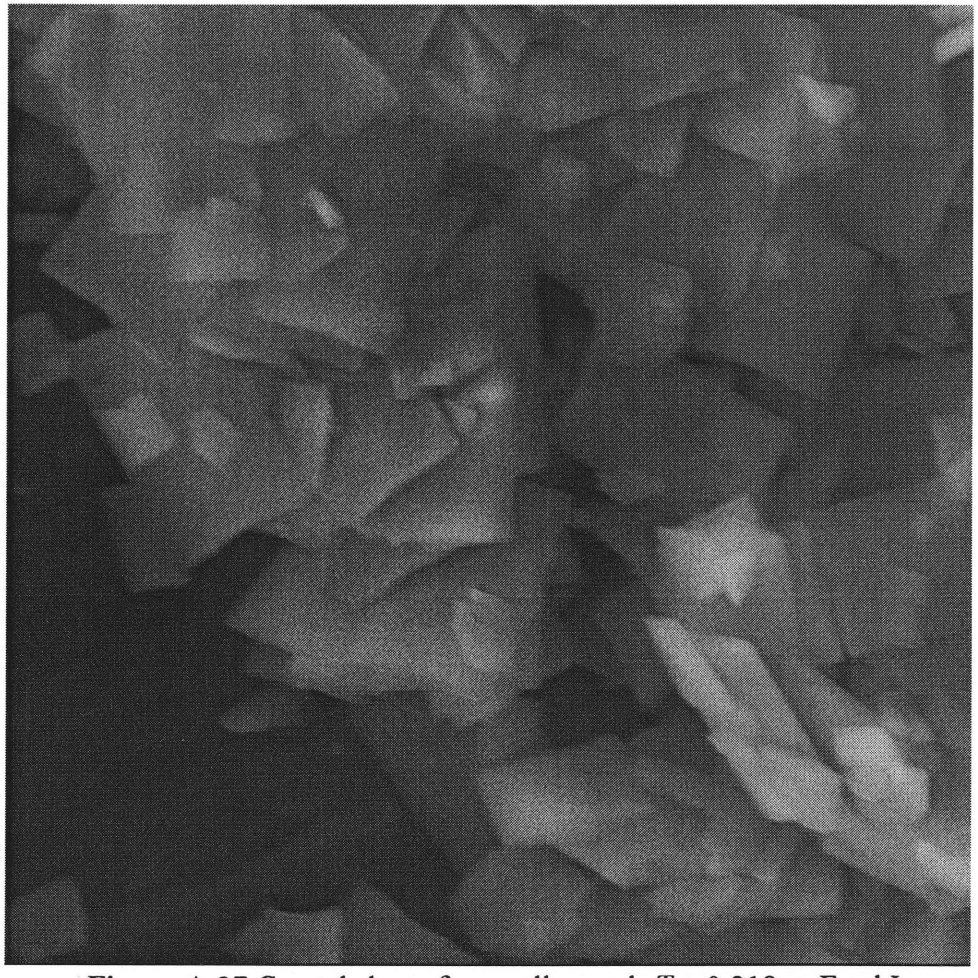

Figure A.27 Crystal shape for small vessel, $T = 0.219$ m-Feed I
$t_f = 45$ min, $\alpha_v = 50$, $C_{BOM} = 0.0045$ kmol/m^3, $\eta = 1$, $D = 0.076$ m, $C/T = 0.33$, $N = 300$ rpm:
$d_{43} = 5.67$ μm, $C.V. = 0.2451$

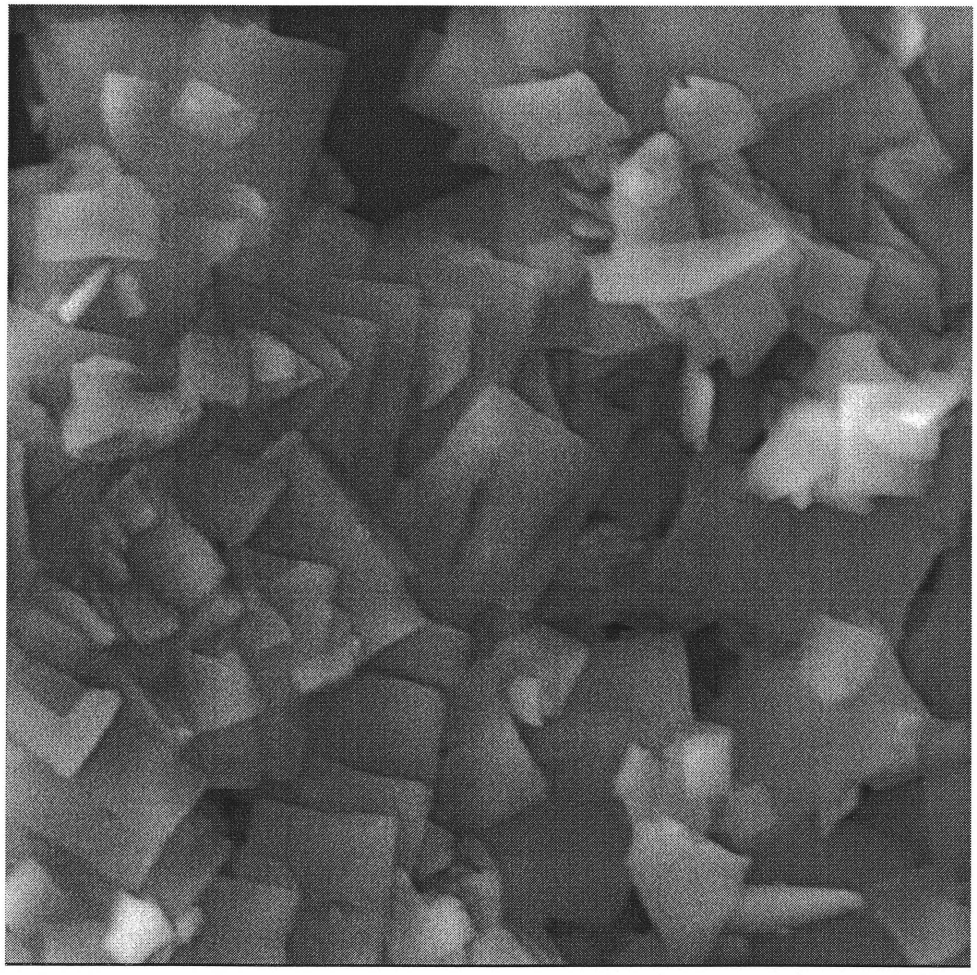

Figure A.28 Crystal shape for small vessel, $T = 0.219$ m-Feed II
$t_f = 45$ min, $\alpha_v = 50$, $C_{BOM} = 0.0045$ kmol/m^3, $\eta = 1$, $D = 0.076$ m, $C/T = 0.33$, $N = 300$ rpm:
$d_{43} = 6.16$ μm, $C.V. = 0.2341$

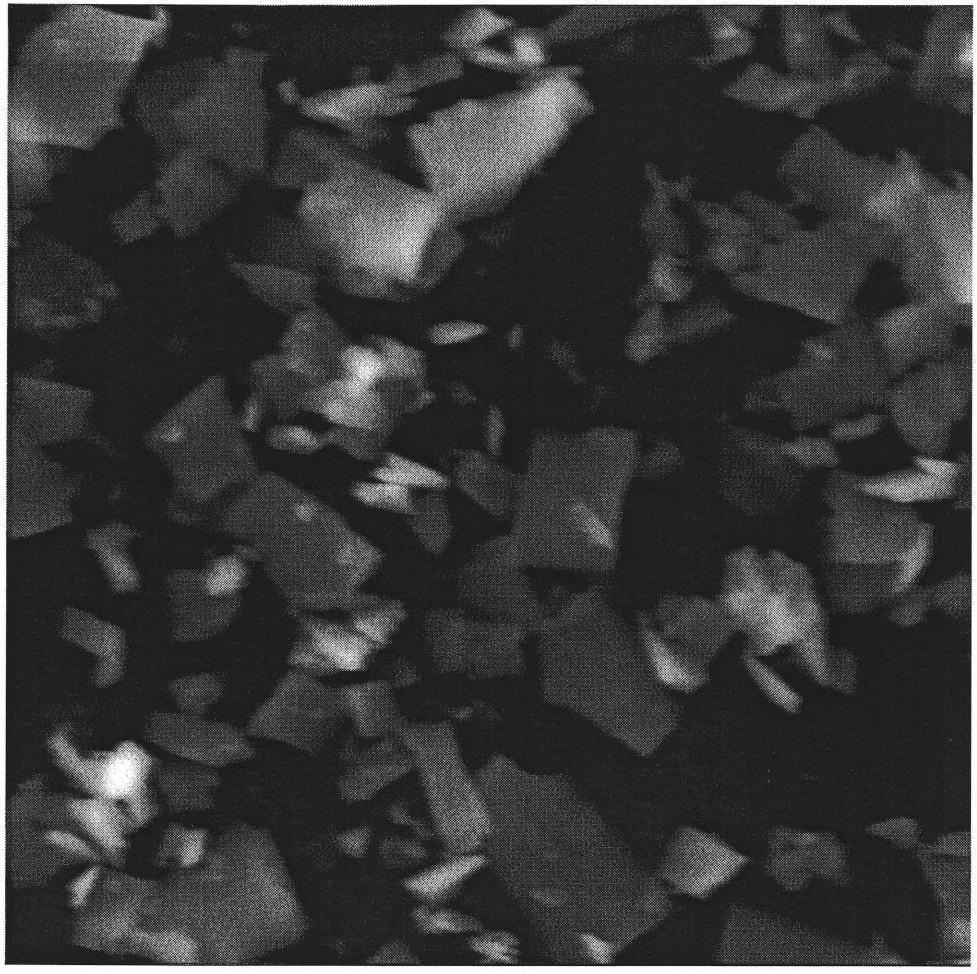

Figure A.29 Crystal shape for large vessel, $T = 0.584$ m-Feed I
$t_f = 45$ min, $\alpha_v = 50$, $C_{BOM} = 0.0045$ kmol/m^3, $\eta = 1$, $D = 0.204$ m, $C/T = 0.33$, $N = 300$ rpm:
$d_{43} = 6.05$ μm, $C.V. = 0.2114$

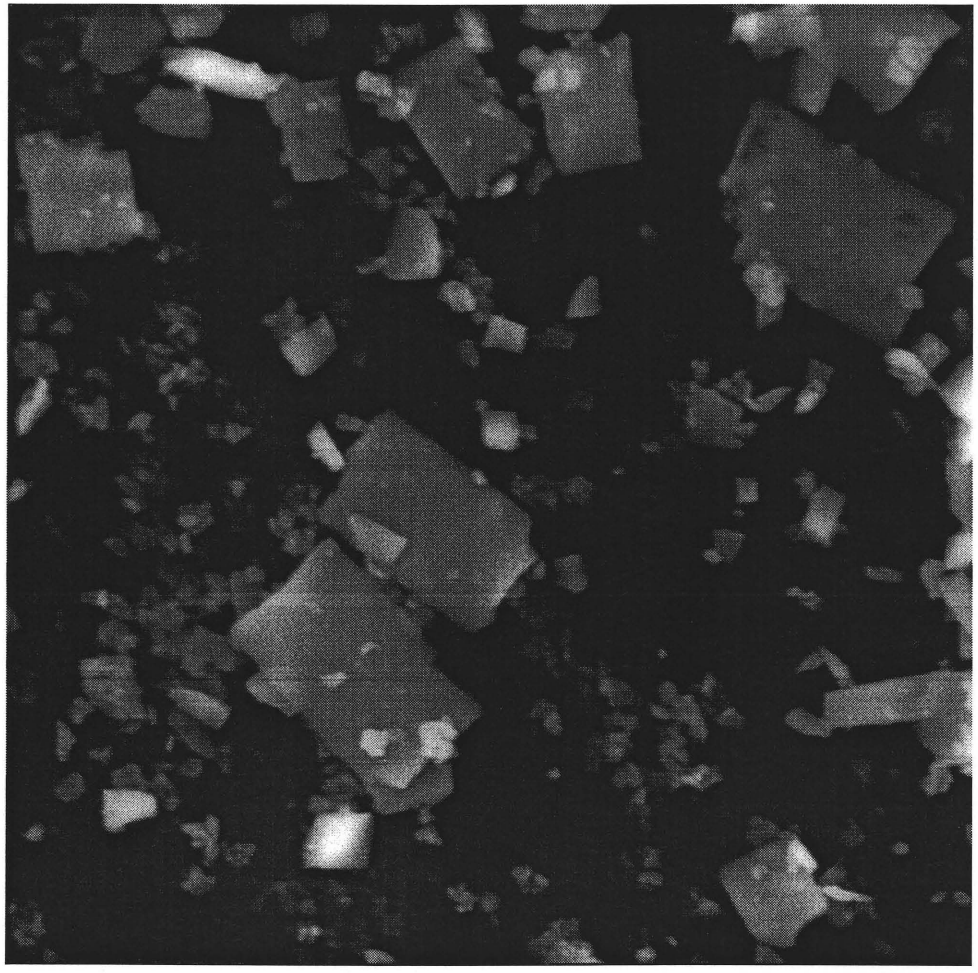

Figure A.30 Crystal shape for large vessel, $T = 0.584$ m-Feed II
$t_f = 45$ min, $\alpha_v = 50$, $C_{BOM} = 0.0045$ kmol/m^3, $\eta = 1$, $D = 0.204$ m, $C/T = 0.33$, $N = 300$ rpm:
$d_{43} = 6.49$ μm, $C.V. = 0.2027$

APPENDIX B

SIMULATION PROGRAM

This appendix contains the computer code for the simulation of the single-feed semi-batch precipitation process. The simulation program consists of three sections:

- Main program
- Subroutine F
- Subroutine GERK

The main program was designed to perform the following actions:

- Read the system parameters and initial conditions.
- Discretize and disperse the feed blob.
- Interface with subroutine F, which calculate the derivatives.
- Interface with subroutine GERK, which solve the system of differential equations.
- Update the boundary conditions.
- Print and storage the numerical solution.

Subroutine F(TIN,Y,YP) evaluates the *NEQN* (number of equations) derivatives:

$$YP(I) = \frac{DY(I)}{DT} = F\left(TIN, Y(1), Y(2), \ldots, Y\left(NEQN\right)\right) \qquad \text{(B.1)}$$

This subroutine also performs the calculation of the nucleation and crystal growth rates. Subroutine GERK (Watts, H. A., and Shampine, L. F.) is designed to solve the system of differential equations in the mixing-precipitation model based on the Runge-Kutta-Fehlberg methods of 4^{th} and 5^{th} order (RKF45). This subroutine is convenient when it is important to have a readily available global error estimate.

B.1 Main Program

```
C------------------------------------------------------------------------------------------ C
C                                                                                          C
C  MAIN PROGRAM                                                                            C
C  SIMULATION OF SINGLE-FEED, SEMIBATCH                                                    C
C  PRECIPITATION OF BARIUM SULFATE                                                         C
C  BaCl2 + Na2SO4 ---- BaSO4 + 2NaCl                                                       C
C                                                                                          C
C  THIS CODE INCLUDES SUBROUTINE GERK,                                                     C
C  AND NEWTON-RAPHSON's CONVERGENE SCHEME AND BISECTION STEPC
C                                                                                          C
C  ERNESTO UEHARA-NAGAMINE                                                                 C
C  DEPARTMENT OF CHEMICAL ENGINEERING, CHEMISTRY                                           C
C  AND ENVIRONMENTAL SCIENCE                                                               C
C  NEW JERSEY INSTITUTE OF TECHNOLOGY                                                      C
C                                                                                          C
C------------------------------------------------------------------------------------------ C

      IMPLICIT DOUBLE PRECISION (A-H,O-Z)
      DOUBLE PRECISION Y(25),YG(25),GERROR(25),WORK(203),IWORK(5)
      DOUBLE PRECISION APOS(100000),RPOS(100000),ZPOS(100000)

      EXTERNAL F

      DOUBLE PRECISION BACLMW,SOSUMW,BASUMW,SOCLMW
      DOUBLE PRECISION CRYDEN,CRYDIF,SHAFAC,VOLFAC
      DOUBLE PRECISION CRBACL,CRSOSU,CRBASU,CRSOCL
      DOUBLE PRECISION AA,BB,PHIVOL,VISSOL,SOLPRO
      DOUBLE PRECISION ENGULF,ENDIRA,TIMESO
      DOUBLE PRECISION ENVBAC,ENVSOS,ENVBAS,ENVSOC
      DOUBLE PRECISION ENVMM0,ENVMM1,ENVMM2
      DOUBLE PRECISION ENVMM3,ENVMM4,ENVMM5

      COMMON BACLMW,SOSUMW,BASUMW,SOCLMW
      COMMON CRYDEN,CRYDIF,SHAFAC,VOLFAC
      COMMON CRBACL,CRSOSU,CRBASU,CRSOCL
      COMMON NEQN,AA,BB,PHIVOL,VISSOL,SOLPRO,REACCO,DROSAT
      COMMON ENGULF,ENDIRA,TIMESO
      COMMON MODNUC,MODGRO,NBRENT
      COMMON ENVBAC,ENVSOS,ENVBAS,ENVSOC
      COMMON ENVMM0,ENVMM1,ENVMM2,ENVMM3,ENVMM4,ENVMM5
C
C NUMBER OF EQUATIONS USED IN THE SIMULATION MODEL
C
```

```
      NEQN = 24
C
C DATA (KG,M,S,KG-MOL): PHYSICAL PROPERTIES AND CONSTANS
C
      DATA BACLMW,SOSUMW /2.08236D2,1.42036D2/
      DATA BASUMW,SOCLMW /2.33386D2,1.16886D2/
      DATA CRYDEN,CRYDIF /4.5D3,9.55D-10/
      DATA REACCO,SHAFAC /6.3D5,8.17D0/
      DATA DENSOL,VISSOL /1.0D3,1.0D-6/
      SOLPRO = 10**(-9.96)
C
C DATA (KG,M,S,KG-MOL): EXPERIMENTAL OPERATING CONDITIONS
C
      DATA TANDIA,TANHEI /0.292D0,0.292D0/
      DATA PBTDIA,PBTCLE /0.1016D0,0.097D0/
      DATA PBTSPE,POWNUM /300.0D0,1.35D0/
      DATA VOLRAT,CONSOS,STOICH /50.0D0,0.0045D0,1.0D0/
      PBTSPE = PBTSPE/60.0
      IFEEDT = 2700
      NUMDRO = 100
      NSUBDR = 10000
C
C DATA (KG,M,S,KG-MOL): FEED POSITION
C
      DATA IFEEDP,MODNUC,MODGRO /1,1,1/

      IF (IFEEDP .EQ. 1) THEN
        ZPOSIT = TANHEI*0.10
        RPOSIT = PBTDIA*0.25
        APOSIT = 45.0D0
      ELSE
        ZPOSIT = (TANHEI-PBTCLE)*0.95
        RPOSIT = PBTDIA*0.25
        APOSIT = 45.0D0
      END IF
C
C THIS INFORMATION HAS TO BE MODIFIED
C ACCORDING TO THE ACTUAL GRID GENERATION
C
      DATA J1,J2,NJOLD,K1,K2,K3,K4,K5,NKOLD /10,17,22,23,26,32,33,37,42/
C
C VERIFICATION OF INITIAL DROP POSITION
C
      IINIT = INT(APOSIT*NI/360.0D0)

      JINIT = NJ
```

```
      IF (RPOSIT .LE. 0.5*TANDIA/NJOLD) THEN
        JINIT = 1
      END IF

      IF ((RPOSIT .GT. 0.5*TANDIA/NJOLD) .AND.
     *   (RPOSIT .LE. 0.5*TANDIA*J1/NJOLD)) THEN
        JINIT = 2+INT((RPOSIT-0.5*TANDIA/NJOLD)*2*NJOLD/(0.5*TANDIA))
      END IF

      IF ((RPOSIT .GT. 0.5*TANDIA*J1/NJOLD) .AND.
     *   (RPOSIT .LE. 0.5*TANDIA*J2/NJOLD)) THEN
        JINIT = 2*J1+INT((RPOSIT-0.5*TANDIA*J1/NJOLD)*NJOLD/(0.5*TANDIA))
      END IF

      IF ((RPOSIT .GT. 0.5*TANDIA*J2/NJOLD) .AND.
     *   (RPOSIT .LE. 0.5*TANDIA*(NJOLD-1)/NJOLD)) THEN
        JINIT = J1+J2-1+
     *        INT((RPOSIT-0.5*TANDIA*J2/NJOLD)*2*NJOLD/(0.5*TANDIA))
      END IF

      KINIT = NK

      IF (ZPOSIT .LE. TANHEI*K1/NKOLD) THEN
        KINIT = 1+INT(ZPOSIT*NKOLD/TANHEI)
      END IF

      IF ((ZPOSIT .GT. TANHEI*K1/NKOLD) .AND.
     *   (ZPOSIT .LE. TANHEI*K2/NKOLD)) THEN
        KINIT = K1+INT((ZPOSIT-TANHEI*K1/NKOLD)*2*NKOLD/TANHEI)
      END IF

      IF ((ZPOSIT .GT. TANHEI*K2/NKOLD) .AND.
     *   (ZPOSIT .LE. TANHEI*K3/NKOLD)) THEN
        KINIT = 2*K2-K1+INT((ZPOSIT-TANHEI*K2/NKOLD)*4*NKOLD/TANHEI)
      END IF

      IF ((ZPOSIT .GT. TANHEI*K3/NKOLD) .AND.
     *   (ZPOSIT .LE. TANHEI*K4/NKOLD)) THEN
        KINIT = 4*K3-2*K2-K1+INT((ZPOSIT-
     *             TANHEI*K3/NKOLD)*2*NKOLD/TANHEI)
      END IF

      IF ((ZPOSIT .GT. TANHEI*K4/NKOLD) .AND.
     *   (ZPOSIT .LE. TANHEI*K5/NKOLD)) THEN
        KINIT = 2*K4+2*K3-2*K2-K1+
```

```
     *       INT((ZPOSIT-TANHEI*K4/NKOLD)*2*NKOLD/TANHEI)
      END IF

      IF ((ZPOSIT .GT. TANHEI*K5/NKOLD) .AND.
     *   (ZPOSIT .LE. TANHEI*(NKOLD-1)/NKOLD)) THEN
        KINIT = K5+K4+2*K3-2*K2-K1+
     *       INT((ZPOSIT-TANHEI*K5/NKOLD)*2*NKOLD/TANHEI)
      END IF

      LINIT = LINDEX(IINIT,JINIT,KINIT)

      IF (ICELL(LINIT) .EQ. ICL) GO TO 100

      PRINT*,'  INITIAL DROP POSITION IS NOT A LIVE CELL'

      GO TO 1000
C
C INITIAL SUBDROPS POSITION
C
 100  TURKIN = E(LINIT)
      ENDIRA = D(LINIT)
      TOTVEL = DSQRT(UCO(LINIT)**2+VCO(LINIT)**2+WCO(LINIT)**2)
C
C PRELIMINAR CALCULATIONS
C
      CRBACL = CRYDEN*SHAFAC*BACLMW
      CRSOSU = CRYDEN*SHAFAC*SOSUMW
      CRBASU = CRYDEN*SHAFAC*BASUMW
      CRSOCL = CRYDEN*SHAFAC*SOCLMW
      VOLFAC = SHAFAC/6.0
      AA = (3*VOLFAC/(SHAFAC*REACCO))**0.25
      PI = 3.141592654D0
      PHIVOL = (PI/(6.0*VOLFAC))**(1.0/3.0)
C
C CALCULATION OF ENVIRONMENT INITIAL VOLUME
C
      ENVVOL = (PI/4)*TANDIA**2*TANHEI
C
C CALCULATION OF CIRCULATION CAPACITY AND TIME
C
      CIRCAP = 2.0*0.75*PBTSPE*PBTDIA**3
      CIRTIM = ENVVOL/CIRCAP
C
C CALCULATION OF TOTAL FEED ADDITION TIME
C
      FEEDRA = (ENVVOL/(VOLRAT*IFEEDT))
```

```
C
C CALCULATION OF DROP INITIAL VIOLUME
C
      DROVOL = ENVVOL/(VOLRAT*NUMDRO)
      DRVOIN = DROVOL
      TOTVOL = ENVVOL+DROVOL
C
C CALCULATION OF INITIAL LOCAL VALUE OF MP VOLUME FRACTION
C
      VOLFRA = DROVOL/(DROVOL+ENVVOL)
C
C CALCULATION OF COMPONENT INITIAL MASS
C
      CONBAC = CONSOS*STOICH
      ENVBAC = CONBAC*(1+1/VOLRAT)*BACLMW
      DRSOIN = CONSOS*(1+VOLRAT)*SOSUMW
      DROSOS = DRSOIN*DRVOIN
      BACMIN = ENVBAC*ENVVOL
      SOSMIN = DRSOIN*DROVOL
      TOTMAS = BACMIN+SOSMIN
C
C PRINT INITIAL DATA (SCREEN)
C
      PRINT*,' ************************************************'
      PRINT*,'          MIXING SYSTEM CONFIGURATION'
      PRINT 2000
      PRINT 2100,TANDIA,TANHEI,TANDIA/10.0
      PRINT 2200
      PRINT 2300,PBTDIA,PBTCLE,PBTSPE
      PRINT*,''
      PRINT*,'       EXPERIMENTAL OPERATING CONDITIONS'
      PRINT 2400
      PRINT 2500,CONSOS,VOLRAT,STOICH
      PRINT*,''
      IF (IFEEDP .EQ. 1) THEN
        PRINT*,'              FEED POSITION I'
      ELSE
        PRINT*,'              FEED POSITION II'
      END IF
      PRINT 2600
      PRINT 2700,ZPOSIT,RPOSIT,APOSIT
      PRINT*,''
      PRINT*,'             INITIAL CONDITIONS'
      PRINT 2800
      PRINT 2900,BACMIN,SOSMIN,TOTMAS
      PRINT 3000
```

```
      PRINT 3100,ENVVOL,DROVOL,TOTVOL
      PRINT*,''
      PRINT 3200,VOLFRA
      PRINT*,' ************************************************'
 2000 FORMAT(5x,5x,'T (m)',10x,'H (m)',10x,'W (m)')
 2100 FORMAT(5x,2x,3(F8.3,7x))
 2200 FORMAT(5x,5x,'D (m)',10x'C (m)',9x,'N (s-1)')
 2300 FORMAT(5x,2x,F8.3,7x,F8.3,6x,F8.1)
 2400 FORMAT(5x,1x,'CBO (Kg/m3)',8x,'VOL RAT',8x,'STOICH')
 2500 FORMAT(5x,2x,F8.4,7x,F8.1,6x,F8.1)
 2600 FORMAT(5x,5x,'Z (m)',10x,'R (m)',7x,'A (DEGREE)')
 2700 FORMAT(5x,2x,2(F8.3,7x),F7.1)
 2800 FORMAT(5x,3x,'BaCl (Kg)',5x,'Na2SO4 (Kg)',5x,'TOTAL (Kg)')
 2900 FORMAT(5x,3x,3(E10.4,5x))
 3000 FORMAT(5x,2x,'ENV VOL (m3)',2x,'DROP VOL (m3)',4x,'TOTAL (m3)')
 3100 FORMAT(5x,3x,3(E10.4,5x))
 3200 FORMAT(5x,5x,'MP ZONE INITIAL VOL FRAC = ',E10.4)
C
C SOLUTION OF SIMULATION MODEL
C
      RELERR = 1.0D-8
      ABSERR = 1.0D-8
      MAXDER = 0
      NBRENT = 0
      NDROPS = 1

      PRINT 3300
 3300 FORMAT(2x,'No',4x,'T (sec)',3x,'L (um)',5x,'C.V.',
     *       4x,'IFLAG',2x,'DER',3x,'ITE')

  200 IF (NDROPS .GT. NUMDRO) GO TO 1100

      DO 300 I=1,NSUBDR
        APOS(I) = APOSIT
        RPOS(I) = RPOSIT
        ZPOS(I) = ZPOSIT
  300 CONTINUE

      IF (NDROPS .EQ. 1) THEN

        OPEN(10,FILE='SAT4A300FI.DATA')

        WRITE(10,3400)
 3400   FORMAT(26x,'SIMPBT4A300')

        IF (IFEEDP .EQ. 1) THEN
```

```
        WRITE(10,3500)
3500    FORMAT(10x,'SUPERSATURATION PROFILE: FEED POSITION I')
      ELSE
        WRITE(10,3600)
3600    FORMAT(10x,'SUPERSATURATION PROFILE: FEED POSITION II')
      END IF

      WRITE(10,*)''

      WRITE(10,3700)
3700  FORMAT(9x,'Time',3x,'Supersaturation',3x,'BaCl',7x,'Na2SO4')
      WRITE(10,3800)
3800  FORMAT(9x,'sec',9x,'ratio',7x,'Kmol/m3',5x,'Kmol/m3')

    END IF
C
C INITIALIZATION OF VALUES
C
    TIN = IFEEDT*(NDROPS-1)*1.0D0/NUMDRO
    TOUT = IFEEDT*NDROPS*1.0D0/NUMDRO

    IFLAG = -1
C
C Y(1-12) ARE DEFINED FOR THE MIXING-PRECIPITATION (MP) ZONE:
C Y(1) = VOLUME, Y(2) = VOLUME FRACTION
C
    Y(1) = DROVOL
    Y(2) = VOLFRA
C
C MOLAR CONCENTRATIONS:
C Y(3) = BaCl2, Y(4) = Na2SO4, Y(5) = BaSO4, Y(6) = 2*NaCl
C
    Y(3) = 0.0
    Y(4) = DRSOIN
    Y(5) = 0.0
    Y(6) = 0.0
C
C MOMENTS:
C Y(7) = ZEROTH MOMENT, Y(8) = FIRST MOMENT, Y(9) = SECOND MOMENT,
C Y(10) = THIRD MOMENT, Y(11) = FOURTH MOMENT, Y(12) = FIFTH
MOMENT
C
    Y(7)  = 0.0
    Y(8)  = 0.0
    Y(9)  = 0.0
    Y(10) = 0.0
```

```
      Y(11) = 0.0
      Y(12) = 0.0
C
C Y(13) IS DEFINED FOR THE SEGREGATED FLUID ZONE:
C Y(13) = VOLUME FRACTION
C
      Y(13) = VOLFRA
C
C Y(14-23) ARE DEFINED FOR THE ENVIRONMENT ZONE:
C Y(14) = VOLUME
C
      Y(14) = ENVVOL
C
C MOLAR CONCENTRATIONS:
C Y(15) = BaCl2, Y(16) = Na2SO4, Y(17) = BaSO4, Y(18) = 2*NaCl
C
      Y(15) = ENVBAC
      Y(16) = ENVSOS
      Y(17) = ENVBAS
      Y(18) = ENVSOC
C
C MOMENTS:
C Y(19) = ZEROTH MOMENT, Y(20) = FIRST MOMENT,
C Y(21) = SECOND MOMENT,
C Y(22) = THIRD MOMENT, Y(23) = FOURTH MOMENT,
C Y(24) = FIFTH MOMENT
C
      Y(19) = ENVMM0
      Y(20) = ENVMM1
      Y(21) = ENVMM2
      Y(22) = ENVMM3
      Y(23) = ENVMM4
      Y(24) = ENVMM5
C
C CALCULATION OF AVERAGE TURBULENCE PARAMETERS
C AND ENGULFMENT FACTOR
C
 400  TURDIF = (0.09/0.7)*TURKIN**2/ENDIRA
      ENGULF = (DLOG(2.0D0)/12.0D0)*DSQRT(ENDIRA/VISSOL)
C
C CALCULATION OF MESO- AND MICROMIXING TIME CONSTANTS
C
      TD = FEEDRA/(TOTVEL*TURDIF)
      AC = DSQRT(FEEDRA/(PI*TOTVEL))
      TS = 2.0*(AC**2/ENDIRA)**(1.0/3.0)
      TIMESO = DMAX1(TD,TS)
```

```
      TIMICR = 1.0/ENGULF
C
C CALL SOLVER
C
      CALL GERK(F, NEQN, Y, TIN, TOUT, RELERR, ABSERR, IFLAG,
     * GERROR, WORK, IWORK)

      IF (NDROPS .EQ. 10000) THEN
        WRITE(10,3900) TIN,DROSAT,Y(3)/BACLMW,Y(4)/SOSUMW
 3900   FORMAT(5x,F8.2,'*',2x,F10.2,'*',4x,F8.4,'*',3x,F8.4)
      END IF

      IF (IFLAG .EQ. 3) THEN
          MAXDER = MAXDER + 1
      END IF

      IF (IFLAG .GT. 3) GO TO 800

      IF (TIN .GE. TOUT) GO TO 900
C
C PHASE DISPERSION
C
      TURKIN = 0.0
      ENDIRA = 0.0
      TOTVEL = 0.0
      VOLUME = 0.0

      DO 600 I = 1,NSUBDR

        AINIT = APOS(I)
        RINIT = RPOS(I)
        ZINIT = ZPOS(I)

        IINIT = INT(APOS(I)*NI/360.0D0)

        IF (IINIT .LT. 3) IINIT = 3

        JINIT = NJ

        IF (RPOS(I) .LE. 0.5*TANDIA/NJOLD) THEN
          JINIT = 1
        END IF

        IF ((RPOS(I) .GT. 0.5*TANDIA/NJOLD) .AND.
     *      (RPOS(I) .LE. 0.5*TANDIA*J1/NJOLD)) THEN
          JINIT = 2+INT((RPOS(I)-0.5*TANDIA/NJOLD)*2*NJOLD/(0.5*TANDIA))
```

```
      END IF

      IF ((RPOS(I) .GT. 0.5*TANDIA*J1/NJOLD) .AND.
     *    (RPOS(I) .LE. 0.5*TANDIA*J2/NJOLD)) THEN
        JINIT = 2*J1+INT((RPOS(I)-
     *             0.5*TANDIA*J1/NJOLD)*NJOLD/(0.5*TANDIA))
      END IF

      IF ((RPOS(I) .GT. 0.5*TANDIA*J2/NJOLD) .AND.
     *    (RPOS(I) .LE. 0.5*TANDIA*(NJOLD-1)/NJOLD)) THEN
        JINIT = J1+J2-1+
     *          INT((RPOS(I)-0.5*TANDIA*J2/NJOLD)*2*NJOLD/(0.5*TANDIA))
      END IF

      IF (JINIT .LT. 3) JINIT = 3

      KINIT = NK

      IF (ZPOS(I) .LE. TANHEI*K1/NKOLD) THEN
        KINIT = 1+INT(ZPOS(I)*NKOLD/TANHEI)
      END IF

      IF ((ZPOS(I) .GT. TANHEI*K1/NKOLD) .AND.
     *    (ZPOS(I) .LE. TANHEI*K2/NKOLD)) THEN
        KINIT = K1+INT((ZPOS(I)-TANHEI*K1/NKOLD)*2*NKOLD/TANHEI)
      END IF

      IF ((ZPOS(I) .GT. TANHEI*K2/NKOLD) .AND.
     *    (ZPOS(I) .LE. TANHEI*K3/NKOLD)) THEN
        KINIT = 2*K2-K1+INT((ZPOS(I)-
     *             TANHEI*K2/NKOLD)*4*NKOLD/TANHEI)
      END IF

      IF ((ZPOS(I) .GT. TANHEI*K3/NKOLD) .AND.
     *    (ZPOS(I) .LE. TANHEI*K4/NKOLD)) THEN
        KINIT = 4*K3-2*K2-K1+INT((ZPOS(I)-
     *            TANHEI*K3/NKOLD)*2*NKOLD/TANHEI)
      END IF

      IF ((ZPOS(I) .GT. TANHEI*K4/NKOLD) .AND.
     *    (ZPOS(I) .LE. TANHEI*K5/NKOLD)) THEN
        KINIT = 2*K4+2*K3-2*K2-K1+
     *          INT((ZPOS(I)-TANHEI*K4/NKOLD)*2*NKOLD/TANHEI)
      END IF

      IF ((ZPOS(I) .GT. TANHEI*K5/NKOLD) .AND.
```

```
*      (ZPOS(I) .LE. TANHEI*(NKOLD-1)/NKOLD)) THEN
       KINIT = K5+K4+2*K3-2*K2-K1+
*            INT((ZPOS(I)-TANHEI*K5/NKOLD)*2*NKOLD/TANHEI)
       END IF

       IF (KINIT .LT. 3) KINIT = 3

       LINIT = LINDEX(IINIT,JINIT,KINIT)
C
C GENERATION OF NORMALLY DISTRIBUTED RANDOM NUMBERS
C

         RANUN1 = RAND(KINIT*I*1.0/NSUBDR)
         IF (RANUN1 .EQ. 0.0) RANUN1 = 1D-5
         RANUN2 = RAND(JINIT*I*1.0/NSUBDR)
         IF (RANUN2 .EQ. 0.0) RANUN2 = 1D-5
         RANUN3 = RAND(IINIT*I*1.0/NSUBDR)
         IF (RANUN3 .EQ. 0.0) RANUN3 = 1D-5
         RANUN4 = RAND((KINIT+JINIT+IINIT)*I*0.33/NSUBDR)
         IF (RANUN4 .EQ. 0.0) RANUN4 = 1D-5

         RANNO1 = DSQRT(-2*DLOG(RANUN1))*DCOS(2*PI*RANUN2)
         RANNO2 = DSQRT(-2*DLOG(RANUN1))*DSIN(2*PI*RANUN2)
         RANNO3 = DSQRT(-2*DLOG(RANUN3))*DCOS(2*PI*RANUN4)
         RANNO4 = DSQRT(-2*DLOG(RANUN3))*DSIN(2*PI*RANUN4)

       UVELOC = UCO(LINIT)+RANNO1*DSQRT(UU(LINIT))
       VVELOC = VCO(LINIT)+RANNO2*DSQRT(VV(LINIT))
       WVELOC = WCO(LINIT)+RANNO3*DSQRT(WW(LINIT))
       TVELOC = DSQRT(UVELOC**2+VVELOC**2+WVELOC**2)

       APOS(I) = APOS(I)+(WVELOC*360/(2*PI*RPOS(I)))*WORK(NEQN+1)
       RPOS(I) = RPOS(I)+VVELOC*WORK(NEQN+1)
       ZPOS(I) = ZPOS(I)+UVELOC*WORK(NEQN+1)

       IF (APOS(I) .GT. 360) THEN
         APOS(I) = APOS(I)-INT(APOS(I)/360)*360.0
       END IF

       IF (APOS(I) .LT. 0) THEN
         APOS(I) = APOS(I)-(INT(APOS(I)/360)-1)*360
       END IF

       INEXT = INT(APOS(I)*NI/360)

       JNEXT = NJ
```

```
      IF (RPOS(I) .LE. 0.5*TANDIA/NJOLD) THEN
        JNEXT = 1
      END IF

      IF ((RPOS(I) .GT. 0.5*TANDIA/NJOLD) .AND.
     *    (RPOS(I) .LE. 0.5*TANDIA*J1/NJOLD)) THEN
        JNEXT = 2+INT((RPOS(I)-0.5*TANDIA/NJOLD)*2*NJOLD/(0.5*TANDIA))
      END IF

      IF ((RPOS(I) .GT. 0.5*TANDIA*J1/NJOLD) .AND.
     *    (RPOS(I) .LE. 0.5*TANDIA*J2/NJOLD)) THEN
        JNEXT = 2*J1+INT((RPOS(I)-
     *              0.5*TANDIA*J1/NJOLD)*NJOLD/(0.5*TANDIA))
      END IF

      IF ((RPOS(I) .GT. 0.5*TANDIA*J2/NJOLD) .AND.
     *    (RPOS(I) .LE. 0.5*TANDIA*(NJOLD-1)/NJOLD)) THEN
        JNEXT = J1+J2-1+
     *        INT((RPOS(I)-0.5*TANDIA*J2/NJOLD)*2*NJOLD/(0.5*TANDIA))
      END IF

      KNEXT = NK

      IF (ZPOS(I) .LE. TANHEI*K1/NKOLD) THEN
        KNEXT = 1+INT(ZPOS(I)*NKOLD/TANHEI)
      END IF

      IF ((ZPOS(I) .GT. TANHEI*K1/NKOLD) .AND.
     *    (ZPOS(I) .LE. TANHEI*K2/NKOLD)) THEN
        KNEXT = K1+INT((ZPOS(I)-TANHEI*K1/NKOLD)*2*NKOLD/TANHEI)
      END IF

      IF ((ZPOS(I) .GT. TANHEI*K2/NKOLD) .AND.
     *    (ZPOS(I) .LE. TANHEI*K3/NKOLD)) THEN
        KNEXT = 2*K2-K1+INT((ZPOS(I)-
     *              TANHEI*K2/NKOLD)*4*NKOLD/TANHEI)
      END IF

      IF ((ZPOS(I) .GT. TANHEI*K3/NKOLD) .AND.
     *    (ZPOS(I) .LE. TANHEI*K4/NKOLD)) THEN
        KNEXT = 4*K3-2*K2-K1+INT((ZPOS(I)-
     *              TANHEI*K3/NKOLD)*2*NKOLD/TANHEI)
      END IF

      IF ((ZPOS(I) .GT. TANHEI*K4/NKOLD) .AND.
```

```
*      (ZPOS(I) .LE. TANHEI*K5/NKOLD)) THEN
       KNEXT = 2*K4+2*K3-2*K2-K1+
*            INT((ZPOS(I)-TANHEI*K4/NKOLD)*2*NKOLD/TANHEI)
       END IF

       IF ((ZPOS(I) .GT. TANHEI*K5/NKOLD) .AND.
*      (ZPOS(I) .LE. TANHEI*(NKOLD-1)/NKOLD)) THEN
       KNEXT = K5+K4+2*K3-2*K2-K1+
*            INT((ZPOS(I)-TANHEI*K5/NKOLD)*2*NKOLD/TANHEI)
       END IF

       LNEXT = LINDEX(INEXT,JNEXT,KNEXT)

       IF (ICELL(LNEXT) .EQ. ICL) GO TO 500
C
C REFLECTION
C
       IF ((KNEXT .LT. 3) .OR. (KNEXT .GT. NK-2)) THEN
         KNEXT = KINIT
         ZPOS(I) = ZINIT
         JNEXT = JNEXT+(JNEXT-JINIT)
         RPOS(I) = RPOS(I)+(RPOS(I)-RINIT)
       END IF

       IF ((JNEXT .LT. 3) .OR. (JNEXT .GT. NJ-2)) THEN
         JNEXT = JINIT
         RPOS(I) = RINIT
         KNEXT = KNEXT+(KNEXT-KINIT)
         ZPOS(I) = ZPOS(I)+(ZPOS(I)-ZINIT)
       END IF

       INEXT = INEXT+(INEXT-IINIT)

       IF (INEXT .LT. 0) THEN
         INEXT = INEXT-(INT(INEXT/NI)-1)*NI
       END IF

       IF (INEXT .GT. NI) THEN
         INEXT = INEXT-(INT(INEXT/NI))*NI
       END IF

       IF (INEXT .EQ. 0) THEN
         INEXT = NI-2
       END IF

       APOS(I) = (1.0*INEXT/NI)*360.0
```

```
      LNEXT = LINDEX(INEXT,JNEXT,KNEXT)

      IF (ICELL(LNEXT) .EQ. ICL) GO TO 500
C
C SALTATION: WALLS
C
      IF (JNEXT .LT. 4) THEN
        JNEXT = 4
        RPOS(I) = 0.0133
      END IF

      IF (JNEXT .GT. NJ-2) THEN
        JNEXT = NJ-2
        RPOS(I) = 0.133
      END IF

      IF (KNEXT .LT. 3) THEN
        KNEXT = 3
        ZPOS(I) = 0.0195
      END IF

      IF (KNEXT .GT. NK-2) THEN
        KNEXT = NK-2
        ZPOS(I) = 0.28
      END IF

      LNEXT = LINDEX(INEXT,JNEXT,KNEXT)

      IF (ICELL(LNEXT) .EQ. ICL) GO TO 500
C
C SALTATION: BAFFLES
C
      IF ((INEXT .EQ. 1) .OR. (INEXT .EQ. 2) .OR.
     *    (INEXT .EQ. 37) .OR. (INEXT .EQ. 38) .OR.
     *    (INEXT .EQ. 73) .OR. (INEXT .EQ. 74) .OR.
     *    (INEXT .EQ. 109) .OR. (INEXT .EQ. 110) .OR.
     *    (INEXT .EQ. 145) .OR. (INEXT .EQ. 146)) THEN
        IF (JNEXT .GE. 26) THEN
          JNEXT = 25
          RPOS(I) = 0.098
        END IF
      END IF

      LNEXT = LINDEX(INEXT,JNEXT,KNEXT)
```

```
      IF (ICELL(LNEXT) .EQ. ICL) GO TO 500
C
C SALTATION: HUB
C
      IF ((KNEXT .GE. 32) .OR. (KNEXT .LE. 39)) THEN
        IF (JNEXT .LE. 5) THEN
          JNEXT = 6
          RPOS(I) = 0.020
        END IF
      END IF

      LNEXT = LINDEX(INEXT,JNEXT,KNEXT)
C
C SALTATION: IMPELLER
C
      IF ((INEXT .EQ. 11) .OR. (INEXT .EQ. 12) .OR.
     *    (INEXT .EQ. 35) .OR. (INEXT .EQ. 36) .OR.
     *    (INEXT .EQ. 59) .OR. (INEXT .EQ. 60) .OR.
     *    (INEXT .EQ. 83) .OR. (INEXT .EQ. 84) .OR.
     *    (INEXT .EQ. 131) .OR. (INEXT .EQ. 132) .OR.
     *    (INEXT .EQ. 145) .OR. (INEXT .EQ. 146)) THEN
        IF (JNEXT .LE. 15) THEN
          INEXT = INEXT-2
          APOS(I) = (1.0*INEXT/NI)*360.0
        END IF
      END IF

      LNEXT = LINDEX(INEXT,JNEXT,KNEXT)

500    TURKIN = TURKIN + E(LNEXT)
      ENDIRA = ENDIRA + D(LNEXT)
      TOTVEL = TOTVEL + TVELOC
      VOLUME = VOLUME + YACOB(LNEXT)

600  CONTINUE

    TURKIN = TURKIN/NSUBDR
    ENDIRA = ENDIRA/NSUBDR
    TOTVEL = TOTVEL/NSUBDR

    GO TO 400

700  IF (IFLAG .EQ. 2) THEN
        PRINT*,' <NOTE> IFLAG = 2:'
        PRINT 4000,TOUT
4000    FORMAT (9x,'SUCCESSFUL INTEGRATION REACHED TOUT =',F8.2)
```

```
      END IF

      IF (IFLAG .EQ. -2) THEN
          PRINT*,' <NOTE> IFLAG = -2:'
          PRINT*,'      A SINGLE SUCCESFUL STEP IN THE DIRECTION'
        PRINT*,'      OF TOUT HAS BEEN TAKEN'
      END IF

      GO TO 900

  800 IF (IFLAG .EQ. 4) THEN
          PRINT*,' <NOTE> IFLAG = 4:'
          PRINT*,'      INTEGRATION WAS NOT COMPLETED BECAUSE'
          PRINT*,'      SOLUTION VANISHED MAKING A PURE RELATIVE'
          PRINT*,'      ERROR TEST IMPOSSIBLE.'
          PRINT*,'      (CHANGES THE NUMBER OF DROPS)'
      END IF

      IF (IFLAG .EQ. 5) THEN
          PRINT*,' <NOTE> IFLAG = 5:'
          PRINT*,'      INTEGRATION WAS NOT COMPLETED BECAUSE'
          PRINT*,'      REQUESTED ACCURACY COULD NOT BE ACHIEVED'
          PRINT*,'      USING SMALLEST ALLOWABLE STEPSIZE.'
          PRINT*,'      (INCREASES THE ERROR TOLERANCE)'
      END IF

      IF (IFLAG .EQ. 6) THEN
          PRINT*,' <NOTE> IFLAG = 6:'
          PRINT*,'      SOLVER IS BEING USED INEFFICIENTLY.'
          PRINT*,'      (USE THE ONE-STEP INTEGRATOR MODE)'
      END IF

      IF (IFLAG .EQ. 7) THEN
          PRINT*,' <NOTE> IFLAG = 7:'
          PRINT*,'      INVALID INPUT PARAMETERS'

          IF (NEQN .LE. 0) THEN
            PRINT*,'      NEQN .LT. 0'
        END IF

          IF ((TIN .EQ. TOUT) .AND. (ABS(IFLAG) .NE. 1)) THEN
            PRINT*,'      INITIAL TIME .EQ. FINAL TIME'
        END IF

          IF (RELERR .LT. 0) THEN
            PRINT*,'      RELERR .LT. 0'
```

```
      END IF

        IF (ABSERR .LT. 0) THEN
          PRINT*,'      ABSERR .LT. 0'
        END IF

    END IF

    GO TO 1000
C
C FINAL MP ZONE VOLUME, MP ZONE VOLUME FRACTION, AND
ENVIRONMENT VOLUME
C
 900  DROVOL = Y(1)
    VOLFRA = Y(2)
    ENVVOL = Y(14)
C
C FINAL MP ZONE COMPONENT MASS
C
    DROBAC = Y(1)*Y(3)
    DROSOS = Y(1)*Y(4)
    DROBAS = Y(1)*Y(5)
    DROSOC = Y(1)*Y(6)
C
C FINAL ENVIRONMENT ZONE COMPONENT MASS
C
    ENVBAC = Y(14)*Y(15)
    ENVSOS = Y(14)*Y(16)
    ENVBAS = Y(14)*Y(17)
    ENVSOC = Y(14)*Y(18)
C
C CALCULATION OF TOTAL MASS
C
    BACMAS = ENVBAC+DROBAC
    SOSMAS = ENVSOS+DROSOS
    BASMAS = ENVBAS+DROBAS
    SOCMAS = ENVSOC+DROSOC
    TOTMAS = BACMAS+SOSMAS+BASMAS+SOCMAS
C
C FINAL MP ZONE MOMENTS
C
    DROMM0 = Y(1)*Y(7)
    DROMM1 = Y(1)*Y(8)
    DROMM2 = Y(1)*Y(9)
    DROMM3 = Y(1)*Y(10)
    DROMM4 = Y(1)*Y(11)
```

```
      DROMM5 = Y(1)*Y(12)
C
C FINAL ENVIRONMENT ZONE MOMENTS
C
      ENVMM0 = Y(14)*Y(19)
      ENVMM1 = Y(14)*Y(20)
      ENVMM2 = Y(14)*Y(21)
      ENVMM3 = Y(14)*Y(22)
      ENVMM4 = Y(14)*Y(23)
      ENVMM5 = Y(14)*Y(24)
C
C CALCULATION OF TOTAL MOMENTS
C
      TOTMM0 = ENVMM0+DROMM0
      TOTMM1 = ENVMM1+DROMM1
      TOTMM2 = ENVMM2+DROMM2
      TOTMM3 = ENVMM3+DROMM3
      TOTMM4 = ENVMM4+DROMM4
      TOTMM5 = ENVMM5+DROMM5
C
C CALCULATION OF CRYSTAL SIZE AND COEFFICIENT OF VARIATION
C
      IF (TOTMM3 .GT. 0.0) THEN
          AMWMCS = TOTMM4*1.0D6/(TOTMM3*PHIVOL)
      ENDIF

      IF (TOTMM4**2 .GT. 0.0) THEN

          IF (TOTMM3*TOTMM5 .LT. TOTMM4**2) THEN
            COEVAR = 0.0
          ELSE
            COEVAR = DSQRT(TOTMM3*TOTMM5/TOTMM4**2-1)
          END IF

      ENDIF
C
C CALCULATION OF ERROR AND CONVERSION IN MASS BALANCE
C
      BACTHE = (SOSMIN*NDROPS-SOSMAS)*BACLMW/SOSUMW
      ERRORM = ((BACMIN-BACMAS)-BACTHE)*100/BACTHE
      CONVER = 1-SQRT(BACMAS*SOSMAS/(BACMIN*SOSMIN*NDROPS))
      CLOSUR = (1-TOTMAS/(BACMIN+SOSMIN*NDROPS))*100
C
C UPDATE OF ENVIRONMENT BEFORE NEXT DROP
C
      ENVVOL = ENVVOL+DROVOL
```

```
      ENVBAC = BACMAS/ENVVOL
      ENVSOS = SOSMAS/ENVVOL
      ENVBAS = BASMAS/ENVVOL
      ENVSOC = SOCMAS/ENVVOL
      ENVMM0 = TOTMM0/ENVVOL
      ENVMM1 = TOTMM1/ENVVOL
      ENVMM2 = TOTMM2/ENVVOL
      ENVMM3 = TOTMM3/ENVVOL
      ENVMM4 = TOTMM4/ENVVOL
      ENVMM5 = TOTMM5/ENVVOL
C
C INITIALIZATION OF NEXT DROP
C
      DROBAC = 0.0
      DROSOS = DRSOIN*DRVOIN
      DROBAS = 0.0
      DROSOC = 0.0
      DROMM0 = 0.0
      DROMM1 = 0.0
      DROMM2 = 0.0
      DROMM3 = 0.0
      DROMM4 = 0.0
      DROMM5 = 0.0
      DROVOL = DRVOIN
      VOLFRA = DROVOL/(ENVVOL+DROVOL)
C
C PRINT RESULTS AFTER EACH DROP
C
      PRINT 4600,NDROPS,TOUT,AMWMCS,COEVAR,IFLAG,MAXDER,NBRENT
 4600 FORMAT(I4,2x,F8.2,2x,F8.4,2x,F8.4,2x,I4,2x,I4,2x,I4)

      IF (NDROPS .EQ. NUMDRO) THEN

        OPEN(20,FILE='SIM4A300FI.DATA')
C
C PRINT INITIAL DATA (FILE)
C
      WRITE(20,*)'                SIMPBT4A300FI'
      WRITE(20,*)'                INITIAL  DATA'
      WRITE(20,*)' ************************************************'
      WRITE(20,*)'          MIXING SYSTEM CONFIGURATION'
      WRITE(20,5000)
      WRITE(20,5100) TANDIA,TANHEI,TANDIA/10.0
      WRITE(20,5200)
      WRITE(20,5300) PBTDIA,PBTCLE,PBTSPE
      WRITE(20,*)"
```

```
      WRITE(20,*)'        EXPERIMENTAL OPERATING CONDITIONS'
      WRITE(20,5400)
      WRITE(20,5500) CONSOS,VOLRAT,STOICH
      WRITE(20,*)''
      IF (IFEEDP .EQ. 1) THEN
        WRITE(20,*)'              FEED POSITION I'
      ELSE
        WRITE(20,*)'              FEED POSITION II'
      END IF
      WRITE(20,5600)
      WRITE(20,5700) ZPOSIT,RPOSIT,APOSIT
      WRITE(20,*)''
      WRITE(20,*)'              INITIAL CONDITIONS'
      WRITE(20,5800)
      WRITE(20,5900) BACMIN,SOSMIN,TOTMAS
      WRITE(20,6000)
      WRITE(20,6100) ENVVOL,DROVOL,TOTVOL
      WRITE(20,*)''
      WRITE(20,6200) VOLFRA
      WRITE(20,*)' ***************************************************'
 5000 FORMAT(5x,5x,'T (m)',10x,'H (m)',10x,'W (m)')
 5100 FORMAT(5x,2x,3(F8.3,7x))
 5200 FORMAT(5x,5x,'D (m)',10x'C (m)',9x,'N (s-1)')
 5300 FORMAT(5x,2x,F8.3,7x,F8.3,6x,F8.1)
 5400 FORMAT(5x,1x,'CBO (Kg/m3)',8x,'VOL RAT',8x,'STOICH')
 5500 FORMAT(5x,2x,F8.4,7x,F8.1,6x,F8.1)
 5600 FORMAT(5x,5x,'Z (m)',10x,'R (m)',7x,'A (DEGREE)')
 5700 FORMAT(5x,2x,2(F8.3,7x),F7.1)
 5800 FORMAT(5x,3x,'BaCl (Kg)',5x,'Na2SO4 (Kg)',5x,'TOTAL (Kg)')
 5900 FORMAT(5x,3x,3(E10.4,5x))
 6000 FORMAT(5x,2x,'ENV VOL (m3)',2x,'DROP VOL (m3)',4x,'TOTAL (m3)')
 6100 FORMAT(5x,3x,3(E10.4,5x))
 6200 FORMAT(5x,5x,'MP ZONE INITIAL VOL FRAC = ',E10.4)
C
C PRINT FINAL RESULTS
C
      WRITE(20,*)'              FINAL RESULTS'
      WRITE(20,*)' ***************************************************'
      WRITE(20,7000) TIN
      WRITE(20,7100) NDROPS
      WRITE(20,*)''
      WRITE(20,7200)
      WRITE(20,7300) BACMAS,SOSMAS,BASMAS,SOCMAS
      WRITE(20,*)''
      WRITE(20,7400)
      WRITE(20,7500) TOTMAS,ERRORM,CONVER,CLOSUR
```

```
      WRITE(20,*)''
      WRITE(20,7600)
      WRITE(20,7700) TOTMM0,TOTMM1,TOTMM2,TOTMM3
      WRITE(20,*)''
      WRITE(20,7800)
      WRITE(20,7900) TOTMM4,TOTMM5
      WRITE(20,*)''
      WRITE(20,8000)
      WRITE(20,8100) AMWMCS,COEVAR
      WRITE(20,*)' ************************************************'

7000   FORMAT(4x,15x,'TIME (S) =',F8.2)
7100   FORMAT(4x,19x,'DROP =',I4)
7200   FORMAT(4x,'BaCl  (Kg)',2x,'Na2SO4  (Kg)',2x,'BaSO4 (Kg)'
  *      ,3x,'2NaCl (Kg)')
7300   FORMAT(4x,4(E10.4,3x))
7400   FORMAT(4x,'TOTAL (Kg)',3x,'ERROR  (%)',4x,'CONVERSION'
  *      ,3x,'CLOSURE (%)')
7500   FORMAT(4x,4(E10.4,3x))
7600   FORMAT(4x,1x,'MOM0 (#)',4x,'MOM1 (#-M)',2x,'MOM2  (#-M2)'
  *      ,1x,'MOM3  (#-M3)')
7700   FORMAT(4x,4(E10.4,3x))
7800   FORMAT(4x,11x,'MOM4  (#-M4)',1x,'MOM5  (#-M5)')
7900   FORMAT(16x,2(E10.4,3x))
8000   FORMAT(4x,13x,'SIZE (uM)',5x,'C.V.')
8100   FORMAT(16x,2(F8.4,4x))

      CLOSE(20)

    END IF

    IF (NDROPS .EQ. 1) CLOSE(10)
    NDROPS = NDROPS+1
    MAXDER = 0
    NBRENT = 0
    GO TO 200

1000 PRINT*,'CHECK INITIAL DATA'

1100 PRINT*,'END OF PROGRAM'
```

B.2 Subroutine F

```
C------------------------------------------------------------------------------------------------ C
C                                                                                                 C
C  SUBROUTINE F(TIN,Y,YP) TO EVALUATE DERIVATIVES                                                 C
C                YP(T) = dY(T)/dT                                                                 C
C                                                                                                 C
C------------------------------------------------------------------------------------------------ C
      SUBROUTINE F(TIN,Y,YP)
      IMPLICIT DOUBLE PRECISION (A-H,O-Z)
      DOUBLE PRECISION Y(NEQN),YP(NEQN)
      DOUBLE PRECISION BACLMW,SOSUMW,BASUMW,SOCLMW
      DOUBLE PRECISION CRYDEN,CRYDIF,SHAFAC,VOLFAC
      DOUBLE PRECISION CRBACL,CRSOSU,CRBASU,CRSOCL
      DOUBLE PRECISION AA,BB,PHIVOL,VISSOL,SOLPRO
      DOUBLE PRECISION ENGULF,ENDIRA,TIMESO
      DOUBLE PRECISION ENVBAC,ENVSOS,ENVBAS,ENVSOC
      DOUBLE PRECISION ENVMM0,ENVMM1,ENVMM2,
      DOUBLE PRECISION ENVMM3,ENVMM4,ENVMM5

      COMMON BACLMW,SOSUMW,BASUMW,SOCLMW
      COMMON CRYDEN,CRYDIF,SHAFAC,VOLFAC
      COMMON CRBACL,CRSOSU,CRBASU,CRSOCL
      COMMON NEQN,AA,BB,PHIVOL,VISSOL,SOLPRO,REACCO,DROSAT
      COMMON ENGULF,ENDIRA,TIMESO
      COMMON MODNUC,MODGRO,NBRENT
      COMMON ENVBAC,ENVSOS,ENVBAS,ENVSOC
      COMMON ENVMM0,ENVMM1,ENVMM2,ENVMM3,ENVMM4,ENVMM5

      IZONE = 0
C
C FOR THE MIXING-PRECIPITATION (MP) ZONE : IZONE = 1
C FOR THE ENVIRONMENT ZONE: IZONE = 2
C CALCULATION OF NUCLEATION AND GROWTH RATES
C
 900  IZONE = IZONE + 1
      ANUCLE = 0.0
      GROWTH = 0.0
C
C CALCULATION OF DRIVING FORCES: SUPERSATION AND SATURATION
RATIO
C
      IF (IZONE .EQ. 1) THEN
        BACCON = Y(3)
        SOSCON = Y(4)
```

```
        AMOME3 = Y(10)
        AMOME4 = Y(11)
      ELSE
        BACCON = Y(15)
        SOSCON = Y(16)
        AMOME3 = Y(22)
        AMOME4 = Y(23)
      END IF

      IF ((BACCON .GT. 0.0) .AND. (SOSCON .GT. 0.0)) THEN
          SATRAT = DSQRT((BACCON/BACLMW)*(SOSCON/SOSUMW)/SOLPRO)

          IF (SATRAT .GT. 1) THEN

            SUPSAT = (SATRAT-1.0)*DSQRT(SOLPRO)
C
C CALCULATION OF NUCLEATION RATE:
C MODNUC = 1, BALDYGA et al. (1995)
C MODNUC = 2, DIRKSEN AND RING (1999)
C MODNUC = 3, WEI AND GARSIDE (1997)
C MODNUC = 4, AOUN et al. (1996)
C
          IF (MODNUC .EQ. 1) THEN

            IF (SUPSAT .LT. 1.0D-2) THEN
              ANUCLE = 6.00D15*SUPSAT**1.775
            ELSE
              ANUCLE = 2.53D42*SUPSAT**15
            END IF

          END IF

          IF (MODNUC .EQ. 2) THEN

            IF (SATRAT .LT. 1000) THEN
              ANUCLE = 1.00D11*10.0**(-2.0/(DLOG10(SATRAT))**2)
            ELSE
              ANUCLE = 1.00D36*10.0**(-200.0/(DLOG10(SATRAT))**2)
            END IF

          END IF

          IF (MODNUC .EQ. 3) THEN

            IF (SATRAT .LT. 1000) THEN
              ANUCLE = 1.46D12*DEXP(-67.3/(DLOG(SATRAT))**2)
```

```
          ELSE
            ANUCLE = 1.00D36*DEXP(-2686.0/(DLOG(SATRAT))**2)
          END IF

        END IF


        IF (MODNUC .EQ. 4) THEN

          IF (SUPSAT .LT. 1.0D-2) THEN
            CONRAT = (Y(3)/BACLMW)/(Y(4)/SOSUMW)
            IF (CONRAT .LT. 1.0) THEN
              ANUCLE = 2.5D11*CONRAT**(-1.25)*DEXP(-(14.9+67.57*
     *              DABS(DLOG(CONRAT)))/(DLOG(SATRAT))**2)
            ELSE
              ANUCLE = 2.5D11*CONRAT**(2.28)*DEXP(-(14.9+67.57*
     *              DABS(DLOG(CONRAT)))/(DLOG(SATRAT))**2)
            END IF
          END IF

        END IF

C
C CALCULATION OF MASS TRANSFER COEFFICIENT:
C MODGRO = 1, ARMENANTE AND KIRWAN (1989)
C MODGRO = 2, CONSTANT KD <1D-5, 1D-4>
C MODGRO = 3, WEI AND GARSIDE (1997)
C MODGRO = 4, AOUN et al. (1996)
C
        IF (MODGRO .GE. 3) GO TO 1300

        IF (MODGRO .EQ. 1) THEN

          IF ((AMOME3 .GT. 0) .AND. (AMOME4 .GT. 0)) THEN
            CRYSIZ = AMOME4/(AMOME3*PHIVOL)
          ELSE
            CRYSIZ = 1D-10
          END IF

          SHERWD = 2.0+0.52*(CRYSIZ**(4.0/3.0)*ENDIRA**(1.0/3.0)/VISSOL)
     *          **0.52*(VISSOL/CRYDIF)**(1.0/3.0)
          AMASCO = SHERWD*(CRYDIF/CRYSIZ)*(BASUMW/CRYDEN)

        END IF

        IF (MODGRO .EQ. 2) AMASCO = 4D-5
```

```
          BB = 3*VOLFAC/(SHAFAC*AMASCO)

C-----------------------------------------------------------------------------------------------
C
C  CALCULATION OF GROWTH RATE USING A COMBINATION
C  OF NEWTON-RAPHSON's CONVERGENCE SCHEME AND BISECTION STEP
C
C-----------------------------------------------------------------------------------------------
C
C MAXITE IS THE MAXIMUM ALLOWED NUMBER OF ITERATIONS
C TOLER IS THE ACCURACY
C THE ROOT WILL BE FOUND BETWEEN ALIM AND BLIM
C
        MAXITE = 100
        TOLER = 1D-20
        ITER = 0
        ALIM = 0.0
        BLIM = 0.0001

        FLLOW = AA*ALIM**0.25+BB*ALIM-SUPSAT
        FHIGH = AA*BLIM**0.25+BB*BLIM-SUPSAT

        IF (FLLOW .LT. 0.0) THEN
          XLLOW = ALIM
          XHIGH = BLIM
        ELSE
          XHIGH = ALIM
          XLLOW = BLIM
        END IF

        ABAVG = 0.5*(ALIM+BLIM)
        DXOLD = ABS(BLIM-ALIM)
        DXNEW = DXOLD

        FG = AA*ABAVG**0.25+BB*ABAVG-SUPSAT
        DFG = (AA/4.0)*ABAVG**(-0.75)+BB

1000     ITER = ITER+1

        IF (ITER .GT. MAXITE) GO TO 1100
        XX= ((ABAVG-XHIGH)*DFG-FG)*((ABAVG-XLLOW)*DFG-FG)

        IF ((XX .GE. 0.0) .OR. (ABS(2.0*FG) .GT. ABS(DXOLD*DFG))) THEN
          DXOLD = DXNEW
          DXNEW = 0.5*(XHIGH-XLLOW)
```

```
        ABAVG = XLLOW+DXNEW

        IF (XLLOW.EQ.ABAVG) GO TO 1200

      ELSE
        DXOLD = DXNEW
        DXNEW = FG/DFG
        ABTEM = ABAVG
        ABAVG = ABAVG-DXNEW
        IF (ABTEM .EQ. ABAVG) GO TO 1200
      ENDIF

      IF(ABS(DXNEW) .LT. TOLER) GO TO 1200

      FG = AA*ABAVG**0.25+BB*ABAVG-SUPSAT
      DFG = (AA/4.0)*ABAVG**(-0.75)+BB

      IF (FG .LT. 0.0) THEN
        XLLOW = ABAVG
      ELSE
        XHIGH = ABAVG
      ENDIF

      GO TO 1000

1100    PRINT*,'MAXIMUM NUMBER OF ITERATIONS =',MAXITE
      PRINT*,'WAS EXCEEDED IN GROWTH RATE CALCULATION'

1200    GROWTH = ABAVG

1300    IF (MODGRO .EQ. 3) GROWTH = 4E-11*(SATRAT-1)**2

      IF (MODRGO .EQ. 4) THEN
        CONRAT = (Y(3)/BACLMW)/(Y(4)/SOSUMW)
        IF (CONRAT .LT. 1.0) THEN
          GROWTH = 2.73D-5*10**(-1.99*CONRAT)*(Y(3)/BACLMW-
     *      DSQRT(SOLPRO))**1.15*(Y(4)/SOSUMW-DSQRT(SOLPRO))**0.95
        ELSE
          GROWTH = 1.05D-5*10**(-1.57*CONRAT)*(Y(3)/BACLMW-
     *      DSQRT(SOLPRO))**1.15*(Y(4)/SOSUMW-DSQRT(SOLPRO))**0.95
        END IF
      END IF

       END IF

    END IF
```

```
      IF (IZONE .EQ. 1) THEN
        DRONUC = ANUCLE
        DROGRO = GROWTH
      ELSE
        ENVNUC = ANUCLE
        ENVGRO = GROWTH
      END IF

      IF (IZONE .EQ. 1) GO TO 900
C
C CALCULATION OF MESOMIXING EFFECT
C
      EM = 1.0
C
C CALCULATION OF DERIVATIVE OF SOLUTION VECTOR AT T
C
C FOR MIXING PRECIPITATION (MP) ZONE GROWTH:
C
      YP(1)  = ENGULF*(1-Y(2)*EM)*Y(1)
      YP(2)  = ENGULF*(1-Y(2)*EM)*Y(2)
C
C  FOR MIXING-PRECIPITATION (MP) ZONE MASS BALANCE:
C
      YP(3)  = ENGULF*(1-Y(2)*EM)*(Y(15)-Y(3))-
(CRBACL/(2*BASUMW))*DROGRO*Y(9)
      YP(4)  = ENGULF*(1-Y(2)*EM)*(Y(16)-Y(4))-
(CRSOSU/(2*BASUMW))*DROGRO*Y(9)
      YP(5)  = ENGULF*(1-Y(2)*EM)*(Y(17)-
Y(5))+(CRBASU/(2*BASUMW))*DROGRO*Y(9)
      YP(6)  = ENGULF*(1-Y(2)*EM)*(Y(18)-
Y(6))+(CRSOCL/(2*BASUMW))*DROGRO*Y(9)
C
C FOR MIXING-PRECIPITATION (MP) ZONE MOMENT BALANCE:
C
      YP(7)  = ENGULF*(1-Y(2)*EM)*(Y(19)-Y(7)) +DRONUC
      YP(8)  = ENGULF*(1-Y(2)*EM)*(Y(20)-Y(8)) +1*DROGRO*Y(7)
      YP(9)  = ENGULF*(1-Y(2)*EM)*(Y(21)-Y(9)) +2*DROGRO*Y(8)
      YP(10) = ENGULF*(1-Y(2)*EM)*(Y(22)-Y(10))+3*DROGRO*Y(9)
      YP(11) = ENGULF*(1-Y(2)*EM)*(Y(23)-Y(11))+4*DROGRO*Y(10)
      YP(12) = ENGULF*(1-Y(2)*EM)*(Y(24)-Y(12))+5*DROGRO*Y(11)
C
C FOR SEGREGATED ZONE VOLUME:
C
      YP(13) = (Y(13)/TIMESO)*(1-Y(13))
C
```

```
C FOR ENVIRONMENT ZONE VOLUME:
C
      YP(14) = ENGULF*(Y(2)*EM-1)*Y(1)
C
C  FOR ENVIRONMENT ZONE MASS BALANCE:
C
      YP(15) = -(CRBACL/(2*BASUMW))*ENVGRO*Y(21)
      YP(16) = -(CRSOSU/(2*BASUMW))*ENVGRO*Y(21)
      YP(17) = +(CRBASU/(2*BASUMW))*ENVGRO*Y(21)
      YP(18) = +(CRSOCL/(2*BASUMW))*ENVGRO*Y(21)
C
C FOR ENVIRONMENT ZONE MOMENT BALANCE:
C
      YP(19) = ENVNUC
      YP(20) = 1*ENVGRO*Y(19)
      YP(21) = 2*ENVGRO*Y(20)
      YP(22) = 3*ENVGRO*Y(21)
      YP(23) = 4*ENVGRO*Y(22)
      YP(24) = 5*ENVGRO*Y(23)

      RETURN
      END
```

B.3 Runge-Kutta-Fehlberg (4, 5) Solver

The Runge-Kutta-Fehlberg (4, 5) used to solve the differential equations in the model was obtained from the online numerical library *Netlib Repository*:

Toms/504

Keywords: ODE, IVP, global error estimation, Runge-Kutta-Fehlberg

Gams: I1ala

Title: GERK

For: nonlinear systems of ordinary differential equations with global error estimate integration is performed on different meshes and global extrapolation is used to estimate the global error in the more accurate solution. The integration is done using Runge-Kutta-Fehlberg methods of 4^{th} and 5^{th} order.

By: L. F. Shampire and H. A. Watts (Sandia Laboratories)

Ref: ACM TOMS 2 (1976) 200-203

Score: 100%

Subroutine GERK is used to solve the systems of differential equations in the mixing-precipitation model based on the Runge-Kutta-Fehlberg methods of 4^{th} and 5^{th} order (RKF45). It includes a numerical algorithm in the solution procedure which automatically adjust the integration step time, Δt, as the solution evolves to produce a solution with a user-specified accuracy. An estimate of the error in the numerical solution is made to determine whether the integration Δt step should be changed. Parallel integration is performed to yield two solutions on different mesh spacing and global interpolation is applied to provide an estimate of the global error.

Subroutine GEK was tested by solving a dynamic model for a fluid-bed reactor and comparing the numerical solution with the exact solution:

Aiken, R. C., and Lapidus, L. (1974) An Effective Numerical Integration for Typical Stiff Systems. *A.I.Ch.E. J.*, **20**(2), 368-375.

The comparison between the numerical solution using the Runge-Kutta-Fehlberg (4, 5) and the exact solution is shown in Table A.1:

Table A.1: Dynamic model for a fluid-bed reactor

	y_1	y_2
RKF (4,5)	703.28	9.0667
Exact solution	703.92	9.0502

A second test was made by solving a set of rate equation and comparing the numerical solution with the exact solution:

Robertson, H. H. (1967) Solution of a Set of Reaction Rate Equations, *in Numerical Analysis*. Thompson Book Co. (Edited by J. Wlash), Washington, pp. 78.

The comparison between the numerical solution using the Runge-Kutta-Fehlberg (4, 5) and the exact solution is shown in Table A.2:

Table A.2: Set of reaction rate equations

	y_1	$10^4 \times y_2$	y_3
RKF (4,5)	0.841370	0.162339	0.158614
Exact solution	0.841370	0.162340	0.158614

In both cases, the comparisons show a good agreement between the numerical solutions and the exact solutions, respectively.

APPENDIX C

EQUIPMENT PHOTOGRAPHS

This appendix shows the photograph of the equipments mentioned in Chapter 4 (Experimental Section). These photographs include:

Figure C.1 Laser-Doppler velocimetry
(DANTEC 55X)

Figure C.2 Mixing-Precipitation System
(MIXING LAB-NJIT)

Figure C.3 Coulter Multisizer
(COULTER ELECTRONICS, Model TA))

Figure C.4 Environmental Scanning Electron Microscope
(PHILIPS ELECTRO SCAN 2020)

Figure C.5 Workstation
(SILICON GRAPHICS)

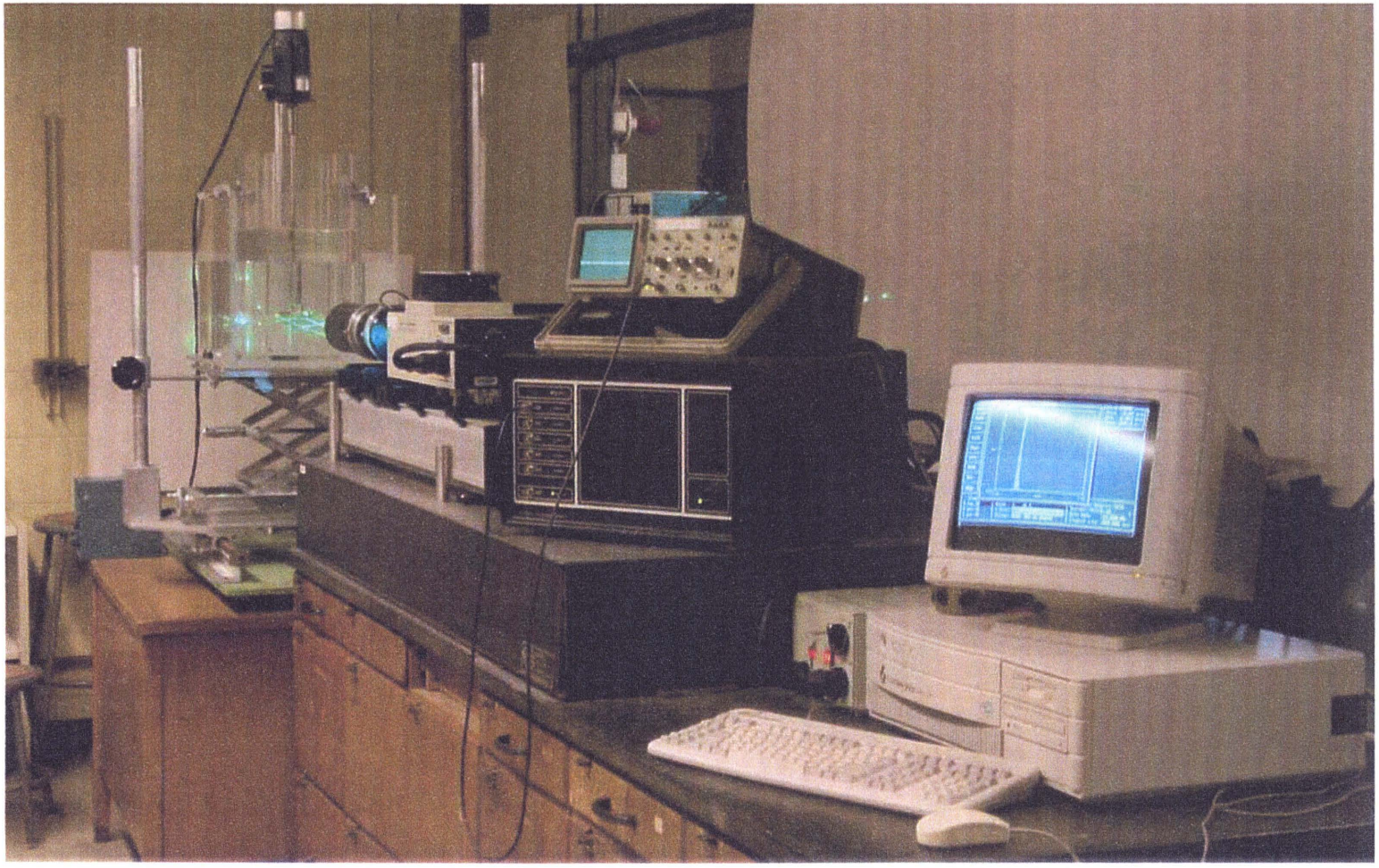

Figure C.1 Laser-Doppler velocimetry (DANTEC 55X)

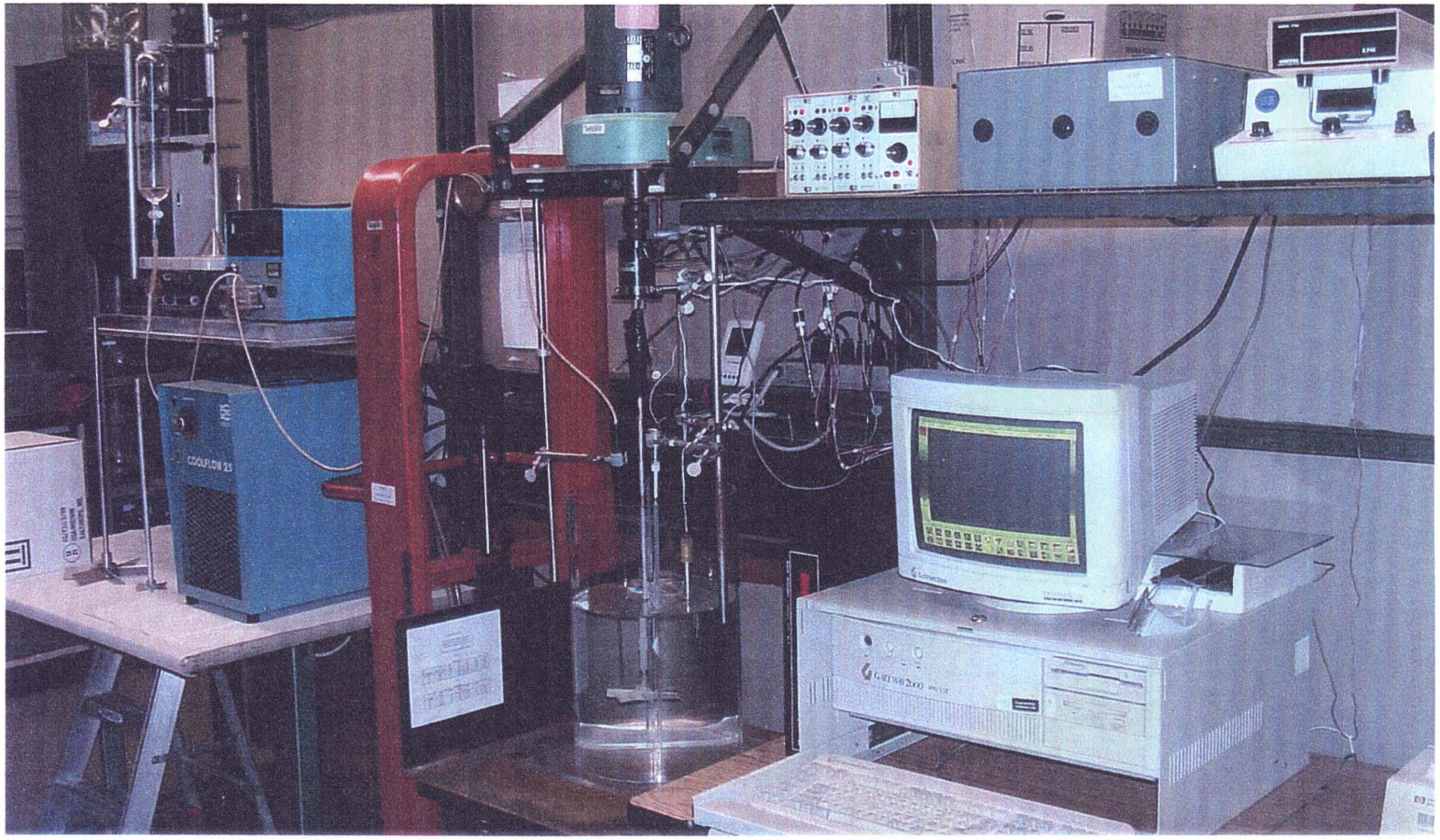

Figure C.2 Mixing-precipitation system (MIXING LAB-NJIT)

Figure C.3 Coulter Multisizer (COULTER ELECTRONICS, Model TA)

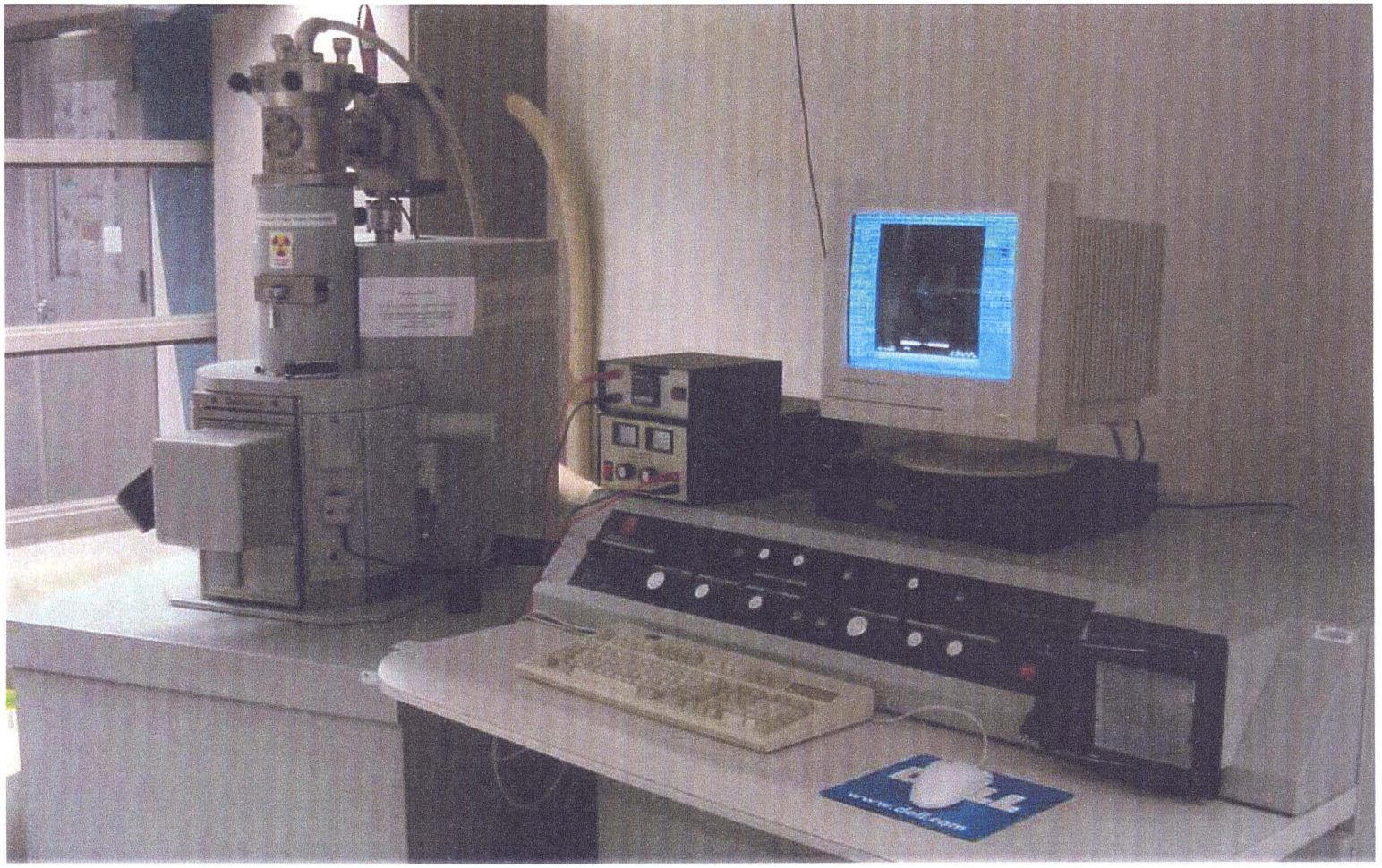

Figure C.4 Environmental Scanning Electron Microscope (PHILIPS ELECTRO SCAN 2020)

Figure C.5 Workstation (SILICON GRAPHICS)

REFERENCES

Abujelala, M. T. and Lilley, D. G. (1984). Limitations and empirical extensions of the k-ε model as applied to turbulent confined swirling flow. *Chemical Engineering Communications*, **31**, 223-236.

Aoun, M., Plasari, E., David, R. and Villermaux, J. (1996). Are barium sulphate kinetics sufficiently known for testing precipitation reactor models?. *Chemical Engineering Science*, **51**(10), 2449-2458.

Armenante, P. M. and Chang, G.-M. (1998). Power consumption in agitated vessels provided with multiple-disk turbines. *Industrial & Engineering Chemistry Research*, **37**(1), 284-291.

Armenante, P. M. and Chou, C. (1996). Velocity profiles in a baffled vessel with single or double pitched-blade turbine. *A.I.Ch.E. Journal*, **42**,(1), 42-54.

Armenante, P. M. and Kirwan, D. J. (1989). Mass transfer to microparticles in agitated systems. *Chemical Engineering Science*, **44**(12), 2781-2796.

Armenante, P. M. and Uehara-Nagamine, E. (1998). Effect of low off-bottom impeller clearance on the minimum agitation speed for complete suspension of solids in stirred tanks. *Chemical Engineering Science*, **53**(9), 1757-1775.

Armenante, P. M., Uehara-Nagamine, E. and Susanto, J. (1998). Determination of correlations to predict the minimum agitation speed for complete solid suspension in agitated vessels. *Canadian Journal of Chemical Engineering*, **76**(3), 413-419.

Åslund, B. L. and Rasmuson, Å. C. (1992). Semibatch reaction crystallization of benzoic acid. *A.I.Ch.E. Journal*, **38**(3), 328-342.

Bakker, R. A. and Van den Akker, H. E. A. (1994a). A computational study of chemical reactors on the basis of micromixing models. *Institution of Chemical Engineers Symposium Series*, **136**, 259-266, *Transactions of the Institution of Chemical Engineers*, **72**(A), 733-738.

Bakker, R. A. and Van den Akker, H. E. A. (1994b). Single-phase flow in stirred reactors. *Transactions of the Institution of Chemical Engineers*, **72**(A), 583-593.

Bakker, R. A. and Van den Akker, H. E. A. (1996). A Lagrangian description of micromixing in a stirred tank reactor using 1D-micromixing models in a CFD flow field. *Chemical Engineering Science*, **51**(11), 2643-2648.

Bakker, R. A., Myers, K. J., Ward, R. W. and Lee, C. K. (1996). The laminar and turbulent flow pattern of a pitched blade turbine. *Transactions of the Institution of Chemical Engineers*, **76**(A), 485-491.

Baldyga, J. (1989). Turbulent mixer model with application to homogeneous, instantaneous chemical reactions. *Chemical Engineering Science*, **44**(5), 1175-1182.

Baldyga, J. and Bourne, J. R. (1984). A fluid mechanical approach to turbulent mixing and chemical reaction. *Chemical Engineering Communications*, **28**, 231-281.

Baldyga, J. and Bourne, J. R. (1988). Micromixing in inhomogeneous turbulence. *Chemical Engineering Science*, **43**(1), 107-112.

Baldyga, J. and Bourne, J. R. (1989). Simplification of micromixing calculations. *Chemical Engineering Journal*, **42**(2), 83-101.

Baldyga, J. and Bourne, J. R. (1990). Comparison of the engulfment and the interaction-by-exchange-with-the-mean micromixing models. *Chemical Engineering Journal*, **45**(1), 25-31.

Baldyga, J. and Bourne, J. R. (1992). Interactions between mixing on various scales in stirred tank reactors. *Chemical Engineering Science* **47**(8), 1839-1848.

Baldyga, J. and Bourne, J. R. (1999). *Turbulent Mixing and Chemical Reactions*. John Wiley & Sons, New York.

Baldyga, J. and Orciuch, W. (1997). Closure problem for precipitation. *Transactions of the Institution of Chemical Engineers*, **75**(A), 160-170.

Baldyga, J. and Rohani, S. (1987). Micromixing described in terms of inertial-convective disintegration of large eddies and viscous-convective interactions among small eddies. *Chemical Engineering Science*, **42**(11), 2611-2619.

Baldyga, J., Bourne, J. R. and Hearn, S. J. (1997b). Interaction between chemical reactions and mixing on various scales. *Chemical Engineering Science*, **52**(4), 457-466.

Baldyga, J., Bourne, J. R. and Yang Yang (1993). Influence of feed pipe diameter on mesomixing in stirred tank reactors. *Chemical Engineering Science*, **48**(19), 3383-3390.

Baldyga, J., Henczka, M. and Orciuch, W. (1997a). Closure problem for mixing and precipitation in inhomogeneous turbulent flow. *Proceedings of the Symposium on Crystallization and Precipitation,* Lappeenranta, Finland, (Edited by S. Palosaari and H. Niemi), May 12-14 1997, Acta Polytechnica Scandinavica, Helsinki, Finland, pp. 41-43.

Baldyga, J., Podgórska, W. and Pohorecki, R. (1995). Mixing-precipitation model with application to double feed semibatch precipitation. *Chemical Engineering Science*, **50**(8), 1281-1300.

Barresi, A. A., Marchisio, D. and Baldi, G. (1999). On the role of micro- and mesomixing in a continuous Couette-type precipitator. *Chemical Engineering Science*, **54**(14), 2339-2349.

Becker, G. E. and Larson, M. A. (1969). Mixing effects in continuous crystallization. *Chemical Engineering Progress Symposium Series*, **65**(95), 14-23.

Bernard-Michel, B., Pons, M. N., Vivier, H. and Rohani, S. (1999). The study of calcium oxalate precipitation using image analysis. *Chemical Engineering Journal*, **75**(2), 93-103.

Bernard-Michel, B., Testa, J. P., Pons, M. N. and Vivier, H. (1997). Quantification of mixing effects. Effects on barium sulfate morphology. *Recents Progres en Genie des Procedes, Mixing IX, Multiphase Systems* **11**(51), 365-372.

Bird, R. W., Stewart, W. E. and Lightfoot, E. N. (1960). *Transport Phenomena*. John Wiley and Sons, New York.

Bourne, J. R. (1993). What does the modelling of reactive flows ask of CFD?. *Revue de l'Institut Francais du Pétrole*, **48**(6), 615-631.

Bourne, J. R. and Dell'Alva, P. (1987). Micro- and macro-mixing in stirred tank reactors of different sizes. *Chemical Engineering Research and Design*, **65**(2), 180-186.

Bourne, J. R. and Hilber, C. P. (1990). The Productivity of micromixing-controlled reactions: effect of feed distribution in stirred tanks. *Transactions of the Institution of Chemical Engineers*, **68**(A), 51-56.

Bourne, J. R. and Thoma, S. A. (1991). Some factors determining the critical feed time of a semi-batch reactor. *Transactions of the Institution of Chemical Engineers*, **69**(A), 321-323.

Bourne, J. R. and Yu, S. (1994). Investigation of micromixing in stirred tank reactors using parallel reactions. *Industrial & Engineering Chemistry Research*, **33**(1), 41-55.

Bourne, J. R., Gholap, V. and Rewatkar, V. B. (1995). The influence of viscosity on the product distribution of fast parallel reactions. *Chemical Engineering Journal*, **58**(1), 15-20.

Box, G. E., Hunter, W. G. and Hunter, J. S. (1978). *Statistics for Experimenters, An Introduction to Design, Data Analysis and Model Building*. John Wiley & Sons, New York.

Boysan, F., Ayers, W. H. and Swithenbank, J. (1882). A fundamental mathematical modelling approach to cyclone design. *Transactions of the Institution of Chemical Engineers*, **60**(3), 222-230.

Bromley, L. A. (1972). Thermodynamic properties of strong electrolytes in aqueous solutions. *A.I.Ch.E. Journal*, **19**(2), 313-320.

Brucato, A., Ciofalo, M., Grifasi, F. and Micale, G. (1998). Numerical prediction of flow fields in baffled stirred vessels: a comparison of alternative modelling approaches. *Chemical Engineering Science*, **53**(21), 3653-3684.

Brucato, A., Ciofalo, M., Grisafi, F. and Micale, G. (1994). Complete numerical simulation of flow fields in baffled stirred vessels: the Inner-Outer approach. *Institution of Chemical Engineers Symposium Series*, **136**, 155-162.

Chang, L.-J., Mehta, R. V. and Tarbell, J. M. (1986). An evaluation of models of mixing and chemical reaction with a turbulence theory. *Chemical Engineering Communications*, **42**, 139-155.

Chen, J., Zheng, C. and Chen, G. (1996). Interaction of macro- and micromixing on particle size distribution in reactive precipitation. *Chemical Engineering Science*, **51**(10), 1957-1966.

Corrsin, S. (1964). The isotropic turbulent mixer: Part II. Arbitrary Schmidt number. *A.I.Ch.E. Journal*, **10**(6), 870-877.

Daskopoulos, Ph. and Harris, C. K. (1996). Three dimensional CFD simulations of turbulent flow in baffled stirred tanks: an assessment of the current position. *Institution of Chemical Engineers Symposium Series*, **140**, 1-8.

David, R. and Marcant, B. (1994). Prediction of micromixing effects in precipitation: case of double-jet precipitators. *A.I.Ch.E. Journal*, 40(3), 424-432.

Dirksen, J. A. and Ring, T. A. (1991). Fundamentals of crystallization: kinetics effects on particle size distributions and morphology. *Chemical Engineering Science*, **46**(10), 2389-2427.

Durst, F., Melling, A. and Whitelaw (1981). *Principles and Practice of Laser-Doppler Anemometer*, Second edition, Academic Press, London.

Eggels, J. G. M. (1996) Direct and Large Eddy Simulation of turbulent fluid flow using the Lattice-Boltzmann Scheme. *International Journal of Heat and Fluid Flow*, **17**, 307-323.

Falk, L., Fournier, M. C. and Villermaux, J. (1994). Scale-up of micromixing effects in stirred tank reactors by a parallel competing reaction system. *Industrial Chem. Symposium Series*, **136**, 251-258.

Fasano, J. B. and Penney, W. R. (1991a). Avoid blending mix-ups. *Chemical Engineering Progress*, **87**(10), 56-63.

Fasano, J. B. and Penney, W. R. (1991b). Cut reaction by-products by proper feed blending. *Chemical Engineering Progress*, **87**(12), 46-52.

Fitchett, D. E. and Tarbell, J. M. (1990). Effect of mixing on the precipitation of barium sulfate in an MSMPR reactor. *A.I.Ch.E. Journal*, **36**(4), 511-522.

Fluent, Inc. (1995) *FLUENT, Computational Fluid Dynamics Software User's Manual*, Hanover, New Hampshire.

Fokema, M. D. and Kresta, S. M. (1994). Importance of using the correct impeller boundary conditions for CFD simulations of stirred tanks. *Canadian Journal of Chemical Engineering*, **72**(2), 177-183.

Fort, I. (1986). Flow and Turbulence in Vessels with Axial Impellers, in *Mixing. Theory and Practice*, Vol. III (Edited by V. W. Uhl and J. B. Gray), Academic Press, Orlando, pp. 133.

Garside, J. (1991). Tailoring crystal products in precipitation processes and the role of mixing. *A.I.Ch.E. Symposium Series*, **87**(284), 16-25.

Garside, J. and Wei, H. (1998). Pumped, stirred and maybe precipitated: simulation of precipitation processes using CFD. *Proceedings of the 1997 Symposium on Crystallization and Precipitation,* Acta Polytechnica Scandinavica, Chemical Technology Series, May 12-14 1997, n 244.

Garside, J. and Tavare, S. (1985). Mixing, reaction and precipitation: limits of micromixing in an MSMPR crystallizer. *Chemical Engineering Science*, **40**(8), 1485-1493.

Genck, W. J. (1997). Crystallization's forgotten fact. *Chemical Engineering*, **44**(5), 94-100.

Genck, W. J. (2000). Better growth in batch crystallizers. *Chemical Engineering*, **47**(8), 90-95.

Gunn, D. J. and Murthy, M. S. (1972). Kinetics and mechanisms of precipitation. *Chemical Engineering Science*, **27**(6), 1293-1313.

Houcine, I., Plasari, R., David, R. and Villermaux, J. (1997). Influence of mixing characteristics on the quality and size of precipitated calcium oxalate in a pilot plant scale reactor. *Transactions of the Institution of Chemical Engineers*, **75**(A), 252-256.

Hulburt, H. M. and Katz, S. (1964). Some problems in particle technology. A statistical mechanical formulation. *Chemical Engineering Science*, **19**(8), 555-574.

Jaworski, Z. and Fort, I. (1991). Energy dissipation rate in a baffled vessel with pitched blade turbine impeller. *Collection Czechoslovakian Chemical Communications*, **56**, 1856-1867.

Jaworski, Z., Nienow, A. W. and Dyster, K. N. (1996). An LDA study of turbulent flow in a baffled vessel agitated by an axial, down-pumping hydrofoil impeller. *Canadian Journal of Chemical Engineering*, **74**(1), 3-15.

Jaworski, Z., Nienow, A. W., Koutsakos, E., Dyster, K. and Bujalski, W. (1991). An LDA study of turbulent flow in a baffled vessel agitated by a pitched blade turbine. *Transactions of the Institution of Chemical Engineers*, **69**(A), 313-320.

Jenne, M. and Resuss, M. (1999). A critical assessment on the use of k-ε turbulence models for simulation of the turbulent liquid flow induced by a rushton-turbine in baffled stirred-tank reactors. *Chemical Engineering Science*, **54**(17), 3921-3941.

Jo, M.-C. and Penney, W. R. (1994). Backmixing into reactor feedpipes caused by turbulence in an agitated vessel. *A.I.Ch.E. Symposium Series*, **90**(299), 41-49.

Karpinski, P. H. (1985). Importance of the two-step crystal growth model. *Chemical Engineering Science*, **40**(4), 641-646.

Khang, S. J. and Fitzgerald, T. J. (1975). A new probe and circuit for measuring electrolyte conductivity. *Industrial & Engineering Chemistry Fundamentals*, **14**(3), 208-213.

Kim, W.-S. and Tarbell, J. M. (1996). Micromixing effects on barium sulfate precipitation in an MSMPR reactor. *Chemical Engineering Communications*, **146**, 33-56.

Kresta, S. M. and Wood, P. E. (1991). Prediction of the three-dimensional turbulent flow in stirred tanks. *A.I.Ch.E. Journal*, **37**(3), 448-460.

Kresta, S. M. and Wood, P. E. (1993a). The flow field produced by a pitched blade turbine: characterization of turbulence and estimation of the dissipation rate. *Chemical Engineering Science*, **48**(10), 1761-1774.

Kresta, S. M. and Wood, P. E. (1993b). The mean flow field produced by a 45° pitched blade turbine: changes in the circulation pattern due to off bottom clearance. *Canadian Journal of Chemical Engineering*, **71**(1), 42-53.

Kuboi, R., Harada, M., Winterbottom, J. M. Anderson, A. J. S. and Nienow, A. W. (1986). Mixing effects in double-jet and single-jet precipitation. *Proceedings of the World Congress III of Chemical Engineering*, Tokyo, Japan, Paper 8g-302, 1040-1043.

Lane, G. L., Schwarz, M. P. and Evans, G. M. (2000). Comparison of CFD Methods for Modelling of Stirred Tanks. *Proceedings of the 10th European Conference on Mixing*, Delft, The Netherlands, July 2-5 2000, pp. 273-280.

Launder, B. E. (1989). Second-moment closure: present... and future?. *International Journal of Heat and Fluid Flow*, **10**(4), 282-300.

Liu, S. T., Nancollas, G. H. and Gasiecki, E. A. (1976). Scanning electron microscopic and kinetics studies of the crystallization and dissolution of barium sulfate crystals. *Journal of Crystal Growth*, **33**(1), 11-20.

Luo, J. Y., Gosman, A. D., Issa, R. I., Middleton, J. C. and Fitzgerald, M. K. (1993). Full flow field computation of mixing in baffled stirred vessels. *Transactions of the Institution of Chemical Engineers*, **71**(A), 342-344.

Luo, J. Y., Issa, R. I. and Gosman, a. D. (1994). Prediction of impeller induced flows in mixing vessels using multiple frames of references. *Institution of Chemical Engineers Symposium Series*, **136**, 549-556.

MacInnes, J. M. and Bracco, F. V. (1992). Stochastic particle dispersion modeling and the tracer-particle limit. *Physics of Fluids A*, **4**(12), 2809-2824.

MacTaggart, R. S., Nasr-El-Din and Masliyah, J. H. (1993). Sample withdrawal from a slurry mixing tank. *Chemical Engineering Science*, **48**(5), 921-931.

Marcant, B. and David, R. (1991). Experimental evidence for and prediction of micromixing effects in precipitation. *A.I.Ch.E. Journal*, **37**(11), 1698-1710.

Marchisio, D. L., Barresi, A. A., Baldi, G. and Fox, R. O. (2000). Comparison of different modelling approaches to turbulent precipitation. *Proceedings of the 10th European Conference on Mixing*, Delft, The Netherlands, July 2-5 2000, pp. 77-84.

Mersmann, A., Laufhütte, H. D. (1985). Scale-up of agitated vessels for different mixing processes. *Proceedings of the 5th European Conference on Mixing*, Wurzburg, West Germany: 10-12 June 1985, pp. 273-284.

Mullin, J. W. (1993). *Crystallization.* Butterworth-Heinemann, London.

Murthy, J. M., Mathur, S. R. and Choudhury, D. (1994). CFD simulation of flows in stirred tank reactors using a sliding mesh technique. *Institution of Chemical Engineers Symposium Series*, **136**, 341-348.

Nagata, S. and Nishikawa, M. (1972). Mass transfer from suspended micro particles in agitated liquids. *Proceedings of the First Pacific Chemical Engineering Congress, Society of Chemical Engineering (Japan) and A.I.Ch.E.*, Kyoto, 10-14 October, Part 3, Session 18, pp. 301-320.

Nasr-El-Din, H. A., MacTaggart, R. S. and Masliyah, J. H. (1996). Local solids concentration measurement in a slurry mixing tank. *Chemical Engineering Science*, **51**(8), 1209-1220.

Nielsen, A. E. (1957). Nucleation in barium sulfate precipitation. *Acta Chemica Scandinavica*, **11**(9), 1512-1515.

Nielsen, A. E. (1958). The kinetics of crystal growth in barium sulfate precipitation. *Acta Chemica Scandinavica*, **12**(5), 951-956.

Nielsen, A. E. (1961). Homogeneous nucleation in barium sulfate precipitation. *Acta Chemica Scandinavica*, **15**(2), 441-442.

Nielsen, A. E. (1964). *Kinetics of Precipitation.* Pergamon Press, Oxford.

Nielsen, A. E. (1969). Nucleation and growth of crystals at high supersaturation. *Kristall. Und Technik*, **4**, 17-20.

Nielsen, A. E. (1984). Electrolyte crystal growth mechanisms. *Journal of Crystal Growth*, **67**(2), 289-310.

Okamoto, Y., Nishikawa, M. and Hashimoto, K. (1981). Energy dissipation rate distribution in mixing vessels and its effects on liquid-liquid dispersion and solid-liquid mass transfer. *International Chemical Engineering*, **21**(1), 88-94.

Oldshue, J. Y. (1983). Fluid Mixing Technology and Practice. *Chemical Engineering*, **90**(12), 82-108.

Oshinowo, L., Jaworski, Z., Dyster, K. N., Marshall, E. and Nienow, A. W. (2000). Predicting the tangential velocity field in stirred tanks using the Multiple Reference Frames (MRF) Model with validation by LDA measurements. *Proceedings of the 10th European Conference on Mixing*, Delft, The Netherlands, July 2-5 2000, pp. 281-288.

Ottino, J. M. (1994). Mixing and chemical reactions a tutorial. *Chemical Engineering Science*, **49**(24A), 4005-4027.

Pagliolico, S., Marchisio, D. and Barresi, A. A. (1999). Influence of operating conditions on $BaSO_4$ crystal size and morphology in a continuous Couette precipitator. *Journal of Thermal Analysis and Calorimetry*, **56**, 1423-1433.

Paul. E. L. (1988). Design of reaction systems for specialty organic chemicals. *Chemical Engineering Science*, **43**(8), 1774-1882.

Paul. E. L. (1990). Reaction systems for bulk pharmaceutical production. *Chemistry & Industry*, No. 10, 320-325.

Pettersson, M. and Rasmuson, Å. C. (1997). Application of three-dimensional phase-Doppler anemometer to mechanically agitated crystallizers. *Transactions of the Institution of Chemical Engineers*, **75**(A), 132-141.

Pettersson, M. and Rasmuson, Å. C. (1998). Hydrodynamics of suspensions agitated by pitched-blade turbine. *A.I.Ch.E. Journal*, **44**(3), 513-527.

Phillips, R., Rohani, S. and Baldyga, J. (1999). Micromixing in a single-feed semi-batch precipitation process. *A.I.Ch.E. Journal*, **45**(1), 82-92.

Pohorecki, R. and Baldyga, J. (1983). The use of a new model of micromixing for determination of crystal size in precipitation. *Chemical Engineering Science*, **38**(1), 79-83.

Pohorecki, R. and Baldyga, J. (1988). The effects of micromixing and the manner of reactor feeding on precipitation in stirred tank reactors. *Chemical Engineering Science*, **43**(8), 1949-1954.

Press, W., Vetterling, W., Teukolsky, S. and Flannery, B. (1992). *Numerical Recipes*. Cambridge University Press, New York.

Price, C. J. (1997). Take some solid steps to improve crystallization. *Chemical Engineering Progress*, **93**(9), 34-43.

Raghava Rao, K. S. M. S. and Joshi, J. B. (1988). Liquid phase mixing in mechanically agitated vessels. *Chemical Engineering Communications*, **74**, 1-25.

Ranade, V. V. and Joshi, J. B. (1989). Flow generated by pitched blade turbines. *Chemical Engineering Communications*, **81**, 197-248.

Ranade, V. V., Mishra, V. P., Saraph, V. S., Deshpande, G. B. and Joshi, J. B. (1992). Comparison of axial flow impellers using a laser Doppler anemometer. *Industrial & Engineering Chemistry Research*, **31**(9), 2370-2379.

Randolph, A. D. and Larson, M. A. (1988). *Theory of Particulate Processes*. Second Edition. Academic Press, New York and London.

Rewatkar, V. B., Raghava Rao, K. S. M. S. and Joshi, J. B. (1990). Power consumption in mechanically agitated contactors using pitched bladed turbine impellers. *Chemical Engineering Communications*, **88**, 69-90.

Rice, R. W. and Baud, R. E. (1990). The role of micromixing in the scale-up of geometrically similar batch reactors. *A.I.Ch.E. Journal*, **36**(2), 293-298.

Rodi, W. (1984). *Turbulence Models and Their Applications in Hydraulics – A State of the Art Review*. Second Edition. Delft, The Netherlands: International Association for Hydraulic Research.

Rubinstein, R. Y. (1981). *Simulation and the Monte Carlo Method*. John Wiley & Sons, New York.

Sahu, A. K. and Joshi, J. B. (1995). Simulation of flow in stirred vessel with axial flow impeller: effects of various numerical schemes and turbulence model parameters. *Industrial & Engineering Chemistry Research*, **34**(2), 626-639.

Sahu, A. K., Kumar, P. and Joshi, J. B. (1998). Simulation of flow in stirred vessel with axial flow impeller: zonal modeling and optimization of parameters. *Industrial & Engineering Chemistry Research*, **37**(6), 2116-2130.

Samant, K. D. and Ng, K. M. (1999). Development of liquid-phase agitated reactors: synthesis, simulation and scaleup. *A.I.Ch.E. Journal*, **45**(11), 2371-2390.

Schäfer, M., Yiannekis, M., Wächter, P. and Durst, F. (1998). Trailing vortices around 45° pitched-blade impeller. *A.I.Ch.E. Journal*, **44**(6), 1233-1246.

Seckler, M. M., Bruinsma, O. S. L. and Van Rosmalen, G. M. (1995). Influence of hydrodynamics on precipitation: a computational study. *Chemical Engineering Communications*, **135**, 113-131.

Sha, Z. and Palosaari, S. (2000). Mixing and crystallization in suspensions. *Chemical Engineering Science*, **55**(11), 1797-1806.

Sturesson, C., Theliander, H. and Rasmuson, Å. C. (1995). An experimental (LDA) and numerical study of the turbulent flow behavior in the near wall and bottom regions in an axially stirred vessel. *A.I.Ch.E. Symposium Series*, **91**,102-114.

Syrjänen, J. K. and Manninen, M. T. (2000). Detailed CFD prediction of flow around a 45° pitched blade turbine. *Proceedings of the 10th European Conference. on Mixing*, Delft, The Netherlands, July 2-5 2000, pp. 265-272.

Tavare, N. S. (1986). Mixing in continuous crystallizers. *A.I.Ch.E. Journal*, **32**(5), 705-732.

Tavare, N. S. (1992). Mixing, reaction and precipitation: environment micromixing models in continuous crystallizers-I. Premixed feeds. *Computers & Chemical Engineering*, **16**(10/11), 923-936.

Tavare, N. S. and Garside, J. (1990). Simulation of reactive precipitation in a semi-batch crystallizer. *Transactions of the Institution of Chemical Engineers*, **68**(A), 115-122.

Templeton, Ch. C. (1960). Solubility of barium sulfate in sodium chloride solutions from 25° to 95°C. *Journal of Chemical Engineering Data*, **5**(4), 514-516.

Toor, H. L. (1969). Turbulent mixing of two species with and without chemical reactions. *Industrial & Engineering Chemistry Fundamentals*, **8**(4), 655-659.

Tosun, G. (1988). An experimental study of the effect of mixing on the particle size distribution in $BaSO_4$ precipitation reaction. *Proceeding of the 6th European Conference on Mixing*, Pavia, Italy: 24-26 May, pp. 161-170.

Van Leeuwen, M. L. J., Bruinsma, O. S. L. and Van Rosmalen, G. M. (1996). Influence of mixing on the product quality in precipitation. *Chemical Engineering Science*, **51**(11), 2595-2600.

Villermaux, J. and Falk, L. (1994). A generalized mixing model for initial contacting of reactive fluids. *Chemical Engineering Science*, **49**(24B), 5127-5140.

Wei, H. and Garside, J. (1997). Application of CFD modelling to precipitation systems, *Transactions of the Institution of Chemical Engineers*, **75**(A), 219-227.

Xu, Y. and McGrath, G. (1996). CFD predictions of stirred tank flows. *Transactions of the Institution of Chemical Engineers* **74**(A), 471-475.

Zauner, R. and Jones, A. G. (2000a). Mixing effects on product particle characteristics from semi-batch crystal precipitation. *Transactions of the Institution of Chemical Engineers*, **78**(A), 894-902.

Zauner, R. and Jones, A. G. (2000b). Scale-up of continuous and semibatch precipitation processes. *Industrial & Engineering Chemistry Research*, **39**(7), 2392-2403.

Zhou, G. and Kresta, S. M. (1996a). Impact of tank geometry on the maximum turbulence energy dissipation rate for impellers. *A.I.Ch.E. Journal*, **42**(9), 2476-2490.

Zhou, G. and Kresta, S. M. (1996b). Distributions of energy between convective and turbulent flow for three frequently used impellers. *Transactions of the Institution of Chemical Engineers*, **76**(A), 379-389.